Advances in Computer Vision and Pattern Recognition

ACVPR

Marco Alexander Treiber

Optimization for Computer Vision

An Introduction to Core Concepts and Methods

Springer

Advances in Computer Vision and Pattern Recognition

For further volumes:
http://www.springer.com/series/4205

Marco Alexander Treiber

Optimization for Computer Vision

An Introduction to Core Concepts and Methods

Springer

Marco Alexander Treiber
ASM Assembly Systems GmbH & Co. KG
Munich, Germany

Series Editors
Prof. Sameer Singh
Research School of Informatics
Loughborough University
Loughborough
UK

Dr. Sing Bing Kang
Microsoft Research
Microsoft Corporation
Redmond, WA
USA

ISSN 2191-6586 ISSN 2191-6594 (electronic)
Advances in Computer Vision and Pattern Recognition
ISBN 978-1-4471-5282-8 ISBN 978-1-4471-5283-5 (eBook)
DOI 10.1007/978-1-4471-5283-5
Springer London Heidelberg New York Dordrecht

Library of Congress Control Number: 2013943987

Printed on acid-free paper

Springer is part of Springer Science+Business Media (www.springer.com)

This book is dedicated to my family:
My parents Maria and Armin
My wife Birgit
My children Lilian and Marisa
I will always carry you in my heart

Preface

In parallel to the much-quoted enduring increase of processing power, we can notice that that the effectiveness of the computer vision algorithms themselves is enhanced steadily. As a consequence, more and more real-world problems can be tackled by computer vision. Apart from their traditional utilization in industrial applications, progress in the field of object recognition and tracking, 3D scene reconstruction, biometrics, etc. leads to a wide-spread usage of computer vision algorithms in applications such as access control, surveillance systems, advanced driver assistance systems, or virtual reality systems, just to name a few.

If someone wants to study this exciting and rapidly developing field of computer vision, he or she probably will observe that many publications primarily focus on the vision algorithms themselves, i.e. their main ideas, their derivation, their performance compared to alternative approaches, and so on.

Compared to that, many contributions place less weight on the rather "technical" issue of the methods of optimization these algorithms employ. However, this does not come up to the actual importance optimization plays in the field of computer vision. First, the vast majority of computer vision algorithms utilize some form of optimization scheme as the task often is to find a solution which is "best" in some respect. Second, the choice of the optimization method seriously affects the performance of the overall method, in terms of accuracy/quality of the solution as well as in terms of runtime. Reason enough for taking a closer look at the field of optimization.

This book is intended for persons being about to familiarize themselves with the field of computer vision as well as for practitioners seeking for knowledge how to implement a certain method. With existing literature, I feel that there are the following shortcomings for those groups of persons:

- The original articles of the computer vision algorithms themselves often don't spend much room on the kind of optimization scheme they employ (as it is assumed that readers already are familiar with it) and often confine themselves at reporting the impact of optimization on the performance.

- General-purpose optimization books give a good overview, but of course lack in relation to computer vision and its specific requirements.
- Dedicated literature dealing with optimization methods used in computer vision often focusses on a specific topic, like graph cuts, etc.

In contrast to that, this book aims at

- Giving a comprehensive overview of a large variety of topics of relevance in computer vision-related optimization. The included material ranges from classical iterative multidimensional optimization to up-to-date topics like graph cuts or GPU-suited total variation-based optimization.
- Bridging the gap between the computer vision applications and the optimization methods being employed.
- Facilitating understanding by focusing on the main ideas and giving (hopefully) clearly written and easy to follow explanations.
- Supplying detailed information how to implement a certain method, such as pseudocode implementations, which are included for most of the methods.

As the main purpose of this book is to introduce into the field of optimization, the content is roughly structured according to a classification of optimization methods (i.e. continuous, variational, and discrete optimization). In order to intensify the understanding of these methods, one or more important example applications in computer vision are presented directly after the corresponding optimization method, such that the reader can immediately learn more about the utilization of the optimization method at hand in computer vision. As a side effect, the reader is introduced into many methods and concepts commonly used in computer vision as well.

Besides hopefully giving easy to follow explanations, the understanding is intended to be facilitated by regarding each method from multiple points of view. Flowcharts should help to get an overview of the proceeding at a coarse level, whereas pseudocode implementations ought to give more detailed insights. Please note, however, that both of them might slightly deviate from the actual implementation of a method in some details for clarity reasons.

To my best knowledge, there does not exist an alternative publication which unifies all of these points. With this material at hand, the interested reader hopefully finds easy to follow information in order to enlarge his knowledge and develop a solid basis of understanding of the field.

Dachau
March 2013

Marco Alexander Treiber

Contents

Chapter 1
Introduction

Abstract The vast majority of computer vision algorithms use some form of optimization, as they intend to find some solution which is "best" according to some criterion. Consequently, the field of optimization is worth studying for everyone being seriously interested in computer vision. In this chapter, some expressions being of widespread use in literature dealing with optimization are clarified first. Furthermore, a classification framework is presented, which intends to categorize optimization methods into the four categories continuous, discrete, combinatorial, and variational, according to the nature of the set from which they select their solution. This categorization helps to obtain an overview of the topic and serves as a basis for the structure of the remaining chapters at the same time. Additionally, some concepts being quite common in optimization and therefore being used in diverse applications are presented. Especially to mention are so-called energy functionals measuring the quality of a particular solution by calculating a quantity called "energy", graphs, and last but not least Markov Random Fields.

1.1 Characteristics of Optimization Problems

Optimization plays an important role in computer vision, because many computer vision algorithms employ an optimization step at some point of their proceeding. Before taking a closer look at the diverse optimization methods and their utilization in computer vision, let's first clarify the concept of optimization. Intuitively, in optimization we have to find a solution for a given problem which is "best" in the sense of a certain criterion.

Consider a satnav system, for example: here the satnav has to find the "best" route to a destination location. In order to rate alternative solutions and eventually find out which solution is "best," a suitable criterion has to be applied. A reasonable criterion could be the length of the routes. We then would expect the optimization algorithm to select the route of shortest length as a solution. Observe, however, that

M.A. Treiber, *Optimization for Computer Vision: An Introduction to Core Concepts and Methods*, Advances in Computer Vision and Pattern Recognition,
DOI 10.1007/978-1-4471-5283-5_1, © Springer-Verlag London 2013

other criteria are possible, which might lead to different "optimal" solutions, e.g., the time it takes to travel the route leading to the fastest route as a solution.

Mathematically speaking, optimization can be described as follows: Given a function $f : S \rightarrow \mathbb{R}$ which is called the *objective function*, find the argument x^* which minimizes f:

$$x^* = \arg \min_{x \in S} f(x) \tag{1.1}$$

S defines the so-called solution set, which is the set of all possible solutions for our optimization problem. Sometimes, the unknown(s) x are referred to *design variables*. The function f describes the optimization criterion, i.e., enables us to calculate a quantity which indicates the "goodness" of a particular x.

In the satnav example, S is composed of the roads, streets, motorways, etc., stored in the database of the system, x^* is the route the system has to find, and the optimization criterion $f(x)$ (which measures the optimality of a possible solution) could calculate the travel time or distance to the destination (or a combination of both), depending on our preferences.

Sometimes there also exist one or more additional constraints which the solution x^* has to satisfy. In that case we talk about *constrained optimization* (opposed to *unconstrained optimization* if no such constraint exists). Referring to the satnav example, constraints could be that the route has to pass through a certain location or that we don't want to use toll roads.

As a summary, an optimization problem has the following "components":

- One or more design variables x for which a solution has to be found
- An objective function $f(x)$ describing the optimization criterion
- A solution set S specifying the set of possible solutions x
- (optional) One or more constraints on x

In order to be of practical use, an optimization algorithm has to find a solution in a reasonable amount of time with reasonable accuracy. Apart from the performance of the algorithm employed, this also depends on the problem at hand itself. If we can hope for a numerical solution, we say that the problem is *well-posed*. For assessing whether an optimization problem can be solved numerically with reasonable accuracy, the French mathematician Hadamard established several conditions which have to be fulfilled for well-posed problems:

1. A solution exists.
2. There is only one solution to the problem, i.e., the solution is *unique*.
3. The relationship between the solution and the initial conditions is such that small perturbations of the initial conditions result in only small variations of x^*.

If one or more of these conditions is not fulfilled, the problem is said to be *ill-posed*. If condition (3) is not fulfilled, we also speak of *ill-conditioned* problems.

Observe that in computer vision, we often have to solve so-called inverse problems. Consider the relationship $y = T(x)$, for example. Given some kind of observed data y, the inverse problem would be the task to infer a different data representation x from y. The two representations are related via some kind of transformation T. In order to infer x from y directly, we need to know the inverse of T, which explains the name. Please note that this inverse might not exist or could be ambiguous. Hence, inverse problems often are ill-posed problems.

An example of an inverse problem in computer vision is the task of image restoration. Usually, the observed image I is corrupted by noise, defocus, or motion blur. $I(x, y)$ is related to the uncorrupted data R by $I = T(R) + n$, where T could represent some kind of blur (e.g., defocus or motion) and n denotes an additive noise term. Image restoration tries to calculate an estimate of R (termed $\hat{R}$ in the following) from the sensed image I.

A way out of the dilemma of ill-posedness here is to turn the ill-posed problem into a well-posed optimization problem. This can be done by the definition of a so-called energy E, which measures the "goodness" of $\hat{R}$ being an estimation of R. Obviously, E should measure the data fidelity of $\hat{R}$ to I and should be small if $\hat{R}$ doesn't deviate much from I, because usually R is closely related to I. Additional (a priori) knowledge helps to ensure that the optimization problem is well-posed, e.g., we can suppose that the variance of $\hat{R}$ should be as small as possible (because many images contain rather large regions of uniform or slowly varying brightness/color).

In general, the usage of optimization methods in computer vision offers a variety of advantages; among others there are in particular to mention:

- Optimization provides a suitable way of dealing with noise and other sources of corruption.
- The optimization framework enables us to clearly separate between problem formulation (design of the objective function) and finding the solution (employing a suitable algorithm for finding the minimum of the objective function).
- The design of the objective function provides a natural way to incorporate multiple source of information, e.g., by adding multiple terms to the energy function E, each of them capturing a different aspect of the problem.

1.2 Categorization of Optimization Problems

Optimization methods are widely used in numerous computer vision applications of quite diverse nature. As a consequence, the optimization methods which are best suited for a certain application are of quite different nature themselves. However, the optimization methods can be categorized according to their properties. One popular categorization is according to the nature of the solution set S (see e.g. [7]), which will be detailed below.

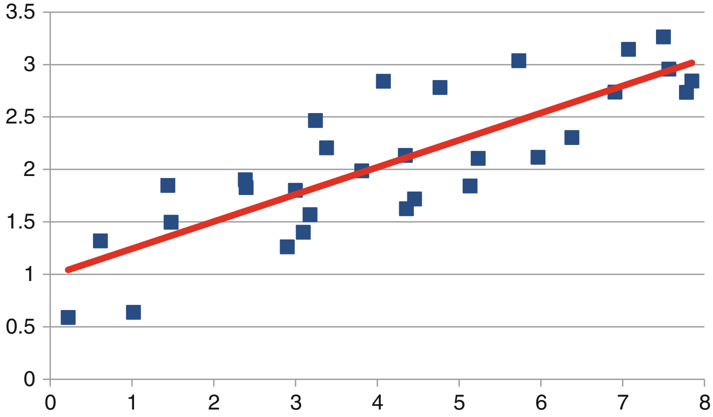

Fig. 1.1 Depicting a set of data points (*blue squares*) and the linear regression line (*bold red line*) minimizing the total sum of squared errors

1.2.1 Continuous Optimization

We talk about *continuous optimization* if the solution set S is a continuous subset of $\mathbb{R}^n$. Typically, this can be a bounded region of $\mathbb{R}^n$, such as a subpixel position $[x, y]$ in a camera image (which is bounded by the image width W and height H: $[x, y] \in [0, \ldots, W-1] \times [0, \ldots, H-1]$) or an m-dimensional subspace of $\mathbb{R}^n$ where m (e.g., a two-dimensional surface of a three-dimensional space – the surface of an object). Here, the bounds or the subspace concept acts as constraints, and these are two examples why continuous optimization methods often have to consider constraints.

A representative application of continuous optimization is *regression*, where observed data shall be approximated by functional relationship. Consider the problem of finding a line that fits to some measured data points $[x_i, y_i]$ in a two-dimensional space (see Fig. 1.1). The line l to be found can be expressed through the functional relationship $l : y = mx + t$. Hence, the problem is to find the parameters m and t of the function. A criterion for the goodness of a particular fit is how close the measured data points are located with respect to the line. Hence, a natural choice for the objective function is a measure of the overall squared distance:

$$f_l(\mathbf{x}) = \sum_i |y_i - (m \cdot x_i + t)|^2$$

Continuous optimization methods directly operate on the objective function and intend to find its minimum numerically. Typically, the objective function $f(\mathbf{x})$ is multidimensional where $\mathbf{x} \in \mathbb{R}^n$ with $n > 1$. As a consequence, the methods often are of iterative nature, where a one-dimensional minimum search along a certain search direction is performed iteratively: starting at an initial solution $\mathbf{x}_{i-1}$, each step i first determines the search direction $\mathbf{a}_i$ and then performs a one-dimensional optimization of $f(\mathbf{x})$ along $\mathbf{a}_i$ yielding an updated solution $\mathbf{x}_i$. The next step repeats this proceeding until convergence is achieved.

A further categorization of continuous optimization methods can be done according to the knowledge of $f(\mathbf{x})$ which is taken into account during optimization: some methods only use knowledge of $f(\mathbf{x})$, some additionally utilize knowledge of its first derivative $\nabla f(\mathbf{x})$ (gradient), and some also make use of its second derivative, i.e., the Hessian matrix $\mathbf{H}(f(\mathbf{x}), \mathbf{x})$.

1.2.2 Discrete Optimization

Discrete optimization deals with problems where the elements of the solution set S take discrete values, e.g., $S \subseteq \mathbb{Z}^n = \{i_1, i_2, \ldots, i_n\}; i_n \in \mathbb{Z}$.

Usually, discrete optimization problems are *NP-hard* to solve, which, informally speaking, in essence states that there is no known algorithm which finds the correct solution in polynomial time. Therefore, execution times soon become infeasible as the size of the problem (the number of unknowns) grows.

As a consequence, many discrete optimization methods aim at finding approximate solutions, which can often be proven to be located within some reasonable bounds to the "true" optimum. These methods are often compared in terms of the quality of the solution they provide, i.e., how close the approximate solution gets to the "true" optimal solution. This is in contrast to continuous optimization problems, which aim at optimizing their rate of convergence to local minima of the objective function.

In practice it turns out that the fact that the solution can only take discrete values, which acts as an additional constraint, often complicates matters when we efficiently want to find a solution. Therefore, a technique called *relaxation* can be applied, where the discrete problem is transformed into its continuous version: The objective function remains unchanged, but now the solution can take continuous values, e.g., by replacing $S_\mathrm{d} \subseteq \mathbb{Z}^n$ with $S_\mathrm{c} \subseteq \mathbb{R}^n$, i.e., the (additional) constraint that the solution has to take discrete values is dropped. The continuous representation can be solved with an appropriate continuous optimization technique. A simple way of deriving the discrete solution x_d^* from the thus obtained continuous one x_c^* is to choose that element of the discrete solution set S_d which is closest to x_c^*. Please note that there is no guarantee that x_d^* is the optimal solution of the discrete problem, but under reasonable conditions it should be sufficiently close to it.

1.2.3 Combinatorial Optimization

In *combinatorial optimization*, the solution set S has a finite number of elements, too. Therefore, any combinatorial optimization problem is also a discrete problem. Additionally, however, for many problems it is impractical to build S as an explicit enumeration of all possible solutions. Instead, a (combinatorial) solution can be expressed as a *combination* of some other representation of the data.

To make things clear, consider to the satnav example again. Here, S is usually not represented by a simple enumeration of all possible routes from the start to a destination location. Instead, the data consists of a map of the roads, streets, motorways, etc., and each route can be obtained by combining these entities (or parts of them). Observe that this allows a much more compact representation of the solution set.

This representation leads to an obvious solution strategy for optimization problems: we "just" have to try all possible combinations and find out which one yields the minimum value of the objective function. Unfortunately, this is infeasible due to the exponential growth of the number of possible solutions when the number of elements to combine increases (a fact which is sometimes called *combinatorial explosion*).

An example of combinatorial optimization methods used in computer vision are the so-called graph cuts, which can, e.g., be utilized in segmentation problems: consider an image showing an object in front of some kind of background. Now we want to obtain a reasonable segmentation of the foreground object from the background. Here, the image can be represented by a graph $G = (V, E)$, where each pixel i is represented by a vertex $v_i \in V$, which is connected to all of its neighbors via an edge $e_{ij} \in E$ (where pixels i and j are adjacent pixels; typically a 4-neighborhood is considered).

A solution s of the segmentation problem which separates the object region from the background consists of a set of edges (where each of these edges connects a pixel located at the border of the object to a background pixel) and can be called a cut of the graph. In order to find the best solution, a cost c_{ij} can be assigned to each edge e_{ij}, which can be derived from the intensity difference between pixel i and j: the higher the intensity difference, the higher c_{ij}. Hence, the solution of the problem is equal to find the cut which minimizes the overall cost along the cut. As each cut defines a combination of edges, graph cuts can be used to solve combinatorial optimization problems. This combinatorial strategy clearly is superior to enumerate all possible segmentations and seek the solution by examination of every element of the enumeration.

1.2.4 Variational Optimization

In *variational optimization,* the solution set S denotes a subspace of *functions* (instead of values in "normal" optimization), i.e., the goal is to find a function which best models some data.

A typical example in computer vision is *image restoration*, where we want to infer an "original" image $R(x, y)$ without perturbations based on a noisy or blurry observation $I(x, y)$ of that image. Hence, the task is to recover the function $R(x, y)$ which models the original image. Consequently, restoration is an example of an inverse problem.

Observe that this problem is ill-posed by nature, mainly because the number of unknowns is larger than the number of observations and therefore many solutions can be aligned with the observation. Typically, we have to estimate $W \times H$ pixel in R and, additionally, some other quantities which model the perturbations like noise variance or a blur kernel, but we have only $W \times H$ observations in I.

Fortunately, such problems can often be converted into a well-posed optimization problem by additionally considering prior knowledge. Based on general considerations, we can often state that some solutions are more likely than others. In this context, the usage of the so-called smoothness assumption is quite common. This means that solutions which are "smooth," i.e., take constant or slowly varying values, are to be favored and considered more likely.

A natural way to consider such a priori information about the solution is the usage of a so-called energy functional$E$as objective function (a more detailed description is given below in the next section). E measures the "energy" of a particular explanation $\hat{R}$ of the observed data I. If E has low values, $\hat{R}$ should be a good explanation of I. Hence, seeking the minimum of E solves the optimization problem.

In practice E is composed of multiple terms. At first, the so-called external energy models the fidelity of a solution $\hat{R}$ to the observed data I. Obviously, $\hat{R}$ is a good solution if it is close to I. In order to resolve the discrepancy between the number of observed data and unknowns, additional prior knowledge is introduced in E. This term is called *internal energy*. In our example, most natural images contain large areas of uniform or smoothly varying brightness, so a reasonable choice for the internal energy is to integrate all gradients observed in I. As a consequence, the internal energy acts as a regularization term which favors solutions which are in accordance with the smoothness assumption.

To sum it up, the introduction of the internal energy ensures the well-posedness of variational optimization problems. A smoothness constraint is quite common in this context.

Another example are so-called active contours, e.g., "snakes," where the course of a parametric curve has to be estimated. Imagine an image showing an object with intensity distinct from background intensity, but some parts of its boundary cannot be clearly separated from the background. The sought curve should pass along the borders of this object. Accordingly, its external energy is measured by local intensity gradients along the curve. At the same time, object boundaries typically are smooth. Therefore, the internal energy is based on first- and second-order derivatives. These constraints help to fully describe the object boundary by the curve, even at positions where, locally, the object cannot be clearly separated from the background.

A graphical summarization of the four different types of solution sets can be seen in Fig. 1.2.

1.3 Common Optimization Concepts in Computer Vision

Before taking a closer look at the diverse optimization methods, let's first introduce some concepts which are of relevance to optimization and, additionally, in widespread use in computer vision.

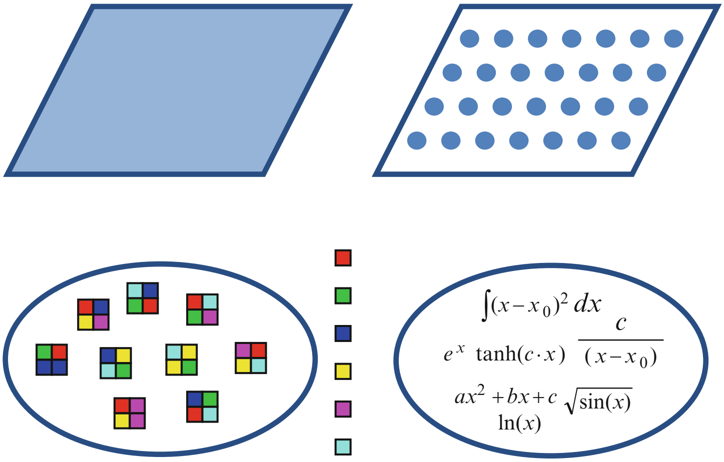

Fig. 1.2 Illustrating the different types of solution sets: continuous (blue two-dimensional region, *upper left*), discrete (grid, *upper right*), combinatorial (combinations of four color squares, *lower left*), and variational (space of functions, *lower right*)

With the help of energy functions, for example, it is possible to evaluate and compare different solutions and thus use this measure to find the optimal solution. The well-known MAP estimator, which finds the best solution by estimating the "most likely" one, given some observed data, can be considered as one form of energy minimization.

Markov Random Fields (MRFs) are a very useful model if the "state" of each pixel (e.g., a label or intensity value) is related to the states of its neighbors, which makes MRFs suitable for restoration (e.g., denoising), segmentation, or stereo-matching tasks, just to name a few.

Last but not least, many computer vision tasks rely on establishing correspondences between two entities. Consider, for example, an object which is represented by a set of characteristic points and their relative position. If such an object has to be detected in a query image, a common proceeding is to extract characteristic points for this image as well and, subsequently, try to match them to the model points, i.e., to establish correspondences between model and query image points.

In addition to this brief explanation, the concepts of energy functions, graphs, and Markov Random Fields are described in more detail in the following sections.

1.3.1 Energy Minimization

The concept of so-called energy functions is a widespread approach in computer vision. In order to find the "best" solution, one reasonable way is to quantify how "good" a particular solution is, because such a measure enables us to compare different solutions and select the "best". Energy functions E are widely used in this context (see, e.g., [6]).

Generally speaking, the "energy" is a measure how plausible a solution is. High energies indicate bad solutions, whereas a low energy signalizes that a particular solution is suitable for explaining some observed data. Some energies are so-called functionals. The term "functional" is used for operators which map a functional relationship to a scalar value (which is the energy here), i.e., take a function as argument (which can, e.g., be discretely represented by a vector of values) and derive a scalar value from this. Functionals are needed in variational optimization, for example.

With the help of such a function, a specific energy can be assigned to each element of the solution space. In this context, optimization amounts to finding the argument which minimizes the function:

$$x^* = \arg\min_{x \in S} E(x) \tag{1.2}$$

As already mentioned in the previous section, E typically consists of two components:

1. A data-driven or external energy E_{ext}, which measures how "good" a solution explains the observed data. In restoration tasks, for example, E_{ext} depends on the fidelity of the reconstructed signal $\hat{R}$ to the observed data I.
2. An internal energy E_{int}, which exclusively depends on the proposed solution (i.e., is independent on the observed data) and quantifies its plausibility. This is the point where a priori knowledge is considered: based on general considerations, we can consider some solutions to be more likely than others and therefore assign a low internal energy to them. In this context it is often assumed that the solution should be "smooth" in a certain sense. In restoration, for example, the proposed solution should contain large areas with uniform or very smoothly varying intensity, and therefore E_{int} depends on some norm of the sum of the gradients between adjacent pixels.

Overall, we can write:

$$E = E_{\text{ext}} + \lambda \cdot E_{\text{int}} \tag{1.3}$$

where the parameter λ specifies the relative weighting between external and internal energy. High values of λ tend to produce smoothly varying optimization results (if E_{int} measures the smoothness of the solution), whereas low values of λ favor results being close to the observed values.

Please observe that the so-called MAP (maximum a posteriori) estimation, which is widely used, too, is closely related to energy minimization. MAP estimation tries to maximize the probability $p(M|D)$ of some model M, given some observed data D ($p(M|D)$ is called the *posterior probability*, because it denotes a probability *after* observing the data). However, it is difficult to quantify $p(M|D)$ in practice. A way out is to apply Bayes' rule:

$$p(M|D) = \frac{p(D|M) \cdot p(M)}{p(D)} \tag{1.4}$$

where $p(D|M)$ is called the *likelihood* of the data and $p(M)$ the *prior*, which measures how probable a certain model is.

If we are only interested in finding the most likely model M^* (and not in the absolute value of the posterior at this position M^*), we can drop $p(D)$ and, additionally, take the logarithm of both sides of (1.4). As a common way to model the probabilities are Gaussian distributions, taking the logarithm simplifies calculations considerably, because it eliminates the exponentials. If we take the negative logarithm, we have:

$$M^* = \arg\min(-\log[p(D|M)] - \log[p(M)]) \tag{1.5}$$

If we set $E_{\text{ext}} = -\log[p(D|M)]$ and $E_{\text{int}} = -\log[p(M)]$, we can see that the structure of (1.5) is the same as we encountered in (1.2).

However, please note that MAP estimation is not completely equivalent to energy-based optimization in every case, as there are many possibilities how to model the terms of the energy functional, and the derivation from MAP estimation is just one kind, albeit a very principled one. Because of this principled proceeding, Bayesian modeling has several potential advantages over user-defined energy functionals, such as:

- The parameters of probability distributions can be *learned* from a set of examples, which in general is more accurate than just estimating or manually setting weights of the energy functional, at least if a suitable training base is available.
- It is possible to estimate complete probability *distributions* over the unknowns instead of determining one single value for each of them at the optimum.
- There exist techniques for optimizing unordered variables (e.g., the labels assigned to different regions in image segmentation tasks) with MAP estimations, whereas unordered variables pose a serious problem when they have to be compared in an energy function.

1.3.2 Graphs

The concept of graphs can be found in various vision applications. In the context of optimization, graphs can be used to model the problem at hand. An optimization procedure being based on a graph model can then utilize specific characteristics of the graph – such as a special structure – in order to get a fast result. In the following,

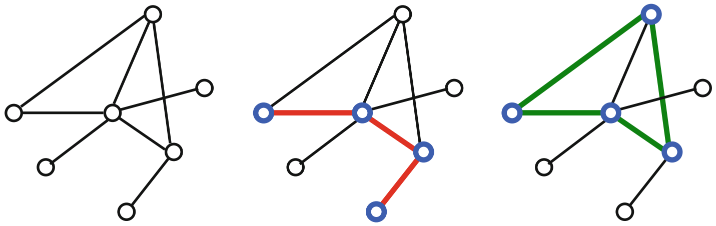

Fig. 1.3 Exemplifying a graph consisting of nodes (*circles*), which are linked by edges (*lines*) (*left*). In the graph shown in the *middle*, the *blue nodes* form a path, which are connected by the *red edges*. *Right*: example of a cycle (*blue nodes*, *green edges*)

some definitions concerning graphs and their properties are introduced (a more detailed introduction can be found in, e.g., [4]).

A *graph* $G = \{N, E\}$ is a set of *nodes* $N = \{n_1, n_2, \ldots, n_L\}$, which are also called *vertices*. The nodes are connected by *edges*, where the edges model the relationship between the nodes: Two nodes n_i and n_j are connected by an edge e_{ij} if they have a special relationship. All edges are pooled in the edge set $E = \left\{e_{ij}\right\}$ (see the left of Fig. 1.3 with *circles* as *nodes* and *lines* as *edges* for an example).

Graphs are suitable for modeling a wide variety of computer vision problems. Typically, the nodes model individual pixels or features derived from the image, such as interest points. The edges model the relationship between the pixels and features. For example, an edge e_{ij} indicates that the pixels i and j influence each other. In many cases this influence is limited to a rather small local neighborhood or adjacent pixels. Consequently, edges are confined to nearby or, even more restrictive, adjoining pixels.

Additionally, an edge can feature a direction, i.e., the edge e_{ij} can point from node n_i to node n_j, e.g., because pixel i influences pixel j, but not vice versa. In that case, we talk about a *directed* graph (otherwise the graph is called *undirected*).

Moreover, a weight w_{ij} can be associated to an edge e_{ij}. The weights serve as a measure how strongly two nodes are connected.

A *path* in a graph from node n_i to node n_k denotes a sequence of nodes starting at n_i and ending at n_k, where two consecutive nodes are connected by an edge at a time (see *blue nodes*/*red edges* in the *middle part* of Fig. 1.3). If n_i is equal to n_k, i.e., start node and termination node are the same, the path is termed a *cycle* (*right part* of Fig. 1.3). The *length* of the path is the sum of the weights of all edges along the path.

An important special case of graphs are trees. A graph is said to be a *tree* if it is undirected, contains no cycles, and, additionally, is connected, which means that there is a path between any two nodes of the graph (see *left* of Fig. 1.4). In a tree, one node can be arbitrarily picked as root node (*light red node* in *right tree* of Fig. 1.4). All other nodes have a certain *depth* from the root, which is related to the number of edges along the path between them and the root (as depth increases, color saturation of the *circles* decreases in the *right part* of Fig. 1.4).

Another subclass of graphs are *bipartite* graphs. A graph is said to be bipartite if its nodes can be split into two disjoint subsets A and B such that any edge of the

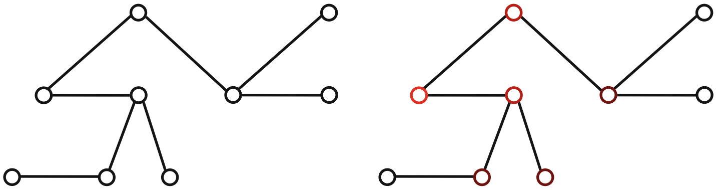

Fig. 1.4 Showing a tree example (*left*). *Right*: same tree, with specification of a root node (*light red*). Depending on their depth, the nodes get increasingly darker

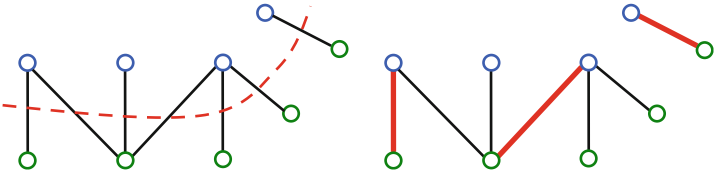

Fig. 1.5 Illustrating a bipartite graph (*left*), where the edges split the nodes into the two *blue* and *green* subsets (separated by *dashed red line*). *Right*: the same bipartite graph, with a matching example (*red edges*)

graph connects one node of A to one node of B. This means that for any edge, exactly one of the nodes it connects is an element of A and exactly one is an element of B (see *left part* of Fig. 1.5, where the *nodes* are split by the *edges* into the *blue* and the *green* subset). Bipartite graphs can be useful for so-called assignment problems, where a set of features has to be matched to another feature set, i.e., for each feature of one set, the "best corresponding" feature of the other set has to be found.

Last but not least, we talk about a *matching* M, if M is a subset of the edge set E with the property that each node of the bipartite graph belongs to at most one edge of M (see *right part* of Fig. 1.5). If each node is connected by exactly one edge $\in M$, M is said to be a *perfect matching*. Observe that the red edge set of the right graph of Fig. 1.5 is not a perfect matching, because some nodes are not connected to any of the red edges.

1.3.3 Markov Random Fields

One example of graphs are so-called Markov Random Fields (or *MRFs*), which are two-dimensional lattices of variables and were introduced for vision applications by [3]. Over the years, they found widespread use in computer vision (see, e.g., [1] for an overview).

In computer vision tasks, it is natural to regard each of those variables as one pixel of an image. Each variable can be interpreted as one node n_i of a graph $G = \{N, E\}$ consisting of a set of nodes N, which are connected by a set of edges E, as described in the previous section. The value each pixel takes is referred to the *state* of the corresponding node.

In practice, the state of each node (pixel) is influenced by other nodes (pixels). This influence is represented in the MRF through edges: if two nodes n_i and n_j influence each other, they are connected by an edge e_{ij}. Without giving the exact mathematical definition here, we note that the nature of MRFs defines that:

- Each node n_i is influenced only by a well-defined neighborhood $S(n_i)$ around it, e.g., 4-neighborhood.
- If $n_j \in S(n_i)$, the relation $n_i \in S(n_j)$ is also true, i.e., if n_j is within the local neighborhood of n_i, then the same observation holds vice versa: n_i is located within the neighborhood of n_j.

A weight s_{ij} can be assigned to each edge e_{ij}. The s_{ij} determines how strong neighboring nodes influence each other and are called *pairwise interaction potentials*. Another characteristic of Markovian models is that a future state of a node depends only on the *current* states of the nodes in the neighborhood. In other words, there is no direct dependency (on past states of them).

Normally, the nodes N represent "hidden" variables, which cannot be measured directly. However, each n_i can be related to a variable o_i which is observable. Each (n_i, o_i) pair is connected by an edge, too. A weight w_i can be assigned to each of these edges as well, and each w_i defines how strong the state of n_i is influenced by o_i.

Markov Random Fields are well suited for Bayesian-modeled energy functionals as introduced in the previous section and in particular for reconstruction or restoration problems: Given a measured image I, which is corrupted by noise, blur, etc., consider the task to reconstruct its uncorrupted version R. In order to represent this problem with an MRF, we make the following assignments:

- Each node (hidden variable) represents one unknown of the optimization problem, i.e., the state of a particular node n_i represents the (unknown) value $R(x_i, y_i)$ of the pixel $[x_i, y_i]$ of the image to be reconstructed.
- Each $R(x_i, y_i)$ is related to the measured value at this position $I(x_i, y_i)$, i.e., each o_i is assigned to one observed value $I(x_i, y_i)$.
- The weight $w(x_i, y_i)$ models how strong $R(x_i, y_i)$ is influenced by the observation $I(x_i, y_i)$. Therefore, high values of w ensure a high fidelity of the R to the measured image data. This corresponds to the relative weighting of the external energy (see parameter λ in (1.3)).
- The edges e_{ij} between the hidden variables can be considered as a way of modeling the influence of the prior probability. One way to do this is to compare the values of neighboring hidden variables (cf. the smoothness assumption, where low intensity differences between adjacent pixels are considered more likely than high differences). In doing so, the weights s_{ij} determine which neighbors influence a particular hidden variable and how strong they do this. Due to its simplicity, it is tempting to use a 4-neighborhood. In many cases, this simple neighborhood proves to be sufficient enough for modeling reality, which makes it the method of choice for many applications.

If we assume a 4-neighborhood, we can model the MRF graphically as demonstrated in Fig. 1.6. The grid of hidden variables, where each variable represents

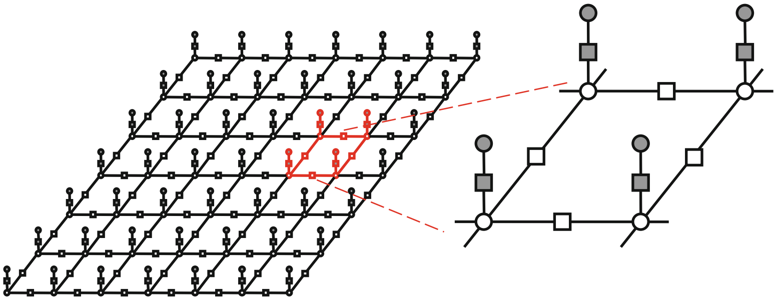

Fig. 1.6 Showing a graphical illustration of a Markov Random Field (*left*) and a more detailed illustration of a part of it (*right*)

a pixel, is shown on the left side of the figure. The right side of the figure illustrates a (zoomed) part of the MRF (red) in more detail. The hidden variables are illustrated via white circles. Each hidden variable is connected to its four neighbors via edges with weights s_x and s_y (symbolized by white squares). An observed data value (gray circles) is associated to each hidden variable with weight w (gray square). It is possible to utilize spatially varying weights $s_x(x,y)$, $s_y(x,y)$, and $w(x,y)$, if desired, but in many cases it is sufficient to use weights being constant over the entire MRF.

If the MRF models an energy functional, the following relationships are frequently used: The external or data-driven energy $E_{\mathrm{ext}}(x,y)$ of each pixel depends on the difference between the state of the hidden variable and the observed value:

$$E_{\mathrm{ext}}(x,y) = w(x,y) \cdot \rho_{\mathrm{ext}}(R(x,y) - I(x,y)) \tag{1.6}$$

The energy being based on the prior follows a smoothness assumption and therefore penalizes adjacent hidden variables of highly differing states:

$$\begin{aligned} E_{\mathrm{int}}(x,y) = & s_x(x,y) \cdot \rho_{\mathrm{int}}(I(x,y) - I(x+1,y)) + s_y(x,y) \cdot \\ & \rho_{\mathrm{int}}(I(x,y) - I(x,y+1)) \end{aligned} \tag{1.7}$$

In both (1.6) and (1.7), ρ denotes a monotonically increasing function, e.g., a linear (total variation) penalty $\rho(d) = |d|$ or a quadratic penalty $\rho(d) = |d|^2$. In the case of quadratic penalties, we talk about Gaussian Markov Random Fields (GMRFs), because quadratic penalties are best suited when the corruption of the observed signal is assumed to be of Gaussian nature.

However, in many cases, a significant fraction of measurements is disturbed by outliers with gross errors, and a quadratic weighting puts too much emphasis on the influence of these outliers. Therefore, hyper-Laplacian penalties of the type $\rho(d) = |d|^p$; $p < 1$ are also common.

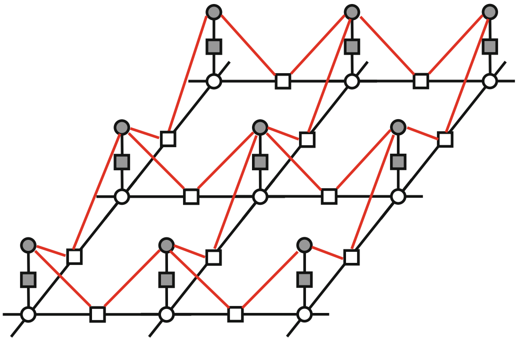

Fig. 1.7 Illustrating the structure of a so-called conditional random field. The influence of the observed data values on the pairwise interaction weights to neighboring nodes is indicated by *red lines*

The total energy associated to the current state of an MRF equals the sum of the external as well as internal energy terms over all pixels:

$$E_{\text{MRF}} = \sum_{x,y} E_{\text{int}}(x,y) + \sum_{x,y} E_{\text{ext}}(x,y) \tag{1.8}$$

Minimization of these types of MRF-based energies used to be performed by a method called *simulated annealing* (cf. [5]) when MRFs were introduced to the vision community (see [3]). Simulated annealing is an iterative scheme which, at each iteration, randomly picks a variable which is to be changed in this iteration. In later stages, the algorithm is rather "greedy," which means that it has a strong bias toward changes which reduce the energy. In early stages, however, a larger fraction of changes which does not immediately lead to lower energies is allowed. The justification for this is that the possibility to allow changes which increase the energy helps to avoid being "trapped" in a local minimum of the energy functional.

In the meantime, however, it was shown that another class of algorithm called *graph cuts* is better suited for optimization and outperforms simulated annealing in most vision applications (see, e.g., [2]). Here, the algorithm works on the graph representation of the MRF and intends to find a "cut" which separates the graph into two parts where the total sum of the weights of edges to be cut attains a minimum.

MRFs have become popular to model problems where a reasonable prior is to assume that the function to be found varies smoothly. Therefore, it can be hypothesized that each pixel has a high probability to take values identical or very similar to its neighbors, and this can be modeled very well with an MRF. Apart from the already mentioned restoration task, MRFs are also suited for segmentation, because it is unlikely that the segmentation label (all pixels belonging to the same region are "labeled" with identical value) changes frequently between neighboring pixels, which would result in a very fragmented image. The same fact applies for stereo matching tasks, where the disparity between associated pixels, which is a measure of depth of the scene, should vary slowly spatially.

A variant of MRFs are so-called conditional random fields (CRF), which differ from standard MRFs in the influence of the observed data values: More specifically, the weights of the pairwise interaction potentials can be affected by the observed values of the neighboring pixels (see Fig. 1.7). In that case, the prior depends not only on the hidden variables but additionally on the sensed data in the vicinity of each pixel.

The answer to the question whether an MRF or CRF is better depends on the application. For some applications, the additional connections between observed data values and the prior (which for MRFs do not exist) are advantageous. For example, we can observe that the smoothness assumption of MRFs has a bias toward slowly varying states of the hidden variables, which is not desirable in the presence of edges, because then they are smoothed, too. If, however, the smoothness weights $s_x(x,y)$ and $s_y(x,y)$ are reduced for pixels where a strong edge is present in the observed data, these edges are more likely to be preserved. Hence, CRFs are one means of attenuating this bias.

References

1. Blake A, Kohli P, Rother C (2011) Markov random fields for vision and image processing. MIT Press, Cambridge, MA. ISBN 978-0262015776
2. Boykov J, Veksler O, Zabih R (2001) Fast approximate energy minimization via graph cuts. IEEE Trans Pattern Anal Mach Intell 23(11):1222–1239
3. Geman S, Geman D (1984) Stochastic relaxation, Gibbs distributions, and the Bayesian restoration if images. IEEE Trans Pattern Anal Mach Intell 6(6):721–741
4. Gross JL, Yellen J (2005) Graph theory and its applications, 2nd edn. Chapman & Hall/CRC, Boca Raton. ISBN 978-1584885054
5. Kirkpatrick S, Gelatt CD, Vecchi MP (1983) Optimization by simulated annealing. Science 220 (4598):671–680
6. Rangarajan A, Vemuri B, Yuille A (eds) (2005) Energy minimization methods in computer vision and pattern recognition: 5th international workshop (proceedings). Springer, Berlin. ISBN 978-3540302872
7. Velho L, Gomes J, Pinto Carvalho PC (2008) Mathematical optimization in computer graphics and vision. Morgan Kaufmann, Amsterdam. ISBN 978-0127159515

Chapter 2
Continuous Optimization

Abstract A very general approach to optimization are local search methods, where one or, more typically, multiple variables to be optimized are allowed to take continuous values. There exist numerous approaches aiming at finding the set of values which optimize (i.e., minimize or maximize) a certain objective function. The most straightforward way is possible if the objective function is a quadratic form, because then taking its first derivative and setting it to zero leads to a linear system of equations, which can be solved in one step. This proceeding is employed in linear least squares regression, e.g., where observed data is to be approximated by a function being linear in the design variables. More general functions can be tackled by iterative schemes, where the two steps of first specifying a promising search direction and subsequently performing a one-dimensional optimization along this direction are repeated iteratively until convergence. These methods can be categorized according to the extent of information about the derivatives of the objective function they utilize into zero-order, first-order, and second-order methods. Schemes for both steps of the general proceeding are treated in this chapter.

In continuous optimization problems, the solution set S is a continuous subset of $\mathbb{R}^n$. Usually we have $n > 1$, and, therefore, we talk about multidimensional optimization. The nature of this kind of optimization problem is well understood, and there exist numerous methods for solving this task (see, e.g., [3] for a comprehensive overview). In order to find the most appropriate technique for a given problem, it is advisable (as always in optimization) to consider as much knowledge about the specific nature of the problem at hand as possible, because this specific knowledge usually leads to (sometimes dramatically) faster as well as more accurate solutions.

Hence, the techniques presented in the following are structured according to their specific characteristics. Starting with the special case of regression, where the problem leads to a quadratic form, we move on to more general techniques which perform an iterative local search. They differ in the knowledge available about first- and second-order derivatives of the objective function. Clearly, additional

M.A. Treiber, *Optimization for Computer Vision: An Introduction to Core Concepts and Methods*, Advances in Computer Vision and Pattern Recognition,
DOI 10.1007/978-1-4471-5283-5_2, © Springer-Verlag London 2013

knowledge about derivatives helps in speeding up the process in terms of iterations needed, but may not be available or time-consuming to calculate.

2.1 Regression

2.1.1 General Concept

A special case of objective functions $f(\mathbf{x})$ are quadratic forms, where the maximum order in the design variables is two. In multidimensional optimization, a quadratic objective function can be written as

$$f(\mathbf{x}) = \tfrac{1}{2} \cdot \mathbf{x}^T \cdot \mathbf{H} \cdot \mathbf{x} - \mathbf{a}^T \cdot \mathbf{x} + c \tag{2.1}$$

The minimum of such an objective function can be found analytically by setting its first derivative $\partial f(\mathbf{x})/\partial \mathbf{x}$ to zero. This leads to a system of linear equations

$$\mathbf{H} \cdot \mathbf{x}^* = \mathbf{a} \tag{2.2}$$

with $\mathbf{x}^*$ being the desired minimizer of $f(\mathbf{x})$. $\mathbf{x}^*$ can be obtained by solving the linear equation system (2.2) using standard techniques. Please observe that $\partial f(\mathbf{x})/\partial \mathbf{x} = 0$ is just a necessary condition that $f(\mathbf{x})$ takes a minimal value at $\mathbf{x}^*$ (e.g., a point with zero derivative could also be a maximum or a saddle point). However, by design of $f(\mathbf{x})$ it is usually assured that $f(\mathbf{x})$ has a unique minimum.

Obtaining a proper (unique) solution of (2.2) is possible if the so-called pseudo-inverse $\mathbf{H}^+$ exists. This is fulfilled if the columns of $\mathbf{H}$ are linearly independent. We will come back to this point later when we see how $\mathbf{H}$ is built during regression.

Now let's turn to regression. The goal of regression is to approximate observed data by some function. The kind/structure of the function is usually specified in advance (e.g., a polynomial of order up to seven), and hence, the remaining task is to determine the coefficients of the function such that it fits best to the data.

As we will see shortly, regression problems can be turned into quadratic optimization problems if the function is linear in the coefficients to be found. A typical example is an approximation of observed data $g(x)$ by a polynomial $p(x) = c_0 + c_1 \cdot x + c_2 \cdot x^2 + \cdots + c_n \cdot x^n$, which is performed quite often in practice. Clearly, this function is linear in its coefficients. A generalization to the multidimensional case where $\mathbf{x}$ is a vector is straightforward.

Now the task of polynomial regression is to determine the coefficients such that the discrepancy between the function and the observed data becomes minimal. A common measure of the error is the sum of the squared differences (SSD) between the observed data $g(x_i)$ and the values $p(\mathbf{c}, x_i)$ of the approximation function (which is a polynomial in our case) at these positions x_i. Consequently, this sum of squared differences is to be minimized. Therefore, we talk about *least* *squares regression*. Under certain reasonable assumptions about the error being introduced when observing the data (e.g., noise), the least squares solution minimizes the variance of the errors while keeping the mean error at zero at the same time (unbiased error). Altogether, the objective function in polynomial least squares regression can be formulated as

$$f_R(\mathbf{c}) = \sum_{i=1}^{N} |\, p(\mathbf{c}, x_i) - g(x_i)|^2 \tag{2.3}$$

where $g(x_i)$ is a measured data value at position x_i and N denotes the number of data values available. As can easily be seen, $f_R(\mathbf{c})$ is a quadratic form in $\mathbf{c}$ (as it is a summation of terms containing powers of the c_i's up to order two), and, therefore, its minimizer $\mathbf{c}^*$ can be determined by the solution of a suitable system of linear equations.

2.1.2 Example: Shading Correction

In order to show how this works in detail, let's consider an image processing example named *shading correction*: Due to inhomogeneous illumination as well as optical effects, the observed intensity values often decrease at image borders, even if the camera image depicts a target of uniform reflectivity which should appear uniformly bright all over the image. This undesirable effect can be compensated by determining the intensity decline at the image borders (shading) with the help of a uniformly bright target. To this end, the decline is approximated by a polynomial function $p_S(\mathbf{c}, \mathbf{x})$. Based on this polynomial, a correction function $l_S(\mathbf{x})$ can be derived such that $p_S(\mathbf{c}, \mathbf{x}) \cdot l_S(\mathbf{x}) \equiv 1$ for every pixel position $\mathbf{x}$. Subsequently, $l_S(\mathbf{x})$ can be used in order to compensate the influence of shading.

The first question to be answered is what kind of polynomial $p_S(\mathbf{c}, \mathbf{x})$ we choose. This function should be simple, but approximate the expected shading well at the same time. Typically, shading is symmetrical to the center of the camera image. Therefore, it suffices to include terms of even order only in $p_S(\mathbf{c}, \mathbf{x})$ if $\mathbf{x}$ specifies the position with respect to the camera center. Next, in order to limit the number of coefficients $\mathbf{c}$, it is assumed that a maximum order of four is sufficient for $p_S(\mathbf{c}, \mathbf{x})$ being a good approximation to observed shading. Hence, we can define $p_S(\mathbf{c}, \mathbf{x})$ as follows:

$$\begin{aligned} p_S(\mathbf{c}, \mathbf{x}) =& c_0 + c_1 \cdot u^2 + c_2 \cdot v^2 + c_3 \cdot u^2 \cdot v^2 + c_4 \cdot u^4 + \\ &+ c_5 \cdot v^4 + c_6 \cdot u^4 \cdot v^2 + c_7 \cdot u^2 \cdot v^4 + c_8 \cdot u^4 \cdot v^4 \end{aligned} \tag{2.4}$$

where $u = |x - x_c|\, y$ and $v = |y - y_c|$ denote the pixel distances to the image center $[x_c, y_c]$ in x- and y -directions. Altogether, we have nine parameters c_0 to c_8, whose numerical values are to be determined during regression. Consequently, c_0 to c_8 act as design variables in the optimization step.

In order to generate data values to which we can fit $p_S(\mathbf{c}, \mathbf{x})$, we take an image of a special target with well-defined and uniform brightness and surface properties (which should appear with uniform intensity in the camera image if shading was not present). As we want to be independent of the absolute intensity level, we take the observed intensity values $I(\mathbf{x})$ normalized with respect to the maximum observed intensity:

$$\tilde{I}(\mathbf{x}) = \frac{I(\mathbf{x})}{I_{\max}}$$

Our goal is to find a parameter setting $\mathbf{c}$ such that $p_S(\mathbf{c}, \mathbf{x})$ approximates the normalized intensities well. Hence, we can write $\tilde{I}(\mathbf{x}) = p_S(\mathbf{c}, \mathbf{x}) + e$ or, equivalently,

$$\begin{bmatrix} 1 & u^2 & v^2 & \dots & u^4 v^4 \end{bmatrix} \cdot \begin{bmatrix} c_0 \\ c_1 \\ \vdots \\ c_8 \end{bmatrix} = \tilde{I}(\mathbf{x}) + e \tag{2.5}$$

where e denotes the error to be minimized. If we compare observed data values and the polynomial at different locations $\mathbf{x}_i; i \in [1 \dots N]$, we can build one equation according to (2.5) for each data point i and stack them into a system of N equations:

$$\begin{bmatrix} 1 & {u_1}^2 & {v_1}^2 & {u_1}^2{v_1}^2 & {u_1}^4 & {v_1}^4 & {u_1}^4{v_1}^2 & {u_1}^2{v_1}^4 & {u_1}^4{v_1}^4 \\ 1 & {u_2}^2 & {v_2}^2 & {u_2}^4{v_2}^4 & {u_2}^4 & {v_2}^4 & {u_2}^4{v_2}^2 & {u_2}^2{v_2}^4 & {u_2}^4{v_2}^4 \\ \vdots & \vdots & \vdots & \vdots & \vdots & \vdots & \vdots & \vdots & \vdots \\ 1 & {u_N}^2 & {v_N}^2 & {u_N}^2{v_N}^2 & {u_N}^4 & {v_N}^4 & {u_N}^4{v_N}^2 & {u_N}^2{v_N}^4 & {u_N}^4{v_N}^4 \end{bmatrix} \cdot \begin{bmatrix} c_0 \\ c_1 \\ \vdots \\ c_8 \end{bmatrix} \approx \begin{bmatrix} \tilde{I}(\mathbf{x}_1) \\ \tilde{I}(\mathbf{x}_2) \\ \vdots \\ \tilde{I}(\mathbf{x}_N) \end{bmatrix}$$
$$\text{or } \mathbf{X} \cdot \mathbf{c} \approx \mathbf{d} \tag{2.6}$$

where the matrix $\mathbf{X}$ summarizes the position information and the data vector $\mathbf{d}$ is composed of the normalized observed intensity values $\tilde{I}$.

The goal of regression in this case is to find some coefficients $\mathbf{c}^*$ such that the sum of squared distances between the observed $\tilde{I}$ and their approximation $\mathbf{X} \cdot \mathbf{c}^*$ is minimized:

$$\mathbf{c}^* = \arg\min \|\mathbf{X} \cdot \mathbf{c} - \mathbf{d}\|^2 \tag{2.7}$$

This minimizer $\mathbf{c}^*$ of this quadratic form can be found by setting the derivative $\partial \|\mathbf{X} \cdot \mathbf{c} - \mathbf{d}\|^2 / \partial \mathbf{c}$ to zero, which leads to

$$\mathbf{X}^T \cdot \mathbf{X} \cdot \mathbf{c}^* = \mathbf{X}^T \cdot \mathbf{d} \tag{2.8}$$

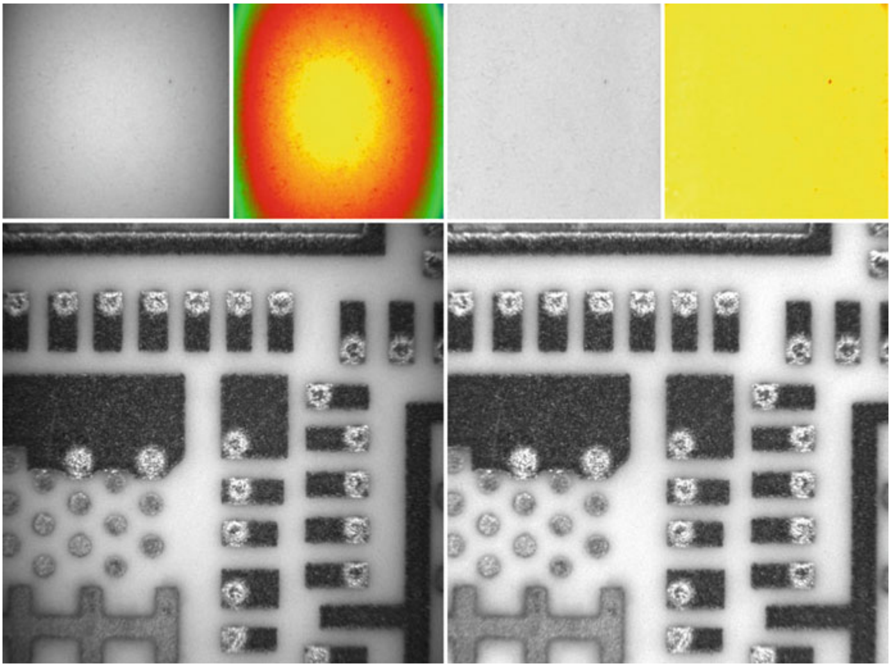

Fig. 2.1 *Top row*: camera image of a uniformly bright object showing considerable shading at image borders in grayscale and in pseudo-color (*left*) and corrected camera image of the same object in grayscale and in pseudo-color (*right*). Clearly, the shading has efficiently been removed. *Bottom row*: camera image of a PCB (*left*) and corrected image (*right*). The correction coefficients have been estimated with the calibration part shown in the *upper row*

which is called the *normal equation* of the least squares problem. A solution is possible if $\mathbf{X}^T \cdot \mathbf{X}$ is non-singular, i.e., $\mathbf{X}^T \cdot \mathbf{X}$ has linearly independent columns. This constraint can be fulfilled by a proper choice of the positions $[u, \; v]$. In that case, the pseudo-inverse exists and the solution is unique.

The system of normal equations can be solved by performing either a LR or QR decomposition of $\mathbf{X}^T \cdot \mathbf{X}$ (e.g., see [6]). The former has the advantage of being faster, whereas the latter is usually numerically more stable, especially if the matrix $\mathbf{X}^T \cdot \mathbf{X}$ is almost singular. Another way to find $\mathbf{c}^*$ is to calculate the pseudo-inverse $\left(\mathbf{X}^T \cdot \mathbf{X}\right)^+$ by performing a singular value decomposition (SVD) of $\mathbf{X}^T \cdot \mathbf{X}$ [6].

The performance of the method is illustrated in Fig. 2.1, where the upper row shows real camera pictures of a uniform calibration target featuring shading (left), especially in x-direction. After estimating the regression coefficients as described and applying a brightness correction according to them, the target appears with uniform intensity in the corrected image (right). A 3D plot of the shading function estimated with this target can be seen in Fig. 2.2.

In order to make clear that shading is mainly attributed to the camera (and not to the object being depicted in the camera images), the bottom row shows a PCB as a

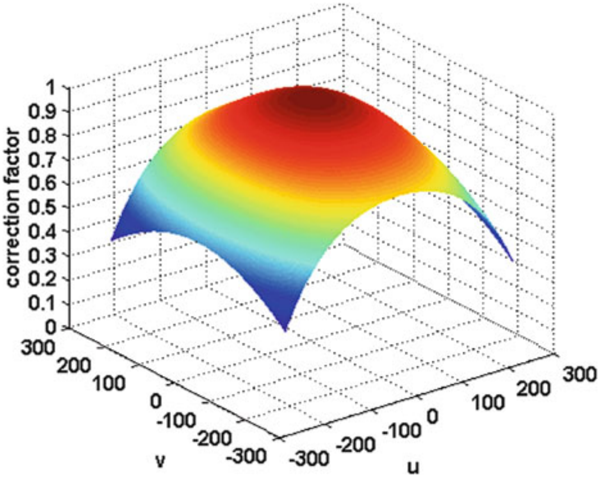

Fig. 2.2 Plot of the estimated shading function based on regression of the intensity data of the *upper left image* of Fig. 2.1

highly structured object, where shading is clearly visible. The right image shows the same PCB after correction according to the coefficients calculated through the usage of the calibration target. Observe that the background of the PCB appears uniformly bright after correction, so the results obtained with the calibration target can be transferred to other objects as well.

The matrix $\mathbf{X}$ is of dimensionality $M \times N$, which means that we have M unknowns (the coefficients of the polynomial) and N equations. Hence, $\mathbf{X}^T \cdot \mathbf{X}$ is of dimensionality $N \times N$. In order to get a unique solution, it has to be ensured that we have at least as much equations than unknowns, i.e., $N \geq M$. Usually however, there are so many data points available such that $N >> M$, which would mean that the system of normal equations to be solved would become extremely large. Consider the shading example: if we took every pixel as a separate data value, N would be in the order of hundreds of thousands or millions. In order to get to manageable data sizes, the image can be partitioned into horizontal as well as vertical tiles. For each tile, a mean intensity value can be calculated, which serves as input for (2.6). The tile position is assumed to be the center position of the tile. Taking just the mean value of the tiles significantly reduces N and also reduces the noise influence drastically.

2.2 Iterative Multidimensional Optimization: General Proceeding

The techniques presented in this chapter are universally applicable, because they:

- Directly operate on the energy function $f(x)$.
- Do not rely on a special structure of $f(x)$.

The broadest possible applicability can be achieved if only information about the values of $f(x)$ themselves is required.

The other side of the coin is that these methods are usually rather slow. Therefore, some of the methods of the following sections additionally utilize knowledge about the first- and second-order derivatives $f'(x)$ and $f''(x)$. This restricts their applicability a bit in exchange for an acceleration of the solution calculation. As was already stated earlier, it usually is best to make use of as much specific knowledge about the optimization problem at hand as possible. The usage of this knowledge will typically lead to faster algorithms.

Furthermore, as the methods of this chapter typically perform a *local* search, there is no guarantee that the *global* optimum is found. In order to avoid to get stuck in a local minimum, a reasonably good first estimate x_0 of the minimal position x^* is required for those methods.

The general proceeding of most of the methods presented in this chapter is a two-stage iterative approach. Usually, the function $f(\mathbf{x})$ is vector valued, i.e., $\mathbf{x}$ consists of multiple (say N) elements. Hence, the optimization procedure has to find N values simultaneously. Starting at an initial solution $\mathbf{x}^k$, this can be done by an iterated application of the following two steps:

1. Calculation of a so-called search direction $\mathbf{s}^k$ along which the minimal position is to be searched.
2. Update the solution by finding a $\mathbf{x}^{k+1}$ which reduces $f\left(\mathbf{x}^{k+1}\right)$ (compared to $f\left(\mathbf{x}^k\right)$) by performing a *one-dimensional search* along the direction $\mathbf{s}^k$. Because $\mathbf{s}^k$ remains fixed during one iteration, this step is also called a *line search*.

Mathematically, this can be written as

$$\mathbf{x}^{k+1} = \mathbf{x}^k + \alpha^k \cdot \mathbf{s}^k \tag{2.9}$$

where, in the most simple case, α^k is a fixed step size or – more sophisticated – is estimated during the one-dimensional search such that $\mathbf{x}^{k+1}$ minimizes the objective function along the search direction $\mathbf{s}^k$. The repeated procedure stops either if convergence is achieved, i.e., $f\left(\mathbf{x}^{k+1}\right)$ is sufficiently close to $f\left(\mathbf{x}^k\right)$ and hence we assume that no more progress is possible, or if the number of iterations exceeds an upper threshold $K_{\max}$. This iterative process is visualized in Fig. 2.3 with the help of a rather simple example objective function.

As should have become apparent, this proceeding basically involves performing a local search, meaning that there is no guarantee that the global minimum of $f(\mathbf{x})$ is found. However, in most cases of course, the global optimum would be the desired solution. In order to be sure that a local minimum also is the global one, the function has to be *convex*, i.e., the following inequality has to hold for every $\mathbf{x}_1, \mathbf{x}_2 \in \mathrm{R}^N$ and $0 < \lambda < \mathbf{1}$:

$$f(\lambda \cdot \mathbf{x}_1 + (1-\lambda) \cdot \mathbf{x}_2) \leq \lambda \cdot f(\mathbf{x}_1) + (1-\lambda) \cdot f(\mathbf{x}_2) \tag{2.10}$$

For most problems, convexity is only ensured in a limited area of the solution space, which is called the *area of convergence*. As a consequence, the iterative local

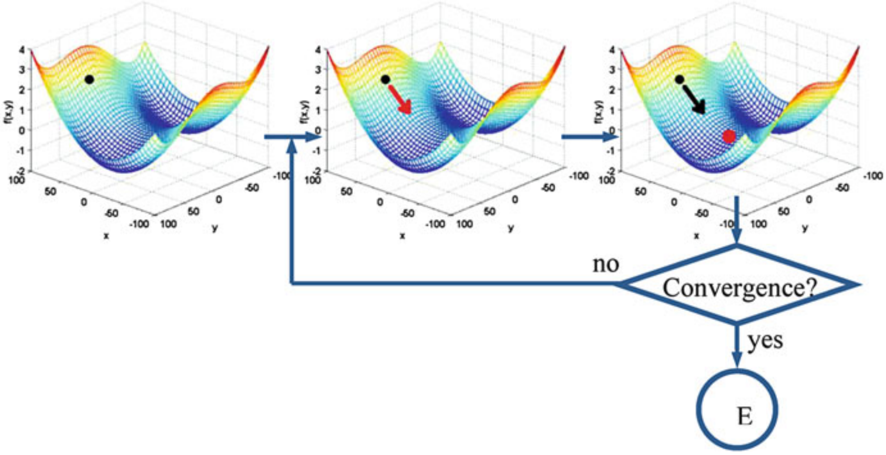

Fig. 2.3 Visualizing the iterative proceeding in multidimensional optimization when performing a local search: starting from some position (*black dot in left image*), the search direction is calculated first (*red arrow in middle image*), and then a one-dimensional optimization is performed in this direction (result: *red dot in right image*). The new position serves as a starting point for the next iteration until convergence is achieved

search methods presented below rely on a sufficiently "good" initial solution $\mathbf{x}^0$, which is located within the area of convergence of the global optimum. This also means that despite being applicable to arbitrary objective functions $f(\mathbf{x})$, local search methods are typically not suited to optimize highly non-convex functions, because then the area of convergence is very small and, as a result, there is a large risk that the local search gets stuck in a local minimum being arbitrarily far away from the desired global optimum.

In order to overcome this restriction, the local iterative search can be performed at multiple starting points $\mathbf{x}_l^0, l \in [1, 2, \ldots, L]$. However, there still is no guarantee that the global minimum is found. But the probability that the found solution is sufficiently close to the true optimum is increased significantly. Of course the cost of such a proceeding is that the total runtime of the algorithm is increased significantly.

Methods for both parts of the iterative local search (estimation of $\mathbf{s}^k$ and the one-dimensional search along $\mathbf{s}^k$) shall be presented in more detail below. Observe that some methods (like Newton's method) slightly deviate from the general proceeding just outlined, because they don't perform a one-dimensional optimization along the search direction, but take a step of fixed, predefined, or estimated size in that direction instead.

Pseudocode

```
function optimizeContinuousMultidim (in Image $I$, in objective function $f(\mathbf{x})$, in initial solution $\mathbf{x}^0$, in convergence criterion $\varepsilon$, out refined solution $\mathbf{x}^*$)
```

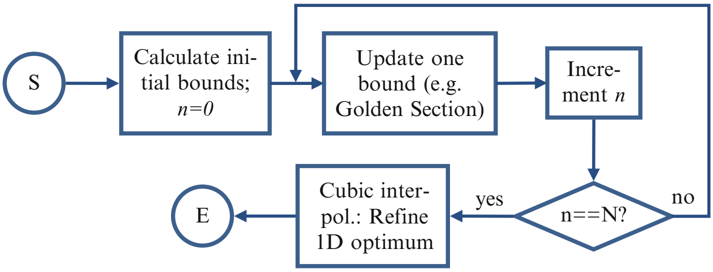
S
Calculate initial bounds; n=0
Update one bound (e.g. Golden Section)
Increment n
n==N?
no
yes
Cubic interpol.: Refine 1D optimum
E

Fig. 2.4 Flowchart of the golden section method

```
$k \leftarrow 0$
// main optimization loop
repeat
    calculate search direction $\mathbf{s}^k$ (see section 2.2.2)
    find one-dimensional minimum along direction $\mathbf{s}^k$ (see (2.9)
    and section 2.2.1) OR take one step of a fixed predefined
    or estimated size in the search direction, yielding $\mathbf{x}^{k+1}$
    $k \leftarrow k + 1$
until $\frac{f(\mathbf{x}^k)-f(\mathbf{x}^{k+1})}{f(\mathbf{x}^k)+f(\mathbf{x}^{k+1})} \leq \varepsilon$ OR $k > K_{\max}$
$\mathbf{x}^* \leftarrow \mathbf{x}^k$
```

2.2.1 One-Dimensional Optimization Along a Search Direction

In this section, step two of the general iterative procedure is discussed in more detail. The outline of the proceeding of this step is to first bound the solution and subsequently iteratively narrow down the bounds until it is possible to interpolate the solution with good accuracy. In more detail, the one-dimensional optimization comprises the following steps (see also flowchart of Fig. 2.4):

1. Determine upper and lower bounds $\mathbf{x}_u^k = \mathbf{x}^k + \alpha_u^0 \cdot \mathbf{s}^k$ and $\mathbf{x}_l^k = \mathbf{x}^k + \alpha_l^0 \cdot \mathbf{s}^k$ which bound the current solution $\mathbf{x}^k$ (α_u^0 and α_l^0 have opposite signs).
2. Recalculate the upper and lower bounds $\mathbf{x}_u^i$ and $\mathbf{x}_l^i$ in an iterative scheme, i.e., decrease the distance between $\mathbf{x}_u^i$ and $\mathbf{x}_l^i$ as the iteration proceeds. Please note that, for a better understanding, the superscript $\boldsymbol{k}$ indicating the index of the multidimensional iteration is dropped and replaced by the index $\boldsymbol{i}$ of the current one-dimensional iteration. One possibility to update the bounds is the so-called golden section method, which will be presented below. As the distance between the bounds is reduced by a fixed fraction at each iteration there, we can set the number of iterations necessary to a fixed value N.

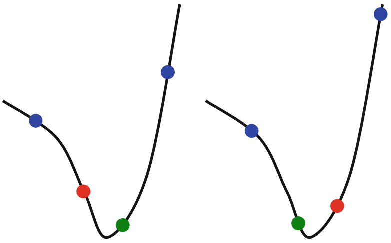

Fig. 2.5 Illustrating the refinement of the bounds of the solution. The *blue points* indicate current lower and upper bounds, whereas the *red color* of a point indicates that the point becomes a new bound. *Left*: as $\mathbf{x}_1$ (*red*) takes a higher function value than $\mathbf{x}_2$ (*green*), $\mathbf{x}_1$ is a new lower bound. *Right*: as $\mathbf{x}_2$ (*red*) takes a higher function value than $\mathbf{x}_1$ (*green*), $\mathbf{x}_2$ is a new upper bound

3. Refine the solution by applying a polynomial interpolation to the data found in step 2, where the refined bounds $\mathbf{x}_u^i$ and $\mathbf{x}_l^i$ as well as two intermediate points were found (see below). Hence, we have four data points and can perform a cubic interpolation based on these four points.

At the end of step 3, we have determined an estimate of α^k such that the update of the multidimensional solution can be calculated according to (2.9). Hence, the task of one-dimensional optimization here is to find an appropriate α^k. For the moment, let's start with a closer look at step 2 and assume that some upper as well as lower bounds α_u^0 and α_l^0 are already determined by step 1.

An important point to mention is that it is assumed that the function to be minimized is *unimodal* between $\mathbf{x}_u^k$ and $\mathbf{x}_l^k$. This means that it is convex and has only one minimum in between those two points. As we already know that the desired optimal position has to be located within the bounds $\mathbf{x}_u^0$ and $\mathbf{x}_l^0$, the task of step two can be interpreted as an iterative refinement of the upper and lower bounds until the distance between those two points is sufficiently small. To this end, the function is evaluated at two intermediate points $\mathbf{x}_1^0 = \mathbf{x}^k + \alpha_1^0 \cdot \mathbf{s}^k$ and $\mathbf{x}_2^0 = \mathbf{x}^k + \alpha_2^0 \cdot \mathbf{s}^k$. α_1^0 and α_2^0 are chosen such that $\alpha_l^0 < \alpha_1^0 < \alpha_2^0 < \alpha_u^0$, and, therefore, it is guaranteed that $\mathbf{x}_1^0$ and $\mathbf{x}_2^0$ are both located within the current bounds. Furthermore, $\mathbf{x}_1^0$ is closer to $\mathbf{x}_l^0$ than $\mathbf{x}_2^0$ is $\left|\mathbf{x}_1^0 - \mathbf{x}_l^0\right| < \left|\mathbf{x}_2^0 - \mathbf{x}_l^0\right|$. In other words, it is ensured that the four points $\mathbf{x}_l^0$, $\mathbf{x}_1^0$, $\mathbf{x}_2^0$, and $\mathbf{x}_u^0$ are strictly ordered.

Now consider the values $f\left(\mathbf{x}_1^0\right)$ and $f\left(\mathbf{x}_2^0\right)$ of the objective at the two intermediate positions: because of the unimodality constraint, we can conclude that either $f\left(\mathbf{x}_1^0\right)$ will form a new lower bound or $f\left(\mathbf{x}_2^0\right)$ will form a new upper bound of the solution. If $f\left(\mathbf{x}_1^0\right) < f\left(\mathbf{x}_2^0\right)$, then $\mathbf{x}_2^0$ will become a new upper bound of the solution, i.e., $\mathbf{x}_u^1 = \mathbf{x}_2^0$. If $f\left(\mathbf{x}_1^0\right) > f\left(\mathbf{x}_2^0\right)$, however, then $\mathbf{x}_1^0$ will form a new lower bound of the solution, i.e., $\mathbf{x}_l^1 = \mathbf{x}_1^0$ (see Fig. 2.5 for both of the two cases). Hence, at each iteration step either the lower or the upper bound is replaced by one of the two intermediate points. A repeated application of this proceeding leads to narrower bounds at each step. Eventually, they are so close that convergence is achieved.

Please note that if the unimodality constraint is violated, this proceeding might get stuck in a local minimum.

What remains to be answered is the question of where to place the intermediate points. (From now on, we replace the superscript 0 of the above equations by the index i, as we consider the iterated scheme now and the basic principle remains the same for all iteration steps.) Obviously, $\mathbf{x}_1^i$ and $\mathbf{x}_2^i$ have to be positioned such that the average performance of the method is optimized. To this end, the following two criteria must hold:

- The positions $\mathbf{x}_1^i$ and $\mathbf{x}_2^i$ should be placed symmetric about the center of the interval between the upper and lower bound, i.e., $\alpha_u^i - \alpha_2^i = \alpha_1^i - \alpha_l^i$. This is in accordance with intuition that convergence is on average achieved fastest if the distance between the two bounds is reduced by a fixed fraction, regardless of whether the upper or the lower bound is altered.
- Additionally, it is desirable to minimize the number of function evaluations as much as possible. Therefore, it is advisable to reuse the data calculated in previous iteration steps. More specifically, if, e.g., $\mathbf{x}_1^i$ becomes the new lower bound, then it would be good if we could set $\mathbf{x}_1^{i+1} = \mathbf{x}_2^i$ (or, equivalently, $\alpha_1^{i+1} = \alpha_2^i$). In turn, if $\mathbf{x}_2^i$ becomes the new upper bound, we must aim to set $\mathbf{x}_2^{i+1} = \mathbf{x}_1^i$ (or, equivalently, $\alpha_2^{i+1} = \alpha_1^i$). In order to achieve this as well, the following relation must hold: $\frac{\alpha_1^i - \alpha_l^i}{\alpha_u^i - \alpha_l^i} = \frac{\alpha_2^i - \alpha_1^i}{\alpha_u^i - \alpha_1^i}$.

  This leads to the following rules:

$$\begin{aligned} \alpha_1^i &= (1-\tau)\cdot\alpha_l^i + \tau\cdot\alpha_u^i \\ \alpha_2^i &= (1-\tau)\cdot\alpha_u^i + \tau\cdot\alpha_l^i \end{aligned} \quad \text{with} \quad \tau = \frac{3-\sqrt{5}}{2} \approx 0.38197 \tag{2.11}$$

The ratio defined by τ is called the golden section number, and therefore, this one-dimensional search method is called *golden section algorithm.*

In order to identify convergence, a suitable convergence criterion has to be defined. A reasonable choice is to reduce the size of the interval between upper and lower bound to a fixed small fraction of the size of the starting interval. By definition of τ it is ensured that the interval is reduced by a fixed fraction at each iteration step. Accordingly, convergence is achieved after a fixed number N of iteration steps are performed. Taking the above value of τ into account, N can be calculated as follows:

$$N \approx -2.078\cdot\ln\varepsilon + 3 \tag{2.12}$$

where ε defines the fraction of the original interval size to be fallen below. For example, if it is requested that convergence is achieved when the interval size is below 0.1 % of the original size (i.e., $\varepsilon = 0.001$), we have to perform $N = 18$ iteration steps.

After the iteration has terminated, the values α_l^i, α_1^i, α_2^i, and α_u^i are available. Thus, we can use these for values for an interpolation with a cubic polynomial, as the four

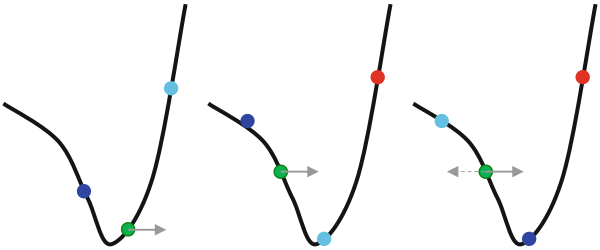

Fig. 2.6 Showing three different situations in the calculation of the initial lower and upper bounds, starting from the current solution (*green dots*). The search direction is indicated by *gray arrows*. See text for details

coefficients of the cubic polynomial can be calculated straightforward from α_l^i, α_1^i, α_2^i, and α_u^i as well as their function values (step three of the one-dimensional method). The final result of one-dimensional optimization α^k can be set according to that one of the possibly two real roots of the cubic polynomial which is located in between α_l^i and α_u^i.

Now let's come back to step one of our one-dimensional optimization scheme, the search for the initial bounds of the one-dimensional solution. The first estimate of the bounds can be done by taking a fixed step in the direction of $\mathbf{s}^k$ and another one with opposite sign, both starting from the current estimate of the minimum $\mathbf{x}^k$. As the step size is somehow arbitrary, we can simply take $\mathbf{x}_l^0 = \mathbf{x}^k - \mathbf{s}^k$ and $\mathbf{x}_u^0 = \mathbf{x}^k + \mathbf{s}^k$. If both $f\left(\mathbf{x}_l^0\right)$ and $f\left(\mathbf{x}_u^0\right)$ are larger than $f\left(\mathbf{x}^k\right)$, we're finished and the bounds are found. This situation can be seen in the left part of Fig. 2.6: The function values of the left bound estimate (blue, opposite to current search direction) as well as the right bound estimate (light blue, in current search direction) are both larger than at the current solution. Therefore, the two points can be taken as new lower and upper bounds, respectively.

If not, the exact search direction can be defined by comparing $f\left(\mathbf{x}_l^0\right)$ and $f\left(\mathbf{x}_u^0\right)$. If $f\left(\mathbf{x}_l^0\right) > f\left(\mathbf{x}_u^0\right)$, the function has a negative slope in the direction of $\mathbf{s}^k$ at $\mathbf{x}^k$ (middle picture in Fig. 2.6), which is usually the case if $\mathbf{s}^k$ was chosen properly (because we want to find a minimum, it should be expected that the slope in the search direction is negative). We can also observe that the step size was taken too small and therefore $\mathbf{x}_l^0$ and $\mathbf{x}_u^0$ don't bracket the solution yet.

Therefore, we have to update $\mathbf{x}_u^0$ iteratively. To this end, set $\mathbf{x}_u^0$ as a new intermediate point $\mathbf{x}_1 = \mathbf{x}_u^0$ and update $\mathbf{x}_u^0$ according to

$$\mathbf{x}_u^{j+1} = (1+a) \cdot \mathbf{x}_u^j - a \cdot \mathbf{x}_l^j \quad \text{with} \quad a = \frac{1+\sqrt{5}}{2} \tag{2.13}$$

This choice of the step size a ensures that $\mathbf{x}_l^j$, $\mathbf{x}_1$, and $\mathbf{x}_u^j$ can be taken directly as starting values $\mathbf{x}_l^0$, $\mathbf{x}_1^0$, and $\mathbf{x}_u^0$ of the golden section method. Furthermore, it also ensures that the steps increase in size from iteration to iteration such that a valid bracketing of the minimum is achieved in reasonable time if the (arbitrary) starting step size chosen was far too small.

The iteration stops if $f\left(\mathbf{x}_u^{j+1}\right) > f(\mathbf{x}_1)$, because then the negative slope at $\mathbf{x}_l^0$ in the direction of $\mathbf{x}_u^0$ has turned into a positive one when going further in this direction and eventually arriving at $\mathbf{x}_u^{j+1}$. If $f\left(\mathbf{x}_u^{j+1}\right) \leq f(\mathbf{x}_1)$, then set $\mathbf{x}_l^{j+1} = \mathbf{x}_1$ (because the slope is still negative when moving from $\mathbf{x}_1$ to $\mathbf{x}_u^{j+1}$) and apply (2.13) again. Take a look at the middle part of Fig. 2.6: here, the function value of the right bound estimate is lower than the value at the current solution. Therefore, we have to search further in this direction until the function value becomes larger than at the current solution (red point).

If $f\left(\mathbf{x}_l^0\right) < f\left(\mathbf{x}^k\right) < f\left(\mathbf{x}_u^0\right)$, in fact we have to search the minimum in direction opposite to $\mathbf{s}^k$, because now the slope in the direction of $\mathbf{s}^k$ is positive. This can be achieved by interchanging $\mathbf{x}_l^0$ and $\mathbf{x}_u^0$ and then applying the iterative bounds search just described with the interchanged positions. Observe the right picture of Fig. 2.6: here, we have the same situation as in the middle part, except that the current search direction has the wrong sign (shown by dotted arrow and indicated by the fact that the border estimate in search direction (light blue) takes a higher function value compared to the value at the green position but in the opposite direction the function value is lower (blue)). Therefore, the search direction is turned around (solid arrow) and the iteration proceeds until a proper bound is found (red).

Pseudocode

```
function **optimizeContinuousOnedim** (in Image $I$, in objective function $f(\mathbf{x})$, in current solution $\mathbf{x}^k$, in search direction $\mathbf{s}^k$, in convergence criterion $\varepsilon$, out refined solution $\mathbf{x}^{k+1}$)

// step 1: estimate initial lower and upper bounds $\mathbf{x}_l^k$ and $\mathbf{x}_u^k$
calculate $\mathbf{x}_l^0 = \mathbf{x}^k - \mathbf{s}^k$ and $\mathbf{x}_u^0 = \mathbf{x}^k + \mathbf{s}^k$
if $f\left(\mathbf{x}_l^0\right) < f\left(\mathbf{x}^k\right) < f\left(\mathbf{x}_u^0\right)$ then // right picture of Figure 2.6
    $\mathbf{s}^k \leftarrow -\mathbf{s}^k$          // invert search direction
    interchange $\mathbf{x}_l^0$ and $\mathbf{x}_u^0$
end if
if $f\left(\mathbf{x}_u^0\right) < f\left(\mathbf{x}^k\right)$ then   // middle picture of Figure 2.6
    // iterative search until a "valid" upper bound is found
    repeat
        $j \leftarrow 0$
        $\mathbf{x}_1 \leftarrow \mathbf{x}_u^j$
        calculate $\mathbf{x}_u^{j+1}$ according to (2.13)
        $j \leftarrow j + 1$
    until $f\left(\mathbf{x}_u^j\right) > f\left(\mathbf{x}^k\right)$
end if

// iterative refinement of the bounds (golden section method)
calculate $N$ according to (2.12)
calculate $\alpha_l^0$ and $\alpha_u^0$, based on $\mathbf{x}_l^j$, $\mathbf{x}_u^j$, and $\mathbf{s}^k$.
calculate $\mathbf{x}_1^0$ (if not known already) and $\mathbf{x}_2^0$ by determining $\alpha_1^0$ and
$\alpha_2^0$ according to (2.11)
for i = 0 to $N-1$
    if $f(\mathbf{x}_1^i) < f(\mathbf{x}_2^i)$ then
        // new upper bound found
        $\mathbf{x}_u^{i+1} \leftarrow \mathbf{x}_2^i$
        $\mathbf{x}_2^{i+1} \leftarrow \mathbf{x}_1^i$
        calculate $\mathbf{x}_1^{i+1}$ by determining $\alpha_1^{i+1}$ according to (2.11)
    else
    // new lower bound found
        $\mathbf{x}_l^{i+1} \leftarrow \mathbf{x}_1^i$
        $\mathbf{x}_1^{i+1} \leftarrow \mathbf{x}_2^i$
        calculate $\mathbf{x}_2^{i+1}$ by determining $\alpha_2^{i+1}$ according to (2.11)
    end if
next

// final refinement of solution by cubic interpolation
calculate $\mathbf{x}^{k+1}$ based on cubic interpolation at the four points
$\mathbf{x}_l^i$, $\mathbf{x}_1^i$, $\mathbf{x}_2^i$, and $\mathbf{x}_u^i$
```

2.2.2 Calculation of the Search Direction

The choice of the search direction is very important for the runtime performance of the entire optimization method, because the total number of one-dimensional optimization steps is to a large extent influenced by this choice. Hence, a proper choice of the search direction plays an important role in the algorithm design.

Having this in mind, some algorithms are designed such that they try to make use of the performance of the past steps when the search direction of the current optimization step is estimated. Apart from that, it is advisable to incorporate as much knowledge about the objective function $f(\mathbf{x})$ as possible. One way to do this is to make use of the derivatives of $f(\mathbf{x})$. In fact, optimization methods can be categorized according to the maximum order of the derivatives they make use of:

- *Zero-order methods*: The search directions $\mathbf{s}^k$ are calculated solely based on $f(\mathbf{x})$ itself; no derivative information is taken into account.
- *First-order methods*: The gradient $\nabla f(\mathbf{x})$ is also considered in the calculations of $\mathbf{s}^k$.
- *Second-order methods*: Here the matrix $\mathbf{H}(\mathbf{x})$ consisting of the second-order derivatives (also called *Hessian matrix*) influences the search direction $\mathbf{s}^k$, too.

The gradient $\nabla f(\mathbf{x})$ is defined as

$$\nabla f(\mathbf{x}) = \left[\frac{\partial f}{\partial x_1}, \frac{\partial f}{\partial x_2}, \ldots, \frac{\partial f}{\partial x_N}\right]^T \tag{2.14}$$

where N denotes the number of elements of the vector $\mathbf{x}$. The Hessian matrix $\mathbf{H}(\mathbf{x})$ can be written as

$$\mathbf{H}(\mathbf{x}) = \begin{bmatrix} \frac{\partial^2 f}{\partial x_1 \partial x_1} & \cdots & \frac{\partial^2 f}{\partial x_1 \partial x_N} \\ \vdots & \ddots & \vdots \\ \frac{\partial^2 f}{\partial x_N \partial x_1} & \cdots & \frac{\partial^2 f}{\partial x_N \partial x_N} \end{bmatrix} \tag{2.15}$$

As can easily be seen, $\mathbf{H}(\mathbf{x})$ is symmetric.

Clearly, the more derivative information is taken into account, the fewer iteration steps should be needed. Bear in mind, however, that the additional calculation/estimation of the derivatives itself takes time, too. Apart from that, it might not be possible to calculate the derivatives analytically in some cases, or their numerical estimation might be error-prone. Therefore, methods of all three categories mentioned above have its justification and some representatives of each category will be presented in the following sections.

2.3 Second-Order Optimization

2.3.1 *Newton's Method*

Newton's method is a classical example of second-order continuous optimization (see, e.g., [2] for a more detailed description). Here, the function $f(\mathbf{x})$ is approximated by a second-order Taylor expansion T at the current solution $\mathbf{x}^k$:

$$f(\mathbf{x}) \cong T(\delta\mathbf{x}) = f\left(\mathbf{x}^k\right) + \nabla f\left(\mathbf{x}^k\right) \cdot \delta\mathbf{x} + \frac{1}{2}\delta\mathbf{x}^T \cdot \mathbf{H}\left(\mathbf{x}^k\right) \cdot \delta\mathbf{x} \tag{2.16}$$

with $\delta\mathbf{x}$ being the difference $\mathbf{x} - \mathbf{x}^k$. As long as $\delta\mathbf{x}$ remains sufficiently small, we can be quite sure that the second-order Taylor expansion $T(\delta\mathbf{x})$ is a sufficiently good approximation of $f(\mathbf{x})$.

As $f(\mathbf{x})$ is approximated by a quadratic form, a candidate of its minimum can be found analytically in a single step by setting the derivative of the quadratic form to zero. This yields a linear system of equations which can be solved with standard techniques (see also Sect. 2.1). Because the Taylor expansion is just an approximation of $f(\mathbf{x})$, its minimization at a single position is usually not sufficient for finding the desired solution. Hence, finding a local minimum of $f(\mathbf{x})$ involves an iterative application of the following two steps:

1. Approximate $f(\mathbf{x})$ by a second-order Taylor expansion $T(\delta\mathbf{x})$ (see (2.16)).
2. Calculate the minimizing argument $\delta\mathbf{x}^*$ of this approximation $T(\delta\mathbf{x})$ by setting its first derivative to zero: $\nabla T(\delta\mathbf{x}) = \mathbf{0}$

In order for $\delta\mathbf{x}^*$ to be a local minimum of $T(\delta\mathbf{x})$, the following two conditions must hold:

1. $\nabla T(\delta\mathbf{x}^*) = \mathbf{0}$.
2. $\mathbf{H}(\mathbf{x}^k)$ is positive, i.e., $\mathbf{d}^T \cdot \mathbf{H}(\mathbf{x}^k) \cdot \mathbf{d} > 0$ for every vector $\mathbf{d}$. This is equivalent to the statement that all eigenvalues of $\mathbf{H}(\mathbf{x}^k)$ are positive real numbers. This condition corresponds to the fact that for one-dimensional functions, their second derivative has to be positive at a local minimum.

Now let's see how the two steps of Newton's method can be implemented in practice. First, a differentiation of $T(\delta\mathbf{x})$ with respect to $\delta\mathbf{x}$ yields:

$$\nabla f(\mathbf{x}) \cong \nabla T(\delta\mathbf{x}) = \nabla f(\mathbf{x}^k) + \mathbf{H}(\mathbf{x}^k) \cdot \delta\mathbf{x} \tag{2.17}$$

Setting (2.17) to zero leads to the following linear system of equations:

$$\mathbf{H}(\mathbf{x}^k) \cdot \delta\mathbf{x} = -\nabla f(\mathbf{x}^k) \tag{2.18}$$

The minimizer $\delta\mathbf{x}^*$ of (2.18) can be found by, e.g., a QR or LR decomposition of the matrix of the normal equation of (2.18) or directly via a singular value decomposition of $\mathbf{H}(\mathbf{x}^k)$ (see, e.g., [6]). Now that $\delta\mathbf{x}^*$ is found, the solution can be updated as follows:

$$\mathbf{x}^{k+1} = \mathbf{x}^k + \delta\mathbf{x}^* \tag{2.19}$$

In the notion of (2.9), we can alternatively formulate the following update rule for Newton's method:

$$\mathbf{x}^{k+1} = \mathbf{x}^k - \mathbf{H}(\mathbf{x}^k)^{-1} \cdot \nabla f(\mathbf{x}^k), \quad i.e. \quad \mathbf{s}^k = -\mathbf{H}(\mathbf{x}^k)^{-1} \cdot \nabla f(\mathbf{x}^k) \tag{2.20}$$

As far as implementation is concerned, (2.20), which involves explicitly calculating the inverse $\mathbf{H}(\mathbf{x}^k)^{-1}$, is not applied. The linear equation system (2.18) is solved instead. Note also that no separate one-dimensional optimization is performed in this method. Instead, the direction as well as the step size are estimated together in one step, as can be seen in (2.20). The whole process is summarized in Fig. 2.7.

Please observe that Newton's method has only a limited area of convergence, i.e., the initial solution $\mathbf{x}^0$ has to be sufficiently close to the true minimum of $f(\mathbf{x}^*)$, because $T(\delta\mathbf{x})$ is a sufficiently good approximation of $f(\mathbf{x})$ in just a limited local neighborhood around the optimum. This also relates to the fact that the second of the above-mentioned conditions has to be fulfilled (positivity of the Hessian): if we are too far away from the minimum, the Hessian might not be positive any longer. Please note that this condition is not checked explicitly in the method, and consequently, if the condition is violated, the method will have poor performance. On the other hand, the convergence of Newton's method is very fast. Therefore, it is well suited for a fast and accurate refinement of a sufficiently "good" initial solution.

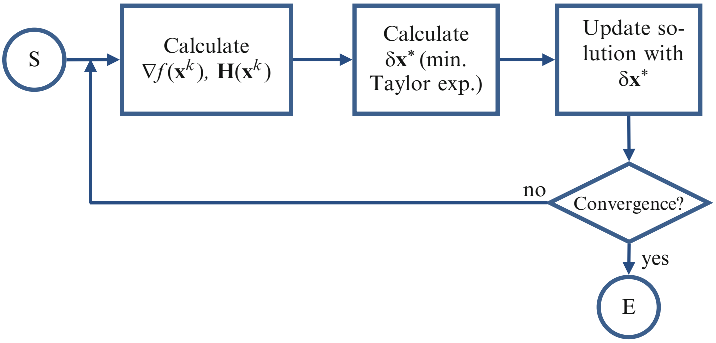
S
Calculate $\nabla f(\mathbf{x}^k)$, $\mathbf{H}(\mathbf{x}^k)$
Calculate $\delta\mathbf{x}^*$ (min. Taylor exp.)
Update solution with $\delta\mathbf{x}^*$
Convergence?
no
yes
E

Fig. 2.7 Flowchart of Newton's method

Pseudocode

```
function optimizeMultidimNewton (in Image $I$, in objective function $f(\mathbf{x})$, in initial solution $\mathbf{x}^0$, in convergence criterion $\varepsilon$, out final solution $\mathbf{x}^*$)

// main search loop (each pass is one iteration)
$k \leftarrow 0$
repeat
    approximate $f(\mathbf{x})$ by a second-order Taylor expansion around $\mathbf{x}^k$ according to (2.16), i.e. calculate $\mathbf{H}(\mathbf{x}^k)$ and $\nabla f(\mathbf{x}^k)$
    build linear system of equations according to (2.18)
    solve this linear equation system, e.g. by QR decomposition, yielding $\delta\mathbf{x}^*$
    $\mathbf{x}^{k+1} \leftarrow \mathbf{x}^k + \delta\mathbf{x}^*$
    $k \leftarrow k+1$
until convergence: $|f(\mathbf{x}^{k-1}) - f(\mathbf{x}^k)| \leq \varepsilon \cdot (|f(\mathbf{x}^{k-1})| + |f(\mathbf{x}^k)|)$
$\mathbf{x}^* \leftarrow \mathbf{x}^k$
```

2.3.2 *Gauss-Newton and Levenberg-Marquardt Algorithm*

2.3.2.1 Basic Principles

A special case occurs if the objective function$f(\mathbf{x})$ is composed of a sum of squared values:

$$f(\mathbf{x}) = \sum_{i=1}^{N} r_i(\mathbf{x})^2 \tag{2.21}$$

Such a specific structure of the objective can be encountered, e.g., in least squares problems, where the $r_i(\mathbf{x})$ are deviations from the values of a regression function to observed data values (so-called residuals). There are numerous vision applications where we want to calculate some coefficients $\mathbf{x}$ such that the regression function fits "best" to the sensed data in a least squares sense.

If the residuals are linear in $\mathbf{x}$, we can apply the linear regression method already presented in Sect. 2.1. Nonlinear $r_i(\mathbf{x})$, however, are a generalization of this regression problem and need a different proceeding to be solved.

Please bear in mind that in order to obtain a powerful method, we always should utilize knowledge about the specialties of the problem at hand if existent. The *Gauss-Newton algorithm* (see, e.g., [1]) takes advantage of the special structure of $f(\mathbf{x})$ (i.e., $f(\mathbf{x})$ is composed of a sum of residuals) by approximating the second-order derivative by first-order information.

To understand this, let's examine how the derivatives used in Newton's method can be written for squared residuals. Applying the chain rule, the elements of the gradient $\nabla f(\mathbf{x})$ can be written as

$$\nabla f_j(\mathbf{x}) = 2\sum_{i=1}^{N} r_i(\mathbf{x}) \cdot J_{ij}(\mathbf{x}) \quad \text{with} \quad J_{ij}(\mathbf{x}) = \frac{\partial r_i(\mathbf{x})}{\partial x_j} \tag{2.22}$$

where the $J_{ij}(\mathbf{x})$ are the elements of the so-called Jacobi matrix $\mathbf{J_r}(\mathbf{x})$, which pools first-order derivative information of the residuals. With the help of the product rule, the Hessian $\mathbf{H}$ can be derived from $\nabla f(\mathbf{x})$ as follows:

$$\begin{aligned} H_{jl}(\mathbf{x}) = \frac{\nabla f_j(\mathbf{x})}{\partial x_l} &= 2\sum_{i=1}^{N}\left(\frac{\partial r_i(\mathbf{x})}{\partial x_l}\cdot J_{ij}(\mathbf{x}) + r_i(\mathbf{x})\cdot\frac{\partial J_{ij}(\mathbf{x})}{\partial x_l}\right) \\ &= 2\sum_{i=1}^{N}\left(J_{il}(\mathbf{x})\cdot J_{ij}(\mathbf{x}) + r_i(\mathbf{x})\cdot\frac{\partial^2 r_i(\mathbf{x})}{\partial x_j\cdot\partial x_l}\right) \end{aligned} \tag{2.23}$$

If we drop the second term of the summands, which contains the second-order derivatives, the Hessian can be approximated by first-order information only:

$$\mathbf{H}(\mathbf{x}) \approx 2\cdot\mathbf{J_r}(\mathbf{x})^T\cdot\mathbf{J_r}(\mathbf{x}) \tag{2.24}$$

In this case we obtain the following update rule for Newton's method (according to (2.22), the gradient is obtained by $\nabla f(\mathbf{x}) = 2\cdot\mathbf{J_r}(\mathbf{x})^T\cdot\mathbf{r}$):

$$\mathbf{x}^{k+1} = \mathbf{x}^k + \mathbf{s}^k \quad \text{with } \mathbf{s}^k = -\left(\mathbf{J_r}(\mathbf{x})^T\cdot\mathbf{J_r}(\mathbf{x})\right)^{-1}\cdot\mathbf{J_r}(\mathbf{x})^T\cdot\mathbf{r} \tag{2.25}$$

Usually, the inverse $\left(\mathbf{J_r}(\mathbf{x})^T\cdot\mathbf{J_r}(\mathbf{x})\right)^{-1}$ is not calculated explicitly. Instead, the normal equations are solved, e.g., by a QR decomposition of $\mathbf{J_r}(\mathbf{x})$. Observe that N has to be at least equal to the number of elements of $\mathbf{x}$ (the number of unknowns; otherwise, the inverse doesn't exist.

However, there is no guarantee that in general the method converges (or even that an iteration step improves the solution). However, we can expect convergence if the approximation of (2.24) holds, i.e., if we can ignore the second-order terms of (2.23). This is usually the case in either of the two following cases:

- The residuals $r_i(\mathbf{x})$ are small, which is usually fulfilled if we are near the optimum.
- The second-order terms are small, i.e., $f(\mathbf{x})$ can be approximated well by a linear function, at least near the current position $\mathbf{x}^k$.

Then we can expect the Gauss-Newton method to converge (almost) as fast as Newton's method. Compared to Newton's method, though, each iteration can be calculated much quicker, because we don't have to calculate second-order derivatives. However, the method usually relies on a quite well initial solution $\mathbf{x}^0$.

In order to overcome this problem, Levenberg [10] suggested to combine the Gauss-Newton method with gradient descent, where the search direction points to the negative gradient: $\mathbf{s}^k = -\nabla f\left(\mathbf{x}^k\right)$ (a more detailed presentation of gradient descent methods will be given later on). Roughly speaking, gradient descent is very likely to improve the solution but has a poor convergence rate, at least in some situations.

Consequently, the search direction at each step of the iterative optimization is a combination of (2.25) and the direction of the negative gradient $-\nabla f\left(\mathbf{x}^k\right)$:

$$\mathbf{x}^{k+1} = \mathbf{x}^k + \mathbf{s}^k \quad \text{with } \mathbf{s}^k = -\left(\mathbf{J}_\mathbf{r}(\mathbf{x})^T \cdot \mathbf{J}_\mathbf{r}(\mathbf{x}) + \lambda \cdot \mathbf{I}\right)^{-1} \cdot \mathbf{J}_\mathbf{r}(\mathbf{x})^T \cdot \mathbf{r} \tag{2.26}$$

where $\mathbf{I}$ is the identity matrix and the parameter λ controls the relative weight between the Gauss-Newton update and gradient descent. For small values of λ, the method is close to the Gauss-Newton method, whereas for large λ, the large influence of the gradient steers the method to behave similar to the gradient descent approach.

The performance of the method is largely influenced by a suitable choice of λ, which will be described below in more detail. For the moment, let's just state that in early iterations, large values of λ ensure that the situation improves (because the search direction is dominated by gradient descent for large λ). As the method proceeds, λ can be reduced successively such that later iterations benefit from the fast convergence of the Gauss-Newton method near the optimum.

Please note the method of Levenberg (2.26) has the drawback that for large values of λ, second-order approximations via the Jacobi matrix are not used at all. However, exploiting information of estimated curvature could be useful in early steps of the iteration, too. Imagine a situation where the gradient in the direction of a specific element of $\mathbf{x}$ is small but curvature in that direction is quite high. This leads to a poor convergence rate, because the small gradient involves small steps in that direction, whereas the high curvature suggests it would be promising to take larger steps. Therefore, Marquardt [12] suggested to modify the method of Levenberg such that each component of the gradient is scaled according to the curvature (which is estimated based on $\mathbf{J_r}(\mathbf{x})^T \cdot \mathbf{J_r}(\mathbf{x})$). This leads to the well-known *Levenberg-Marquardt algorithm*:

$$\begin{aligned} &\mathbf{x}^{k+1} = \mathbf{x}^k + \mathbf{s}^k \quad \text{with} \\ &\mathbf{s}^k = -\left[\mathbf{J_r}(\mathbf{x})^T \cdot \mathbf{J_r}(\mathbf{x}) + \lambda \cdot \mathrm{diag}\left(\mathbf{J_r}(\mathbf{x})^T \cdot \mathbf{J_r}(\mathbf{x})\right)\right]^{-1} \cdot \mathbf{J_r}(\mathbf{x})^T \cdot \mathbf{r} \end{aligned} \tag{2.27}$$

where, compared to (2.26), the identity matrix is replaced by a diagonal matrix, whose elements are based on the Jacobian.

For the choice of the λ parameter, [12] suggests an adjustment of λ at each iteration step as follows: Starting with a rather large $\lambda = \lambda_0$ and a factor $\nu > 1$, (2.27) is performed twice at each iteration, once with λ and another time with λ/ν, yielding $f(\mathbf{x})_\lambda^{k+1}$ and $f(\mathbf{x})_{\lambda/\nu}^{k+1}$. Then we have to decide whether to update λ according to the following cases:

- $f(\mathbf{x})_{\lambda/\nu}^{k+1} < f(\mathbf{x})^k$: Reducing λ improves the situation. Consequently, set $\lambda_{\text{new}} = \lambda/\nu$.
- $f(\mathbf{x})_\lambda^{k+1} < f(\mathbf{x})^k$ and $f(\mathbf{x})_{\lambda/\nu}^{k+1} > f(\mathbf{x})^k$: Only the safer method with more emphasis on gradient descent improves the situation. Consequently, leave λ unchanged.
- $f(\mathbf{x})_\lambda^{k+1} > f(\mathbf{x})^k$ and $f(\mathbf{x})_{\lambda/\nu}^{k+1} > f(\mathbf{x})^k$: Both current steps don't improve the situation. Therefore, it is better to modify λ such that the safer steps of gradient decent are favored. Consequently, increase λ by multiplying it with ν: $\lambda_{\text{new}} = \lambda \cdot \nu$. Repeat the multiplication with ν until the situation improves, i.e., $f(\mathbf{x})_{\lambda \cdot \nu}^{k+1} < f(\mathbf{x})^k$.

  Convergence is indicated if:

- The reduction of the objective after appropriate update of λ becomes sufficiently small or
- a suitable update of λ cannot be found in reasonable amount of time, i.e., a repeated increase of λ being performed $L_{\max}$ times still results in $f(\mathbf{x})_\lambda^{k+1} > f(\mathbf{x})^k$ and $f(\mathbf{x})_{\lambda/\nu}^{k+1} > f(\mathbf{x})^k$.

A schematic overview of the proceeding is given in the flowchart of Fig. 2.8, whereas a more detailed insight is given in the pseudocode implementation below.

Pseudocode

```
function optimizeLevenbergMarquardt (in Image $I$, in objective function $f(\mathbf{x}) = \sum_{i=1}^{N} r_i(\mathbf{x})^2$, in initial solution $\mathbf{x}^0$, in parameters $\lambda_0$ and $\nu$, in convergence criterion $\varepsilon$, out final solution $\mathbf{x}^*$)
// main iterative multidimensional search loop
$k \leftarrow 0$
repeat
```

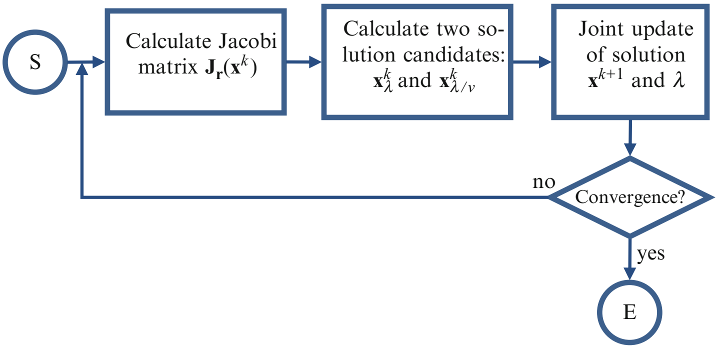
S
Calculate Jacobi matrix $\mathbf{J_r}(\mathbf{x}^k)$
Calculate two solution candidates: $\mathbf{x}_\lambda^k$ and $\mathbf{x}_{\lambda/\nu}^k$
Joint update of solution $\mathbf{x}^{k+1}$ and λ
no
Convergence?
yes
E

Fig. 2.8 Flowchart of the Levenberg-Marquardt method

```
    calculate the Jacobi matrix $\mathbf{J_r}\left(\mathbf{x}^k\right)$ at the current position $\mathbf{x}^k$
    update the solution according to (2.27) twice: with $\lambda$
    yielding $\mathbf{x}_\lambda^{k+1}$ and $f(\mathbf{x})_\lambda^{k+1}$, and with $\lambda/\nu$ yielding $\mathbf{x}_{\lambda/\nu}^{k+1}$ and $f(\mathbf{x})_{\lambda/\nu}^{k+1}$
    // update weighting of the components (lambda parameter)
    if $f(\mathbf{x})_{\lambda/\nu}^{k+1} < f(\mathbf{x})^k$ then
        $\lambda \leftarrow \lambda/\nu$
        $\mathbf{x}^{k+1} \leftarrow \mathbf{x}_{\lambda/\nu}^{k+1}$
    else
        if $f(\mathbf{x})_\lambda^{k+1} < f(\mathbf{x})^k$ then
            $\mathbf{x}^{k+1} \leftarrow \mathbf{x}_\lambda^{k+1}$ // lambda remains unchanged
        else
            // successive update of lambda
            $l \leftarrow 0$
            repeat
                $\lambda \leftarrow \lambda \cdot \nu$
                calculate $\mathbf{x}_{\lambda\cdot\nu}^{k+1}$ and $f(\mathbf{x})_{\lambda\cdot\nu}^{k+1}$
                $\mathbf{x}^{k+1} \leftarrow \mathbf{x}_{\lambda\cdot\nu}^{k+1}$
                    if $l > L_{\max}$ then    // convergence
                    $\mathbf{x}^* \leftarrow \mathbf{x}^k$
                    return
                    end if
                    $l \leftarrow l+1$
                until $f(\mathbf{x})_{\lambda\cdot\nu}^{k+1} < f(\mathbf{x})^k$
        end if
    end if
    $k \leftarrow k+1$
until convergence: $\left|f\left(\mathbf{x}^{k-1}\right) - f\left(\mathbf{x}^k\right)\right| \leq \varepsilon \cdot \left(\left|f\left(\mathbf{x}^{k-1}\right)\right| + \left|f\left(\mathbf{x}^k\right)\right|\right)$
$\mathbf{x}^* \leftarrow \mathbf{x}^k$
```

2.3.2.2 Example: Shape Registration

Nonlinear parametric regression, where the coefficients of some nonlinear function have to be estimated, is applied in various vision tasks. One example is nonlinear shape registration: suppose we have knowledge about a reference shape, the so-called template. The aim of registration is to find the parameters of a transform aligning this template to some observed shape. Many transforms are linear, but some important transformations like the planar homography or transformations allowing for local distortions are nonlinear in its coefficients. Hence, one means of estimating their coefficients is nonlinear regression, which can be performed with the help of the Levenberg-Marquardt algorithm.

Domokos et al. [5] suggest a scheme for nonlinear shape registration for binary shapes which applies the Levenberg-Marquardt algorithm. Unlike classical registration methods – where the shapes to be registered are represented by a set of landmark points and the transformation can be estimated by detecting corresponding points between template and observation (see Chap. 5) – the algorithm of [5] is not based on correspondences. The authors argue that some types of objects contain no or at least very little texture (e.g., prints or traffic signs). Textural information, however, is utilized in many correspondence-based methods in order to find correct correspondences between template and observation.

In the following, just the outline of the method of [5] is presented. Our main goal is not to explain the mode of operation in detail, instead it shall be demonstrated that although introduced many decades ago, nonlinear regression with the Levenberg-Marquardt algorithm still is used in state-of-the-art methods of computer vision.

Let $\mathbf{x}$ denote a position in the (2D) template coordinate frame, and $\mathbf{y}$ its transformed position in the observed frame, respectively. If the transformation is represented by $\varphi(\cdot)$, we can write $\mathbf{y} = \varphi(\mathbf{x})$. Please note that the method presented here provides just a framework, which can be applied to various kinds of aligning transforms, like perspective transformation, thin plate splines (TPS), etc. If an appropriate φ is chosen for an application at hand, the goal is to estimate the parameters of φ.

To this end, Domokos et al. make use of the observation that, if template shape and observation belong to the same object class and the aligning transform is represented by a particular φ, the center of mass of the shapes ($\mathbf{y}_{\mathrm{c,o}}$ and $\mathbf{x}_{\mathrm{c,t}}$, respectively) can also be converted by the same aligning transform:

$$\mathbf{y}_{\mathrm{c,o}} = \varphi\left(\mathbf{x}_{\mathrm{c,t}}\right) \tag{2.28}$$

If we have a binary representation of a shape, the center of mass can easily be calculated by summing the positions of all foreground pixels: $\mathbf{x}_{\mathrm{c}} = (1/N) \sum_{\mathbf{x} \in F} \mathbf{x}$ (where F denotes the foreground region and N denotes the number of foreground pixels). If we replace each center of mass in (2.28) with this sum, we can write:

$$\sum_{\mathbf{y} \in F_{\mathrm{o}}} \mathbf{y} = \sum_{\mathbf{x} \in F_{\mathrm{t}}} \varphi(\mathbf{x}) \cdot \left| J_{\varphi}(\mathbf{x}) \right| \tag{2.29}$$

where $\left|J_{\varphi}(\mathbf{x})\right|$ is the determinant of the Jacobi matrix of $\varphi(\mathbf{x})$ consisting of the partial derivatives of φ with respect to the components of $\mathbf{x}$. The multiplication with $\left|J_{\varphi}(\mathbf{x})\right|$ is necessary, because otherwise a bias would be introduced due to the differing areas covered by one pixel in the two different coordinate spaces of $\mathbf{x}$ and $\mathbf{y}$.

If we want to evaluate the suitability of a particular φ for characterizing the aligning transform between template and observation, we can evaluate the squared difference between both sides of (2.29). As $\mathbf{x}$ and $\mathbf{y}$ are 2D variables, (2.29) actually is a system of two equations. Consequently, the squared error E is given by

$$E = \left[\sum_{y_1 \in F_o} y_1 - \sum_{x_1 \in F_t} \varphi(x_1) \cdot \left|J_{\varphi}(\mathbf{x})\right|\right]^2 + \left[\sum_{y_2 \in F_o} y_2 - \sum_{x_2 \in F_t} \varphi(x_2) \cdot \left|J_{\varphi}(\mathbf{x})\right|\right]^2 \quad (2.30)$$

(2.30) is of the form of (2.21); hence, one might think that the solution φ^* can be calculated by utilization of the Levenberg-Marquardt algorithm. Unfortunately, though, most φ contain more than two coefficients (say the number of coefficients is K), i.e., unknowns. Consequently, the matrix inverse used in the calculation of the search direction (see (2.25)) does not exist and a direct application of the Levenberg-Marquardt algorithm is not possible. Therefore, the authors of [5] suggest the following trick: they create additional equations by transforming the $\mathbf{x}$ and $\mathbf{y}$ with the help of some nonlinear function ω_i on both sides of (2.29). This leads to

$$\sum_{\mathbf{y} \in F_o} \omega_i(\mathbf{y}) = \sum_{\mathbf{x} \in F_t} \omega_i[\varphi(\mathbf{x})] \cdot \left|J_{\varphi}(\mathbf{x})\right|; \quad i = [0, 1, 2, \ldots, L] \quad (2.31)$$

If we extend (2.30) accordingly, it consists of L summands. If $L > K$, there should be enough information in order to derive the K coefficients. Observe that the new functions do not provide any new information; they act as additional constraints instead. Geometrically, (2.31) compares the volumes over the shapes, where the "height" is modulated by the ω_i (see Fig. 2.9).

In principle, the algorithm of Domokos et al. tries to find the transformation coefficients by applying the Levenberg-Marquardt with as many residuals as necessary. However, in order to compensate the weighting inherently introduced with the utilization of the ω_i, some normalization of each squared error has to be done. Moreover, the method can be sped up if φ as well as all ω_i are polynomials (if φ is not in polynomial form, a Taylor approximation can be used). The interested reader is referred to [5] for details.

The aligning performance of the method can be shown in Fig. 2.10, where some images containing traffic signs are to be registered. As can be seen, the algorithm performs quite well.

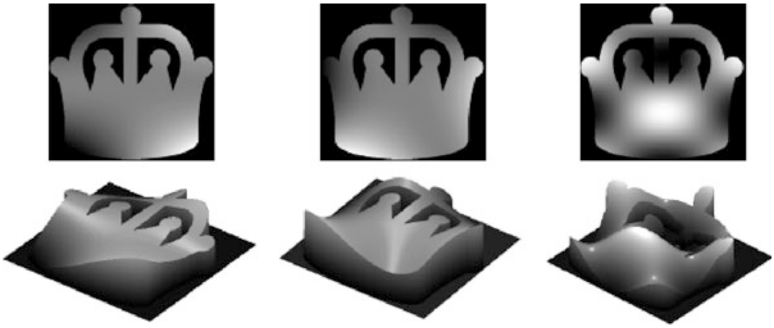

Fig. 2.9 Exemplifying the height modulation of a shape with three different ω_i (3D views in *bottom row*) (© 2012 IEEE. Reprinted, with permission, from Domokos et al. [5])

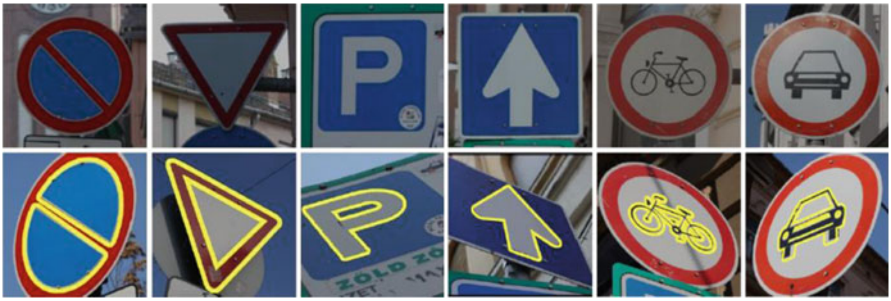

Fig. 2.10 Illustrating the aligning performance for some traffic signs. *Top row*: template shapes. *Bottom row*: matched templates in some query images visible as *yellow overlays* (© 2012 IEEE. Reprinted, with permission, from Domokos et al. [5])

2.4 Zero-Order Optimization: Powell's Method

For some problems, gradient and/or second-order derivative information about$f(\mathbf{x})$ might not be available, e.g., because $f(\mathbf{x})$ is not continuously differentiable or because it is difficult to derive $\mathbf{H}(\mathbf{x})$ analytically and/or very costly to estimate it numerically. In those cases, zero-order methods like the method proposed by *Powell* can be applied. In the following, the method itself is presented in detail first before an example application is provided.

2.4.1 General Proceeding

An obvious and simple proceeding for doing zero-order search is to perform an iterative one-dimensional search along the standard base vectors $\mathbf{e}_i = [0, \ldots, 0, 1_i, 0, \ldots, 0]^{\mathrm{T}}$ where only the *i*th element is unequal to zero. For *N*-dimensional optimization, we can perform *N* such steps with *i* varying from 1 to *N*. The sequence of these *N* steps can be repeated until convergence is achieved. This proceeding is sometimes referred to the

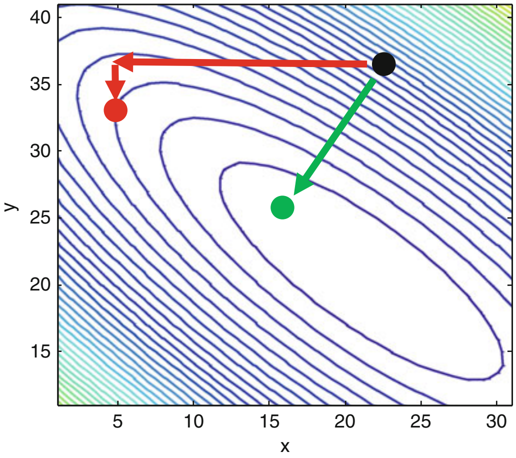

Fig. 2.11 Illustrating the poor performance of a simple search along the standard base vectors (see text for details)

taxi-cab method (because taxis in cities like Manhattan can only move along a rectangular grid structure).

While being simple, the taxi-cab method clearly is inefficient, even for simple functions. The example of Fig. 2.11 shows that, depending on the objective, there are much better search directions than the standard base vectors, which achieve much faster convergence. Figure 2.11 depicts the contour plot of a simple two-dimensional function, where the isobars are shown in different colors according to the value at these positions (blue-cyan-green-yellow-red, in ascending order). Starting from the position indicated by the black dot, one iteration of the taxi-cab optimization (red) clearly does not improve the situation as much as a single step along the negative gradient (green).

The central idea of Powell's method is to utilize information of past one-dimensional optimization steps in order to accelerate the search. More mathematically, the scheme tries to estimate and iteratively update the Hessian matrix $\mathbf{H}(\mathbf{x})$, based on the experience of past steps. For an N-dimensional optimization problem, one step of Powell's method consists of N one-dimensional searches. Powell's method consists of the following proceeding:

Starting at the initial solution $\mathbf{x}^0$, the method first performs N one-dimensional searches along the standard base vectors $\mathbf{e}_i$. As no information about optimization performance is available yet, this is the best we can do at this point. After this, we reach point $\mathbf{x}^N$. From each of these N one-dimensional searches, we know its step size α^i (because the local one-dimensional optimum was found at offset $\alpha^i \cdot \mathbf{e}_i$ to the respective starting point). This information can be used to initialize a first estimate $\tilde{\mathbf{H}}^0$ of the Hessian matrix:

$$\tilde{\mathbf{H}}^0 = \begin{bmatrix} \alpha^1 & & & \mathbf{0} \\ & \alpha^2 & & \\ & & \ddots & \\ \mathbf{0} & & & \alpha^N \end{bmatrix} \tag{2.32}$$

Furthermore, a combined search direction can be calculated from the N steps by setting $\mathbf{s}^{N+1} = \sum_{i=1}^{N} \alpha^i \mathbf{e}_i$, which is equivalent to the sum of the columns of $\tilde{\mathbf{H}}^0$. For most kinds of functions $f(\mathbf{x})$, $\mathbf{s}^{N+1}$ should be a much better search direction compared to the $\mathbf{e}_i$. Consequently, we perform a one-dimensional search along direction $\mathbf{s}^{N+1}$, thus reaching $\mathbf{x}^{N+1}$. Furthermore, we update $\tilde{\mathbf{H}}^0$ by replacing one column by $\mathbf{s}^{N+1}$, yielding $\tilde{\mathbf{H}}^1$.

Now we can repeat N one-dimensional searches in the directions of the columns of the current Hessian estimate $\tilde{\mathbf{H}}^1$, i.e., each of the N one-dimensional search directions equals one column of $\tilde{\mathbf{H}}^1$. As a result, the position $\mathbf{x}^{2N+1}$ is reached. After this, we can again calculate a combined search direction $\mathbf{s}^{2N+2}$, do a single search in this direction, and update $\tilde{\mathbf{H}}^1$ (reaching $\mathbf{x}^{2N+2}$ and obtaining $\tilde{\mathbf{H}}^2$). This process can be repeated until convergence is achieved. The entire proceeding can be summarized in the following steps:

1. *Initialization with a first successive search*: Perform N one-dimensional searches along the standard base vectors $\mathbf{e}_i$ and estimate $\tilde{\mathbf{H}}^0$ according to (2.32) yielding the current solution estimate $\mathbf{x}^N$. Set $k = 0$.
2. *Search integration*: Calculate $\mathbf{s}^{(k+1)\cdot(N+1)}$, where each element is the sum over all columns of $\tilde{\mathbf{H}}^k$ ($\tilde{h}_{jl}^k$ denotes the element in the jth row and lth column of $\tilde{\mathbf{H}}^k$):

$$s_j^{(k+1)\cdot(N+1)} = \sum_l \tilde{h}_{jl}^k \tag{2.33}$$

3. *Combined search*: Perform a single one-dimensional optimization in the direction of $\mathbf{s}^{(k+1)\cdot(N+1)}$ yielding the current solution estimate $\mathbf{x}^{(k+1)\cdot(N+1)}$.
4. *Update*: Build $\tilde{\mathbf{H}}^{k+1}$ by replacing one column of $\tilde{\mathbf{H}}^k$ with $\mathbf{s}^{(k+1)\cdot(N+1)}$.
5. *Convergence check*: Stop when the iteration slows down, e.g., when $\left|\mathbf{x}^{(k+1)\cdot(N+1)} - \mathbf{x}^{k(N+1)}\right| \leq \varepsilon$; otherwise, increment k and go on with step 6.
6. *Successive search*: Perform N one-dimensional searches along the column vectors of the current Hessian estimate $\tilde{\mathbf{H}}^k$ (yielding the current solution estimate $\mathbf{x}^{(k+1)\cdot(N+1)-1}$) and go on with step 2.

One remaining question is which column of $\tilde{\mathbf{H}}^k$ is to be replaced by the average search direction $\mathbf{s}^{(k+1)\cdot(N+1)}$ in step 4. In the standard method, the first row of $\tilde{\mathbf{H}}^k$ is replaced in each iteration step. A better choice, however, is to replace the column $\tilde{\mathbf{h}}_{l_{\max}}^k$ (with column index $l_{\max}$), which specifies the search direction along which the greatest decrease of $f(\mathbf{x})$ (denoted by $\Delta f_{\max}$) occurred. This proceeding, which is employed in the *enhanced Powell method*, is justified by the fact that column $l_{\max}$ has a major influence when calculating the average search direction $\mathbf{s}^{(k+1)\cdot(N+1)}$ and therefore shouldn't be considered twice.

This alleviates the drawback that, after a few iterations, the columns of $\tilde{\mathbf{H}}^k$ tend to become parallel and thus some directions are "lost," as we cannot move toward these directions any longer. As a consequence, the scheme might not converge anymore. When replacing the direction being the most significant part of $\mathbf{s}^{(k+1)\cdot(N+1)}$, the trend to linear dependency between the columns of $\tilde{\mathbf{H}}^k$ will become less likely.

In addition to that, two checks are introduced after step 2 in the enhanced Powell method. The combined search of step 3 is only performed if both checks are positive. These two checks can be described as follows:

- The first check evaluates whether a further processing along the average search direction $\mathbf{s}^{(k+1)\cdot(N+1)}$ will actually be likely to improve the result. This is considered to be true if the following condition holds:

$$f\left(\mathbf{x}^{(k+1)\cdot(N+1)-1} + 2\cdot\mathbf{s}^{(k+1)\cdot(N+1)}\right) < f\left(\mathbf{x}^{(k+1)\cdot(N+1)-1}\right) \tag{2.34}$$

  In detail, (2.34) evaluates whether the values of the function after considering the extended average search direction (it is taken twice) are lower compared to the function value at the current solution. If this is not the case, the assumption that the average search direction represents a good direction for continuing the search is supposed to be not true and, consequently, the method proceeds directly with step 6.

- The second check helps ensuring that the columns of $\tilde{\mathbf{H}}^k$ will be less likely to become linear dependent. If the search direction $\tilde{\mathbf{h}}^k_{l_{\max}}$, i.e., the direction in which the greatest decrease $\Delta f_{\max}$ occurred during the last successive search, actually contributes a major part to the total decrease of this last successive search, we should replace $\tilde{\mathbf{h}}^k_{l_{\max}}$ by the combined search direction in order to avoid linear dependency (otherwise, this simply is not necessary). This can be considered to be true if the following condition holds:

$$\begin{aligned}
&2\cdot(f_{\text{Start}} - 2\cdot f_N + f_E)\cdot(f_{\text{Start}} - f_N - \Delta f_{\max})^2 < \Delta f_{\max}\cdot(f_{\text{Start}} - f_E)^2 \quad \text{with}\\
&f_E = f\left(\mathbf{x}^{(k+1)\cdot(N+1)-1} + 2\cdot\mathbf{s}^{(k+1)\cdot(N+1)}\right)\\
&f_N = f\left(\mathbf{x}^{(k+1)\cdot(N+1)-1}\right)\\
&f_{\text{Start}} = f\left(\mathbf{x}^{k\cdot(N+1)}\right)
\end{aligned} \tag{2.35}$$

Otherwise the method proceeds directly with step 6 (without performing the average search and update of $\tilde{\mathbf{H}}^k$). An overview of the method is given in the flowchart of Fig. 2.12.

Some implementations of the method re-initialize the proceeding if no improvement can be achieved in any direction employed in the successive search of step 6: If none of the search directions $\tilde{\mathbf{h}}^k_i, i \in [1, 2, \ldots, N]$ yields a decrease of the function

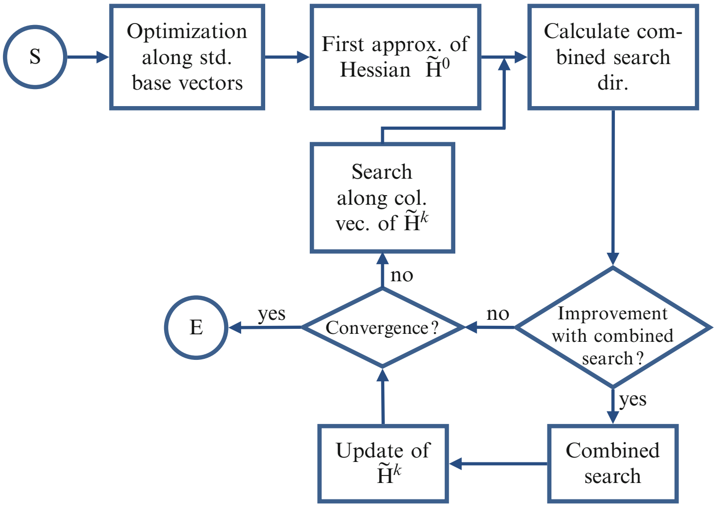
S
Optimization along std. base vectors
First approx. of Hessian $\tilde{\mathrm{H}}^0$
Calculate combined search dir.
Search along col. vec. of $\tilde{\mathrm{H}}^k$
no
E
yes
Convergence?
no
Improvement with combined search?
yes
Update of $\tilde{\mathrm{H}}^k$
Combined search

Fig. 2.12 Flowchart of the enhanced Powell method

$f(\mathbf{x})$, $\tilde{\mathbf{H}}$ is re-initialized with the standard base vectors $\mathbf{e}_i$ and the method restarts with step 1. Please note, however, that this case could also be a sign of convergence: if we are sufficiently close to the minimum, no improvement can be made either. Therefore, the algorithm has to deal with this as well.

Convergence criteria can be based on the displacement between solutions of successive iteration steps (as stated above) or on the relative change of the function values at these positions. In the second case, convergence is achieved if the following inequality holds:

$$|f_{\mathrm{Start}} - f_N| \leq \varepsilon \cdot (|f_{\mathrm{Start}}| + |f_N|) \tag{2.36}$$

To sum it up, Powell's method does not rely on an extensive analytical knowledge of $f(\mathbf{x})$. Instead, it tries to improve its performance by incorporating knowledge gathered in past optimization steps. Typically, this works well for problems up to moderate dimension as well as for problems where there is not much coupling between the individual variables to be minimized. In this case, the Hessian $\mathbf{H}$ is near diagonal.

In cases of several thousands of variables or if there is a strong coupling between the variables (i.e., $\mathbf{H}$ has many off-diagonal terms significantly differing from zero), higher-order optimization methods usually perform better, i.e., need significantly less function evaluations until convergence is achieved. However, please have in mind that each function evaluation could be much more costly if the derivatives are to be calculated as well. Consequently, Powell's method could be an alternative if the calculation and/or estimation of derivative information about $f(\mathbf{x})$ is very time-consuming.

Pseudocode

```
function optimizeMultidimPowell (in Image $I$, in objective
function $f(\mathbf{x})$, in initial solution $\mathbf{x}^0$, in convergence criterion
$\varepsilon$, out final solution $\mathbf{x}^*$)

// initialization
for i = 1 to $N$        // $N$ denotes the number of dimensions
   Perform one-dimensional search along the standard base
   vector $\mathbf{e}_i$, yielding $\mathbf{x}^i$ and $\alpha^i$
next
estimate $\tilde{\mathbf{H}}^0$ according to (2.32) based on the search steps $\alpha^i$
found during the $N$ one-dimensional optimizations

// iterative search loop
$k \leftarrow 0$
repeat
   if $k > 0$ then
      // successive search (not for first step, because it was
      done already during initialization)
      for i = 1 to $N$
         Perform onedimensional search along the column
         vectors of $\tilde{\mathbf{H}}^k$
      next
      // current solution estimate is $\mathbf{x}^{(k+1)\cdot(N+1)-1}$
   end if
   // search integration
   calculate $\mathbf{s}^{(k+1)\cdot(N+1)}$: sum over all columns of $\tilde{\mathbf{H}}^k$ (2.33)
   // check if a search along $\mathbf{s}^{(k+1)\cdot(N+1)}$ improves the solution
   if (2.34) and (2.35) are true then
      // perform combined search
      perform a single one-dimensional optimization in the
      direction of $\mathbf{s}^{(k+1)\cdot(N+1)}$ yielding $\mathbf{x}^{(k+1)\cdot(N+1)}$
      // update hessian estimate
      build $\tilde{\mathbf{H}}^{k+1}$ by replacing column $l_{\max}$ of $\tilde{\mathbf{H}}^k$ with $\mathbf{s}^{(k+1)\cdot(N+1)}$
   end if
   $k \leftarrow k + 1$
until convergence: $|f_{\text{Start}} - f_{\text{N}}| \leq \varepsilon \cdot (|f_{\text{Start}}| + |f_{\text{N}}|)$ (2.36)
$\mathbf{x}^* \leftarrow \mathbf{x}^k$
```

2.4.2 Application Example: Camera Calibration

Many vision applications require accurate measurements of position, size, or dimensional conformance of objects. In this context, camera calibration is indispensable if accurate measurements are required, because only then it is possible to accurately infer metric values from pixel positions. In this section one example of camera calibration, which utilizes Powell's method, is presented. Observe that there exist numerous applications requiring calibration of one or multiple cameras. The book of Hartley and Zisserman [8] gives a good overview of this topic.

In many industrial applications, e.g., when inspecting manufactured objects, the geometric setting of the camera relative to the objects to be measured can be chosen such that simple conversions between metric and pixel values are possible. In a frequently used setup, the camera axis is orthogonal to the object plane and the distance between object and camera is fixed. Hence, if the sensor scale is known, it should be possible to convert positions/sizes measured by the vision algorithm in pixels into metric values in a simple fashion.

However, in practical applications, some imperfections usually occur. For example, the optical properties of the lens usually include some imperfections. Furthermore, it cannot be assured that the camera axis is perfectly orthogonal to the object plane. Both effects reduce the accuracy of the system. Therefore, the influence of these effects has to be quantified, which makes a correction of these errors possible. This is done by modeling a transformation T between ideal and real setup. Once T is known, we can apply T^{-1} for correction. To this end, camera calibration has to estimate the coefficients of this transformation.

This is usually done by inspecting a calibration target, which is assured to be manufactured very accurately and contains structures with known geometry, e.g., a regular grid of points with known pitch of the points (see, e.g., the upper right image of Fig. 2.15, which depicts a camera image of a regular grid of points on a glass calibration target). The coefficients are estimated by comparing measured positions $[\hat{u}_i, \hat{v}_i]$ of the points to their nominal position $[x_i, y_i]$, where the transformation $[u, v] = T([x, y])$ should be chosen such that the deviation (squared distance) E between transformed and measured position becomes minimal (the vector $\mathbf{t}$ summarizes all transformation coefficients):

$$\mathbf{t}^* = \arg\min_{\mathbf{t}} (E) = \arg\min_{\mathbf{t}} \left(\sum_i \left| [\hat{u}_i, \hat{v}_i] - T([x_i, y_i], \mathbf{t}) \right|^2 \right) \tag{2.37}$$

This is the point where optimization comes into play: optimization reveals the desired parameters $\mathbf{t}^*$, which can be utilized for correction. In this example of camera calibration, two effects are modeled:

- *Perspective distortion*: Here, rectangular structures are transformed into general quadrangles, i.e., the angle between lines is not preserved (see Fig. 2.13). Such a transformation is able to model out-of-plane rotation of the sensor chip of the camera and hence the deviations between optical axis and object plane normal in our case. Through the usage of so-called homogeneous coordinates (where the 2D positions are augmented by a third coordinate), this nonlinear relationship can be modeled by a linear transform (see Fig. 2.13).

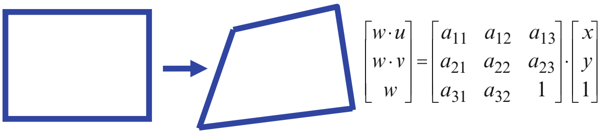
$\begin{bmatrix} w\cdot u \\ w\cdot v \\ w \end{bmatrix} = \begin{bmatrix} a_{11} & a_{12} & a_{13} \\ a_{21} & a_{22} & a_{23} \\ a_{31} & a_{32} & 1 \end{bmatrix} \cdot \begin{bmatrix} x \\ y \\ 1 \end{bmatrix}$

Fig. 2.13 Illustrating the effects of perspective transformation: generally, a *rectangle* is mapped to a *quadrangle* (*left*). Using homogeneous coordinates, the transformation can be described by a linear relationship (*right*)

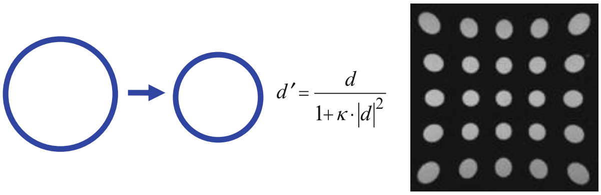

Fig. 2.14 Illustrating the effects of radial distortion: here, circles are mapped to circles of different diameter (*left*). The relationship between original and mapped diameter is stated in the middle. The effect of radial distortion can be visualized with the help of rectangular point grids: the grid is distorted especially in the image borders (*right*, with pincushion distortion)

- *Radial distortion*: Typical lens imperfections result in a nonideal projection of concentric circles. Each circle is projected to a circle again, but the diameter is altered depending on the position of the circle with respect to the image center (see equation in Fig. 2.14): the diameter of circles in the outer areas of the image is mapped either too small (barrel distortion) or too large (pincushion distortion; see Fig. 2.14).

If we combine both effects, each position $[x_i, y_i]$ is mapped to $[u_i, v_i]$ as follows (where $[x_c, y_c]$ is the center of the radial distortion):

$$\begin{aligned} u_i(\mathbf{t}) &= \cos\left[\arctan\left(\frac{p_{2,i}(\mathbf{t})}{p_{1,i}(\mathbf{t})}\right)\right]\cdot d_i(\mathbf{t}) + x_c \\ v_i(\mathbf{t}) &= \sin\left[\arctan\left(\frac{p_{2,i}(\mathbf{t})}{p_{1,i}(\mathbf{t})}\right)\right]\cdot d_i(\mathbf{t}) + y_c \\ d_i(\mathbf{t}) &= \frac{\sqrt{p_{1,i}(\mathbf{t})^2 + p_{2,i}(\mathbf{t})^2}}{1+\kappa\cdot\left(p_{1,i}(\mathbf{t})^2 + p_{2,i}(\mathbf{t})^2\right)} \quad \text{with} \\ p_{1,i}(\mathbf{t}) &= \frac{a_{11}x_i + a_{12}y_i + a_{13}}{a_{31}x_i + a_{32}y_i + 1} - x_c \\ p_{2,i}(\mathbf{t}) &= \frac{a_{21}x_i + a_{22}y_i + a_{23}}{a_{31}x_i + a_{32}y_i + 1} - y_c \end{aligned} \tag{2.38}$$

The task of optimization here is to find a parameter vector parameter vector $\mathbf{t}= [a_{11}, a_{12}, a_{13}, a_{21}, a_{22}, a_{23}, a_{31}, a_{32}, \kappa, x_c, y_c]$ such that the sum of squared

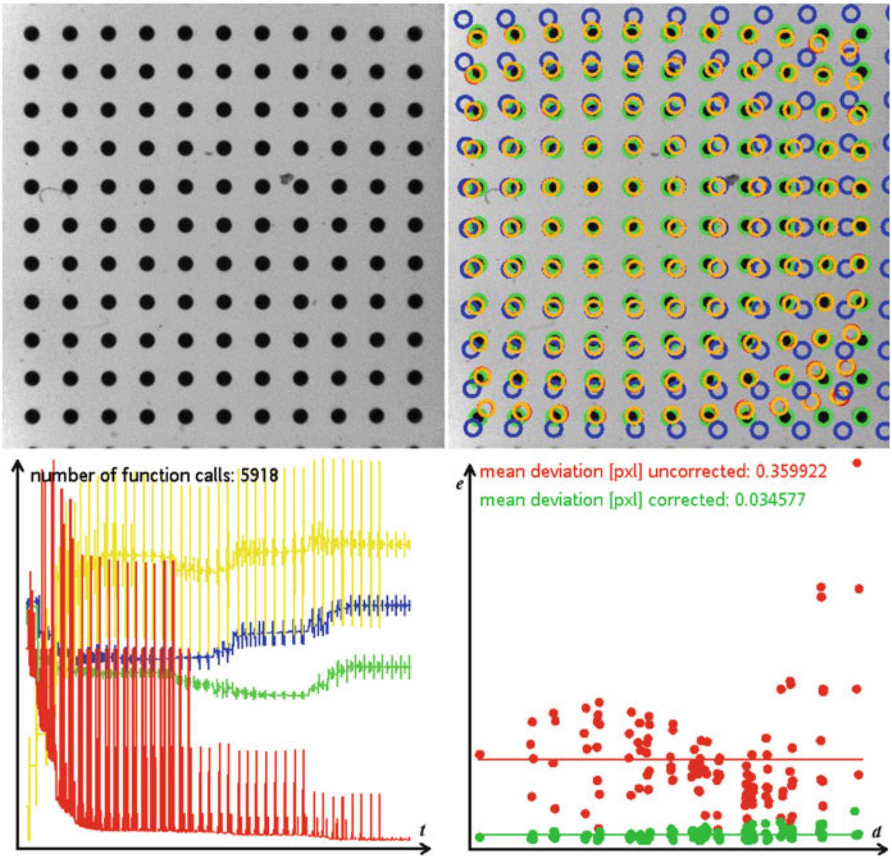

Fig. 2.15 Depicting some aspects of camera calibration (combination of perspective and radial distortion) with Powell's method: calibration target (*upper left*), calibration results (*upper right*), optimization details (*lower left*), and error analysis (*lower right*). See text for details

deviations between measured and expected positions is minimized. This is a classical nonlinear regression problem, where the Levenberg-Marquardt algorithm could be used. However, to this end, derivative information of the transformation T with respect to the parameter vector $\mathbf{t} = [a_{11}, a_{12}, a_{13}, a_{21}, a_{22}, a_{23}, a_{31}, a_{32}, \kappa, x_c, y_c]$ would be required. If we look at (2.38), it should be clear that this information is difficult to be obtained. Therefore, Powell's method seems suitable for a numerical solution of (2.37).

The results of applying Powell's method to this optimization can be seen in Fig. 2.15: the upper left part depicts a camera image of the calibration target used, which consists of a regular 11 × 11 grid of dark points. Usually the geometry of the calibration target (particularly the spacing of the points) as well as the (mean) sensor scale are known. Consequently, we can derive the expected pixel position $[u_i, v_i]$ for each grid point from its corresponding position in metric coordinates

$[x_i, y_i]$. A scheme detecting the dark circles reveals the actual positions $[\hat{u}_i, \hat{v}_i]$ in the camera image. Hence, all input data needed for an application of Powell's method in order to reveal the transformation coefficients $\mathbf{t}$ is known.

The overlaid circles shown in the upper right part of Fig. 2.15 illustrate the optimization result: the green circles indicate the nominal position of each point, whereas the red circles indicate the measured position (sometimes barely visible). The blue circles show the estimated perspective part of the transformation, whereas the orange circles indicate the entire transformation estimation (perspective+radial distortion combined). Deviations of red, blue, and orange circles are magnified by a constant factor for better visibility.

Ideally, the red and orange circles should coincide, if the estimated transformation parameters were able to perfectly model the distortion. As clearly can be seen, the actual conditions come very close to this: most red circles are at least partly shadowed by the orange ones (which relate to the estimated model), because their positions are very close to each other.

This can also be seen in the lower right part of Fig. 2.15, where the deviation between measured and nominal position of the points can be seen (y-axis), depending on the distance of the point to the image center (x-axis) before (red) and after correction (green). Before correction, distortion is largest at positions far away from the image center. After correction, the error at each point is virtually independent from the distance and can be reduced by approximately one order of magnitude here. These residual errors are mainly due to measurement accuracy when estimating the actual position of each point, e.g., because of camera noise.

The course of a few parameters as optimization proceeds can be seen in the upper left part of Fig. 2.15: here, the value of the objective function (red), the center of radial distortion x_c (green), and y_c (blue) as well as the value of κ (yellow) are shown for each calculation of (2.37). In total there are about 6,000 evaluations of the objective function, with quite accurate results obtained after approximately 1,000 evaluations.

As far as performance is concerned, typical runtime of the optimization is about 200 ms on a notebook with a 2.2 GHz Intel Core i7 CPU (only one core is used).

2.5 First-Order Optimization

The methods presented so far utilize second-order derivatives of the objective function (either explicitly or at least approximations) or no derivative information at all. Instead of completely ignoring derivatives, there is something better we can do, even if second-order information sometimes is difficult or impossible to be obtained: we can take account of first-order information. The most simple way to exploit first-order information is to take the negative gradient as search direction, i.e., we can set $\mathbf{s}^k = -\nabla f\left(\mathbf{x}^k\right)$. This simple proceeding, which is also known as *steepest descent method*, is locally the best which can be done, because the negative gradient indicates the direction in which the function decreases fastest at the current position. However, the actual rate of convergence can be quite poor in some situations. In case of high curvature, e.g., the direction of fastest decrease might change quite quickly if we move away from the current position.

Nevertheless, the steepest descent is often used as initialization step of more sophisticated methods. One of them, which is termed *conjugate gradient method*, is presented in the following.

2.5.1 Conjugate Gradient Method

The conjugate gradient method (see, e.g., [13, 14]) picks search directions which are *conjugate* to the search directions of the previous step. Two search directions $\mathbf{s}_i$ and $\mathbf{s}_j$ are conjugate with respect to each other if the following relationship holds for symmetric, positive definite matrices $\mathbf{H}$:

$$\mathbf{s}_i^T \cdot \mathbf{H} \cdot \mathbf{s}_j = 0 \tag{2.39}$$

Why is picking conjugate search directions a good idea? In order to clarify this, let's assume that the objective function is an N-dimensional convex quadratic form, e.g., $f(\mathbf{x}) = \frac{1}{2} \cdot \mathbf{x}^T \cdot \mathbf{H} \cdot \mathbf{x} - \mathbf{a}^T \cdot \mathbf{x} + c$ (where the $N \times N$ matrix $\mathbf{H}$ is symmetric and positive definite). Now it can be shown that the minimum of this objective can be found by successively performing line searches along the elements of a set of at most N linearly independent search directions, which are mutually conjugate as defined in (2.39). In other words, if we utilize "suitable" conjugate search directions, we are able to find the minimum of a convex quadratic form in at most N one-dimensional searches.

If we want to take gradient information into account, the best start is to perform a steepest descent search, i.e., set $\mathbf{s}^0 = -\nabla f(\mathbf{x}^0)$. Subsequent iterations now can try to make use of the nice convergence properties of conjugate searches by searching along directions which are conjugate with respect to the previous search direction. The search direction of step k is calculated as follows:

$$\begin{aligned} \mathbf{s}^k &= -\nabla f\left(\mathbf{x}^k\right) + \beta^k \mathbf{s}^{k-1} \\ \beta^k &= \frac{\left|\nabla f\left(\mathbf{x}^k\right)\right|^2}{\left|\nabla f\left(\mathbf{x}^{k-1}\right)\right|^2} \end{aligned} \tag{2.40}$$

Clearly, the current search direction $\mathbf{s}^k$ is a combination of the direction of steepest descent and the search direction of the last step. This utilization of information about previous steps helps in improving the rate of convergence (compared to steepest descent). As already said, this method is guaranteed to converge in at most N steps for the special case of convex quadratic functions of dimensionality N. For non-quadratic functions, however, of course more iterations are necessary, but the expectation is that for those more general situations, the rate of convergence is improved, too, at least as long the objective can be locally approximated by a quadratic form sufficiently well.

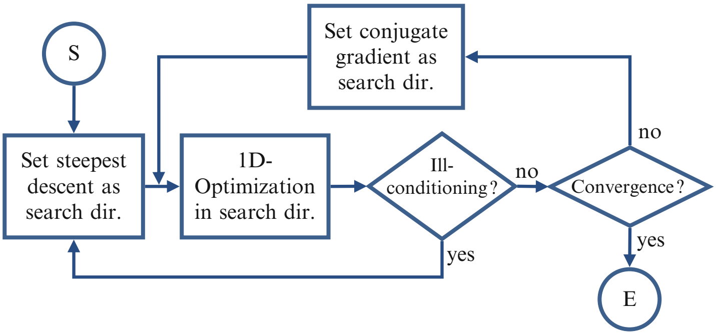
S
Set steepest descent as search dir.
1D-Optimization in search dir.
Set conjugate gradient as search dir.
Ill-conditioning?
no
yes
Convergence?
no
yes
E

Fig. 2.16 Flowchart of the conjugate gradient method

The choice of β^k as given in (2.40) ensures that $\mathbf{s}^k$ and $\mathbf{s}^{k-1}$ are conjugate. It was first proposed by Fletcher and Reeves, and that's why the update rule in the form of (2.40) is also known as *Fletcher-Reeves method*. Over the last decades, many alternative rules for updating the β^k aiming at increasing convergence properties for non-quadratic objectives have been proposed (see, e.g., [7] for an overview).

Observe, however, that the repeated application of (2.40) might result in numerical ill-conditioning in some cases. In order to resolve numerical ill-conditioning, two criteria can be applied. If one of them is fulfilled, the method can be restarted with a steepest descent step. The resulting general proceeding can be seen in the flowchart of Fig. 2.16.

In detail, these criteria are:

1. The one-dimensional search doesn't improve the solution, i.e.,$f\left(\mathbf{x}^k\right) > f\left(\mathbf{x}^{k-1}\right)$. Please observe that this fact could also indicate that convergence is achieved. Therefore, if a subsequent one-dimensional search in the direction of the steepest descent doesn't improve the search direction either, it is assumed that the method has converged.
2. The slope of f with respect to the step size α of the general proceeding (see Sect. 2.2) is positive: $\frac{\partial f}{\partial \alpha} = \left\langle \nabla f\left(\mathbf{x}^k\right), \mathbf{s}^k \right\rangle > 0$ (where $\langle \cdot \rangle$ denotes the dot product operator). This indicates numerical ill-conditioning. Consequently, the method is restarted with steepest descent.

In general, this rather small modification compared to steepest descent results in quite good rates of convergence. In particular, the conjugate gradient method is able to follow "narrow valleys" of the objective rather quickly, whereas steepest descent searches slow down in these situations.

Nevertheless, there exist other first-order methods trying to do better. For example, in the so-called variable metric methods, information of previous steps isn't considered via a simple scalar β, but via an n-dimensional array, which is capable of transporting more detailed information, of course. Examples of variable metric methods are the *Davidson-Fletcher-Powell algorithm* (DFP) [14] or the *Broydon-Fletcher-Goldfarb-Shanno method* (BFGS) [14].

Pseudocode

```
function optimizeMultidimConjugateGradient (in Image $I$, in objective function $f(\mathbf{x})$, in initial solution $\mathbf{x}^0$, in convergence criterion $\varepsilon$, out final solution $\mathbf{x}^*$)

// initializazion
$k \leftarrow 0$
bSteepestDescent ← true // calculate search direction according to steepest descent in the next iteration

// iterative main search loop
repeat
  if bSteepestDescent == true then
    // set search direction to steepest descent
    $\mathbf{s}^k \leftarrow -\nabla f(\mathbf{x}^k)$
    bSteepestDescent ← false
  else
    // search direction is based on conjugate gradient
    set search direction $\mathbf{s}^k$ conjugate to the search direction of the last iteration according to (2.40)
  end if
  perform one-dimensional search along $\mathbf{s}^k$ yielding $\mathbf{x}^k$
  // check for ill-conditioning
  if $f(\mathbf{x}^k) > f(\mathbf{x}^{k-1})$ || $\langle \nabla f(\mathbf{x}^k), \mathbf{s}^k \rangle > 0$ then
      // ill-conditioning → restart with steepest descent
      bSteepestDescent ← true
      if $f(\mathbf{x}^k) > f(\mathbf{x}^{k-1})$ && $f(\mathbf{x}^{k-1}) > f(\mathbf{x}^{k-2})$ then
        // no improvement could be made in two successive iterations → convergence is achieved
        $\mathbf{x}^* \leftarrow \mathbf{x}^k$
        return
      end if
  end if
  $k \leftarrow k+1$
until convergence: $\left| f(\mathbf{x}^k) - f(\mathbf{x}^{k-1}) \right| \leq \varepsilon \cdot (f(\mathbf{x}^k))$
$\mathbf{x}^* \leftarrow \mathbf{x}^k$
```

2.5.2 Application Example: Ball Inspection

Certain, mainly industrial, applications involve the usage of metal balls, e.g., ball bearings, ball pens, or ball valves. In order to ensure proper functionality, it has to be ensured that the ball shape is undamaged. Normally, this is done via dedicated

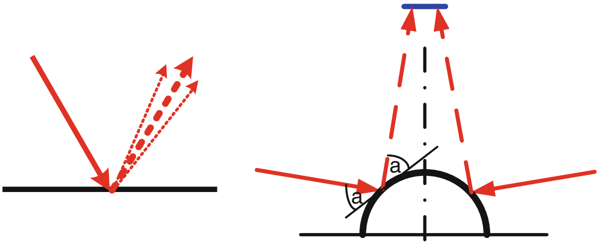

Fig. 2.17 Illustrating the reflectance properties of mostly shiny reflections (*left*), where the main part of the light from the object surface is a direct reflection of the incoming light. Consequently, ball-shaped objects appear as bright rings with slanted illumination, as the reflected light hits the sensor only if the surface patch has a specific normal angle (*right*, sensor in *blue*)

3D inspection systems (e.g., based on laser triangulation or structured light), allowing for accurate 3D measurements. However, inspection with limited accuracy can also be performed with "conventional" 2D intensity images. If the position of the balls has to be determined anyway, e.g., for gripping them during production, a "conventional" camera system might already be in place. Inspection of the shape can then be done without additional hardware.

Consider a scenario where the camera axis is perpendicular to the object plane and the images of the ball(s) to be inspected are taken with slanted illumination. As the mostly shiny surface of the metal balls leads to mainly direct reflections of the incident light, the balls appear as bright rings in the grayscale camera image, where the ring diameter depends on the slant angle.

This is illustrated in Fig. 2.17. The left part illustrates the reflectance model of mostly shiny surfaces like polished metal. For those materials direct reflections dominate (the dashed lines indicate reflected light and the thickness indicates illumination strength). Applied to ball-shaped objects (right picture of Fig. 2.17), we can see that only a small range of surface orientations leads to reflections into the sensor chip (blue), in case the ball is illuminated from the side (indicated by solid lines). Due to the ball shape, the surface patches with "correct" orientation are arranged as a ring. Consequently, the ball appears as a bright ring with slanted illumination, where the diameter depends on the slant angle.

Inspection can then be fulfilled by designing a parametric model for the brightness appearance of a ball in the camera image (which should take the shape of a ring) and then fitting this model to the camera image showing a particular ball to inspect. This fitting represents an optimization task, which can be accomplished with the method just presented above, as we will see shortly. During optimization, the parameters of the model are optimized such that they best represent the image. Subsequently, the optimization result can be used twofold for inspection:

- First, it can be checked whether the estimated model parameters are within the expected range.
- Second, the difference between the optimized model and the ball appearance in the camera image (which is the value of the objective function after convergence of the optimization algorithm) has to remain below a certain threshold; otherwise, the ball features a deformation which is too large.

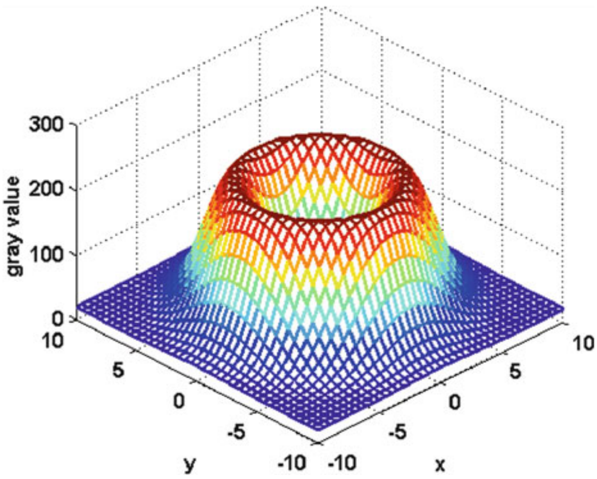

Fig. 2.18 Depicting a 3D plot of the circular ring brightness model of (2.41)

An appropriate model M of a bright ring is a radially shifted two-dimensional Gaussian, which can be expressed in Cartesian coordinates by

$$M(x,y) = o + m \cdot \exp\left[-\left(\frac{\sqrt{(x-x_\mathrm{c})^2 + (y-y_\mathrm{c})^2} - r}{a}\right)^2\right] \tag{2.41}$$

where $[x, y]$ represents the pixel coordinate, $[x_\mathrm{c}, y_\mathrm{c}]$ the center of the ring, r and a its radius and width, o the brightness offset, and m the intensity magnitude of the ring (see Fig. 2.18).

The objective function can be defined as the sum of the squared differences between observed image data and the model in a local neighborhood $\mathcal{N}$ where the ball is expected:

$$F(\mathbf{x}) = \sum_{x,y \in N} \left[I(x,y) - M(x,y,\mathbf{x})\right]^2 \tag{2.42}$$

where $I(x,y)$ denotes the intensity of the camera image at position $[x, y]$, $\mathcal{N}$ defines the neighborhood for which camera image and model are to be compared, and $\mathbf{x}= [x_\mathrm{c}, y_\mathrm{c}, r, a, m, o]^\mathrm{T}$ is the vector containing the design variables of the model to be optimized. Hence, we end up with a six-dimensional continuous optimization problem.

In order to improve convergence, we can also consider derivative information during the optimization process. By repeatedly applying the chain rule, the partial derivatives of $F(\mathbf{x})$ with respect to the model parameters are (for convenience, let's introduce $d = \sqrt{(x-x_\mathrm{c})^2 + (y-y_\mathrm{c})^2}$ and $k = -((d-r)/a)^2$):

$$\begin{aligned}
\frac{\partial F(\mathbf{x})}{\partial x_{\mathrm{c}}} &= \sum_{x,y\in N}\left[(2M(x,y)-2I(x,y))\cdot m\cdot e^{k}\cdot\left(\frac{2(x-x_{\mathrm{c}})}{a^2}\left(1-\frac{r}{d}\right)\right)\right]\\
\frac{\partial F(\mathbf{x})}{\partial y_{\mathrm{c}}} &= \sum_{x,y\in N}\left[(2M(x,y)-2I(x,y))\cdot m\cdot e^{k}\cdot\left(\frac{2(y-y_{\mathrm{c}})}{a^2}\left(1-\frac{r}{d}\right)\right)\right]\\
\frac{\partial F(\mathbf{x})}{\partial r} &= \sum_{x,y\in N}\left[(2M(x,y)-2I(x,y))\cdot m\cdot e^{k}\cdot\left(-\frac{2r-2d}{a^2}\right)\right]\\
\frac{\partial F(\mathbf{x})}{\partial a} &= \sum_{x,y\in N}\left[(2M(x,y)-2I(x,y))\cdot m\cdot e^{k}\cdot\left(-\frac{2(d-r)^2}{a^3}\right)\right]\\
\frac{\partial F(\mathbf{x})}{\partial m} &= \sum_{x,y\in N}\left[(2M(x,y)-2I(x,y))\cdot e^{k}\right]\\
\frac{\partial F(\mathbf{x})}{\partial o} &= \sum_{x,y\in N}\left[2M(x,y)-2I(x,y)\right]
\end{aligned} \tag{2.43}$$

When regarding the first derivatives of (2.43), it is evident that it would be very cumbersome to derive second-order information analytically (apart from the computational effort to calculate the Hessian numerically in each iteration step). Consequently, only first-order derivative information shall be considered during optimization and the conjugate gradient method is chosen in order to minimize $F(\mathbf{x})$.

Now each ball can be checked individually for deformations. Figure 2.19 shows two example balls where the images were taken with flat illumination: a good ball (top row) and a bad ball (bottom row). In the top row the model approximates the image region very well (small differences for all pixels; see right column). Compared to that, the bottom row reveals that the ring diameter is larger (r too large), its thickness is slightly smaller (small a), and, additionally, there are more pixels with significant brightness difference between optimized model and camera image, especially in the right region of the ring as well as within the region composed of the ball center (right column: similar brightness is indicated by gray pixels).

This inspection can be performed for multiple slant angles, where each slant angle could reveal ball deformations on different parts of the ball surface. Clearly, this method is not as powerful as dedicated 3D surface inspection, but it is economical and quite capable of detecting major deformations.

2.5.3 Stochastic Steepest Descent and Simulated Annealing

2.5.3.1 General Proceeding

A special case of objective functions which can be found quite often in practice is characterized by the fact that the objective function can be written as a sum of N elements:

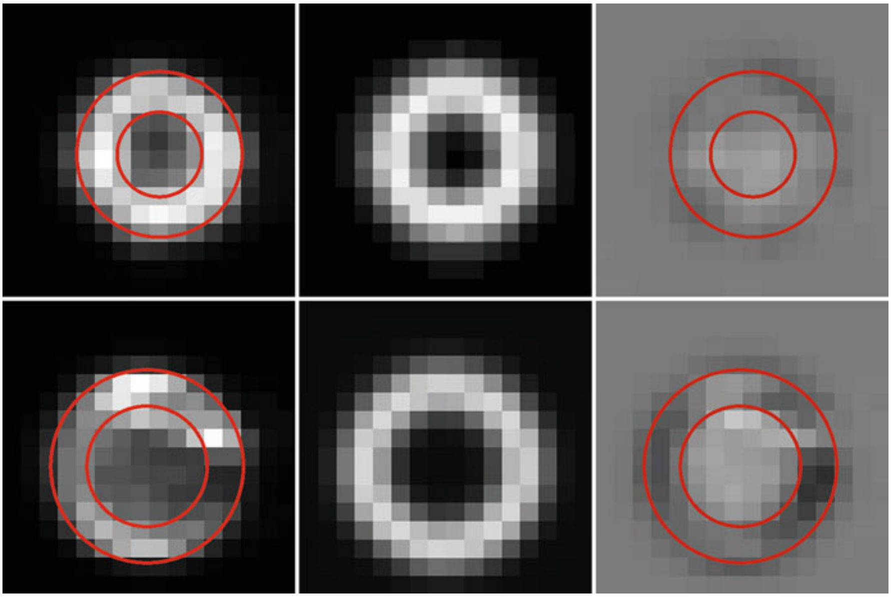

Fig 2.19 Showing the inspection results for two examples of a ball: a good ball (*top row*) and a bad ball (*bottom row*). Each row depicts the camera image of the ball (*left*, with overlaid red circles indicating the optimization result), the optimized model (*middle*), as well as the difference between camera image and optimized model (*right*, again with overlaid optimization result). *White pixels* indicate that the image is brighter than the model, whereas *dark pixels* indicate that the image is darker than the model. Similar brightness is indicated by *gray pixels*

$$f(\mathbf{x}) = \sum_{n=1}^{N} f_n(\mathbf{x}) \tag{2.44}$$

This splitting of $f(\mathbf{x})$ into N summands can be observed, e.g., for MRF-based energy functions. This structure is similar to (2.21), but in contrast to (2.21), the summands are not restricted to be square terms.

If we want to apply gradient-based optimization, even simple methods like steepest descent would involve a calculation of $\partial f_n(\mathbf{x})/\partial \mathbf{x}$ for all N components in every iteration, which could be infeasible as far as time demand is concerned.

An alternative approach is to perform an iterative optimization which considers only one of the summands of (2.44) at each iteration. Clearly, now more iterations are necessary, but at the same time, each iteration can be performed much faster, which should overcompensate for the increase in the number of iterations. The proceeding suggested here comprises the following steps:

1. Pick one $f_n(\mathbf{x})$ at random.
2. Try to reduce $f(\mathbf{x})$ by optimizing $f_n(\mathbf{x})$ with steepest descent, i.e., calculate $\partial f_n(\mathbf{x})/\partial \mathbf{x}$ and perform a one-dimensional optimization in this direction.

Now, the derivative calculation should be rather simple at each step. The procedure is repeated until convergence, e.g., the reduction of $f(\mathbf{x})$ is sufficiently small. This proceeding is called *stochastic steepest descent* (or *stochastic gradient descent*) and is an example of a so-called greedy algorithm, as each iteration seeks to maximize the reduction of $f(\mathbf{x})$.

The main drawback of this proceeding (like any local method presented in this chapter) is its susceptibility to get trapped in a local minimum if the objective function is not convex. A method to overcome this problem is to allow for updates of the solution which actually increase to objective function with a certain probability. Then it should be possible to escape local minima.

Rather than minimizing $f_n(\mathbf{x})$ at each step, we can select a certain state $\mathbf{x}$ with probability $p(\mathbf{x}) \propto \exp[-f_n(\mathbf{x})/T]$. For most of the time, $\mathbf{x}$ is modified such that $f_n(\mathbf{x})$ is reduced (because then $p(\mathbf{x})$ takes a rather high value, which makes $\mathbf{x}$ more likely to be selected), but sometimes states are chosen where the $f_n(\mathbf{x})$ is actually increased, enabling the algorithm to get away from a local minimum. High values of T lead to rather random updates, whereas low values of T effect in a quick decline in $p(\mathbf{x})$ for high energy states and therefore strongly bias updates which reduce the objective.

In an approach called *simulated annealing*, stochastic gradient descent is performed with high T at start, and T is gradually lowered ("annealed") as iteration proceeds (see [9]). Simulated annealing was the method of choice for a long time for applications where local minima trapping is an issue. In the meantime, however, more powerful methods, which have proven to outperform simulated annealing in many situations, emerged. Especially to mention here are so-called graph cuts, which will be presented in Chap. 7.

2.5.3.2 Example: Classified Training for Object Class Recognition

Vijnhoven et al. [15] showed how stochastic gradient descent optimization can be successfully applied to the task of training a decision function for object detection. They considered the application of detecting instances of a certain object category, e.g., "cars" or "pedestrians," in an image, which can be solved by the approach suggested in [4].

Dalal et al. derive a feature vector $\mathbf{d}$ (a so-called descriptor) which they call "*Histograms of Oriented Gradients*" (HOG) from a subregion of the image and, based on $\mathbf{d}$, run a classifier which decides whether an instance of the object category to be searched is present at this particular position or not. The classifier has a binary output: -1 for "object not present" and 1 for "object present." In order to scan the image, they propose a so-called *sliding window* approach, where the region for calculating the descriptor is shifted pixel by pixel over the entire image, with a subsequent classification at every position. Finally, they obtain a position vector where each element reveals the position of a detected instance of the searched object category.

The classifier has to be trained prior to recognition in an off-line teaching phase with the help of example images. A Support Vector Machine (SVM) for classification is used in [4], whereas the authors of [15] suggest to employ SGD in the classifier training step. Through the usage of SGD, they showed to reduce training times by a factor of 100–1,000 with similar recognition performance.

Before we describe in detail how SGD is utilized in training, let's first take a closer look at some different aspects of the proceeding of [4] (HOG descriptor, sliding window, and classifier design) in order to get a better understanding of the method.

HOG Descriptor

Similar to the well-known SIFT descriptor (see [11]), the HOG descriptor proposed by Dalal et al. accumulates intensity gradient orientations into histograms. To this end, the area of interest is partitioned into small "cells," e.g., of 8 × 8 pixel in size (see Fig. 2.20). Now, within each cell, a histogram of gradient orientation is calculated, i.e., the range of possible orientations (0°–360° if we want to consider gradient sign) is partitioned into a certain number of bins (typically 10–20 bins are used), and each pixel votes for the bin which corresponds to its gradient orientation (see Fig. 2.20). The vote can be provided with a weight, e.g., according to gradient magnitude and/or distance between the pixel and a block center (see below).

This proceeding leads to a considerable invariance of the resulting descriptor with respect to typical variations occurring when acquiring images of different instances of the object class to be detected, such as varying illumination, small deformations, and viewpoint change. The usage of gradient orientations makes the descriptor robust with respect to illumination changes, whereas the rather loose spatial pooling of pixels into cells increases the invariance with respect to spatial variations, like local deformations and viewpoint change.

Additionally, neighboring cells can be combined to one so-called block, e.g., 2 × 2 cells form one block. Within each block, a local contrast normalization is performed in order to compensate for illumination variance or effects like shadowing. To this end, the block descriptor vector is normalized with respect to some vector norm. In [4] it was reported that histogram sizes of 18 bins give good results; therefore, a block consisting of 2 × 2 cells results in a descriptor of size 72.

This process of computing normalized descriptors for a block is repeated for all blocks of the area of interest. Note that recognition performs best if overlapping blocks are used. To this end, neighboring blocks are shifted by only one cell with respect to each other, i.e., they share some cells (cf. Fig. 2.20). The descriptors of all blocks being part of the area of interest are concatenated into one common descriptor vector $\mathbf{d}$, which now is a robust representation of the area of interest. The overlapped calculation may seem to be redundant, but Dalal et al. showed that accurate local contrast normalization is crucial for good performance and overlapping helps to achieve this.

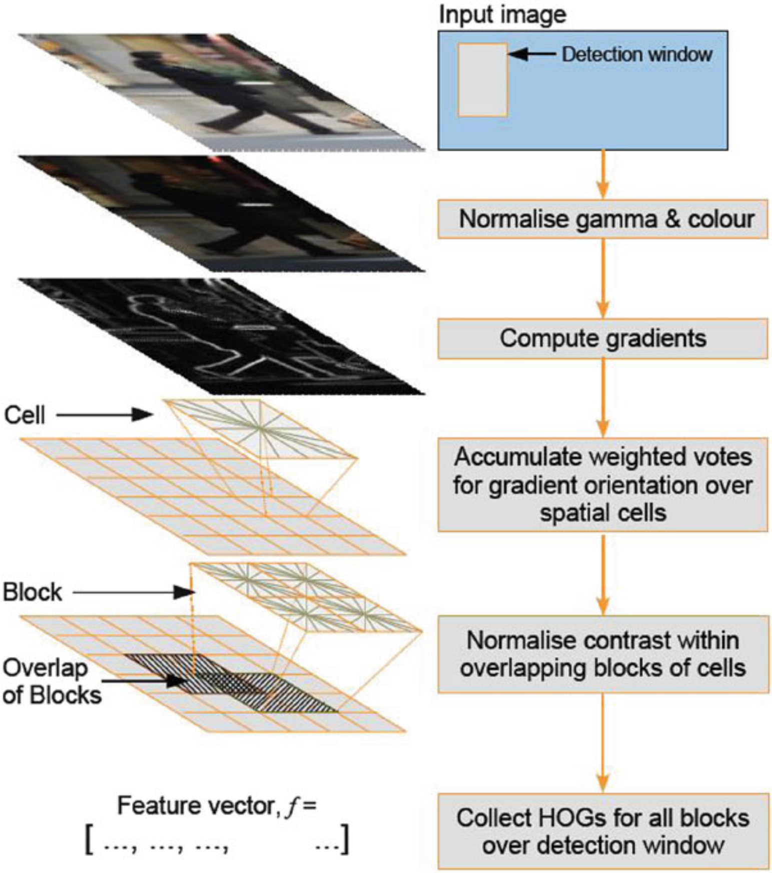
Input image
Detection window
Normalise gamma & colour
Compute gradients
Accumulate weighted votes for gradient orientation over spatial cells
Normalise contrast within overlapping blocks of cells
Collect HOGs for all blocks over detection window
Cell
Block
Overlap of Blocks
Feature vector, f =
[..., ..., ..., ...]

Fig. 2.20 Indicating the flow of the calculation of a HOG descriptor: after gradient calculation, the detection window is partitioned into cells, and within each cell a 1D histogram of gradient orientations is calculated. Several cells are pooled into a block, and a local normalization step is performed for all cells of the block. The final feature vector consists of the information of all blocks in the detection window, whereas the blocks spatially overlap (From Dalal and Triggs [4], with kind permission)

Sliding Window

During recognition, a "dense" calculation of the HOG descriptor is performed, i.e., the window of pixels which contribute to the descriptor is shifted densely, e.g., by just one pixel, and after each shift a new descriptor is calculated. Each HOG descriptor can be used as input for a binary classification, which outputs "object present" or "no object present" for a particular descriptor/position. This dense evaluation is in contrast to other descriptor-based approaches for object detection (like the usage of SIFT descriptors as proposed in [11]), which concentrate on interest points and therefore are “sparse.” A dense calculation is more time-consuming but at the same time considers more information, which increases recognition performance.

Classification

For the classification being performed at each position of the dense sampling grid, a linear classifier is used, i.e., the decision function $c(\mathbf{d})$ is a weighted sum of the elements of the feature vector $\mathbf{d}$:

$$c(\mathbf{d}) = \mathbf{w}^T \cdot \mathbf{d} + b \tag{2.45}$$

where $\mathbf{w}$ is a vector of weights and b is a bias. Values of $c(\mathbf{d}) > 0$ indicate the presence of an object instance. The weights $\mathbf{w}$ and b are to be trained in a training phase, which is performed “off-line” prior to recognition based on a database of training images showing the object class to be detected.

The goal of the training step is to determine the weights $\mathbf{w}^*$ and bias b^* which yields best classification performance if applied to the set of training samples, which consists of N images. Optimal parameters $\mathbf{w}^*$ and b^* can now be found with a stochastic gradient descent method, as shown in [15].

To this end, a HOG descriptor $\mathbf{d}_n; n \in \{1, 2, 3, \ldots, N\}$ is calculated for each training image. We need a supervised training here, which means that a label $l_n \in \{-1, 1\}$ is assigned to each training image by a supervisor, depending on whether the image contains an instance of the object class to be searched or not.

For each training image, we can apply the linear classifier to its HOG descriptor. As a result, we get an estimation $\hat{l}_n$ for its label: $\hat{l}_n = \mathbf{w}^T \cdot \mathbf{d}_n + b$. The difference between the user annotation l_n and its estimation $\hat{l}_n$ can be used to define a loss function E_n, which should be small if there is a small discrepancy between $\hat{l}_n$ and l_n and large if $\hat{l}_n$ differs significantly from l_n

$$E_n = \max\left\{0; 1 - l_n \cdot \left(\mathbf{w}^T \mathbf{d}_n + b\right)\right\} \tag{2.46}$$

The performance of a particular classifier can be measured by the total loss for the entire training set, which is based on a sum of the losses of each individual training sample:

$$E = \frac{\lambda}{2} \cdot \|\mathbf{w}\|^2 + \frac{1}{N} \sum_{n=1}^{N} E_n\left(\hat{l}_n, l_n\right) \tag{2.47}$$

where $\|\mathbf{w}\|$ is a regularization term and λ determines the relative weighting between the regularization term and the correctness of classification. Without using a regularizer there would be the danger that the optimization gives extremely high weights to just a small fraction of the examples which can easily be classified correctly and therefore ignores poor classification performance of a possibly large number of examples with small weights.

With the help of a minimization of the energy function defined in (2.47), we can determine the weight vector $\mathbf{w}^*$ and bias b^* which yield the best partitioning of the training set (into “object” or “no object” classes).

Standard gradient descent now would require to compute all partial derivatives $\partial E_n / \partial \mathbf{w}$ with respect to $\mathbf{w}$ and optimize the entire sum of (2.47) taking all training examples into account at each one-dimensional step. Typically, this joint one-dimensional optimization of E is computationally expensive or even infeasible even for training sets of moderate size.

At this point, stochastic gradient descent comes into play. Here, $\mathbf{w}$ is also updated iteratively, but now the update is performed based on just one training sample at each iteration. Taking just one $\partial E_n / \partial \mathbf{w}$ into account yields the following update formula:

$$\begin{aligned}\mathbf{w}_{t+1} &= \mathbf{w}_t - \frac{\eta}{t} \cdot \frac{\partial E_n}{\partial \mathbf{w}_t} \\ &= \mathbf{w}_t - \eta_t \cdot \left(\lambda \mathbf{w}_t + \frac{\partial E_n \left(l_n \left(\mathbf{w}_t^{\mathrm{T}} \mathbf{d}_n + b \right) \right)}{\partial \mathbf{w}_t} \right) \quad \text{with} \quad \eta_t = \frac{1}{\lambda \cdot (t + t_0)}\end{aligned} \tag{2.48}$$

where the parameters λ and t_0 have to be chosen by the user. At each iteration step t, one training sample n is picked at random, until all training images are used. In [15] training is performed in just one sweep (i.e., the optimization with respect to each training sample is performed exactly once), but it is also conceivable to do multiple sweeps.

Experimental results provided in [15] for the object class “car” indicate that, compared to the standard SVM implementation of the HOG scheme, SGD has the following advantages:

- Training can be sped up by two to three orders of magnitude, depending on the particular SVM implementation.
- A slight increase in recognition performance can be reported for some object classes. In order to get an impression about the performance of the scheme, Fig. 2.21 shows detection results for several challenging scenes for the object class “car”. Red frames indicate wrong detections and green frames correct ones (with a significantly large overlap between detected area and ground truth).
- The nature of the training algorithm admits online training, because we can do an extra iteration of the SGD training step at any time, e.g., when some new samples (which should help to improve classification performance) become available.

2.6 Constrained Optimization

For the methods presented up to now, the only criterion when calculating the solution $\mathbf{x}^*$ is to minimize the objective $f(\mathbf{x})$. In many applications, however, $\mathbf{x}^*$ has to fulfill additional requirements. More specifically, the range of values each

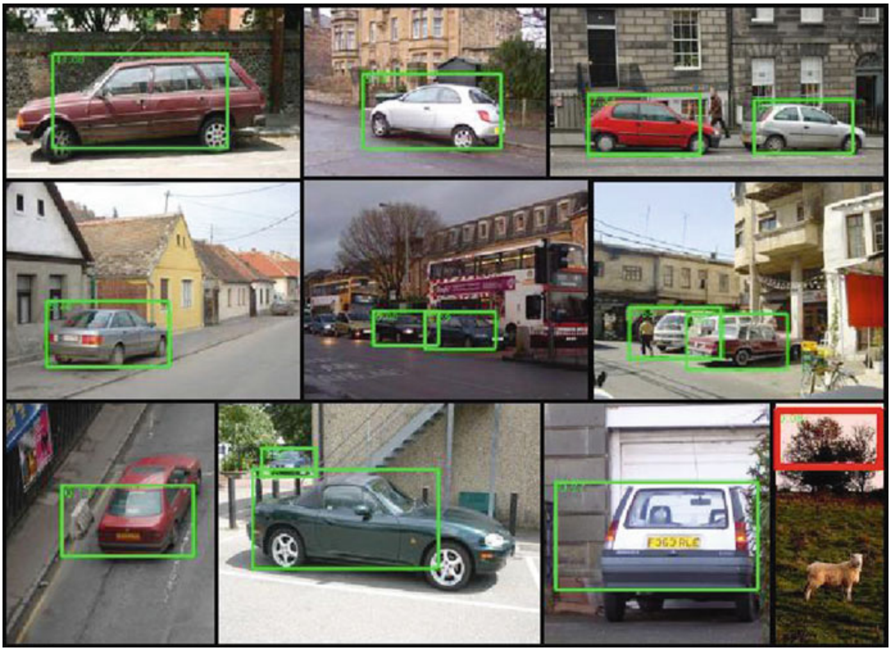

Fig. 2.21 Illustrating the recognition performance of a HOG detector for cars when trained with stochastic gradient descent. Correct detections are boxed by a *green rectangle* and false classifications by a *red* one. As clearly can be seen, the algorithm shows good performance, even if the appearance of the cars varies significantly (© 2010 IEEE. Reprinted, with permission, from Vijnhoven and de Width [15])

element of $\mathbf{x}^*$ can take might be constrained. In other words, the solution space S is constrained to some subspace of $\mathbb{R}^n$. For example, when calibrating a camera as proposed in Sect. 2.4.2, a reasonable assumption is that the center of the radial distortion is located within the image.

Of course, such constraints (if existent) have to be considered when calculating the solution. The field dealing with these additional requirements is called *constrained optimization*. Due to space reasons, we don't give an exhaustive treatment of this topic and just present some important ideas on how to consider additional constraints. The interested reader is referred to, e.g., [3] for a more detailed introduction.

First, we have to note that there are two types of constraints. The first type is called *equality constraint*, because here some function of the elements of $\mathbf{x}^*$ has to be exactly equal to some constant value. Mathematically, this can be expressed by

$$g_m(\mathbf{x}) = 0 \quad \text{with } m \in [1, 2, \ldots, M] \tag{2.49}$$

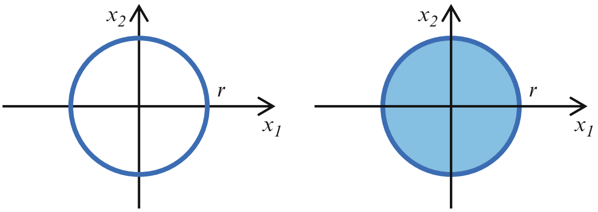

Fig. 2.22 Illustrating the different types of constraints for a two-dimensional example: in the *left figure*, the solution space is restricted to a circle with radius r (equality constraint), whereas in the *right figure* the interior of the circle is part of the solution space, too (inequality constraint)

where each g_m describes a separate constraint. Another type of constraints are the so-called inequality constraints, where some function $h_n(\mathbf{x})$ is restricted to take values which are constrained by an upper bound:

$$h_n(\mathbf{x}) \leq 0 \quad \text{with } n \in [1, 2, \ldots, N] \tag{2.50}$$

A simple example for both types of constraints is given in Fig. 2.22 in the case of a two-dimensional solution space, where in the left illustration the solution is constrained to be located on a circle of radius r (i.e., $x_1^2 + x_2^2 = r$), which is an equality constraint. The right image depicts a situation where the solution has to be located inside some circle (i.e., $x_1^2 + x_2^2 \leq r$), which is an example of an inequality constraint.

In the following, some ideas on how to consider these constraints are given. In the following, the schemes dealing with constraints are categorized into three categories:

- Projection methods
- Penalty methods
- Barrier methods

The main idea of so-called projection methods is to first calculate the solution update with some iterative method as described previously as in the unconstrained case and then project back this update to a "valid" position which meets the constraints. This back-projection is done at the end of each iteration.

A particularly simple proceeding can be performed if each element of $\mathbf{x}$ is constrained to be within a certain range of values, i.e., $x_{i,l} \leq x_i \leq x_{i,u}$. Then we can simply set x_i^k to $x_{i,l}$ if it is below this threshold, and, respectively, to $x_{i,u}$ if is larger than $x_{i,u}$. After this correction step, the iteration can proceed analogously to the unconstrained case.

The back-projection can be integrated very well into iterative the methods presented in the previous chapters. The only modification compared to the unconstrained case is to perform the additional back-projection step at the end of each iteration.

Different from this, *penalty methods* aim at modifying the objective $f(\mathbf{x})$ such that solutions located far away from the constrained solution space are penalized and therefore avoided by the optimization algorithm. To this end, a penalty term is introduced in the objective:

$$p(\mathbf{x}) = f(\mathbf{x}) + c \cdot \left[\sum_{m=1}^{M} g_m(\mathbf{x})^2 + \sum_{n=1}^{N} \max\left(0, h_n(\mathbf{x})^2\right) \right] \tag{2.51}$$

The modified objective $p(\mathbf{x})$ can now be optimized with any unconstrained optimization method. However, please note that there is no guarantee that all constraints are actually met by the found solution, violations of the constraints just become less likely. Therefore, the whole process is performed iteratively, where in each iteration l, the weight c_l of the influence of the penalty term is increased successively in order to be sure that the constraints are met at finish. Observe that here one iteration comprises the application of the complete proceeding of an unconstrained optimization method.

Similar to that, the so-called barrier methods (also termed *interior methods*) modify the objective function through the introduction of a penalty term, too. Additionally, they assume that the optimization starts within the constrained solution space and hence can only be applied to problems with inequality constraints. The penalty term should introduce costs getting larger when we approach the border of the constrained solution space. This can be formulated as

$$b(\mathbf{x}) = f(\mathbf{x}) - c \cdot \sum_{n=1}^{N} \frac{1}{h_n(\mathbf{x})} \tag{2.52}$$

As each $h_n(\mathbf{x}) \leq 0$, this actually introduces costs. These additional costs aim at ensuring that the constrained solution space is never left. Observe that the h_n can always be designed to take nonpositive values by multiplication with -1, if necessary.

Again, $b(\mathbf{x})$ can be optimized through the iterative application of an unconstrained optimization method. This time, however, the c_l is successively reduced, which means that the constraints are loosened if we already are near the optimum in order to get more accurate results.

References

1. Björck A (1996) Numerical methods for least squares problems. Society for Industrial and Applied Mathematics, Philadelphia. ISBN 978-0-898-71360-2
2. Bonnans J-F, Gilbert JC, Lemarechal C, Sagastizábal CA (2006) Numerical optimization – theoretical and practical aspects, 2nd edn. Springer, Berlin\New York. ISBN 978-3-540-35445-1
3. Boyd S, Vandenberghe L (2004) Convex optimization, 2nd edn. Cambridge University Press, Cambridge\New York. ISBN 978-0-521-83378-3
4. Dalal N, Triggs B (2005) Histograms of oriented gradients for human detection. Comput Vis Pattern Recognit 1:886–893

5. Domokos C, Nemeth J, Kato Z (2012) Nonlinear shape registration without correspondences. IEEE Trans Pattern Anal Mach Intell 34(5):943–958
6. Golub GH, Van Loan CF (1996) Matrix computations, 3rd edn. Johns Hopkins University Press, Baltimore. ISBN 0-8018-5414-8
7. Hager WW, Zhang H (2006) A survey of nonlinear conjugate gradient methods. Pac J Optimiz 2(1):35–58
8. Hartley R, Zisserman A (2004) Multiple view geometry in computer vision, 2nd edn. Cambridge University Press, Cambridge. ISBN 978–0521540513
9. Kirkpatrick S, Gelatt CD, Vecchi MP (1983) Optimization by simulated annealing. Science 220(4598):671–680
10. Levenberg K (1944) A method for the solution of certain non-linear problems in least squares. Q Appl Math 2:164–168
11. Lowe DG (2004) Distinctive image features from scale-invariant viewpoints. Int J Comput Vis 60:91–111
12. Marquardt D (1963) An algorithm for least-squares estimation of nonlinear parameters. SIAM J Appl Math 11(2):431–441
13. Shewchuck JR (1994) An introduction to the conjugate gradient method without the agonizing pain. Technical Report Carnegie Mellon University, Pittsburgh
14. Vanderplaats GN (1984) Numerical optimization techniques for engineering design. McGraw Hill, New York. ISBN 0-07-066964-3
15. Vijnhoven R, de Width P (2010) Fast training of object detection using stochastic gradient descent. In: 20th international conference on pattern recognition, Washington DC. pp 424–427

Chapter 3
Linear Programming and the Simplex Method

Abstract Problems where the objective function to be optimized is linear in its design variables are of particular interest, because then a solution can be found very efficiently. Solutions of linear objective functions can only be unique if additional constraints exist. While the constraints bound the solution space, the linear nature of the objective ensures that the solution must be located at the border of this bounded solution space. In the case of linear constraints, the bounded solution space has the form of a polyhedron, and, hence, it suffices to seek for the solution at the vertices of the bounded space. As a consequence, the optimum can be found very fast. One method for solving linear programs is the simplex algorithm, which is one of the most famous optimization algorithms. It identifies the solution by moving from a vertex to one of its neighbors until the value of the objective cannot be reduced further for all neighboring vertices. In order to benefit from the speed advantage of linear programming, it sometimes is promising to approximate a given problem by linear relationships. Such an approximation is presented for the task of stereo disparity estimation at the end of this chapter.

3.1 Linear Programming (LP)

As already stated above, a special case of continuous optimization occurs when the objective function is linear in all its variables, i.e.,

$$f(\mathbf{x}) = c_1x_1 + c_2x_2 + \cdots + c_Nx_N = \sum_{i=1}^{N} c_ix_i = \mathbf{c}^T \cdot \mathbf{x} \tag{3.1}$$

Please note that this function has *no local minima*, as all derivatives are nonzero over the entire solution space: $\partial f(\mathbf{x})/\partial x_i = c_i \neq 0 \;\forall\; i \in [1, \ldots, N]$. Please note that it can be assumed that all c_i's are nonzero, because if a specific c_i was zero, the objective function would be independent of x_i, and, consequently, no optimization

M.A. Treiber, *Optimization for Computer Vision: An Introduction to Core Concepts and Methods*, Advances in Computer Vision and Pattern Recognition,
DOI 10.1007/978-1-4471-5283-5_3, © Springer-Verlag London 2013

Fig. 3.1 Illustrating the solution set of a two-dimensional objective function, which is restricted by several constraints

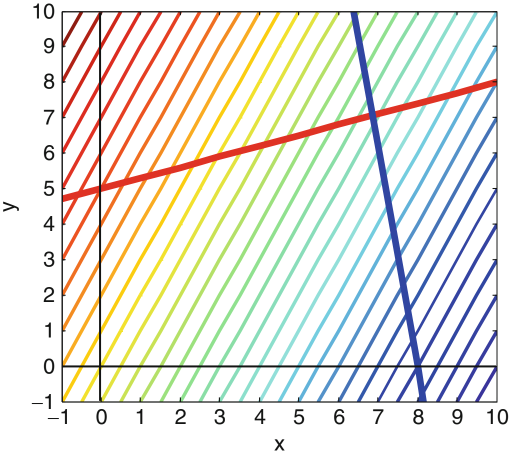

would be possible for this design variable. Consequently, if the solution space is unbounded, no solution exists (as it would be located at some point in infinity).

Hence, a solution can only be obtained if additional constraints are introduced:

$$\sum_{i=1}^{N} a_{ji}\, x_i \geq b_j \text{ or, equivalently, } \mathbf{a}_j^T \cdot \mathbf{x} \geq b_j;\ j \in [1, \ldots, M] \tag{3.2}$$

If the sum on the left-hand side has to be exactly equal to b_j, we talk about an *equality constraint*; otherwise, the constraint is termed an *inequality constraint*. M denotes the number of constraints which exist for a given problem.

Observe that all constraints of the form of (3.2) are linear in the design variables, too. A situation where not only the objective function but also the constraints are linear in all design variables is called a *linear program* (LP) .

A graphical interpretation of linear programs is that all contour lines, where $f(\mathbf{x})$ takes the same value, are straight lines. The constraints are also represented by straight lines. This can be shown with the help of a two-dimensional example: consider the objective function $f(\mathbf{x}) = 3 \cdot x_1 - 1.5 \cdot x_2$, which is represented by its contour lines in Fig. 3.1. The colors of the contour lines indicate the value of the objective at a particular position. Here, the standard MATLAB color palette is used (red-orange-yellow-cyan-blue-dark blue, in decreasing order). Suppose that each design variable is limited to nonnegative values (limits are indicated by the black coordinate axes). After introducing two additional constraints $-0.3 \cdot x_1 + x_2 \leq 5$ (indicated by the thick red line) and $6.25 \cdot x_1 + x_2 \leq 50$ (thick blue line), the solution space is bounded by a quadrangle consisting of segments of the constraints. Considering the extension to N-dimensional problems, the solution set becomes a convex polyhedron.

Fig. 3.2 Illustrating the proceeding when moving from one vertex to another adjacent vertex in order to find the minimum

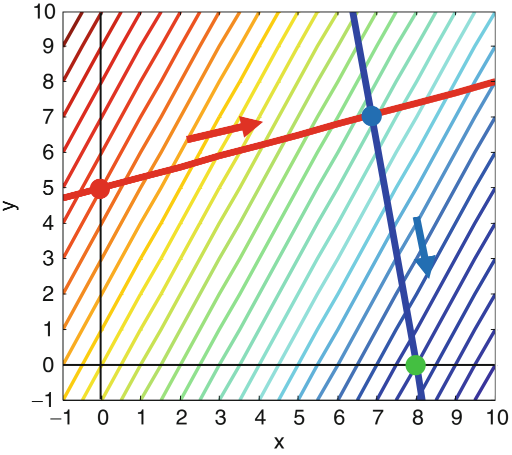

In total, the linear program of this example is given by

$$\begin{aligned} f(\mathbf{x}) &= 3 \cdot x_1 - 1.5 \cdot x_2 \\ \text{subject to } -0.3 \cdot x_1 + x_2 &\leq 5 \\ 6.25 \cdot x_1 + x_2 &\leq 50 \end{aligned} \tag{3.3}$$

Informally speaking, the constraints delimit the solution space. The fact that the objective function is linear over the entire bounded solution space (which means that the derivatives are always nonzero) leads to an important observation: the minimum $\mathbf{x}^*$ must be located at the *border* of the bounded solution space. More specifically, it is located at a vertex of the polyhedron for the following reason: If we take an interior point of the bounded solution set, the gradient at this position (which is always nonzero) involves that better solutions within the set can be found. If we follow the negative gradient, we eventually hit one of the limiting lines of the polyhedron. Normally, the gradient doesn't vanish completely if we move on along the limiting line, so further improvement is still possible until we encounter a vertex (the special case where the gradient along a limiting line becomes zero will be treated below). Each vertex is called a *basic feasible solution*.

As a consequence, we can directly derive the outline of a scheme which finds the solution/minimum $\mathbf{x}^*$ of the linear program: starting at an arbitrary vertex $\mathbf{x}^0$ of the polyhedron, we iteratively move to an adjacent vertex $\mathbf{x}^{k+1}$, which is a better solution, i.e., $f\left(\mathbf{x}^{k+1}\right) < f\left(\mathbf{x}^k\right)$, until no more improvement is possible (all adjacent vertices take larger values of the objective function, compared to the function value of the current vertex). An example can be seen in Fig. 3.2: Starting from the vertex marked red, we can move in the direction of the red arrow to the vertex marked blue, because the objective function takes a lower value there. The same holds when moving from the blue to the green vertex along the blue arrow, which marks the desired solution, as the fourth, unmarked vertex takes a higher function value.

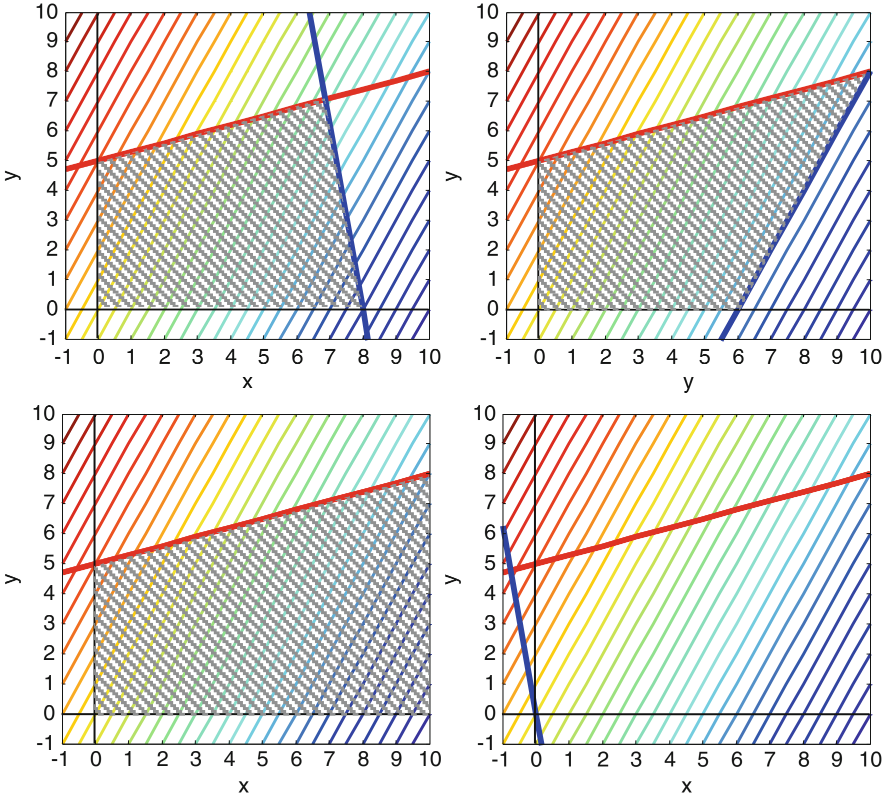

Fig. 3.3 Depicting the solution set for different cases (see text for details)

Please note that the minimum was found in just two iterations. This observation gives a hint why linear programs are so attractive: the fact that the solution (if existent) must lie at the border of the constrained solution set enables us to find it very quickly. Consequently, many researchers try to describe or approximate their problem at hand by a linear program.

However, the existence of a unique solution is not guaranteed. Actually, four types of solution exist for linear programs, depending on the constraints:

1. *Unique solution*: Here, the constraints ensure that the solution set is entirely bounded. This case is shown in the left picture of the upper row of Fig. 3.3 (the solution set is indicated by the ruled area). The solution is located at a vertex of the polyhedron bounding the solution set.
2. *Non-unique solution*: As in case (1), the constraints entirely bound the solution set. In contrast to case (1), however, one of the lines indicating the constraints is parallel to the contour lines. Consequently, the objective function takes the same value at each position of the "constraint line". If the value of the objective function along this line is minimal for the constrained set, there exist multiple

solutions: Each position of this line, which is also part of the bound of the solution set, is a valid solution of the linear program. This case is illustrated in the upper right image of Fig. 3.3, where the second constraint is replaced by $2{\cdot}x_1 - x_2 \leq 12$ (thick blue line). Now the thick blue line coincides with the contour line which takes the minimum function value of the constrained solution set.

3. *Unbounded solution*: If we drop the second constraint, the solution set is not entirely bounded any longer. Hence, the solution set contains an open area where the objective function decreases until negative infinity (see *lower left image* of Fig. 3.3: the value of the objective decreases as x_1 increases).
4. *No solution*: Consider replacing the second constraint by $6.25 \cdot x_1 + x_2 \leq 0$ (*thick blue line* in *lower right part* of Fig. 3.3). Now the solution set is empty, because no position can simultaneously satisfy all constraints.

3.2 Simplex Method

The simplex method, which aims at optimizing linear programs, was introduced by Dantzig in the 1950s (see, e.g., [3, 4]) and is one of the most famous optimization algorithms. Its basic proceeding derives from the fact that the solution of linear programs – if existent and unique – must be one of the vertices of the polyhedron bounding the solution set and, additionally, this solution consists of at most M nonzero design variables, where M denotes the number of constraints (detailed explanations will follow later).

Therefore, the solution can be found by starting at an initial basic feasible solution (vertex) containing M nonzero variables (which are called "active") and iteratively replacing one of the active variables by one of the inactive variables at each step until no more improvement can be made. Geometrically speaking, each replacement corresponds to moving to an adjacent vertex of the polyhedron.

Before presenting the method, we have to note that the simplex method requires a linear program in its *standard form*. The standard form can be written as

$$\begin{aligned} &\text{find } \mathbf{x}^* = \arg\min \left[f(\mathbf{x}) = \sum_{i=1}^{N} c_i x_i = \mathbf{c}^T \cdot \mathbf{x} \right] \\ &\text{subject to} \quad \sum_{i=1}^{N} a_{ji} x_i = \mathbf{a}_j^T \cdot \mathbf{x} = b_j; \quad j \in [1, \ldots, M] \quad \text{or} \quad \mathbf{Ax} = \mathbf{b} \\ &\qquad\qquad\quad x_i \geq 0 \end{aligned} \tag{3.4}$$

At a first glance, this seems like a major restriction, because only equality constraints are allowed and all design variables are constrained to nonnegative values. However, it turns out that any linear program can be converted into standard form with rather little effort. Typically, this conversion is done by the introduction of additional variables, which become part of the optimization:

- Any unbounded design variable x_i can be replaced by the difference of two positive variables: $x_i = x'_i - x''_i; \quad x'_i,\ x''_i \geq 0$.
- Any inequality constraint can be converted into an equality constraint by the introduction of a so-called slack variable x_{N+j}. This means that an inequality constraint $\sum_{i=1}^{N} a_{ji}x_i = \mathbf{a}_j^T \cdot \mathbf{x} \leq b_j$ is replaced by the equality constraint $\sum_{i=1}^{N} a_{ji}x_i + x_{N+j} = b_j$. The newly introduced variable x_{N+j} takes the value of the quantity which is missing from $\mathbf{a}_j^T \cdot \mathbf{x}$ to b_j (the "slack," which by definition is nonnegative).

Please note that if we consider the standard form of a linear program, the number of nonzero design variables in its minimum $\mathbf{x}^*$ is at most M (the number of constraints).

Let's check this for our toy example (3.2). Observe that the solution space in standard form is of dimension four (two design variables and two slack variables, which are necessary to convert the two inequality constraints into equality constraints). Moreover, the bounded solution space contains four vertices.

At the origin (which is one of those vertices), both x_1 and x_2 are equal to zero. In turn, both slack variables x_3 and x_4 have to be different from zero, because both equality constraints are not fulfilled. At the position of the vertex located at the intersection of the lines representing the inequality constraints (red and blue lines), both x_1 and x_2 are different from zero. As equality is fulfilled for both constraints, the two slack variables x_3 and x_4 can both be set to zero. In total, two design variables are different from zero at both vertices.

Now consider a vertex being the intersection of a colored line and one of the coordinate axes: here, only one of the variables x_1 or x_2 is different from zero. However, now one of the slack variables has to be unequal to zero, too, because the vertex is not a part of either the red or the blue line any longer. Accordingly, again two variables are different from zero.

Another two-dimensional example can be seen in Fig. 3.4, where three inequality constraints exist (indicated by the bold red, green, and blue lines). This means also that we have three slack variables in that case. Now even for the vertices where both x_1 and x_2 are different from zero, equality is impossible to be assured for all of the constraints simultaneously. Therefore, one stack variable has to be greater than zero (if both x_1 and x_2 are unequal to zero), which sums up to three nonzero variables in total.

Now let's turn toward the mode of operation of the simplex method. Basically, it consists of two phases:

- *Phase I* finds an initial basic feasible solution (picks one of the vertices of the polyhedron) and thereby converts the program into a so-called canonical form. The characteristics of the canonical form are as follows:
  - The program is available in standard form (as specified by (3.4)).
  - All b_j are nonnegative.
  - All the M "active" variables representing the basic feasible solution (denoted by the set $\{x_l\}; l \in [1, \ldots, N]; |\{x_l\}| = M$) affect only one line of the equation

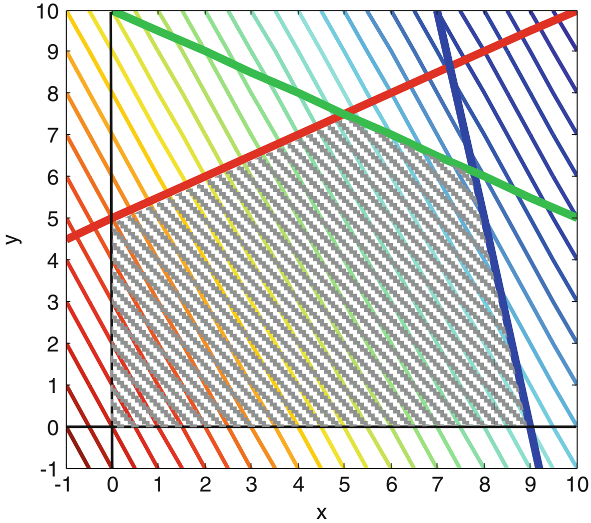

Fig. 3.4 Illustrating the solution set of a two-dimensional objective function, which is restricted by three constraints (*red*, *green,* and *blue bold lines*). Each of the inequality constraints indicated by the *red*, *green,* and *blue* lines involves the introduction of a slack variable when converting the linear program to standard form. Consequently, three slack variables are introduced, and the solution consists of at most three variables different form zero

system representing the linear program (see, e.g., (3.5)). This involves that each of the columns $\mathbf{a}_l$ of $\mathbf{A}$ contains one element equal to one, whereas all other elements of the $\mathbf{a}_l$ are zero.

If originally all constraints are inequality constraints, this condition is fulfilled for all slack variables. Finding an initial basic feasible solution is particularly simple in that case: we can consider all slack variables as active and pick the vertex corresponding to the origin of the space of the initial design variables (where all initial design variables are zero) as initial solution.

- *Phase II* moves from one basic feasible solution/vertex to the next until no more improvement can be made, i.e., the objective function takes higher values for all adjacent vertices and thus a minimum is found. One step of this movement amounts to the replacement of one active variable of the current basic feasible solution (from now on termed x_{out}) by one of the currently inactive variables (termed x_{in}). The canonical form facilitates the search for x_{in} and x_{out}. Therefore, at the end of each step, the program has to be converted into its canonical form again.

The objective function and the equality constraints can be combined in one system of linear equations:

$$\begin{bmatrix} a_{11} & a_{12} & \cdots & a_{1N} & 1 & 0 & \cdots & 0 \\ a_{21} & a_{22} & \cdots & a_{2N} & 0 & 1 & \cdots & 0 \\ \vdots & \vdots & \vdots & \vdots & \vdots & \vdots & \vdots & \vdots \\ a_{M1} & a_{M2} & \cdots & a_{MN} & 0 & 0 & \cdots & 1 \\ c_1 & c_2 & \cdots & c_N & 0 & 0 & \cdots & 0 \end{bmatrix} \cdot \begin{bmatrix} x_1 \\ x_2 \\ \vdots \\ x_N \\ x_{N+1} \\ x_{N+2} \\ \vdots \\ x_{N+M} \end{bmatrix} = \begin{bmatrix} b_1 \\ b_2 \\ \vdots \\ b_M \\ f(\mathbf{x}) - f\left(\mathbf{x}^k\right) \end{bmatrix} \tag{3.5}$$

where the first M rows represent the constraints and the last row represents the objective function, with $f\left(\mathbf{x}^k\right)$ being its value at the current solution. (3.5) is often referred to as the *simplex tableau*. If all M constraints are inequality constraints, only the slack variables x_{N+1} to x_{N+M} are active in the initial basic feasible solution, and, consequently, the last M columns of the matrix contain only one element equal to 1, all others are zero.

For the moment, let's assume that the problem already is available in canonical form. Then, phase II of the simplex algorithm proceeds as follows. Each iteration has to asses which active variable x_{out} is to be substituted and which inactive variable x_{in} will replace x_{out}. Overall, each iteration comprises the following steps:

1. *Specification of* x_{in}: This can be done by examining the coefficients of the last row of (3.4). A negative coefficient $c_i < 0$ indicates that the value of the objective will decrease if the corresponding variable x_i will become greater than zero. Consequently, x_{in} will be chosen such that the corresponding coefficient c_{in} has the most negative value among all c_i belonging to currently inactive variables. If all such c_i have positive values, no more improvement can be made and the iteration stops.
2. *Specification of* x_{out}: In order to find x_{out}, the ratios $b_j / a_{j,\text{in}}$ are calculated for all $j \in [1, \ldots, M]$. The index out is chosen such that $b_{\text{out}} / a_{\text{out,in}}$ has the smallest ratio among all ratios where $a_{j,\text{in}}$ is positive. In order to find the variable x_{out} leaving the basic feasible solution, we search for the active variable which has a coefficient equal to 1 in row out.
3. *Rearrangement of the simplex tableau* such that it is canonical with respect to the updated basic variables. This operation is called *pivoting* on the element $a_{\text{out,in}}$. The goal is to modify the simplex tableau such that column $\mathbf{a}_{\text{in}}$ contains only one nonzero element at position out, which can be set to one, i.e., $a_{\text{out,in}}^{k+1} = 1$ and all other $a_{j,\text{in}}^{k+1} = 0$. Therefore, the following two steps are performed:
    1. Divide row out by $a_{\text{out,in}}$. This ensures that $a_{\text{out,in}}^{k+1} = 1$.
    2. For all other rows j, multiply the updated row out by $a_{j,\text{in}}$ and subtract the result from row j. This ensures that $a_{j,\text{in}}^{k+1} = 0$.

After the iteration has stopped, the c_i of the non-basic (inactive) variables reveal the type of the solution:

- All c_i are positive: the solution is unique.
- One or more c_i's are equal to zero: the solution is not unique.
- One or more c_i's are less than zero: the solution is unbounded.

An overview of the general proceeding can be seen in Fig. 3.5.

Let's illustrate this proceeding with the help of a little example. Consider the objective $f(\mathbf{x}) = -3 \cdot x_1 - 1.5 \cdot x_2 + 20$ and the constraints $-0.5 \cdot x_1 + x_2 \leq 5$, $5 \cdot x_1 + x_2 \leq 45$, and $0.5 \cdot x_1 + x_2 \leq 10$ (see Fig. 3.4). For the initial basic feasible

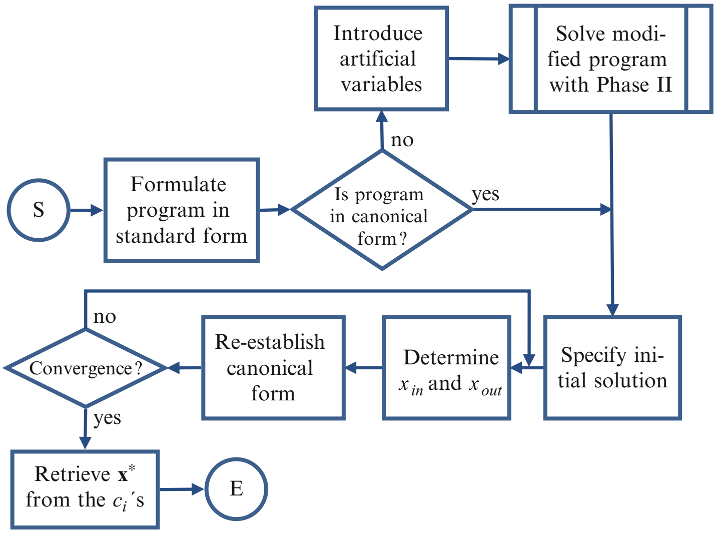
S
Formulate program in standard form
Is program in canonical form?
no
yes
Introduce artificial variables
Solve modified program with Phase II
Specify initial solution
Determine x_{in} and x_{out}
Re-establish canonical form
Convergence?
no
yes
Retrieve $\mathbf{x}^*$ from the c_i's
E

Fig. 3.5 Flowchart of the simplex method

solution $x_1 = x_2 = 0$ (*black point* in Fig. 3.6), the objective takes the value $f(\mathbf{0}) = 20$. Hence, the simplex tableau can be written as

$$\begin{bmatrix} -0.5 & 1 & 1 & 0 & 0 \\ 5 & 1 & 0 & 1 & 0 \\ 0.5 & 1 & 0 & 0 & 1 \\ -3 & -1.5 & 0 & 0 & 0 \end{bmatrix} \cdot \begin{bmatrix} x_1 \\ x_2 \\ x_3 \\ x_4 \\ x_5 \end{bmatrix} = \begin{bmatrix} 5 \\ 45 \\ 10 \\ f(\mathbf{x}) - 20 \end{bmatrix} \tag{3.6}$$

with x_3 to x_5 denoting the slack variables.

As all three constraints are inequality constraints, we have three slack variables in total. (3.5) already is in canonical form, so we can directly proceed with phase II of the simplex algorithm. The most negative coefficient of the last row is -3 in the first column, so x_1 will enter the solution. Consequently, the first column of the matrix has to be considered for determining the variable which has to leave the solution. There, we have two positive elements, with the ratio of $b_2 / a_{2,1}$ being the smallest. Consequently, we have to pivot on $a_{2,1}$. An examination of row 2 reveals that x_4 will leave the solution. Geometrically speaking, this corresponds to a movement along the x-axis (indicated by the black arrow in Fig. 3.6) to the vertex marked green in Fig. 3.6.

In order to rearrange the tableau to canonical form, we first divide row 2 by the value 5 and then subtract the thus updated row -0.5 times from row 1 (thus add it 0.5 times), subtract it 0.5 times from row 3, and subtract it -3 times (add it 3 times) from row 4. This yields the following updated simplex tableau:

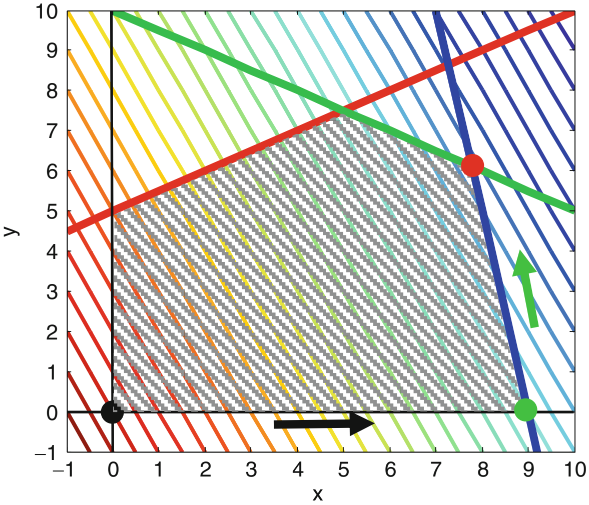

Fig. 3.6 Illustrating the proceeding when optimizing the linear program (3.6) with the simplex method

$$\begin{bmatrix} 0 & 1.1 & 1 & 0.1 & 0 \\ 1 & 0.2 & 0 & 0.2 & 0 \\ 0 & 0.9 & 0 & -0.1 & 1 \\ 0 & -0.9 & 0 & 0.6 & 0 \end{bmatrix} \cdot \begin{bmatrix} x_1 \\ x_2 \\ x_3 \\ x_4 \\ x_5 \end{bmatrix} = \begin{bmatrix} 9.5 \\ 9 \\ 5.5 \\ f(\mathbf{x}) + 7 \end{bmatrix} \tag{3.7}$$

In the next iteration, we see that progress can still be made, as the second coefficient of the last row is negative. Hence, x_2 will enter the solution. As the elements $a_{1,2}$, $a_{2,2}$, and $a_{3,2}$ are all positive, the ratio of all of them has to be calculated. Because $b_3 / a_{3,2}$ yields the smallest value, pivoting is done on $a_{3,2}$, and x_5 leaves the solution (see Fig. 3.6: movement along the *green arrow* until the *red* vertex is reached). According to step 3, the third row is to be divided by 0.9, and the result is to be subtracted 1.1 times from row 1 and 0.2 times from row 2 and added 0.9 times from the last row. As a result, the following updated simplex tableau is obtained:

$$\begin{bmatrix} 0 & 0 & 1 & \frac{2}{9} & -\frac{11}{9} \\ 1 & 0 & 0 & \frac{2}{9} & -\frac{2}{9} \\ 0 & 1 & 0 & -\frac{1}{9} & \frac{10}{9} \\ 0 & 0 & 0 & 0.5 & 1 \end{bmatrix} \cdot \begin{bmatrix} x_1 \\ x_2 \\ x_3 \\ x_4 \\ x_5 \end{bmatrix} = \begin{bmatrix} \frac{25}{9} \\ \frac{70}{9} \\ \frac{55}{9} \\ f(\mathbf{x}) + 12.5 \end{bmatrix} \tag{3.8}$$

Now all coefficients in the last row belonging to non-basic variables are positive. Consequently, the iteration stops and the obtained solution is unique. As x_4 and x_5 are zero, the solution can be seen directly from equation (3.8). The first row reveals that $x_3 = 25/9$, from the second row we obtain $x_1 = 70/9$, and the third row yields $x_2 = 55/9$.

Now let's come back to phase I, which is needed if the standard form of the linear program is not in canonical form at start. Consider replacing the second constraint in the above example by $-x_1 + x_2 \leq -2$. Now b_2 is negative, and consequently, the program is not in its canonical form if the initial basic solution contains the slack variables x_3 to x_5:

$$\begin{bmatrix} -0.5 & 1 & 1 & 0 & 0 \\ -1 & 1 & 0 & 1 & 0 \\ 0.5 & 1 & 0 & 0 & 1 \\ -3 & -1.5 & 0 & 0 & 0 \end{bmatrix} \cdot \begin{bmatrix} x_1 \\ x_2 \\ x_3 \\ x_4 \\ x_5 \end{bmatrix} = \begin{bmatrix} 5 \\ -2 \\ 10 \\ f(\mathbf{x}) - 20 \end{bmatrix} \tag{3.9}$$

In order to make b_2 positive, row 2 can be multiplied by -1, but, in turn, this makes the coefficient of x_4 negative. This means that x_4 is not an active variable any longer. A way out of this dilemma is to introduce another variable x_6 (which is appended to row 2, as row 2 was multiplied by -1) as well as another function $x_6 = r$. The introduction of $x_6 = r$ means that we add another row to the simplex tableau and treat the former last row belonging to the "real" objective as a constraint equation. Now we have

$$\begin{bmatrix} -0.5 & 1 & 1 & 0 & 0 & 0 \\ 1 & -1 & 0 & -1 & 0 & 1 \\ 0.5 & 1 & 0 & 0 & 1 & 0 \\ -3 & -1.5 & 0 & 0 & 0 & 0 \\ 0 & 0 & 0 & 0 & 0 & 1 \end{bmatrix} \cdot \begin{bmatrix} x_1 \\ x_2 \\ x_3 \\ x_4 \\ x_5 \\ x_6 \end{bmatrix} = \begin{bmatrix} 5 \\ 2 \\ 10 \\ f(\mathbf{x}) - 20 \\ r \end{bmatrix} \tag{3.10}$$

This tableau can be converted into canonical form by ensuring that only one coefficient of the last column of the matrix is nonzero. This can be done if row 2 is subtracted from row 6 yielding

$$\begin{bmatrix} -0.5 & 1 & 1 & 0 & 0 & 0 \\ 1 & -1 & 0 & -1 & 0 & 1 \\ 0.5 & 1 & 0 & 0 & 1 & 0 \\ -3 & -1.5 & 0 & 0 & 0 & 0 \\ -1 & 1 & 0 & 1 & 0 & 0 \end{bmatrix} \cdot \begin{bmatrix} x_1 \\ x_2 \\ x_3 \\ x_4 \\ x_5 \\ x_6 \end{bmatrix} = \begin{bmatrix} 5 \\ 2 \\ 10 \\ f(\mathbf{x}) - 20 \\ r - 2 \end{bmatrix} \tag{3.11}$$

which now is in canonical form with the basic variables x_3, x_5, and x_6. However, as x_6 doesn't exist in the original problem, it has to be eliminated again. This can be done by solving (3.11), i.e., finding a basic feasible solution which minimizes r. To this end, the proceeding of phase II can be applied. If we end up with a solution which sets r to zero ($x_6 = r = 0$), we can eliminate x_6 again (drop the last column as well as the last row) and solve the remaining simplex tableau with phase II. However, if the solution of phase I does lead to a solution where $r \neq 0$, a solution without the artificial variable x_6 cannot be found. This means that no solution exists for the original linear program in that case.

Overall, phase I consists of the following steps:

1. Multiplication of all rows j which have a negative b_j by -1, if necessary.
2. Introduction of as many artificial variables as necessary (introduce new variables until there are M variables affecting only one constraint, i.e., “their” column features only one nonzero value which is equal to 1).
3. Creation of a new objective function r, which is equal to the sum of all newly introduced variables.
4. Converting the extended problem into canonical form by subtracting all rows where new variables were introduced from the last row (such that the last row contains zeros in all columns where the variables are part of the initial basic feasible solution).
5. Solution of the just obtained linear program by applying phase II.
6. Elimination of the just introduced artificial variables in the case of $r = 0$. If $r \neq 0$, no solution exists.

Pseudocode

```
function solveLinearProgramSimplex (in objective function
$f(\mathbf{x})$, in constraints specified by $\mathbf{A}$ and $\mathbf{b}$, out solution $\mathbf{x}^*$)

// conversion of linear program to standard form
introduce a slack variable for each inequality constraint in
order to convert it into an equality constraint
split each non-restricted design variable into the difference of two design variables restricted to non-negative
values
create the simplex tableau according to (3.5)

// conversion of simplex tableau into canonical form, if
necessary (phase I)
if linear program is not canonical then
    for each row $j$ where $b_j < 0$
        // not in accordance with canonical form
        multiply row $j$ by -1
    next
    add new artificial design variables until $M$ design
    variables affect only one constraint (one element of
    column equals one, the others are zero)
    create a new objective $r$ which equals the sum of all artificial design variables
```

```
convert the thus obtained tableau into canonical form by row subtraction
  // solve the modified linear program by executing phase II
  call solveSimplexPhaseII ($f(\mathbf{x})$, simplex tabl., out $\mathbf{x}_{PI}^{*}$)
  if $r == 0$ then
    eliminate all artificial design variables again
  else
    exit // no solution exists
  end if
end if

// solve the linear program (phase II of the simplex method)
call solveSimplexPhaseII ($f(\mathbf{x})$, simplex tableau, out $\mathbf{x}^{*}$)
check the $c_i$'s in order to determine the kind of the solution

function solveSimplexPhaseII (in objective function $f(\mathbf{x})$, in
simplex tableau specified by $\mathbf{A}$ and $\mathbf{b}$, out solution $\mathbf{x}^{*}$)

specify initial basic feasible solution (contains only
slack variables)

// iterative search loop (moves from vertex to vertex)
repeat
  // replace design variable $x_{out}$ by $x_{in}$
  find $c_{in}$ which has the most negative value (yields $x_{in}$)
  find the smallest ratio $b_j / a_{j,in}$ for all $j \in [1..M]$ where $a_{j,in} > 0$
  (yields $x_{out}$)
  // pivot on $a_{out,in}$: re-establish canonical form
  divide row $out$ by $a_{out,in}$
  for all other rows $j$
      multiply the updated row $out$ by $a_{j,in}$
      subtract the result from row $j$
  next
until convergence (all $c_i$'s are >=0)
retrieve solution $\mathbf{x}^{*}$ form the $c_i$'s of the current simplex
tableau
```

Over the years, many other solvers for linear programs have been developed. One important class of solvers are the so-called interior point methods (sometimes also called *barrier methods*), where the interior of the solution space is explored (see, e.g., [4–6] or [7]). It can be proven that these methods are able to find the optimum in polynomial time. On average, performance of interior point methods is comparable to the simplex method. For practical examples, however, it depends on the specific nature of the problem whether the simplex method or interior point methods perform better.

If additionally the values of the design variables are required to be integers, the resulting program is called an *integer program*. In contrast to linear programs, the solution of these programs is NP-hard. For special subclasses, however, there exist efficient solutions (see, e.g., [8]).

3.3 Example: Stereo Matching

Bhusnurmath et al. showed that stereo matching can be formulated as a linear program [2]. In stereo matching, a scene is captured by a pair of cameras with known geometric configuration, i.e., the distance between the two cameras as well as the orientations of both cameras are known. Because the two cameras take a different viewpoint, objects which are captured by both cameras appear with a shift between them when we compare the two camera images.

This shift, which is also called *disparity*, is a function of the z-distance between the object and the camera system (the so-called depth of the scene). The closer the object, the larger is the disparity. Many computer vision tasks require an estimation of the scene depth. If the cameras are calibrated, it is possible to infer the depth from the disparity values. Hence, the problem of stereo matching amounts to estimating the disparity d_i for each pixel p_i. This process can also be thought of labeling each p_i with the label d_i.

As already stated above, the z-distance between the object which is depicted at pixel p_i and the camera system can be directly derived from d_i if the camera parameters and geometric relation between the two cameras are known. As a result, a so-called height map can be calculated, which depicts the z-distance to the camera system for each pixel of the image. Height maps can be used, e.g., in obstacle avoidance applications.

The geometric configuration of the two cameras conditions that all disparities appear in the same direction, i.e., the vectors between a pixel p_i in the first image and its "counterpart" in the second image point to the same direction for all pixels. Therefore, we can search along a scan line with known direction when we want to calculate a disparity $d(p_i)$ for a given pixel p_i, which will be denoted d_i for brevity in the following. Usually it can be assumed that the scan line is a horizontal line (which can be assured through the application of a preprocessing step known as *rectification*). Consequently, if we examine all pixels with the same y-coordinate in both images, we can determine the disparities for all pixels of this row. Additionally, a proper choice of the reference camera ensures that all disparities are positive.

Now the question remains how to determine the disparities d_i. In [2], a joint calculation of all disparities of a scan line in one optimization step is suggested. To this end, an energy $E(\mathbf{d})$ can be calculated for each scan line, which is a function of the vector $\mathbf{d}$ accumulating all disparities d_i along this line. $E(\mathbf{d})$ indicates how well the d_i explains the content of the two images. If $\mathbf{d}$ is a good explanation, $E(\mathbf{d})$ should be low. $E(\mathbf{d})$ consists of two parts:

- A *data-driven term* $E_{\text{data}}(d_i)$, which measures how well the observed image data at position p_i in the first image conforms to the observed image data in the second image, shifted by d_i pixels, i.e., at position $p_i + d_i$. A common approach in stereo for measuring how well the image data fits is to calculate some function (match score) based on the cumulated intensity differences between

- all pixels located within an image patch around pixel p_i (whose center position in the first image is (x_i, y_i)) and
- the pixels of the corresponding image patch centered at position $(x_i + d_i, y_i)$ in the second image.

- A so-called smoothness term $E_{\text{smooth}}(d_i)$ takes into account that disparities tend to be "smooth". For example, it is quite common that the image shows multiple planar objects with a surface normal parallel to the camera axis. As a consequence, the disparities should be constant in areas covered by these objects and develop steps at the object borders. Noise or artifacts, however, tend to introduce variations between the disparities of adjacent pixels everywhere in the image plane. In order to reduce the influence of noise, the total sum of the disparity gradients (i.e., the difference of disparities between adjacent pixels) should be small. Consequently, one part of $E_{\text{smooth}}(d_i)$, which we term $E_{\text{grad}}(d_i, d_{i+1})$, measures the sum of disparity gradient magnitudes between adjacent pixels p_i and p_{i+1}. A second component, $E_{\text{lap}}(d_i, d_{i+1}, d_{i-1})$, takes the second derivatives into account: if planar objects show out-of-plane rotation, i.e., their surface normal is not parallel to the camera axis, the disparity map has gradients, but no curvature. Therefore, the total curvature should be minimal.

Overall, the energy $E(d)$ of a scan line can be modeled as follows[1]:

$$E(\mathbf{d}) = \sum_{i=1}^{W} E_{\text{data}}(d_i) + \sum_{i=1}^{W-1} E_{\text{grad}}(d_i, d_{i+1}) + \sum_{i=2}^{W-1} E_{\text{lap}}(d_i, d_{i+1}, d_{i-1}) \tag{3.12}$$

where W denotes the image width. The data-driven energy can be modeled by intensity differences between corresponding image patches. The gradient-based energy term should be high when the difference of the disparities of adjacent pixels is high:

$$E_{\text{grad}}(d_i, d_{i+1}) = \begin{cases} 0 \quad \text{if } |d_i - d_{i+1}| \le \varepsilon \\ w_{g,i} \cdot (|d_i - d_{i+1}| - \varepsilon) \quad \text{otherwise} \end{cases} \tag{3.13}$$

Through the introduction of ε, small disparity changes are not punished. $w_{g,i}$ is a weighting parameter (corresponding to pixel p_i) and allows to adjust the relative importance of a pixel. Consider the disparities at the edge between two objects, for example: usually, the z-distance of the two objects differs, and consequently, the

[1] For convenience, only the one-dimensional solution, where all disparities along one scan line are estimated simultaneously, is presented here. However, the extension to the 2D case is possible and rather straightforward.

disparity shows a discontinuity at the edge between the objects. Therefore, the weighting factors of these “edge pixels” obtain a low value in order to allow for disparity discontinuities at these positions.

The second-order Laplacian term should punish high curvatures of the disparity as many objects are assumed to be at least nearly planar. It can be set to the discrete approximation of the Laplacian (once again with a weighting term $w_{l,i}$):

$$E_{\mathrm{lap}}(d_i, d_{i+1}, d_{i-1}) = w_{l,i} \cdot |-d_{i-1} + 2d_i - d_{i+1}| \tag{3.14}$$

In stereo matching, the goal is to find for each scan line the disparities $\mathbf{d}^*$ such that $E(\mathbf{d})$ gets minimal for the line currently under consideration: $\mathbf{d}^* = \arg\min E(\mathbf{d})$. In order to solve this task, the authors of [2] suggest to convert the problem into a linear program, which can then be solved by an appropriate linear program solver. This problem formulation has the advantage that the continuous nature of linear programs avoids quantization at intermediate steps (opposed to discrete methods, which are widely used for stereo matching).

Concerning the smoothness terms, the objectives E_{grad} and E_{lap} are not linear in the design variables $\mathbf{d}$ because of the absolute values. In order to convert these terms into linear relations, additional variables are introduced and, additionally, constraints are built for these additional variables.

Let’s consider E_{grad}, for example: For each pixel, E_{grad} is set to a proxy variable $y_{g,i}$, weighted by $w_{g,i}$: $E_{\mathrm{grad}}(d_i, d_{i+1}) = w_{g,i} \cdot y_{g,i}$. If $|d_i - d_{i+1}| > \varepsilon$ and therefore $y_{g,i} > 0$, we have to consider two cases: If $d_i > d_{i+1}, y_{g,i}$ is set to $y_{g,i} = d_i - d_{i+1} - \varepsilon$. Respectively, we have to set $y_{g,i} = d_{i+1} - d_i - \varepsilon$ in the case of $d_i < d_{i+1}$. This ambiguity can be resolved by replacing the equality by three inequalities which have to be fulfilled simultaneously:

$$\begin{aligned} &y_{g,i} \geq d_i - d_{i+1} - \varepsilon \\ &y_{g,i} \geq d_{i+1} - d_i - \varepsilon \\ &0 \leq y_{g,i} \leq g_{\max} \end{aligned} \tag{3.15}$$

Considering the first two inequalities, we can see that one of them is more restrictive than the other, i.e., if the more restrictive is fulfilled, the other holds, too. Whether the first or second is more restrictive depends on the sign of $d_i - d_{i+1}$. With the help of this little “trick,” we managed to achieve linearization. The third inequality constraint ensures positivity for $y_{g,i}$ and that it is upper-bounded by $g_{\max}$. Similar considerations can be made for E_{lap} and lead to

$$\begin{aligned} &y_{l,i} \geq -d_{i-1} + 2d_i - d_{i+1} \\ &y_{l,i} \geq d_{i-1} - 2d_i + d_{i+1} \\ &0 \leq y_{l,i} \leq l_{\max} \end{aligned} \tag{3.16}$$

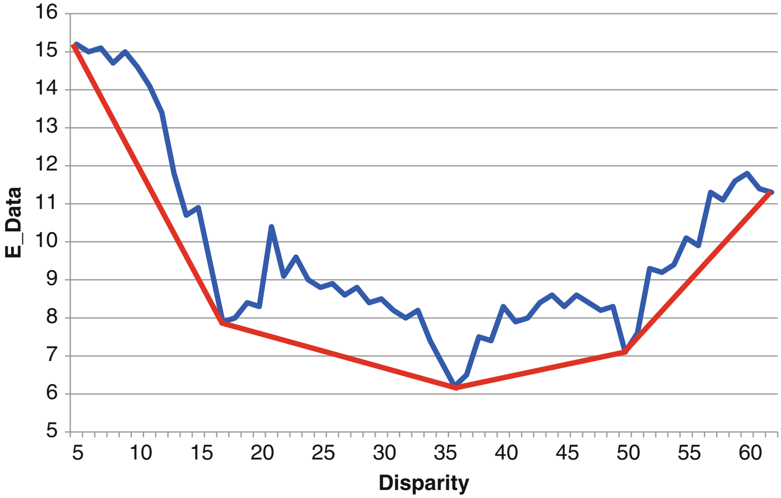

Fig. 3.7 Illustrating the data-driven energy for different disparities (*blue*) and its convex lower-bound approximation

The upper bounds $g_{\max}$ and $l_{\max}$ respect the fact that disparity values are bounded in practice.

Please note that in general the calculation of the data term of the energy by summing up intensity differences as described above is not linear nor convex. However, this would be desirable, because if the objective is known to be convex, it is assured that a found local minimum is also the global minimum. A typical example of the data-driven energy $E_{\text{data}}(d_i)$ at one pixel is shown in the blue curve of Fig. 3.7, where the pixel-wise energy is calculated dependent on the assumed disparity value. Clearly, this function is not linear nor convex. Therefore, the function is approximated by piecewise linear functions $a_{j,i}d_i + b_{j,i}$, which act as a lower bound of the energy $E_{\text{data}}(d_i)$ (see *red curve* in Fig. 3.7).

In order to formulate the stereo problem as a linear program, another auxiliary variable $y_{m,i}$ is introduced for each pixel. $y_{m,i}$ directly measures the data-driven energy at this pixel. The line segments of the piecewise linear convex approximation serve as constraints, which ensure that $y_{m,i}$ is always located above all line segments, e.g., above all red line segments shown in Fig. 3.7. Altogether, concerning $E_{\text{data}}(d_i)$, we have

$$\begin{aligned} &E_{\text{data}}(d_i) = w_{m,i} \cdot y_{m,i} \\ &y_{m,i} \geq a_{j,i}d_i + b_{j,i}, \quad j \in [1, 2, \ldots, J] \\ &0 \leq y_{m,i} \leq y_{\max} \end{aligned} \tag{3.17}$$

The final formulation of the energy is given by

$$E(\mathbf{d}) = \sum_{i=1}^{W} w_{m,i} \cdot y_{m,i} + \sum_{i=1}^{W-1} w_{g,i} \cdot y_{g,i} + \sum_{i=2}^{W-1} w_{l,i} \cdot y_{l,i} \tag{3.18}$$

The weights $w_{m,i}$ should reflect the degree of confidence in the match score (obtained through intensity comparisons) and should be low in occluded areas. Gradient and Laplacian weights $w_{g,i}$ and $w_{l,i}$ are based on the intensity or color difference between the pixels under consideration and therefore should be low if the pixels belong to different objects (which are likely to have differing colors or intensities). Therefore, they allow for clear disparity discontinuities between objects without penalizing.

(3.17) can be written as the linear function $\mathbf{w}^T \cdot \mathbf{x}$, where $\mathbf{x}$ is a vector concatenating all design variables: $\mathbf{x} = \begin{bmatrix} \mathbf{d} & \mathbf{y}_m & \mathbf{y}_g & \mathbf{y}_l \end{bmatrix}^{\mathrm{T}}$ and $\mathbf{w}$ is a vector containing the corresponding weights: $\mathbf{w} = \begin{bmatrix} \mathbf{0} & \mathbf{w}_m & \mathbf{w}_g & \mathbf{w}_l \end{bmatrix}^T$. To sum it up, (3.15, 3.16, 3.17, and 3.18) build a linear program, as all equations and inequality constraints are linear in the design variables. Consequently, this program can be solved by an appropriate optimization scheme for linear programs like the simplex method.

Details of the composition of the constraints as well as the solver employed (Bhusnurmath et al. chose an interior point method as a solver) can be found in [1, 2] and are beyond our scope here.

To sum it up, the algorithm estimating the disparities for one row of the images consists of the following steps:

1. Calculation of $E_{\text{data}}(d_i)$ for all legal disparities and all pixels
2. Approximation of $E_{\text{data}}(d_i)$ with piecewise linear functions for each pixel
3. Estimation of the weights $\mathbf{w} = \begin{bmatrix} \mathbf{0} & \mathbf{w}_m & \mathbf{w}_g & \mathbf{w}_l \end{bmatrix}^T$
4. Formulation of the linear program with the help of the introduction of the auxiliary variables $\mathbf{y}_m$, $\mathbf{y}_g$, and $\mathbf{y}_l$
5. Solution of the linear program with an interior point barrier method

Please observe that the dimensionality of the linear equation system is very large, as the number of design variables is four times the number of pixels. Moreover, the number of constraints is quite high as well. For example, a closer look at (3.16) reveals that for each pixel there exist J constraints, where J denotes the number of line segments used for convex approximation. This leads to rather long execution times, albeit because of linearity a fast optimization scheme can be employed. With a MATLAB-based implementation, the authors of [2] reported running times in the order of minutes.

Results for some images of the Middleburry data set (which is often used to compare the performance of stereo matching algorithms) can be found in the original article [2]. As can be seen there, the height map calculated by the algorithm is very close to the ground truth. Please observe that the algorithm intends to "fill gaps" at pixels where there is no reliable data available due to occlusion.

References

1. Bhusnurmath A (2011) Applying convex optimization techniques to energy minimization problems in computer vision. PhD thesis, Proquest Umi Dissertation Publishing, Philadelphia. ISBN 978–1243494221
2. Bhusnurmath A, Taylor CJ (2008) Solving stereo matching problems using interior point methods. In: Fourth international symposium on 3D data processing, visualization and transmission, pp 321–329
3. Dantzig GB (1951) Maximization of a linear function of variables subject to linear inequalities. In: Activity analysis of production and allocation. Wiley, New York, pp 339–347
4. Dantzig GB, Thapa MN (1997) Linear programming: 1: introduction. Springer, New York. ISBN 978-0387948331
5. Fang S-C, Puthenpura S (1993) Linear optimization and extensions: theory and algorithms. Prentice Hall, Englewood Cliffs. ISBN 978-0139152658
6. Gondzio J, Terlaky T (1994) A computational view of interior point methods for linear programming. In: Advances in linear and integer programming. Oxford University Press, Oxford
7. Karmarkar N (1984) A new polynomial-time algorithm for linear programming. In: Proceedings of the sixteenth annual ACM symposium on theory of computing, New York, pp 302–311
8. Nemhauser G, Wolsey A (1999) Integer and combinatorial optimization. Wiley, New York. ISBN 978-0471359432

Chapter 4
Variational Methods

Abstract The main goal of many computer vision tasks can in summary be described by finding a function which is optimal according to some criteria. Examples of such functions are the two-dimensional intensity/color function of the image itself in image restoration or deblurring, two-dimensional vector fields like optical flow, or the course of a curve separating the image into multiple areas (which are all presented as examples in this chapter). This is the domain of variational optimization, which aims at estimating those functional relationships. The functional quantifying the quality of a particular solution typically consists of two terms: one for measuring the fidelity of the solution to the observed data and a second term for incorporating prior assumptions about the expected solution, e.g., smoothness constraints. There exist several ways of finding the solution, such as closed-form solutions via the so-called Euler-Lagrange equation, or iterative gradient-based schemes. Despite of the iterative and therefore inherently slow nature of the last-mentioned approach, quite simple iterative update rules can be found for some applications, which allow for a very fast implementation on massively parallel hardware like GPUs. Therefore, variational methods currently are an active area of research in computer vision.

4.1 Introduction

4.1.1 Functionals and Their Minimization

Variational optimization deals with the problem of directly finding optimal functions *themselves*. This means that the solution space is composed of functions as elements. Compared to that, the methods presented up to now reduce the degrees of freedom when seeking the solution by fixing the structure of the function in advance. In that case, optimization is about estimating the *parameters* of the specified function type. For example, the shading correction algorithm we encountered already in Chap. 2 as an example of regression a priori specifies that the

M.A. Treiber, *Optimization for Computer Vision: An Introduction to Core Concepts and Methods*, Advances in Computer Vision and Pattern Recognition,
DOI 10.1007/978-1-4471-5283-5_4, © Springer-Verlag London 2013

shading has to be modeled by a two-dimensional polynomial up to a certain order. During optimization, just the values of the coefficients of the polynomial terms are calculated, whereas the design of the objective function remains unchanged. In contrast to that, a variational approach would make no a priori assumptions about the course of the shading function – any course would be allowed for the solution.

Let's further examine this concept with the help of another short example: given two points p and q in the two-dimensional xy-plane, we want to find the curve connecting these two points with minimal arc length. The course of the curve can be expressed by a functional relationship, and therefore, the task is to find the function that minimizes the arc length. Intuitively, we all know that the shortest connection between p and q is given by a straight line segment. But how can we find this solution mathematically? This can be done as follows (see also [6]):

Positions on the curve can be expressed as $(x, y(x))$. Hence, our aim is to find a functional relationship $y^*(x)$ which minimizes the arc length. Let the position of p and q be expressed by $p = (a, y(a))$ and $q = (b, y(b))$. The arc length l_y can be derived by integrating over the length of infinitesimal straight line segments and is given by

$$l_y = \int_a^b \sqrt{1 + y'(x)^2}\mathrm{d}x \tag{4.1}$$

where $y'(x)$ denotes the first derivative of y with respect to x: $y'(x) = \mathrm{d}y/\mathrm{d}x$. Consequently, the desired $y^*(x)$ can be found by minimizing (4.1).

A more general formulation of (4.1) is

$$F[y(x)] = \int_a^b f(x, y(x), y'(x))\mathrm{d}x \tag{4.2}$$

Functions like F are called *functionals*, which have the characteristic that they map a function to a scalar value. The task of variational optimization is then to find the argument $y^*(x)$ (which is a function) of F yielding the smallest value of F, i.e., $y^*(x)$ is the minimizer F. Please note that the goal of finding a function is just conceptually. In practice, usually numerical implementations try to find a discretized version of $y^*(x)$, where the quantities $y_i^*(x_i)$ at sampled positions x_i are to be found. Hence, in practice usually we seek a finite set of function values.

The minimization of (4.2) can be performed with a paradigm called *calculus of variations* (see [6] for a good introduction). We can formulate a necessary condition for $y^*(x)$ being a local minimum of the functional F, which is known as the *Euler-Lagrange equation*. The Euler-Lagrange equation relates to the fact that for minima of "ordinary" functions, the first derivative of the function to be minimized must be equal to zero. The Euler-Lagrange equation transfers this to functionals with functions as arguments. It is a partial differential equation and is given by

$$\frac{\partial f}{\partial y} - \frac{\mathrm{d}}{\mathrm{d}x}\left(\frac{\partial f}{\partial y'}\right) = 0 \tag{4.3}$$

The name "calculus of variations" comes from the proceeding when solving the Euler-Lagrange equation, where a set of functions, whose elements are all variations of $y(x)$, is considered.

The calculus of variations tries to solve (4.3) for a given problem (which is usually done iteratively) and then assumes that this solution is the desired solution $y^*(x)$. Observe, however, that (4.3) is only a *necessary* condition, and, moreover, we don't know whether F has a minimum at all. Consequently, we have no guarantee that we actually find the desired minimum when applying the calculus of variations.

A quite common case is that f does not directly depend on x, i.e., we can write $f(y(x), y'(x))$. Then (4.3) simplifies to

$$f - y' \cdot \frac{\partial f}{\partial y'} = C \tag{4.4}$$

where C is a constant. This is known as the *Beltrami identity*.

The general form of F is suited for many vision applications. Consider the examples of image restoration (e.g., denoising or deconvolution) being described in detail in the next section. In restoration applications, we want to infer the original version of an image $R(x, y)$ (i.e., we seek a function) but only have access to the observed data $I(x, y)$, usually corrupted by noise and/or blur. This kind of problem is said to be an *inverse problem*, where, based on some observations, we want to "infer" the unobservable but uncorrupted original signal.

As $R(x, y)$ should be close to $I(x, y)$, f should reflect a measure of difference between the two signals. Additionally, we can also assume that $R(x, y)$ varies only smoothly in many regions, e.g., because many objects are of uniform or slowly varying brightness/color. This is known as the so-called smoothness assumption. Consequently, f is also influenced by the derivative of $R(x, y)$.

Hence, f can be interpreted as measuring the suitability of $R(x, y)$ being a plausible explanation of $I(x, y)$ at a particular position $[x, y]$. However, we want to find a function which best explains the observed data in the entire image. Accordingly, we integrate f over the image area, which leads us to formulating the problem such that a functional of the form of F is to be minimized.

The general proceeding of utilizing the calculus of variations in variational optimization of computer vision problems can be summarized as follows:

1. Formulate f such that it reflects the suitability for $y(x)$ explaining some observed data x.
2. Add a smoothness constraint to f. Usually, this constraint is independent of x but relates to some derivative information of $y(x)$.
3. Build the variational integral F being based on f.
4. Find the solution by calculating the minimizing argument $y^*(x)$ of F.

Step 4 usually requires some discretization step in practice. There does not exist a standard proceeding for this step. One possibility is to set up the Euler-Lagrange equation explicitly first and then calculate the (discretized) minimizer of a discretized version of it (e.g., for active contours, see Sect. 4.5). Another option

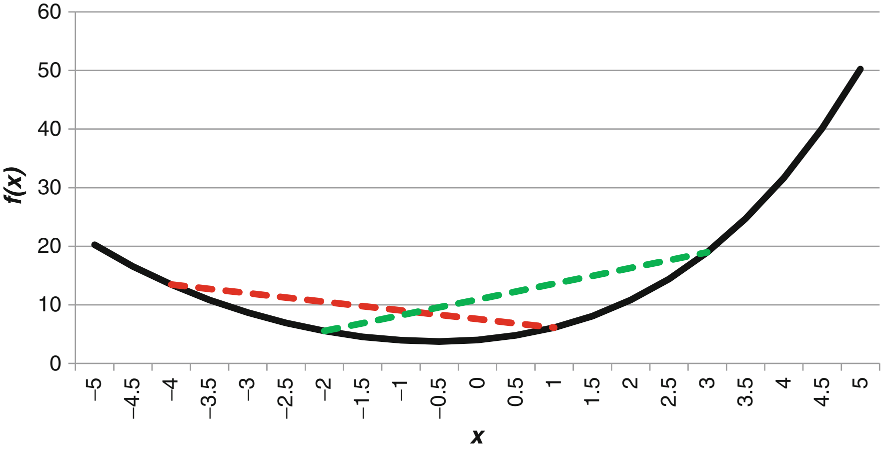

Fig. 4.1 Exemplifying a convex function (*black curve*). Each straight line segment connecting two points on the function lies "above" the function. The *red* and *green dashed lines* are two examples of this

is to perform discretization at an early stage in the domain of f. This proceeding seems natural in image restoration tasks (see Sects. 4.2 and 4.3), where $I(x,y)$ already is available in discretized form along the pixel grid. As a consequence, F is present in a discretized version, too. Its minimizing argument can therefore be expressed by a finite set of values at the sample positions.

Before we take a closer look at some variational methods in detail, let's make some comments on the quality of solutions obtained with variational methods in practice. Please note that many variational schemes are local methods (e.g., the Euler-Lagrange equation acts only locally) and therefore lead to solutions which are the best among just a local neighborhood (local optima). Consequently, we cannot be sure that its solution indeed is the desired global optimum.

However, the functionals utilized in practice in many computer vision applications are so-called convex functions. Geometrically speaking, this means that if we connect any two points $[x_1, f(x_1)]$ and $[x_2, f(x_2)]$ by a straight line, the line segment between these two points is always "above" the course of the function f (see Fig. 4.1). If this condition holds, f is convex. Mathematically speaking, f is convex if

$$f(\theta \cdot x_1 + (1-\theta) \cdot x_2) \leq \theta \cdot f(x_1) + (1-\theta) \cdot f(x_2) \tag{4.5}$$

Convex functions, in turn, have the nice property, that they have only one minimum, which therefore is ensured to be the global one. Consequently, if we know that the functional of our problem at hand is convex, we can be sure that a local optimum found has to be the global one, too.

In situations where the functional does not satisfy (4.5), there often exists the following resort: sometimes we can "relax" the functional to a different functional, which serves as a lower bound of the original functional and is convex at the same time. Thus, the *global* optimum of that relaxed functional can be found. As this relaxed functional is not equal to our original functional, the thus obtained solution is only an approximation of the true optimum. However, it can sometimes be shown that there is an upper bound for the difference between the exact solution and the approximation, e.g., a small constant factor. Thus, the strategy of approximating the functional by a convex lower bound and taking the global optimum of the lower bound functional yields quite good performance in practice.

4.1.2 Energy Functionals and Their Utilization in Computer Vision

Functionals in the form of (4.2) are appropriate to represent many computer vision applications. They often act as an *energy* E being able to judge the suitability of a particular solution y. The energy is high if y doesn't represent an adequate solution.

This can be explained best by considering a typical application, namely, restoration. *Restoration* techniques are applied to reconstruct or infer "cleaned" data without artifacts, given some measured data. In our case we deal with restoration of images, where, given some sensed image data $I(x, y)$, the task is to infer the reconstructed version $\hat{R}(x, y)$ of the original unobserved image $R(x, y)$. Noise and sometimes also other effects like blur, which are inevitably present to some extent in I, should be removed in $\hat{R}$. In this application, the relationship between R and I can be modeled by

$$I(x, y) = K * R(x, y) + n = \int\int K(a, b)R(a - x, b - y)da\,db + n \tag{4.6}$$

where n is a noise term, * is the convolution operator, and K denotes a convolution kernel which typically models some kind of blur, e.g., motion or camera defocus.

The problem of estimating $\hat{R}$ given I is called *ill-posed*, because there exist many solutions for a particular I and we are faced with the problem which one to choose. This comes from the fact that there are more unknowns than observations: Let N denote the number of pixels. Then, considering I, we have N observations, but more than N unknowns, because we have to estimate N pixel values of R and, in addition to that, the blur kernel K.

The removal of the ill-posedness is tackled by designing an energy functional E, which measures the "goodness" of $\hat{R}$ being a proper reconstruction of R. The higher the value ("energy") of E, the less suited is $\hat{R}$ for a reconstruction of R. Hence, through the usage of E, several possible solutions can be rated with respect to their suitability for being a good reconstruction.

Additionally, new information can easily be introduced in E via additional terms. This is necessary in order to overcome the under-determination. This technique is known as *regularization*, which enables us to solve the originally ill-posed problem. In most cases we can make a priori assumptions about the functions to be found (e.g., often the function to be searched is likely to vary only smoothly) and thereby introduce additional information. As a summary, through the usage of E, the original ill-posed problem should be turned into an optimization problem which is well posed.

Now let's come back to the restoration example. To make things simple, the effect of the kernel K is neglected for now. As a consequence, the restoration task is reduced to remove the image noise, which is also known as *denoising*. Then, a reasonable optimization criterion is that $\hat{R}$ should be close to I, which can be expressed by the data-driven energy term E_{d}:

$$E_{\mathrm{d}} = \int\int \left(\hat{R}(x,y) - I(x,y)\right)^2 \mathrm{d}x\,\mathrm{d}y \tag{4.7}$$

Obviously, this criterion is not sufficient, because it is solved by the trivial solution $\hat{R} = I$. Therefore, we have to make additional assumptions in order to obtain a proper solution. This comes in the form of a priori knowledge: most images are composed of a certain number of regions with relatively small intensity (or color) changes inside each region, e.g., because some rather uniform object (like a car where most of the region depicts the (uniform) finish of the car) or background (like blue sky) is depicted there. Therefore, $\hat{R}$ should be smooth, which can be expressed by a smoothness-based energy term E_{s}, which is based on the first derivative of $\hat{R}$:

$$E_{\mathrm{s}} = \int\int \left\|\nabla\hat{R}(x,y)\right\|_2^2 \mathrm{d}x\,\mathrm{d}y \tag{4.8}$$

where $\nabla\hat{R}(x,y)$ denotes the gradient vector of $\hat{R}$: $\nabla\hat{R} = \left[\partial\hat{R}/\partial x, \partial\hat{R}/\partial y\right]^{\mathrm{T}}$ and the operator $\|\cdot\|_2$ refers to the Euclidean vector norm (or L2 norm), i.e., $\left\|\nabla\hat{R}(x,y)\right\|_2^2 = \left(\partial\hat{R}/\partial x\right)^2 + \left(\partial\hat{R}/\partial y\right)^2$. In other words, the accumulated squares of gradient strengths should be as small as possible.

Please note that the sensed data is in general corrupted by noise, which introduces additional gradients and reduces overall smoothness. Therefore, E_{s} ensures that noise is suppressed during reconstruction, which is a desirable effect.

E_{s}, which incorporates prior information (i.e., E_{s} is independent of the observed data), is also called a *regularization term*, because it should regulate the solution such that a "simple" explanation of the observed data is found. "Simple" solutions should be favored among the set of possible solutions, according to a principle called "Occam's razor".

The incorporation of different terms in E is quite common for variational optimization. Typically, E is composed of two or three components:

- The data-driven term E_d measures how well a particular solution is in accord with the sensed data. The lower the E_d, the better is the fidelity of the solution to the data.
- With the help of the so-called internal energy E_int, a priori *knowledge* can be incorporated into the solution. Roughly speaking, E_int is a measure how likely a solution occurs. In the denoising example, we know that R will probably be smooth and therefore E_s represents the total sum of the magnitudes of the squared gradients.
- Sometimes, a third term E_ext, which is called *external energy*, is introduced in E. E_ext captures how well a particular solution represents external specifications. For example, E_ext can be used to represent the accordance to user input.

In our case, the optimization problem can now be formulated by

$$R^* = \min_{\hat{R}} (E) \text{ with } E = E_\mathrm{d}\left(\hat{R}, I\right) + \alpha \cdot E_\mathrm{s}\left(\hat{R}\right) \tag{4.9}$$

where the Lagrange multiplier α controls the effect of smoothing. This design of energy functionals consisting of two parts (data fidelity term and constraint based on prior knowledge) is able of representing a large variety of problems and therefore of widespread use in computer vision. Examples will follow in the next sections.

4.2 Tikhonov Regularization

Tikhonov [26] (see also [1]) provided the mathematical framework for optimization of functionals as defined in (4.7, 4.8, and 4.9) and, in particular, showed that the solution R^* of the now well-posed optimization problem (4.9) is a reasonable approximation of the originally ill-posed problem. We speak of *Tikhonov regularization* if the regularization term involves the usage of square terms (here the integral of the squares of gradient magnitude in (4.8)). The utilization of squared L2 terms also involves differentiability of the energy, and, moreover, the existence of a closed-form solution (which means that a fast calculation of the solution is possible), as we will see shortly.

For a numerical solution, the denoising problem has to be discretized. The data-driven energy E_d turns into

$$E_\mathrm{d} = \sum_{x=0}^{W-1} \sum_{y=0}^{H-1} w(x,y)\left[\hat{R}(x,y) - I(x,y)\right]^2 \tag{4.10}$$

where W and H denote the width and height of the image, respectively. Moreover, due to readability, continuous and discrete versions of some variables are named identically. The contribution of each pixel can be weighted by a factor $w(x,y)$. The introduction of $w(x,y)$ admits to deal with areas where no measurements are available or assumed to be uncertain. If measurements are not available, $w(x,y)$ is set to zero. At positions where measurements are present, $w(x,y)$ can be used to control how strongly the solution is forced to be equal or near sensed data. A reasonable choice of $w(x,y)$ is to set it to the inverse variance of the measured data in a neighborhood around (x,y): If there is little variance, data measurements are supposed to be reliable, and, therefore, the solution should be similar to measured data. Please note that the $w(x,y)$ are known factors during optimization, as they can be calculated solely based on $I(x,y)$ in advance.

The discrete version of the smoothness term E_{s} can be obtained via finite element analysis. Terzopoulos showed in [25] that in our case E_{s} has an especially simple form:

$$\begin{aligned} E_{\mathrm{s}} = & \sum_{x=0}^{W-1}\sum_{y=0}^{H-1} s_x(x,y)\left[\hat{R}(x+1,y) - \hat{R}(x,y) + \partial I/\partial x(x,y)\right]^2 + \\ & + \sum_{x=0}^{W-1}\sum_{y=0}^{H-1} s_y(x,y)\left[\hat{R}(x,y+1) - \hat{R}(x,y) + \partial I/\partial y(x,y)\right]^2 \end{aligned} \tag{4.11}$$

where $s_x(x,y)$ and $s_y(x,y)$ are optional smoothness weights and control the degree of smoothing. They can be set, for example, inversely proportional to the gradient magnitude $|\nabla I(x,y)|$. As a result, in locations with strong gradients, which indicate the presence of an edge in the image, the smoothness constraint is rather loose. Again, $s_x(x,y)$ and $s_y(x,y)$ depend only on $I(x,y)$ and therefore can be calculated in advance. Consequently, they are not part of the optimization.

In its discrete form, it is possible to rearrange the energy functional $E = E_{\mathrm{d}}(\hat{R},I)$ $+\alpha \cdot E_{\mathrm{s}}(\hat{R})$ (which is composed of (4.10) and (4.11)) as a quadratic form:

$$E = \mathbf{r}^T\mathbf{A}\mathbf{r} - 2\mathbf{r}^T\mathbf{b} + c \tag{4.12}$$

The vector $\mathbf{r}$ is obtained by a row-wise stacking of the 2D data $\hat{R}(x,y)$: $\mathbf{r} = \left[\hat{R}(0,0),\ \hat{R}(1,0),\ \ldots,\hat{R}(w-1,0),\ \hat{R}(0,1),\ \hat{R}(1,1),\ \ldots,\ \hat{R}(w-1,1),\ \ldots,\hat{R}(w-1,h-1)\right]^{\mathrm{T}}$. The matrix $\mathbf{A}$ is composed of weighting factors originating from those terms in (4.10) and (4.11) containing the square of some $\hat{R}$. This rearrangement is important, because the quadratic form (4.12) enables us to derive a closed-form solution by setting its first derivative to zero, as illustrated in Chap. 2.

In order to illustrate the calculation of $\mathbf{A}$, let's first rewrite one term of the sum of (4.11) (where no summarization is performed for mixed terms):

$$s_x(x,y)\begin{bmatrix} \hat{R}(x+1,y)^2 - \hat{R}(x+1,y)\hat{R}(x,y) + \hat{R}(x+1,y)\partial I/\partial x(x,y) - \\ - \hat{R}(x,y)\hat{R}(x+1,y) + \hat{R}(x,y)^2 - \hat{R}(x,y)\partial I/\partial x(x,y) + \\ + \partial I/\partial x(x,y)\hat{R}(x+1,y) - \partial I/\partial x(x,y)\hat{R}(x,y) + \partial I/\partial x(x,y)^2 \end{bmatrix} +$$
$$+ s_y(x,y)\begin{bmatrix} \hat{R}(x,y+1)^2 - \hat{R}(x,y+1)\hat{R}(x,y) + \hat{R}(x,y+1)\partial I/\partial y(x,y) - \\ - \hat{R}(x,y)\hat{R}(x,y+1) + \hat{R}(x,y)^2 - \hat{R}(x,y)\partial I/\partial y(x,y) + \\ + \partial I/\partial y(x,y)\hat{R}(x,y+1) - \partial I/\partial y(x,y)\hat{R}(x,y) + \partial I/\partial y(x,y)^2 \end{bmatrix} \tag{4.13}$$

For illustrative purpose, let's assume for the moment that **r** contains only three elements and, accordingly, **A** is a 3×3 matrix. Then, $\mathbf{r}^T\mathbf{At}$ can be written as

$$\begin{bmatrix} r_0 & r_1 & r_2 \end{bmatrix} \cdot \begin{bmatrix} a_{00} & a_{01} & a_{02} \\ a_{10} & a_{11} & a_{12} \\ a_{20} & a_{21} & a_{22} \end{bmatrix} \cdot \begin{bmatrix} t_0 \\ t_1 \\ t_2 \end{bmatrix} = \begin{bmatrix} r_0a_{00} + r_1a_{10} + r_2a_{20} \\ r_0a_{01} + r_1a_{11} + r_2a_{21} \\ r_0a_{02} + r_1a_{12} + r_2a_{22} \end{bmatrix}^{\mathrm{T}} \cdot \begin{bmatrix} t_0 \\ t_1 \\ t_2 \end{bmatrix} =$$
$$(r_0a_{00} + r_1a_{10} + r_2a_{20}) \cdot t_0 + (r_0a_{01} + r_1a_{11} + r_2a_{21}) \cdot t_1 +$$
$$(r_0a_{02} + r_1a_{12} + r_2a_{22}) \cdot t_2 \tag{4.14}$$

A closer look at (4.14) reveals that the row index of **A** selects which component of **r** contributes to the sum, whereas the column index of **A** selects which component of **t** contributes to the sum. For example, if r_0 and t_2 should make a joint contribution, a_{02} has to be different from zero. With this knowledge, we can derive from (4.13) which summand of (4.13) makes a contribution to which element of **A**. For example, in order to consider the term $-\alpha \cdot s_x(x,y) \cdot \hat{R}(x+1,y)\hat{R}(x,y)$, the element $a_{y\cdot w+x+1,y\cdot w+x}$ has to be incremented by $-\alpha \cdot s_x(x,y)$. Now we can go through (4.13) and identify all terms which contribute to some element of **A** (the ones which contain products of two elements of $\hat{R}$, either square products of the same element or a product of two different elements) and, based on the indices of these elements, derive the indices of the element of **A** to which they make a contribution. Observe that we also have one quadratic term of $\hat{R}$ in (4.10), which has to be considered, too. Altogether, one term of the sums of (4.10) and (4.11) contributes to the elements of **A** as follows:

$$\begin{aligned} a_{y\cdot w+x+1,y\cdot w+x+1} + &= \alpha \cdot s_x(x,y) \\ a_{y\cdot w+x+1,y\cdot w+x} - &= \alpha \cdot s_x(x,y) \\ a_{y\cdot w+x,y\cdot w+x+1} - &= \alpha \cdot s_x(x,y) \\ a_{y\cdot w+x,y\cdot w+x} + &= w(x,y) + \alpha \cdot s_x(x,y) + \alpha \cdot s_y(x,y) \\ a_{(y+1)\cdot w+x,(y+1)\cdot w+x} + &= \alpha \cdot s_y(x,y) \\ a_{(y+1)\cdot w+x,y\cdot w+x} - &= \alpha \cdot s_y(x,y) \\ a_{y\cdot w+x,(y+1)\cdot w+x} - &= -\alpha \cdot s_y(x,y) \end{aligned} \tag{4.15}$$

The complete matrix **A** can be built based on (4.15) if all $x \in [0, \ldots, W-2]$ and $y \in [0, \ldots, H-2]$ are considered.

Similarly, we can compute the increments of **b** by considering all terms of (4.10) and (4.11) which contain one element of $\hat{R}$:

$$\begin{aligned} b_{y \cdot w+x+1} + &= 2\alpha \cdot s_x(x,y) \cdot \partial I/\partial x(x,y) \\ b_{y \cdot w+x} - &= 2\alpha \cdot s_x(x,y) \cdot \partial I/\partial x(x,y) + \\ &+ 2\alpha \cdot s_y(x,y) \cdot \partial I/\partial y(x,y) + 2w(x,y) \cdot I(x,y) \\ b_{(y+1) \cdot w+x} + &= 2\alpha \cdot s_y(x,y) \cdot \partial I/\partial y(x,y) \end{aligned} \tag{4.16}$$

Now that we know how to build the energy functional E in its quadratic form (4.12), we can proceed with the question how to calculate the solution R^* which minimizes E. A necessary condition for R^* minimizing E is that the first derivative is zero at this point: $\partial E / \partial \hat{R}(R^*) = 0$. This relates to applying the Euler-Lagrange equation for variational energy functionals. Considering E in its quadratic form, setting its derivative to zero yields a closed-form solution, which has the convenient property that it is linear in the unknowns and therefore simple to calculate. It can be found when we solve the following linear system:

$$\mathbf{A}\mathbf{r}^* = \mathbf{b} \tag{4.17}$$

Provided that **A** is non-singular, this linear system of equations could be solved with a standard method like QR decomposition or directly with singular value decomposition (SVD) of **A** (see, e.g., [7]). However, please consider that **A** is extremely large (its dimensions are $W \cdot H \times W \cdot H$, and, thus, the number of rows/ columns of **A** amounts to several hundreds of thousands or even millions), which usually makes the usage of such general techniques prohibitive in terms of runtime and memory demand.

In order to solve (4.17) efficiently, we have to exploit the special structure of **A**. Taking a closer look at (4.15) reveals that each pixel affects seven elements of **A** which are arranged in a symmetrical structure. It is easy to see that for pixel (0,0) these elements are also symmetric with respect to the diagonal of **A**. As each successive pixel affects elements which are shifted by one row as well as diagonally, the whole matrix **A** is symmetric and multi-banded. Each row has five elements which are nonzero (except for the first and last rows of **A**). As a consequence, **A** is extremely sparse. This fact, in turn, can be exploited when solving (4.17). There exist special techniques making use of this fact like multigrid methods or conjugate gradient methods. A detailed description is beyond the scope of this book. The interested reader is referred to [2].

As far as the capability of the method is concerned, we can conclude that the regularization term efficiently removes noise (see Fig. 4.2, where the Tikhonov solution for a denoising example of a butterfly image is depicted in the *lower left*). However, the L2 norm of the regularizer strongly penalizes large gradients, which has the undesirable effect of oversmoothing step edges. A method avoiding this kind of artifacts is presented in the next section.

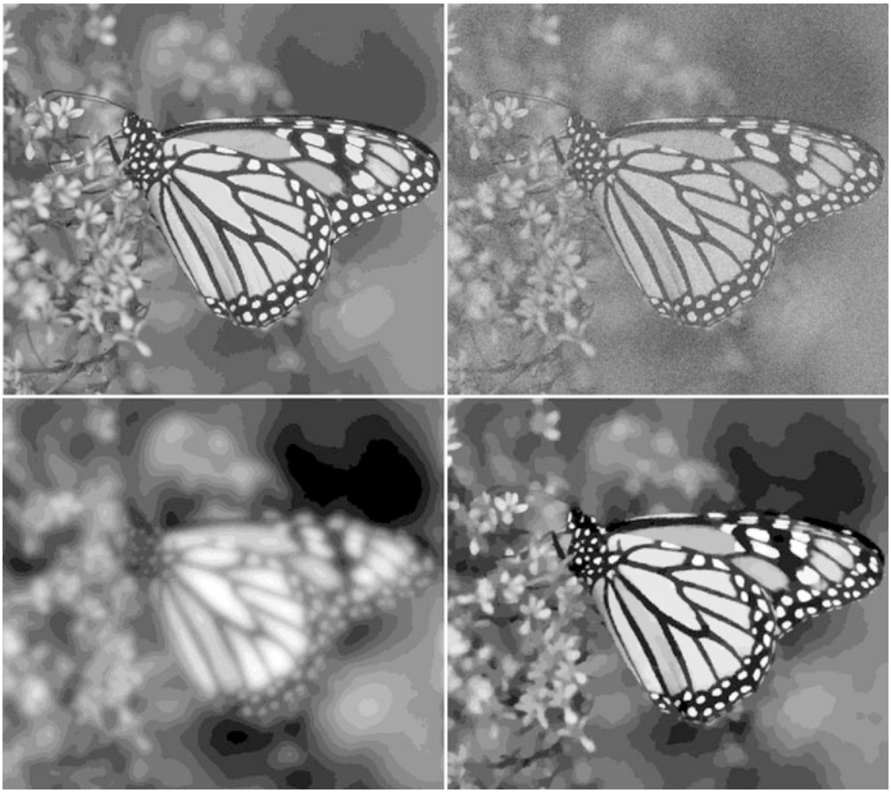

Fig. 4.2 Illustrating the performance of total variation regularization. *Upper left*: original image. *Upper right*: image with synthetically added noise. *Lower left*: denoising solution with Tikhonov regularization. *Lower right*: denoising solution with total variation (From Pock [20], with kind permission)

4.3 Total Variation (TV)

4.3.1 The Rudin-Osher-Fatemi (ROF) Model

There exist implementations of regularization techniques being different from Tikhonov's approach. More specifically, they differ in the calculation of the regularization term E_s. For example, if we take the integral of the absolute gradients instead of the squared magnitudes, we talk about *total variation regularization*, which was first used in an image processing context by Rudin et al. [22] for noise suppression. When we use total variation as a regularizer, we make use of the observation that noise introduces additional gradient strength, too. In contrast to Tikhonov regularization, however, total variation takes the absolute values of the gradient strength as regularization term, which is $\left|\nabla\hat{R}(x,y)\right| = \sqrt{\left(\partial R\hat{R}/\partial x\right)^2 + \left(\partial\hat{R}/\partial y\right)^2}$. Consequently, the energy functional of Rudin et al. can be written as

$$E_{TV} = \frac{1}{2\lambda} \cdot \iint \left(\hat{R}(x,y) - I(x,y)\right)^2 \mathrm{d}x\,\mathrm{d}y + \iint \left|\nabla \hat{R}(x,y)\right| \mathrm{d}x\,\mathrm{d}y \tag{4.18}$$

According to first letters of the names of the authors of [22], Rudin, Osher, and Fatemi, this energy functional is also known as the *ROF model* in literature.

The smoothness term differs from Tikhonov regularization, where the L2 norm of the gradient strength is used. A disadvantage of the L2 norm is that it tends to oversmooth the reconstructed image because it penalizes strong gradients too much. However, sharp discontinuities producing strong gradients actually do occur in real images, typically at the boundary between two objects or object and background. In contrast to the L2 norm, the absolute gradient strength (or L1 norm of the gradient strength) has the desirable property that it has no bias in favor of smooth edges. The shift from L2 to L1 norm seems only a slight modification, but in practice it turns out that the quality of the results can be improved considerably, because the bias to oversmoothed reconstructions is removed efficiently.

Compare two situations where an intensity increase of 100 gray values occurs within just a few pixels (situation A) or is distributed along very many pixels (situation B). Clearly, the square operation in Tikhonov regularization favors situation B, because the gradient is significantly lower at each pixel here, and, therefore, the sum of the squared gradients is lower compared to situation A. Total variation, however, does not favor any of the two situations, because the absolute sum remains 100 gray values for both situations, regardless of its distribution. As a consequence, step edges, which occur quite often, are preserved during regularization.

An example of the impact of moving from Tikhonov regularization to total variation-based denoising can be seen in Fig. 4.2. In the upper left part, we can see an image of a butterfly with many structures at a fine level of detail. Synthetic noise has been added to the upper right image. The two lower images are obtained by applying denoising with Tikhonov regularization (left) as well as total variation denoising (right). Both schemes are able to suppress the noise, but clearly the TV norm yields a much better result, because the edges are preserved much better.

On the other side, albeit E_{TV} is convex and therefore a unique solution exists, the regularization term of E_{TV} is not differentiable when $\nabla \hat{R}$ tends to zero because of the L1 norm. This means that a closed-form solution is not possible here. Consequently, the solution is more difficult to calculate compared to Tikhonov regularization. In particular, the absence of a closed-form solution requires an iterative scheme, which is computationally more complex. However, as we will see later, the iteration can be implemented very efficiently on massively parallel processing units such as GPUs, because it can be parallelized very well.

4.3.2 Numerical Solution of the ROF Model

A technique for solving (4.18) numerically, which leads to a quite simple update procedure, was suggested by Chambolle [3]. The derivation is rather complicated;

therefore, only an outline will be given here. The interested reader is referred to [3, 4, 20] for details.

In order to obtain a solution, Chambolle transforms the original problem into a so-called *primal-dual formulation*. The primal-dual formulation of the problem involves the usage of a 2-dimensional vector field $\mathbf{p}(x,y) = [p_1(x,y), p_2(x,y)]$. The vector field **p** is introduced as an auxiliary variable (also termed dual variable) and helps to convert the regularization term into a differentiable expression. With the help of **p**, the absolute value $|\mathbf{v}|$ of a 2-dimensional vector **v** can be rewritten as

$$|\mathbf{v}| = \sup_{|\mathbf{p}|\leq 1} \langle \mathbf{v}, \mathbf{p} \rangle \tag{4.19}$$

where $\langle \cdot \rangle$ denotes the dot product and can be written as $\langle \mathbf{v}, \mathbf{p} \rangle = |\mathbf{v}| \cdot |\mathbf{p}| \cdot \cos\theta$, i.e., the product of the lengths of the two vectors **v** and **p** with the angle θ in between these two vectors. If $|\mathbf{p}| = 1$ and, furthermore, **v** and **p** point in the same direction (i.e., $\theta = 0$), $\langle \mathbf{v}, \mathbf{p} \rangle$ exactly equals $|\mathbf{v}|$. Therefore, $|\mathbf{v}|$ is the supremum of the dot product for all vectors **p** which are constrained to lie within the unit circle, i.e., $|\mathbf{p}| \leq 1$.

Utilizing (4.19), the total variation $\int\int \left|\nabla\hat{R}(x,y)\right| \mathrm{d}x\,\mathrm{d}y$ can be rewritten as $\max\limits_{|\mathbf{p}|\leq 1} \int\int \left\langle \nabla\hat{R}(x,y), \mathbf{p}(x,y) \right\rangle \mathrm{d}x\,\mathrm{d}y$, because the dot product only equals $\left|\nabla\hat{R}(x,y)\right|$ if we pick the "right" **p**. If we plug this into (4.18), the solution R^* minimizing the TV energy functional can be expressed as

$$R^* = \min E_{\mathrm{TV}} =$$
$$\min_{R} \max_{|\mathbf{p}|\leq 1} \left[\frac{1}{2\lambda} \cdot \int\int \left(\hat{R}(x,y) - I(x,y)\right)^2 \mathrm{d}x\mathrm{d}y + \int\int \left\langle \nabla\hat{R}(x,y), \mathbf{p}(x,y) \right\rangle \mathrm{d}x\mathrm{d}y \right] \tag{4.20}$$

The main advantage of this new primal-dual formulation is that now the regularization term is differentiable, because the dot product can be calculated by $\left\langle \nabla\hat{R}, \mathbf{p} \right\rangle = \partial\hat{R}/\partial x \cdot p_1 + \partial\hat{R}/\partial y \cdot p_2$, which is a differentiable expression. On the other side, however, we have to deal with the additional constraint $|\mathbf{p}| \leq 1$, which requires some care during optimization.

Because what we actually seek now is the minimum of the energy in the $\hat{R}$-direction as well as its maximum in **p**-direction, geometrically speaking we are looking for a saddle point of the rewritten energy functional (see Fig. 4.3 for a schematic illustration of a function containing a saddle point, which is marked *red*). As (4.20) is now differentiable in $\hat{R}$ as well as in **p**, a natural choice for an optimization procedure would be to iteratively perform a gradient ascend step in **p**-direction, followed by a gradient descent step in the $\hat{R}$-direction, until convergence (see Fig. 4.3, where the *blue arrow* indicates the ascend step in the **p**-direction, followed by the descent step in the $\hat{R}$-direction, indicated by a *red arrow* and reaching the saddle point marked *red*). However, it turns out that for a given **p**, it is possible to perform the minimization in the $\hat{R}$-direction explicitly. We should make use of this finding in order to accelerate the method.

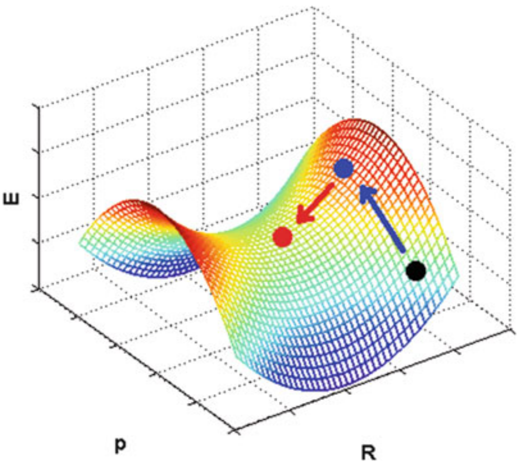

Fig. 4.3 Schematically depicting a function with a saddle point (*red point*), which – starting from e.g. the black point – can be reached by an ascend step in the **p**-direction (*blue*), followed by a descend step in the $\hat{R}$-direction (*red*)

The first part of the iteration deals with the optimization in **p** through gradient ascent. The derivative of E_{TV} with respect to **p** is quite easy to calculate $\partial E_{\mathrm{TV}}\left(\hat{R},\mathbf{p}\right)/\partial\mathbf{p} = \nabla\hat{R}$. Therefore, we could iteratively set $\mathbf{p}^{n+1}(x,y) = \mathbf{p}^{n}(x,y)+ \tau\cdot\nabla\hat{R}^{n}(x,y)$, with some suitably chosen step size τ. However, bear in mind that it has to be ensured that $\left|\mathbf{p}^{n+1}\right| \leq 1$ after the update. Therefore, $\mathbf{p}^{n+1}$ has to be back-projected onto the unit circle, if necessary. In total, the gradient ascent step is defined by

$$\mathbf{p}^{n+1}(x,y) = \frac{\mathbf{p}^{n}(x,y)+\tau\cdot\nabla\hat{R}^{n}(x,y)}{\max\left(1,\mathbf{p}^{n}(x,y)+\tau\cdot\nabla\hat{R}^{n}(x,y)\right)} \tag{4.21}$$

Concerning the optimization in $\hat{R}$, we first notice that we can rewrite the dot product as

$$\int\!\!\int\left\langle\nabla\hat{R}(x,y),\mathbf{p}(x,y)\right\rangle\mathrm{d}x\,\mathrm{d}y = -\int\!\!\int\hat{R}(x,y)\cdot\mathrm{div}[\mathbf{p}(x,y)]\mathrm{d}x\,\mathrm{d}y \tag{4.22}$$

with the div-operator being defined by $\mathrm{div}[\mathbf{p}(x,y)] = \partial p_1/\partial x + \partial p_2/\partial y$. Considering (4.22), the derivative of E_{TV} with respect to $\hat{R}$ is given by $\partial E_{\mathrm{TV}}\left(\hat{R},\mathbf{p}\right)/\partial\hat{R} = -\mathrm{div}(\mathbf{p}) + \frac{1}{\lambda}\cdot\left(\hat{R}-I\right)$. Therefore, if we fix **p**, the explicit update of $\hat{R}$ can be calculated by explicitly setting $\partial E_{\mathrm{TV}}\left(\hat{R},\mathbf{p}\right)/\partial\hat{R} = 0$ as follows:

$$\hat{R}^{n+1}(x,y) = I(x,y) + \lambda\cdot\mathrm{div}\left[\mathbf{p}^{n+1}(x,y)\right] \tag{4.23}$$

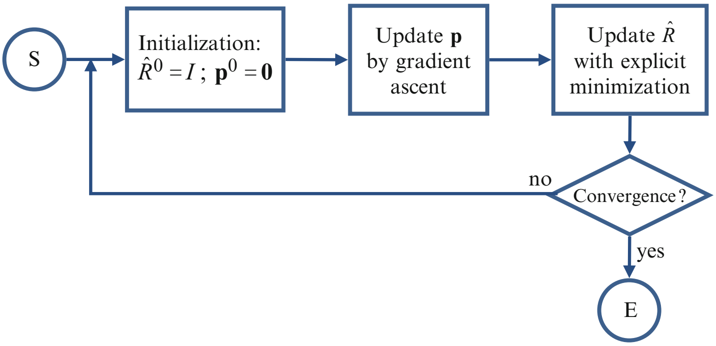
S
Initialization: $\hat{R}^0 = I$; $\mathbf{p}^0 = \mathbf{0}$
Update **p** by gradient ascent
Update $\hat{R}$ with explicit minimization
Convergence ?
no
yes
E

Fig. 4.4 Flowchart of the variational optimization of the ROF model

Altogether, the following update rules are to be performed in alternation:

$$\begin{aligned} \mathbf{p}^{n+1}(x,y) &= \frac{\mathbf{p}^n(x,y) + \tau \cdot \nabla \hat{R}^n(x,y)}{\max\left(1, \mathbf{p}^n(x,y) + \tau \cdot \nabla \hat{R}^n(x,y)\right)} \\ \hat{R}^{n+1}(x,y) &= I(x,y) + \lambda \cdot \operatorname{div}\left[\mathbf{p}^{n+1}(x,y)\right] \end{aligned} \tag{4.24}$$

where $0 < \tau \leq 1/(8\lambda)$ and the iteration is initialized by $\hat{R}^0(x,y) \equiv I(x,y)$ and $\mathbf{p}^0(x,y) \equiv [0,0]$ (i.e., set $\mathbf{p}$ to the zero vector for each position (x,y)). The denominator on the right-hand side of the first line of (4.24) ensures that the magnitudes of the vector field $\mathbf{p}^{n+1}(x,y)$ are always smaller than 1 or equal to 1. Finally, the iteration converges to the desired solution $R^*(x,y)$. Convergence is indicated, for example, if the change of the energy $E_{\mathrm{TV}}^{n+1} - E_{\mathrm{TV}}^{n}$ falls below a certain threshold ε. Some implementations just perform a fixed number of iterations and assume that a more or less steady state has been reached. The general proceeding is illustrated in the flowchart of Fig. 4.4.

If we want to implement (4.24) numerically, we move from the continuous to the discrete domain. To this end, we have to define the finite versions of the gradient and divergence operators. There are several ways to calculate the gradient and divergence numerically. Because (4.22) has to be satisfied in the discrete domain as well, the gradient is calculated by forward differences, whereas the divergence is calculated by backward differences. This yields the following simple calculation rules:

$$\nabla \hat{R}(x,y) = \begin{bmatrix} \hat{R}_x \\ \hat{R}_y \end{bmatrix} \qquad \begin{aligned} \hat{R}_x &= \begin{cases} \hat{R}(x+1,y) - \hat{R}(x,y) & \text{if} \quad 0 < x < W \\ 0 & x = W \end{cases} \\ \hat{R}_y &= \begin{cases} \hat{R}(x,y+1) - \hat{R}(x,y) & \text{if} \quad 0 < y < H \\ 0 & y = H \end{cases} \end{aligned} \tag{4.25}$$

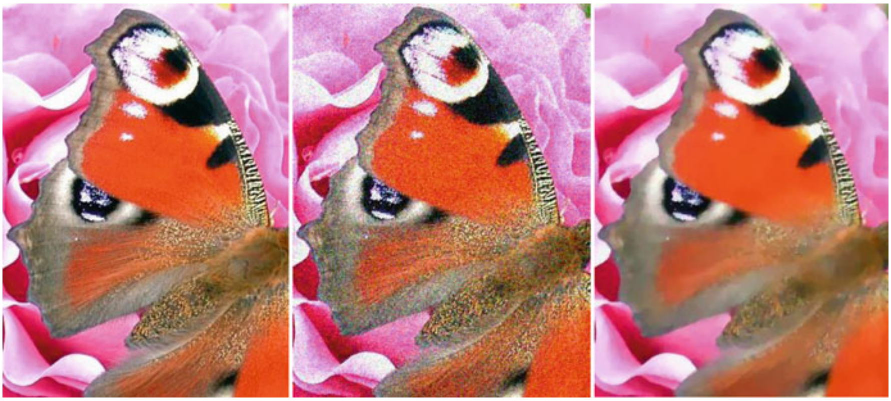

Fig. 4.5 Illustrating the performance of total variation denoising of a color image. *Left*: original image. *Middle*: image with synthetically added noise. *Right*: TV solution (From Pock [20], with kind permission)

$$\operatorname{div}[\mathbf{p}(x,y)] = \begin{cases} p_1(x,y) - p_1(x-1,y) & \text{if} \quad 1 < x \le W \\ p_1(x,y) & x = 1 \end{cases} + \begin{cases} p_2(x,y) - p_2(x,y-1) & \text{if} \quad 1 < y \le H \\ p_2(x,y) & y = 1 \end{cases} \tag{4.26}$$

with W and H being the width and the height of the image, respectively.

Please note that a generalization of the ROF model to color images is straightforward. Color images like RGB images are vector-valued data, where each $\mathbf{I}(x,y)$ is a three-dimensional vector. For vector-valued data, (4.18) can be generalized to

$$E_{\mathrm{TV}} = \frac{1}{2\lambda} \cdot \iint \sum_{i=1}^{m} \left(\hat{R}^i(x,y) - I^i(x,y) \right)^2 \mathrm{d}x\,\mathrm{d}y + \iint \sqrt{\sum_{i=1}^{m} \left| \nabla \hat{R}^i(x,y) \right|^2} \mathrm{d}x\,\mathrm{d}y \tag{4.27}$$

where the superscript i denotes the ith channel of a vector-valued data field. The performance of the method is illustrated in Fig. 4.5, where the total variation solution for a color image of a butterfly with synthetically added noise is shown. Clearly, there is no trend to oversmoothing, whereas the noise is removed efficiently at the same time. However, the method tends to produce regions of uniform color (see, e.g., right part of the body of the butterfly).

Pseudocode

```
function denoiseTotalVariation (in Image $I$ , in algo
parameters $\tau$ and $\lambda$ , in convergence criterion $\varepsilon$ , out
reconstructed image $R^*$)

// initialization
$n \leftarrow 0$
$\hat{R}^0 \leftarrow I$
$\mathbf{p}^0 \leftarrow \mathbf{0}$

// main optimization loop
repeat
  // gradient ascend in $\mathbf{p}$-direction ($\hat{R}$ fixed)
  for y = 0 to $H-1$
    for x = 0 to $W-1$
      calculate $\nabla\hat{R}^n(x,y)$ according to (4.25)
      set $\mathbf{p}^{n+1}(x,y)$ according to (4.21) // update $\mathbf{p}$
    next
  next
  // explicit minimization in $\hat{R}$-direction ($\mathbf{p}$ fixed)
  for y = 0 to $H-1$
    for x = 0 to $W-1$
      calculate $\mathrm{div}[\mathbf{p}^{n+1}(x,y)]$ according to (4.26)
      set $\hat{R}^{n+1}(x,y)$ according to (4.23) // update $\hat{R}$
    next
  next
  calculate energy $E_{TV}^{n+1}$ according to (4.18)
  $n \leftarrow n+1$
until $E_{TV}^n - E_{TV}^{n-1} < \varepsilon$ // convergence criterion
$R^* \leftarrow \hat{R}^n$
```

4.3.3 Efficient Implementation of TV Methods

Despite there is a considerable amount of theoretical background knowledge necessary in order to develop the proceeding for finding the solution of the TV problem formulation of denoising, the numerical procedure itself is very straightforward to calculate. In fact, the nature of the calculations being necessary when the iterative update rule of (4.24) is applied makes the method perfectly suitable for an implementation on massively parallel hardware such as graphical processing units (GPUs). As a result, the method can be implemented very efficiently and thereby the calculations are accelerated significantly.

So why do TV methods benefit so much from GPU implementations? Let's take a look at (4.24) from this perspective. We don't want to go into detail here on how to program GPUs efficiently (see, e.g., [11] for a good and easy to understand introduction). For now, it suffices to mention that the main point is that for a good performance on a GPU, it has to be possible to calculate the result for each pixel separately, because then there will always be enough data to calculate for every processing entity of the GPU. This is true for both left-hand sides of (4.24), as the updated value of each pixel does not depend on the updated value of any other pixel. This also becomes evident in the pseudocode implementation, where the updates are performed in the inner part of the loops iterating over the image plane. As a consequence, it is possible to calculate the updates of each pixel in a separate thread, which results in hundreds of thousands or even more threads for typical image sizes, which are definitely enough to use the massively parallel hardware at full capacity.

Moreover, the numerical operations necessary to calculate the updated value of one pixel are rather simple and therefore very fast to calculate. Apart from some multiplications and additions (and one max-operation), the gradients of $\hat{R}^n$ as well as the $\mathrm{div}(\cdot)$-operators with argument $\mathbf{p}^{n+1}(x, y)$ have to be calculated for each pixel. Both of them depend on only a small amount of input data and can be calculated with just a few multiplications and additions. Additionally, the whole iteration can be processed on the GPU, which avoids extensive copy of data between CPU and GPU, which can occur in algorithms where only parts of the calculation are done on the GPU and the rest on the CPU.

Please note that in spite of being derived for the rather special case of image denoising, the ROF model can be reused as a building block in total variation solutions for quite a variety of vision problems, such as:

- Deconvolution (see, e.g., [19])
- Optical flow calculation (see, e.g., [32])
- Multi-view stereo reconstruction (see, e.g., [12])
- Segmentation/multi-class labeling (see, e.g., [14])
- Globally consistent depth estimation from 4D light fields (see, e.g., [28])

Without going into details, these methods use variants of the iterative TV update of (4.24) or contain it as a building block next to other calculations, and, therefore, all benefit from its particular suitability for a GPU implementation. Consequently, TV methods have been a very active area of research in the last few years. One of these examples, namely, optical flow calculation, will be presented in the following.

4.3.4 Application: Optical Flow Estimation

In this section, we will learn more about how total variation-based approaches can be utilized for the optimization of other vision problems. In particular, we will examine how a variant of the TV-based ROF model can be used to estimate the optical flow between two images.

Consider a scenario where we have two images I_0 and I_1 which both show the same scene, which contains moving objects like animals, cars, pedestrians, etc. If I_0 and I_1 are acquired at different points of time, the moving objects will appear at different locations in both images, whereas the background remains static. As displacement can take place in two directions (x and y), the movement (which can be different for each pixel) can be expressed as a two-dimensional vector $\mathbf{u}(x,y) = [u_1(x,y), u_2(x,y)]^{\mathrm{T}}$ for each pixel. Altogether, the movement is described by the two-dimensional vector field $\mathbf{u}$, which is called *optical flow*.

Taking the two images I_0 and I_1 as input, we can derive $\mathbf{u}$ by assigning a position $\mathbf{x}$ of I_0 to that position $(\mathbf{x} + \mathbf{u}(\mathbf{x}))$ of I_1 depicting the same scene element. By doing this for every pixel, we can derive the optical flow $\mathbf{u}$ for the whole image plane. This is another example of an ill-posed problem, because in addition to the unknowns $\mathbf{u}(x,y)$, I_0 and I_1 are also influenced by unknown perturbations like noise and blur, which also have to be considered somehow during the optimization process if their influence should be suppressed. In total, we again have more unknowns than observations, which results in ill-posedness.

In their seminal work, Horn and Schunck therefore suggested a variational approach in order to estimate $\mathbf{u}$ [8], which minimizes an energy being based on a data term as well as a regularizer. Because their data fidelity term penalizes deviations in a quadratic way, their method is not robust with respect to outliers in the data. Therefore, the authors of [32] suggested a total variation-based energy functional as follows:

$$E_{\mathrm{TVL1}} = \lambda \cdot \iint |I_0(\mathbf{x}) - I_1(\mathbf{x} + \mathbf{u}(\mathbf{x}))| d\mathbf{x} + \iint |\nabla u_1(\mathbf{x})| + |\nabla u_2(\mathbf{x})| d\mathbf{x} \tag{4.28}$$

The regularization part of this energy consists of the sum of the total variation of the two components of the vector field $\mathbf{u}$. The usage of TV here ensures that the optimization preserves discontinuities in the flow field, which typically occur at the borders of moving objects. The data fidelity term sums up the differences between the intensity values $I_0(\mathbf{x})$ in the first image and the intensities at their assumed corresponding positions $I_1(\mathbf{x} + \mathbf{u}(\mathbf{x}))$ in the second image. Because here the data term utilizes L1 norms, too, the impact of data outliers is reduced compared to the model of Horn and Schunck. We therefore speak of TVL1 optimization (instead of TVL2, as used in the ROF model, where the data term contains a sum of squares).

If we want to find the minimizer $\mathbf{u}^*$ of (4.28), we first have to notice that in contrast to the ROF model, the data-driven part does not directly depend on $\mathbf{u}$, as $\mathbf{u}$ only appears in the argument of $I_1(\mathbf{x} + \mathbf{u}(\mathbf{x}))$. Explicit differentiations of the data term with respect to $\mathbf{u}$ are therefore not possible at the moment. This can be resolved by applying a first-order Taylor approximation of the data term at the current estimate $\mathbf{u}_0$ (i.e., the data term is linearized):

$$I_1(\mathbf{x} + \mathbf{u}(\mathbf{x})) \cong I_1(\mathbf{x} + \mathbf{u}_0(\mathbf{x})) + \langle \mathbf{u}(\mathbf{x}) - \mathbf{u}_0(\mathbf{x}), \nabla I_1(\mathbf{x} + \mathbf{u}_0(\mathbf{x})) \rangle \tag{4.29}$$

with $\langle \cdot \rangle$ denoting the dot product. Now we can rewrite E_{TVL1} as follows (for brevity, we will just write $\mathbf{u}$ instead of $\mathbf{u}(\mathbf{x})$):

$$\begin{aligned} E_{\mathrm{TVL1}} = \lambda \cdot \iint & |I_0(\mathbf{x}) - I_1(\mathbf{x} + \mathbf{u}_0) - \langle \mathbf{u} - \mathbf{u}_0, \nabla I_1(\mathbf{x} + \mathbf{u}_0) \rangle| \mathrm{d}\mathbf{x} \\ & + \iint |\nabla u_1| + |\nabla u_2| \mathrm{d}\mathbf{x} \end{aligned} \tag{4.30}$$

The next problem is that here both parts of E_{TVL1} are not continuously differentiable, because the data term contains the L1 norm, too. This problem can be handled well by formulating a convex approximation of (4.30). Convexity can be obtained by decoupling the data term and the regularizer, which currently both depend on $\mathbf{u}$. To this end, an auxiliary variable $\mathbf{v}$ can be introduced, which should approximate $\mathbf{u}$. Therefore, $\mathbf{v}$ is a 2D vector field of the same size as $\mathbf{u}$. When replacing $\mathbf{u}$ with $\mathbf{v}$ in the data term as well as abbreviating the data term by $\rho(\mathbf{v}) = I_0(\mathbf{x}) - I_1(\mathbf{x} + \mathbf{v}_0) - \langle \mathbf{v} - \mathbf{v}_0, \nabla I_1(\mathbf{x} + \mathbf{v}_0) \rangle$, a convex approximation of (4.30) can be formulated by

$$\begin{aligned} E_{\mathrm{TVL1}} = \lambda \iint |\rho(\mathbf{v})| \mathrm{d}\mathbf{x} + \frac{1}{2\theta} \iint (u_1 - v_1)^2 + (u_2 - v_2)^2 \mathrm{d}\mathbf{x} \\ + \iint |\nabla u_1| + |\nabla u_2| \mathrm{d}\mathbf{x} \end{aligned} \tag{4.31}$$

Now the data residuals and the regularization term are decoupled. Through the introduction of the middle term, solutions where $\mathbf{v}$ differs much from $\mathbf{u}$ are penalized and therefore avoided. Typically, θ is chosen as a small constant and ensures that $\mathbf{v}$ stays close to $\mathbf{u}$.

In the form of (4.31), the energy depends on both $\mathbf{u}$ and $\mathbf{v}$. Consequently, it has to be minimized with respect to both variables when calculating the solution. This can be done by an iterative scheme, where in the first step one variable is fixed and (4.31) is minimized with respect to the other. After that, we fix the just optimized variable and minimize (4.31) with respect to the previously fixed variable. These two steps are performed in alternation until finally the scheme converges.

Let's first take a look at how to optimize E_{TVL1} in the form of (4.31) with respect to $\mathbf{u}$ when $\mathbf{v}$ is fixed. As the data term $\rho(\mathbf{v})$ does not depend on $\mathbf{u}$ any longer, it can be neglected during this step. We can now minimize E_{TVL1} with respect to each of the two components of $\mathbf{u}$ in a separate step by calculating

$$\min_{u_d} \left[\frac{1}{2\theta} \iint (u_d - v_d)^2 \mathrm{d}\mathbf{x} + \iint |\nabla u_d| \mathrm{d}\mathbf{x} \right] \tag{4.32}$$

with $d \in \{1, 2\}$. Taking a closer look at (4.32), we can see that this is exactly the ROF model, and, therefore, we can apply the same iterative procedure as previously described in order to optimize it.[1] Please note that this iteration does not have to fully converge; in practice it turned out that good overall solutions can be obtained by just performing a fixed small number of iterations each time when (4.32) is to be optimized.

The second step of the general iterative proceeding deals with minimization of (4.31) with respect to $\mathbf{v}$ when $\mathbf{u}$ is fixed. In that step we have to calculate

$$\min_{\mathbf{v}} \left[\lambda \cdot \int\int |\rho(\mathbf{v})| d\mathbf{x} + \frac{1}{2\theta} \int\int (u_1 - v_1)^2 + (u_2 - v_2)^2 d\mathbf{x} \right] \tag{4.33}$$

which has the desirable property that it can be solved point-wise in the discrete domain, i.e., for each pixel separately, because in its discrete version, the integral is replaced by a sum and each summand just considers a single pixel. Observe that (4.33) does not depend on any derivatives, which would involve neighboring pixels. Therefore, the solution can be calculated very quickly and is particularly suited for a GPU implementation as well. Without giving any details here, the solution of the discretized version of (4.33) is given by

$$\mathbf{v}(x,y) = \mathbf{u}(x,y) + \begin{cases} \lambda\theta \cdot \nabla I_1 \ (x,y) & \text{if} \quad \rho(\mathbf{u}) < -\lambda\theta |\nabla I_1(x,y)|^2 \\ -\lambda\theta \cdot \nabla I_1(x,y) & \text{if} \quad \rho(\mathbf{u}) > \lambda\theta \ |\nabla I_1(x,y)|^2 \\ -\rho(\mathbf{u}) \frac{\nabla I_1(x,y)}{|\nabla I_1(x,y)|^2} & \text{if} \quad |\rho(\mathbf{u})| \leq \lambda\theta |\nabla I_1(x,y)|^2 \end{cases} \tag{4.34}$$

This can be seen as a soft thresholding step, which bounds the distance between $\mathbf{v}$ and $\mathbf{u}$ in cases where the absolute value of the data-driven energy $\rho(\mathbf{u})$ gets too large (first two cases of (4.34)). This way, it is ensured that $\mathbf{v}$ stays close to $\mathbf{u}$. Details of the derivation of (4.34) can be found in [20, 32].

The last thing to mention is that the linearization step of (4.29) might introduce too large errors at positions where $\mathbf{u}(\mathbf{x})$ gets too large. Therefore, [32] suggests a top-down approach, which first calculates a solution at a coarse level of pixel resolution. Subsequently, this solution serves as a starting point and can be successively refined by increasing the resolution until full resolution is reached.

An example of the performance of the method can be seen in Fig. 4.6 for two examples. In the left two rows, we can see two images of the same scene taken at different points of time. Each of the two scenes contains moving objects on a static background. The right images show the optical flow estimate, which is color-coded such that the hue represents the direction of the flow, whereas the saturation indicates its magnitude. All moving objects were captured correctly.

[1] Actually, (4.32) describes two ROF models: one for $\mathbf{u}_1$ (where $d = 1$) and one for $\mathbf{u}_2$ (where $d = 2$). Consequently, we have to perform two (separate) optimizations.

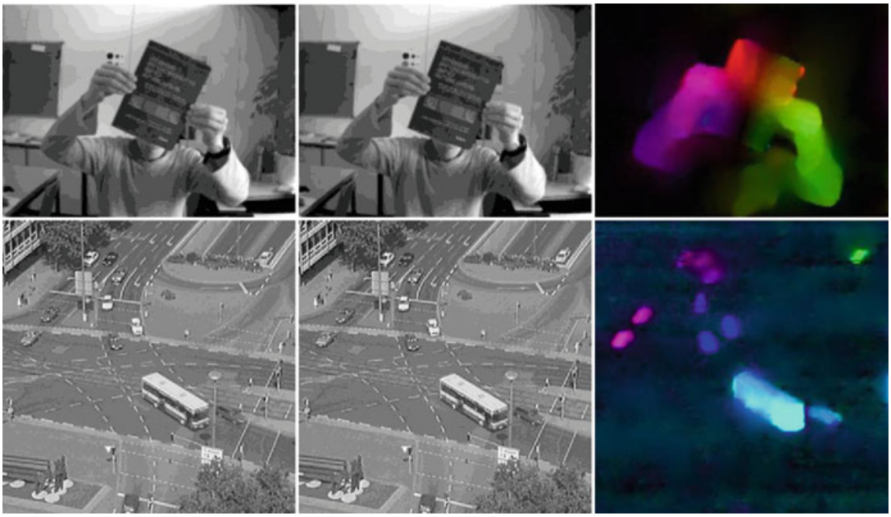

Fig. 4.6 Illustrating the performance of TVL1 optimization when estimating the optical flow between two images. See text for details (From Zach et al. [32], with kind permission from Springer Science and Business Media)

Pseudocode

```
function opticalFlowEstimationTVL1 (in Image $I_0$, in Image $I_1$,
in max. downscale factor $K$, in algo parameters $\tau$, $\lambda$ and $\theta$,
in convergence criterion $\varepsilon$, out optical flow estimate $\mathbf{u}^*$)

// initialization
$\mathbf{u}^{K,0} \leftarrow \mathbf{0}$
$\mathbf{v}^{K,0} \leftarrow \mathbf{u}^{K,0}$

// main iteration loop (controlling pixel resolution)
for $k = K$ to $0$ step -1
  if $k > 0$ then
    downscale $I_0$ and $I_1$ by factor $2^k$
  end if
  $n \leftarrow 0$
  // main optimization loop (at current resolution)
  repeat
    // optimization of $\mathbf{u}$ with ROF model ($\mathbf{v}$ fixed)
    calculate $u_1^{k,n+1}$ by optimizing the ROF model based on
    (4.32) with $d = 1$   // with fixed small number of it.
    calculate $u_2^{k,n+1}$ by optimizing the ROF model based on
    (4.32) with $d = 2$   // with fixed small number of it.
    // point-wise optimization of $\mathbf{v}$ ($\mathbf{u}$ fixed)
    for y = 0 to $(H-1)/2^k$
```

```
            for x = 0 to $(W-1)/2^k$
                calculate $\mathbf{v}^{k,n+1}(x,y)$ according to (4.34)
            next
        next
        calculate energy $E_{TVL1}^{n+1}$ according to (4.31)
        $n \leftarrow n+1$
    until $E_{TVL1}^{n} - E_{TVL1}^{n-1} < \varepsilon$ // convergence criterion
    if $k > 0$ then
        $\mathbf{u}^{k-1,0} \leftarrow$ upscale of $\mathbf{u}^{k,n}$ (by factor of 2)
        $\mathbf{v}^{k-1,0} \leftarrow$ upscale of $\mathbf{v}^{k,n}$ (by factor of 2)
    end if
next
$\mathbf{u}^{*} \leftarrow \mathbf{u}^{0,n}$
```

4.4 MAP Image Deconvolution in a Variational Context

4.4.1 Relation Between MAP Deconvolution and Variational Regularization

The proceeding to recover R from observed image data I in consideration of the blur kernel K (see (4.6)) is referred to as *deconvolution*, and another example of applying variational methods, as our goal, is to estimate some functions R and K. Depending on whether the blur kernel K is known or not, we talk about *blind deconvolution* (K is unknown; see, e.g., [13]) or *non-blind deconvolution*, respectively.

An early technique of blind deconvolution, given the observed image I, is to perform a joint estimation of R and K through a *MAP (maximum a posteriori) estimation*, which means that the goal is to jointly maximize the probability of R and K, given the image data I. As we will see shortly, there is an interesting link between MAP estimation and the energy-based variational approach presented so far.

The quantity $p(R,K|I)$ describes the (joint) probability distribution of R and K *after* observation of the image data I and is therefore denoted as the *posterior* probability As we want to maximize the posterior $p(R,K|I)$ in order to infer the original image, this kind of maximization is referred to as maximum a posteriori estimation.

If we knew the probability distribution $p(R,K|I)$, we could select R^* and K^* such that $p(R,K|I)$ is maximized, i.e., $(R^*,K^*) = \arg\max_{R,K} p(R,K|I)$, under consideration of the observed data I. Unfortunately though, this distribution is usually not known. A way out of this dilemma is the application of Bayes' rule, which states that $p(R,K|I)$ can be modeled by

$$p(R,K|I) = \frac{p(I|R,K) \cdot p(R) \cdot p(K)}{p(I)} \qquad (4.35)$$

The quantity $p(I|R,K)$ is a data-driven term and quantifies the probability that an image observation I occurs given a specific model setting (R,K) and is usually denoted as the *likelihood function*. $p(R)$ and $p(K)$ denote PDFs independent of observing any data and are called *prior probabilities* (or just prior). They represent knowledge about the model which can be assumed without considering observed data, e.g., we can assume that images with very high overall gradient strength are not very likely.

For the moment, let's assume that we don't want to favor any specific kernel, i.e., $p(K)$ is the same for every possible kernel. Moreover, when judging different (R,K) settings during optimization, we always use the same input image I. Therefore, $p(K)$ and $p(I)$ can be dropped.

Please note that it is much easier to model the likelihood $p(I|R,K)$ than the posterior $p(R,K|I)$. A natural choice for $p(I|R,K)$ can be derived from the fact that $p(I|R,K)$ should be high if $\sum|K*R-I|$ is small (where $*$ denotes the convolution operator), because it can be assumed that the observed data is closely related to the ground truth. Please observe the relation to (4.7).

The prior $p(R)$ can be set such that the probability is low when the overall gradient is high (in accordance to (4.8)), because natural images are assumed to contain many uniform or smoothly varying regions.

Because PDFs are often modeled as Gaussian distribution involving exponential terms, it is more convenient to optimize the logarithm of the above function. Taking the negative $-\log[p(R,K|I)]$ converts the optimization problem into the following minimization task:

$$(R^*,K^*) = \arg\min(-\log[p(R,K|I)]) \approx \arg\min(-\log[p(I|R,K)] - \log[p(R)]) \tag{4.36}$$

The term $-\log[p(R,K|I)]$ can be regarded as another representation of the energy E defined in (4.9). Hence, $-\log[p(I|R,K)]$ and $-\log[p(R)]$ can be interpreted as E_d and E_s, respectively. Therefore, MAP estimation in this context is equivalent to a regularization-based variational approach utilizing an energy functional consisting of two terms. In the MAP context, the likelihood is related to a data-driven energy, whereas the priors act as regularization terms (which are often smoothing terms). In other words, a MAP estimation in the form of (4.36) can be considered as one way of performing variational optimization. As with the previous section, the prior should help to overcome ill-posedness.

4.4.2 Separate Estimation of Blur Kernel and Non-blind Deconvolution

Observe that a joint estimation of (R^*,K^*) with the MAP criterion usually fails, mainly because the choice of the prior, which penalizes sharp edges (which

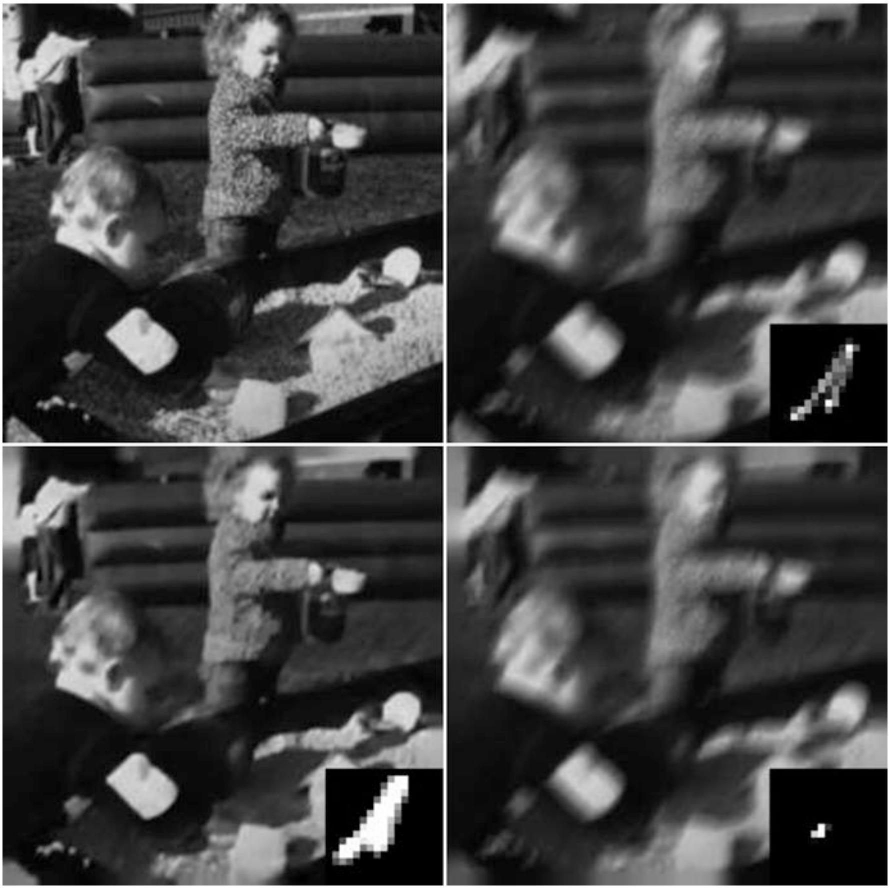

Fig. 4.7 Illustrating the performance of deconvolution: ground truth (*left upper*), blurred image (*right upper*), deconvolution result of [5] (*left lower*), and with a naïve joint MAP estimator (*right lower*). The blue kernel is depicted in the lower right area of the images (From Levin et al. [15], with kind permission)

definitely occur in most images). Eventually, this leads to a bias toward solutions with K^* approaching the delta function ("no-blur solution"), as was shown in [16]. In order to eliminate this problem, an alternative way is to first perform a MAP estimation of K^* only and subsequently apply a non-blind deconvolution scheme in order to recover R^* when K^* is assumed as fixed.

Such an approach was taken in the method suggested by Fergus et al. [5] and showed far superior performance compared to a joint MAP estimator (see Figs. 4.7 and 4.8). It can be seen that with separate blur kernel estimation, the estimated kernel is quite accurate, whereas for a joint MAP estimation of restored image and blur kernel, the result is quite poor as there is a strong bias toward delta blur kernels (no-blur solution).

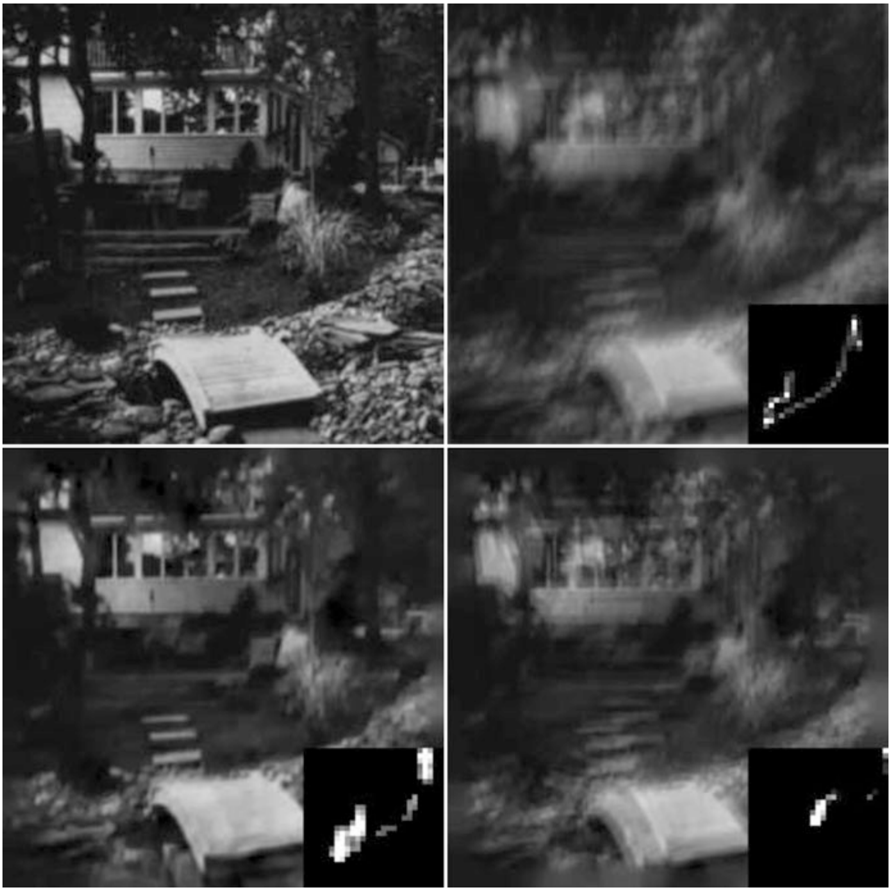

Fig. 4.8 Illustrating the performance of deconvolution: ground truth (*left upper*), blurred image (*right upper*), deconvolution result of [5] (*left lower*), and with a joint MAP estimator with edge reweighting (*right lower*). The blue kernel is depicted in the lower right area of the images (From Levin et al. [15], with kind permission)

The posterior is modeled by Fergus et al. as follows. First, it can be observed that we are only interested in finding the maximum "position" (i.e., R^* and K^*) and not the exact absolute value of $p(R,K|I)$. Consequently, the term $p(I)$ (which does not depend on either R or K and therefore remains constant for all positions) can be dropped. Second, it is more convenient to find a prior for the gradients of R. In their paper, Fergus et al. showed that the distribution of the intensity gradients of most images can be approximated well by a mixture of Gaussians, i.e., a sum of multiple Gaussian distributions, with zero mean and different variances. As taking the derivative is a linear operation, it follows from (4.35) that

$$p(\nabla R, K|I) \propto p(I|\nabla R, K) \cdot p(\nabla R) \cdot p(K) \tag{4.37}$$

The likelihood $p(I|\nabla R, K)$ can be modeled by a Gaussian distribution with mean $\nabla R * K$ and variance σ^2 (which denotes the image noise). As already mentioned, $p(\nabla R)$ is modeled by a mixture of C zero-mean Gaussians $\sum_{c=1}^{C} w_c \cdot \mathcal{N}(\nabla R|0, v_c)$, where w_c is a weighting term and v_c denotes the variance. Hence, $\mathcal{N}(\nabla R|0, v_c)$ denotes the Gaussian probability distribution for ∇R, given zero mean and variance v_c. Both $w_c$and v_c can be specified in advance by evaluating training images, i.e., $p(\nabla R)$ is estimated based on a representative image set and it is assumed that this gradient distribution is also valid for the images to be restored.

The prior $p(K)$ should favor sparse kernels, i.e., only a small proportion of the elements of K should differ significantly from zero. Therefore, a mixture of exponential distributions is chosen: $p(K) = \sum_{d=1}^{D} w_d \cdot \mathcal{E}(K|\lambda_d)$ with $\mathcal{E}(x|\lambda) = \lambda \cdot \exp(-\lambda \cdot x)$ for $x \geq 0$. The constraint that x is not allowed to take negative values relates to the fact that all elements of K have to be nonnegative. To sum it up, (4.37) can be rewritten as

$$p(\nabla R, K|I) \propto \prod_i \mathcal{N}\left(I|\nabla R * K, \sigma^2\right) \cdot \prod_i \sum_{c=1}^{C} w_c \cdot \mathcal{N}\left(\nabla R(i)|0, v_c\right) \cdot \prod_j \sum_{d=1}^{D} w_d \cdot \mathcal{E}\left(K(j)|\lambda_d\right) \tag{4.38}$$

where i indexes over the pixels of the image and j over the elements of the kernel K. Observe that the probabilities for different pixels are modeled as being independent; hence, the product of the contributions of the individual pixels is calculated in (4.38).

The exact optimization algorithm applied by Fergus et al. is quite advanced and beyond our scope here, so it will be just roughly outlined. As a direct optimization of (4.38) (or the negative logarithm of (4.38)) did not yield the desired results, the authors of [5] employed a variational Bayesian approach which computes an approximation of the MAP. This approximation distribution is the product $q(\nabla R, K) = q(\nabla R) \cdot q(K)$. Moreover, they built a cost function representing the distance between the approximation and the true posterior, which was set to the Kullback-Leibler divergence. The minimum of this cost function yields the desired estimate K^* of the blur kernel. The main advantage of using the Kullback-Leibler divergence here is that, in its closed form, it can be expressed as simple as by a sum of several expectations, where each expectation relates to a specific design variable. Details can be found in [5, 9, 17] as well as the references therein.

In a subsequent step, the reconstructed image R^* can be found using the well-known Richardson-Lucy algorithm [21] as a classical non-blind deconvolution scheme.

4.4.3 Variants of the Proceeding

The method of Shan et al. [23] takes a modified approach of the successive blur kernel estimation and non-blind deconvolution. It introduces two major modifications:

- *Reweighting of the gradients* when calculating $-\log[p(R)]$: Similar to the weighting factors $s_x(x,y)$ and $s_y(x,y)$ of (4.11), the gradients in R can be weighted according to the gradients of I. If the sensed data I exhibits a high gradient at a certain position (a,b), the penalty of high gradients at $R(a,b)$ can be lowered. As a consequence, such an edge reweighting favors solutions which are piecewise constant. This is desirable, because this reduces so-called ringing artifacts, which are sinusoidal intensity modulations and are encountered very often in blind deconvolution. As can be seen in the lower right image of Fig. 4.8, this reweighting enables the joint estimator to be pulled away from the no-blur solution (compared to joint MAP estimation without gradient reweighting; cf. *lower right* image of Fig. 4.7) but still is far from the optimum.
- *Iterative update of the likelihood*: Shan et al. proposed an iterative estimation of R^* and K^*, i.e., R^* and K^* are updated in alternation until convergence is achieved. Additionally, the likelihood term is weighted differently at each iteration k. More specifically, they introduced a weighting factor λ for the likelihood term $-\log[p(I|R,K)]$. As the iteration proceeds, λ changes its value. It is advisable to start with low λ values in early iterations and then successively increase λ as k increments. As was shown in [16], low values of λ favor solutions with kernel estimates $K^{*,k}$ being much closer to the true kernel K compared to the naïve joint MAP estimator. As a consequence, there is a much better chance to avoid being stuck at a local minimum if λ is set to low values in early iteration steps. Because the updated solutions $\left(R^{*,k}, K^{*,k}\right)$ are searched only locally at each iteration step, the algorithms stays at a local minimum where the current kernel estimation $K^{*,k}$ is close to the true K. This should also hold when λ takes higher values.

As can be seen in Fig. 4.9, quite impressive results can be obtained for blind deconvolution. However, the algorithm needs a rough initial kernel estimate $K^{*,0}$.

The deconvolution algorithms presented so far assume that the blur kernel K is uniform for the entire image. However, this might be not true. As Whyte et al. found out [30], pixel displacements caused by camera rotation during exposure typically are larger than displacements by camera translation, at least for consumer cameras. Camera rotation, however, causes non-uniform blur, i.e., it varies across the image plane, as illustrated in Fig. 4.10. Therefore, Whyte et al. suggest a modified proceeding capable of removing non-uniform blur caused by camera rotation.

The displacement of an image point $\mathbf{x}$ caused by camera rotation can be modeled by a projective transformation, which can be written as a linear system of equations when homogeneous coordinates are used:

$$\mathbf{x}' = \begin{bmatrix} s \cdot x' \\ s \cdot y' \\ s \end{bmatrix} = \mathbf{H} \cdot \mathbf{x} = \begin{bmatrix} h_{11} & h_{12} & h_{13} \\ h_{21} & h_{22} & h_{23} \\ h_{31} & h_{32} & 1 \end{bmatrix} \cdot \begin{bmatrix} x \\ y \\ 1 \end{bmatrix} \tag{4.39}$$

Homogeneous coordinates can be transformed back into inhomogeneous coordinates by dividing all elements by the last element of the vector, i.e., by the

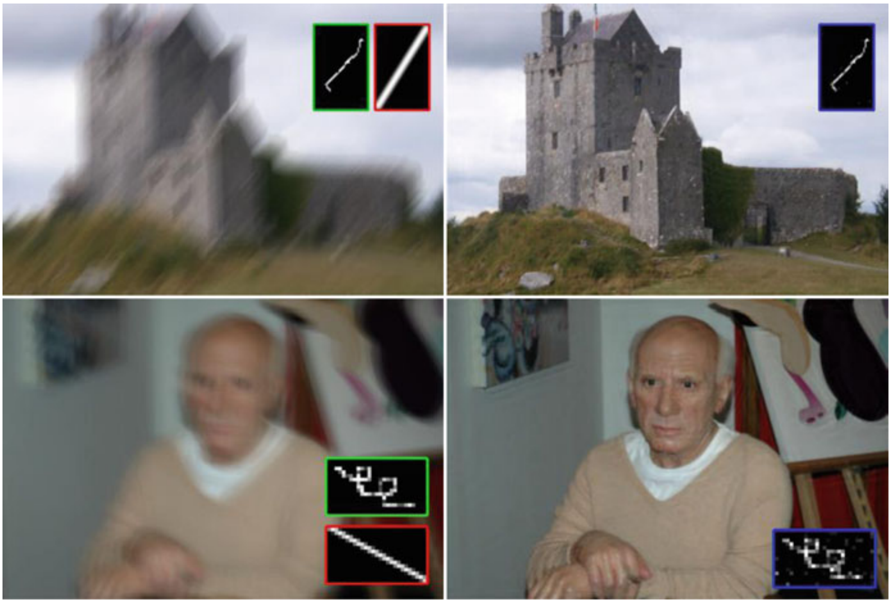

Fig. 4.9 Illustrating the performance of the blind deconvolution algorithm proposed in [23]. The *left column* depicts the blurred image. The reconstructed image is depicted in the *right column*. All examples are shown together with the true kernel (*box framed green*), the initial kernel estimate (*box framed red*), and the final kernel estimate (*box framed blue*) (Shan et al. [23] © 2008 Association for Computing Machinery, Inc. Reprinted by permission)

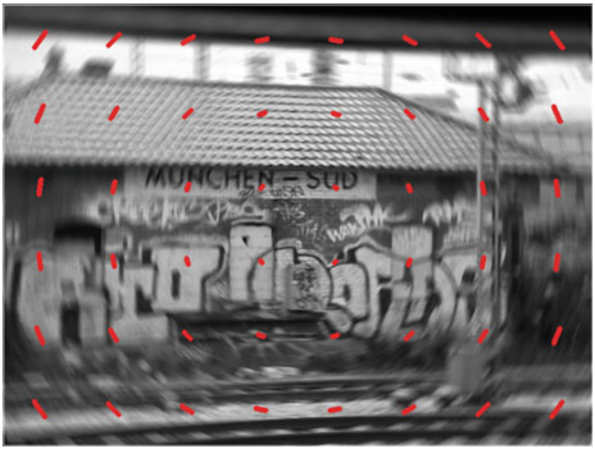

Fig. 4.10 Showing an example image with rotation blur together with some *red* paths defining the pixels being influenced by the same scene element when the camera is rotated around the z-axis (perpendicular to the image plane). Clearly, these paths depend on their position in the camera image. Blur caused by this rotation typically increases significantly in the edges of the image

scale factor s used in (4.39). The matrix $\mathbf{H}$ defines the projective transformation specified by eight independent parameters. If camera parameters are known, the matrix $\mathbf{H}$ can be replaced by a product of the camera's internal calibration matrix and a rotation matrix with only three degrees of freedom, which relate to the rotations about the three axes of a 3D space.

If we consider a non-uniformly blurred image where camera rotation follows a certain profile during exposure, the exposure time can be partitioned into T small time slots t. Within each time slot, the camera rotation can be assumed constant and thus is defined by a single matrix $\mathbf{H}_t$. As a result, the observed image I is a summation of T versions of the transformed non-blurred image R, plus a noise term n:

$$I(\mathbf{x}) = \sum_{t=1}^{T} R(\mathbf{H}_t \cdot \mathbf{x}) + n \tag{4.40}$$

As we do not know the temporal progression of camera rotation, the observed image can be modeled by the weighted summation over all possible camera rotations θ, where each weight w_θ is proportional to the amount of time the camera stays at rotation θ:

$$I(\mathbf{x}) = \sum_{\theta} w_\theta R(\mathbf{H}_\theta \cdot \mathbf{x}) + n \tag{4.41}$$

Consequently, all w_θ can be combined into a blur kernel W, which now consists of quantities specifying the influence of several rotated versions of the unblurred image. For the deconvolution procedure, Whyte et al. used the framework of [5], i.e., they first calculate an estimation W^* of the blur kernel using the variational method of [5] (adapted to non-uniform blur) and subsequently estimate the reconstructed image R^* with the Richardson-Lucy algorithm [21].

In order to illustrate the performance of the method, let's take a look at Fig. 4.11: Here, a street scene (upper left) is blurred by camera rotation about the z-axis during exposure (upper right). The increased influence of the blur in the edges of the image is clearly visible. The deblurring result of Fergus et al. is shown in the lower left image, whereas the result of the non-uniform algorithm proposed by Whyte et al. is shown in the lower right image. Clearly, the non-uniform deconvolution performs much better for this example, especially in the corners of the image.

4.5 Active Contours (Snakes)

Another application where variational optimization can be applied are so-called active contours, which are also termed *snakes*. The following section, which introduces into the concept of active contours and describes lesion detection in

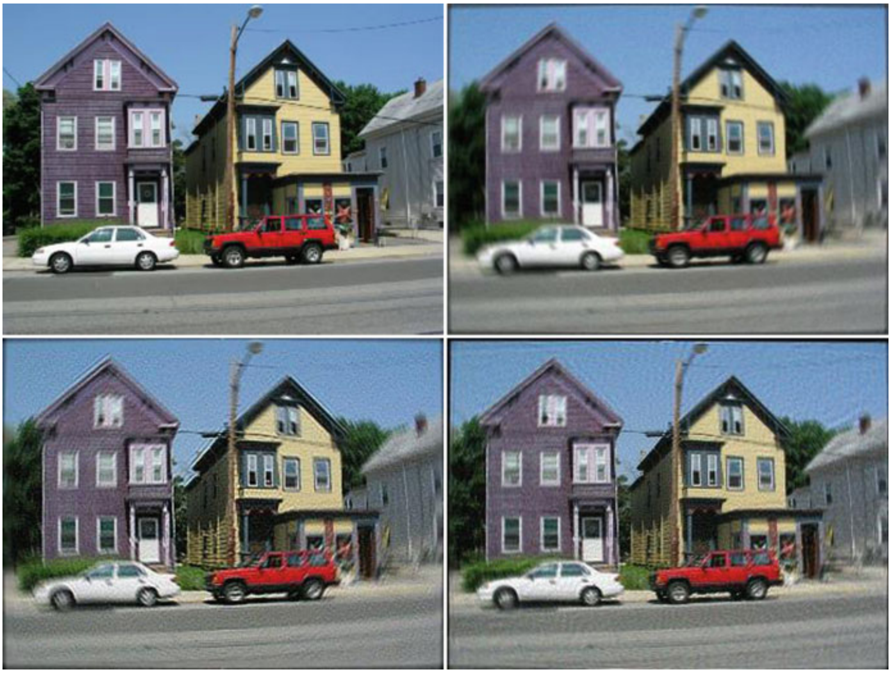

Fig. 4.11 Illustrating the performance of the non-uniform deconvolution presented in [30] (see text for details) (© 2010 IEEE. Reprinted, with permission, from Whyte et al. [30])

skin cancer images as an example application, is a modified version of Sect. 6.2 of [27].

Snakes are parametric curves and can be used, for example, as a description of the outer shape of an object. In such cases the parameters of the curve should be chosen such that the curve follows the object contour, i.e., it proceeds along the border of the object to the background. A parametric curve $\mathbf{v}(s,\varphi)$ can be written as

$$\mathbf{v}(s,\varphi) = [x(s,\varphi), y(s,\varphi)] \tag{4.42}$$

with φ being a vector of model parameters specifying the curve and s being a scalar monotonously increasing from 0 to 1 as the curve is traversed, which is often referred to as the arc length parameter. The run of the curve should approximate the object contour as good as possible. As the curve is represented by a functional relationship, a specific curve $\mathbf{v}(s,\varphi)$ being suitable for describing an object shape accurately can be found by means of variational optimization. Numerical implementations aim at calculating the $[x_i, y_i]$-positions for sampled values s_i of the arc length parameter s.

4.5.1 Standard Snake

4.5.1.1 Main Idea

Snakes have initially been proposed by Kass et al. [10] as a method of detecting contours of deformable objects. They behave like an elastic band which is pulled to the object contour by forces. The run of the curve/band is iteratively updated, and eventually it should converge to the outer shape of the object being searched. The forces affecting the snake are represented by an energy functional, which is iteratively minimized. As a result, the minimizing argument specifies the updated curve positions.

During energy minimization the snakes change their location dynamically, thus showing an active behavior until they reach a stable position being conform with the object contour. For this reason they are also called active contour models. The "movement" of the curve as the iteration proceeds reminds of snakes, which explains the name. See e.g. [18] for a good introduction.

According to Kass et al. [10] the energy functional E accounts for multiple influences and can be written as

$$E = \int_0^1 E_{\mathrm{int}}(\mathbf{v}(s,\varphi)) + E_{\mathrm{d}}(\mathbf{v}(s,\varphi)) + E_{\mathrm{ext}}(\mathbf{v}(s,\varphi))\mathrm{d}s \tag{4.43}$$

Taking a closer look at (4.43), we can see that the total energy consists of three components, which can be described as follows:

- E_{int} denotes the *internal energy*, which exclusively depends on $\mathbf{v}(s,\varphi)$, i.e., it is independent of the observed image. E_{int} plays the role of a smoothness constraint and helps to enforce that the run of the curve is smooth. To this end, E_{int} is influenced by derivative information. More specifically, it depends on the first- and second-order derivatives of $\mathbf{v}(s,\varphi)$ with respect to s. Considering the first-order derivative should exclude discontinuities, whereas second-order information helps punishing curves containing sections of high curvature. In this context, curvature can be interpreted as a measure of the energy which is necessary to bend the curve.
- The *data-driven term* E_{d} measures how well the curve fits to the image data. The curve should be attracted by local intensity discontinuities in the image (locations with high gradients), because usually the object brightness differs from the background intensity, and, therefore, we should observe some rapid intensity changes at the object borders.
- The *external constraints* E_{ext} aim at ensuring that the snake should remain near the desired minimum as the iterative optimization proceeds. This can be achieved by user input (e.g., when E_{ext} is based on the distance of the curve to user-selected "anchor points," which are supposed by the user to be located on the object contour) or by feedback of a higher-level scene interpretation method, which could be run subsequently.

During optimization, the curve has to be estimated numerically. To this end, it is sampled at a certain number of control points. Now, the task is to adjust the positions of these control points such that the energy functional E reaches a minimum. The appropriate optimization procedure is outlined in the following, details can be found in the appendix of [10].

4.5.1.2 Optimization

As already mentioned, the internal energy, which acts as a smoothness constraint, is usually modeled by a linear combination of the first- and second-order derivatives of $\mathbf{v}(s, \varphi)$ with respect to s:

$$E_{\text{int}} = \frac{1}{2} \cdot \left[\alpha |\mathbf{v}_s(s, \varphi)|^2 + \beta |\mathbf{v}_{ss}(s, \varphi)|^2 \right] \tag{4.44}$$

Here, the parameters α and β determine the relative influence of the first- and second-order derivative (which are denoted by $\mathbf{v}_s$ and $\mathbf{v}_{\text{ss}}$, respectively). The purpose of the two terms of (4.44) is to punish discontinuities and high curvature parts, respectively. If β is set to 0, the curve is allowed to contain corners. It is possible to model α and β dynamically dependent on s or statically as constants.

Concerning the data-driven term, E_{d} should take smaller values at points of interest, such as edge points. Consequently, the negative gradient magnitude is a natural measure for E_{d}. However, object borders usually lead to high gradient values (and therefore large negative values of E_{d}) only within a very limited area in the surrounding of the border. As a result, the convergence area, where the curve is driven in the right direction, is usually very limited for this choice of E_{d}. It can be increased, though, by utilizing a spatially blurred version of the gradient magnitude. To this end, a convolution of the image content with a Gaussian kernel $G(x, y, \sigma)$ is applied:

$$\begin{aligned} E_{\text{d}}(x, y) &= -|\nabla[G(x, y, \sigma) * I(x, y)]|^2 \\ \text{with } G(x, y, \sigma) &= \frac{1}{\sqrt{2\pi}\sigma} \cdot e^{-\left(x^2+y^2\right)/2\sigma^2} \end{aligned} \tag{4.45}$$

where ∇ and $*$ denote the gradient and convolution operator, respectively.

As far as the external constraints E_{ext} are concerned, they are often set to zero and therefore aren't considered any longer in this section.

As already said, the minimization of the energy functional is usually performed without explicit calculation of the model parameters φ of the curve. Instead, the curve position is optimized at N discrete positions $\mathbf{v}(s_i) = [x(s_i), y(s_i)]$ with $i \in [1, \ldots, N]$ and $s_{i+1} = s_i + \Delta s$. Δs denotes a suitably chosen step size. In other words, the optimization task is to estimate the position of a discrete set of points $\mathbf{v}(s_i)$.

If the internal and image constraints are modeled as described above and, additionally, we assume that α and β are constants, the snake must satisfy a system of two independent Euler equations in order to minimize E. The Euler equations are defined by

$$\begin{aligned} &\sum_{i=1}^{N} \alpha x_{\mathrm{ss}}(s_i) + \beta x_{\mathrm{ssss}}(s_i) + \frac{\partial E_{\mathrm{d}}(s_i)}{\partial x} = 0 \\ &\sum_{i=1}^{N} \alpha y_{\mathrm{ss}}(s_i) + \beta y_{\mathrm{ssss}}(s_i) + \frac{\partial E_{\mathrm{d}}(s_i)}{\partial y} = 0 \end{aligned} \tag{4.46}$$

with $x_{\mathrm{ss}}(s)$ resp. $y_{\mathrm{ss}}(s)$ being the second-order derivative and $x_{\mathrm{ssss}}(s)$ resp. $y_{\mathrm{ssss}}(s)$ the fourth-order derivative of the components of $\mathbf{v}$ with respect to s. The desired minimum is found if the left-hand side of the Euler equations is equal to zero. (4.46) is derived from the fact that, at the optimum, the derivative of the total energy is equal to zero: $\nabla E = \nabla E_{\mathrm{int}} + \nabla E_{\mathrm{d}} \equiv 0$.

A solution of these partial differential equations can be found numerically by treating $\mathbf{v}$ as a function of time t and iteratively adjusting the discrete $\mathbf{v}(s_i, t)$ until convergence is achieved (see the appendix of [10] for details): starting from an initial solution, an updated solution is calculated by approximating the derivatives numerically at each time step t_k, using the data at the current position of the sample points.

The numerical approximation of the second-order derivatives of $x_{\mathrm{ss}}(s)$ and $y_{\mathrm{ss}}(s)$ is given as follows:

$$\begin{aligned} x_{\mathrm{ss}}(s_i) &= x(s_{i-1}) - 2x(s_i) + x(s_{i+1}) \\ y_{\mathrm{ss}}(s_i) &= y(s_{i-1}) - 2y(s_i) + y(s_{i+1}) \end{aligned} \tag{4.47}$$

The fourth-order derivatives can be approximated by taking the second derivative of (4.47). Consequently, $x_{\mathrm{ssss}}(s)$ is approximated by

$$\begin{aligned} x_{\mathrm{ssss}}(s_i) &= x_{ss}(s_{i-1}) - 2x_{\mathrm{ss}}(s_i) + x_{\mathrm{ss}}(s_{i+1}) \\ &= x(s_{i-2}) - 4x(s_{i-1}) + 6x(s_i) - 4x(s_{i+1}) + x(s_{i+2}) \end{aligned} \tag{4.48}$$

$y_{\mathrm{ssss}}(s)$ can be approximated analogously.

The derivatives $\partial E_{\mathrm{d}}(s_i)/\partial x$ and $\partial E_{\mathrm{d}}(s_i)/\partial y$ of the image constraint can be calculated numerically by first performing a discrete convolution of I with a Gaussian kernel G (whose size in pixel depends on the σ-parameter) yielding I_G and then approximating the derivative by taking the differences between adjacent pixels of I_G in x-direction (or y-direction, respectively).

Through the usage of the numerical approximations defined by (4.47) and (4.48), $\alpha x_{\mathrm{ss}}(s_i) + \beta x_{\mathrm{ssss}}(s_i)$ is defined by $\beta \cdot x(s_{i-2}) + (\alpha - 4\beta) \cdot x(s_{i-1}) + (6\beta - 2\alpha) \cdot x(s_i) + (\alpha - 4\beta) \cdot x(s_{i+1}) + \beta \cdot x(s_{i+2})$. Consequently, the Euler equations of (4.46) can be written in matrix form:

$$\mathbf{A} \cdot \mathbf{x} + \mathbf{g}_x = \mathbf{0}$$
$$\mathbf{A} \cdot \mathbf{y} + \mathbf{g}_y = \mathbf{0}$$

with

$$\mathbf{A} = \begin{bmatrix} 6\beta-2\alpha & \alpha-4\beta & \beta & 0 & \cdots & 0 & \beta & \alpha-4\beta \\ \alpha-4\beta & 6\beta-2\alpha & \alpha-4\beta & \beta & 0 & \cdots & 0 & \beta \\ \beta & \alpha-4\beta & 6\beta-2\alpha & \alpha-4\beta & \beta & 0 & \cdots & 0 \\ 0 & \beta & \alpha-4\beta & 6\beta-2\alpha & \alpha-4\beta & \beta & 0 & 0 \\ \vdots & 0 & \ddots & \ddots & \ddots & \ddots & \ddots & 0 \\ 0 & \cdots & 0 & \beta & \alpha-4\beta & 6\beta-2\alpha & \alpha-4\beta & \beta \\ \beta & 0 & \cdots & 0 & \beta & \alpha-4\beta & 6\beta-2\alpha & \alpha-4\beta \\ \alpha-4\beta & \beta & 0 & \cdots & 0 & \beta & \alpha-4\beta & 6\beta-2\alpha \end{bmatrix}$$

$$\mathbf{x} = \begin{bmatrix} x(s_1) \\ x(s_2) \\ x(s_3) \\ \vdots \\ x(s_{N-1}) \\ x(s_N) \end{bmatrix} \quad \mathbf{y} = \begin{bmatrix} y(s_1) \\ y(s_2) \\ y(s_3) \\ \vdots \\ y(s_{N-1}) \\ y(s_N) \end{bmatrix} \quad \mathbf{g}_x = \begin{bmatrix} \partial E_{\mathrm{d}}(s_1)/\partial x \\ \partial E_{\mathrm{d}}(s_2)/\partial x \\ \partial E_{\mathrm{d}}(s_3)/\partial x \\ \vdots \\ \partial E_{\mathrm{d}}(s_{N-1})/\partial x \\ \partial E_{\mathrm{d}}(s_N)/\partial x \end{bmatrix} \quad \mathbf{g}_y = \begin{bmatrix} \partial E_{\mathrm{d}}(s_1)/\partial y \\ \partial E_{\mathrm{d}}(s_2)/\partial y \\ \partial E_{\mathrm{d}}(s_3)/\partial y \\ \vdots \\ \partial E_{\mathrm{d}}(s_{N-1})/\partial y \\ \partial E_{\mathrm{d}}(s_N)/\partial y \end{bmatrix} \tag{4.49}$$

Observe that for closed contours, the index of the points $\mathbf{v}(s_i)$ is "cyclic", i.e., $\mathbf{v}(s_0) = \mathbf{v}(s_N)$, $\mathbf{v}(s_{-1}) = \mathbf{v}(s_{N-1})$, and $\mathbf{v}(s_{N+1}) = \mathbf{v}(s_1)$.

The solution is now specified by the vectors $\mathbf{x}$ and $\mathbf{y}$. At first glance, it seems that it could be obtained by just solving the linear equation systems specified in (4.49).

However, in practice the solution has to be calculated iteratively. Please note that, as long as the iteration has not converged yet, the right-hand sides of the Euler equations don't vanish, because the time derivative of the left-hand side is not zero. It can be set to the difference between two successive steps of the iteration (multiplied by a step size γ). Therefore, solving the linear system of equations defined in (4.49) once is not enough. Instead, we have to employ an iterative scheme, where, unlike in (4.49), the difference of the solution between two successive steps is considered, too. Eventually, the suggested optimization method is a gradient descent algorithm.

In [10] it is suggested to use explicit Euler for the external forces (and therefore evaluate $\mathbf{g}_x$ and $\mathbf{g}_y$ at position $(\mathbf{x}^t, \mathbf{y}^t)$) and implicit Euler for the internal energy (and therefore multiply $\mathbf{A}$ by $\mathbf{x}^{t+1}$ and $\mathbf{y}^{t+1}$) (see the appendix of [10] for details). Incorporating this in (4.49) yields the following update formulas:

$$\begin{aligned} \mathbf{A} \cdot \mathbf{x}^{t+1} + \mathbf{g}_x(\mathbf{x}^t, \mathbf{y}^t) &= -\gamma \cdot \left(\mathbf{x}^{t+1} - \mathbf{x}^t\right) \\ \mathbf{A} \cdot \mathbf{y}^{t+1} + \mathbf{g}_y(\mathbf{x}^t, \mathbf{y}^t) &= -\gamma \cdot \left(\mathbf{y}^{t+1} - \mathbf{y}^t\right) \end{aligned} \tag{4.50}$$

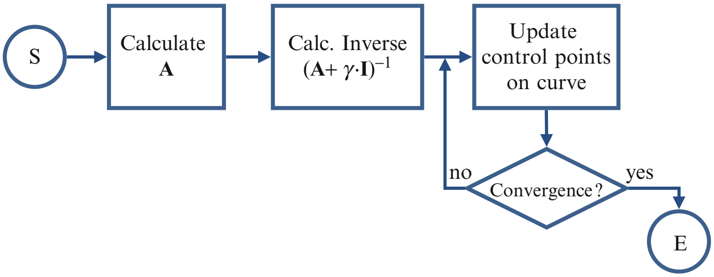

Fig. 4.12 Flowchart of the variational optimization of active contour models

These equations can be solved by matrix inversion, leading to

$$\begin{aligned}\mathbf{x}^{t+1} &= (\mathbf{A} + \gamma \cdot \mathbf{I})^{-1} \cdot (\mathbf{x}^t - \mathbf{g}_x(\mathbf{x}^t, \mathbf{y}^t)) \\ \mathbf{y}^{t+1} &= (\mathbf{A} + \gamma \cdot \mathbf{I})^{-1} \cdot \left(\mathbf{y}^t - \mathbf{g}_y(\mathbf{x}^t, \mathbf{y}^t)\right)\end{aligned} \tag{4.51}$$

where **I** denotes the identity matrix. An iterative application of (4.51) dynamically changes the course of the curve until finally it "snaps" to dominant edges and convergence is achieved. The general flow of the method is illustrated in Fig. 4.12.

For constants α and β, the matrix **A** does not depend on position or time, and therefore, the inverse $(\mathbf{A} + \gamma \cdot \mathbf{I})^{-1}$ can be calculated offline prior to the iterative update of the control point positions. If $\alpha(x, y)$ and $\beta(x, y)$ are location dependent, **A** has to be updated at each iteration step. As the matrix $(\mathbf{A} + \gamma \cdot \mathbf{I})$ has a pentadiagonal structure (cf. (4.49)), its inverse can be calculated fast by an LU decomposition of $(\mathbf{A} + \gamma \cdot \mathbf{I})$.

Figure 4.13 shows an example of fitting an initially circle-shaped curve to a triangle form. The energy is minimized iteratively with the help of sample points located on the current curve representation (indicated by green squares). The images show the location of the sample points in the different steps of the iteration (at start, after 6, 10, 15, 20, and the final iteration, from top left to bottom right). The "movement" of each sample point as the iteration proceeds is shown by a specific curve for each point (green and red curves).

Being a global approach, snakes have the very desirable property of being quite insensitive to contour interruptions or local distortions. For this reason they are often used in medical applications where, due to low SNR images, closed contours often are difficult to obtain. A major drawback of snakes, though, is the fact that they rely on a reasonable starting point of the curve (i.e., a rough idea where the object border could be) for ensuring convergence to the global minimum of the energy functional. If the starting point is located outside the convergence area of the global minimum, the iteration might get stuck in a local minimum being arbitrarily far away from the desired solution. Additionally, snakes sometimes failto penetrate into deep concavities because the smoothness constraint is overemphasized in those scenarios.

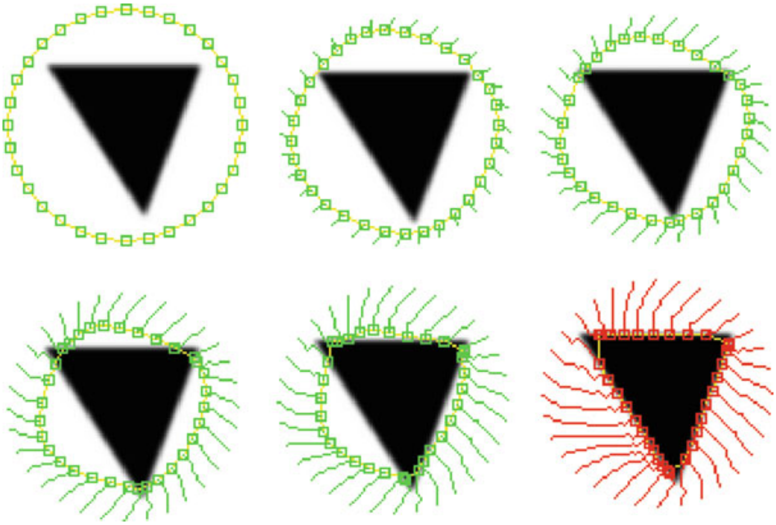

Fig. 4.13 Showing several iteration steps captured during fitting of an initial *circle-shaped* curve to a *triangle* form (From Treiber [27], with kind permission from Springer Science and Business Media)

Please note that active contours are also suited for applying another paradigm of solving variational problems, namely, the reduction to a continuous optimization problem. After this conversion the solution can be found with some standard method as presented in chapter two. An example of this proceeding can be found in [29]. Here, the modeling of the curve is reduced to a series of B-splines, which can be described by a finite set of parameters. Hence, the original variational problem of infinite dimensionality is reduced to the problem of finding a finite number of parameters.

4.5.2 *Gradient Vector Flow (GVF) Snake*

4.5.2.1 Main Idea

In order to overcome the drawback of limited convergence area, Xu and Prince [31] suggested a modification of the classical scheme, aiming at extending the convergence area of the snake as well as enhancing the ability of the snake to penetrate in deep concavities of object boundaries. Having these two goals in mind, they replaced the part which represents the image constraints in the Euler equation (4.46), namely, $-\nabla E_{\text{image}}$, by a more general force field $\mathbf{f}(x,y)$:

$$\mathbf{f}(x,y) = [a(x,y), b(x,y)] \tag{4.52}$$

which they called *gradient vector flow* (GVF). A specific tuning of $\mathbf{f}(x,y)$ intends to enlarge of the convergence area as well as increase the ability to model deep concavities correctly.

The calculation of $\mathbf{f}(x,y)$ is based on the definition of an edge map $e(x,y)$, which should be large near gray value discontinuities. The above definition of a Gaussian-blurred intensity gradient of (4.45), which is used in the standard scheme when defining the data-driven energy, is one example of an edge map. The GVF field is then calculated from the edge map by minimizing the energy functional

$$\varepsilon = \int\int \mu\left(a_x^2 + a_y^2 + b_x^2 + b_y^2\right) + |\nabla e|^2 |\mathbf{f} - \nabla e|^2 \mathrm{d}x\,\mathrm{d}y \tag{4.53}$$

with $(\cdot)_n$ being the partial derivative in the n-direction. A closer look at ε reveals its desirable properties: near object boundaries – where $|\nabla e|$ is large and minimization of ε usually results in setting $\mathbf{f}$ very close to or even identical to ∇e. Consequently, the GVF snake behaves very similar to the standard snake. In homogenous image regions, however, $|\nabla e|$ is rather small, and therefore ε is dominated by the partial derivatives of the vector field. Minimizing ε therefore keeps the spatial change of $\mathbf{f}(x,y)$ small in those regions. Eventually, the property of favoring slow variations when we move away from locations with high gradient magnitude yields in enlarged convergence areas. The parameter μ serves as a regularization term.

Compared to (4.45), the calculation of the (so far unknown) GVF field is not straightforward. However, Xu and Prince showed that indeed it can be calculated prior to snake optimization by separately optimizing $a(x,y)$ and $b(x,y)$. This is done by solving the two Euler equations

$$\mu\nabla^2 a - (a - e_x)\left(e_x^2 + e_y^2\right) = 0 \tag{4.54a}$$

and

$$\mu\nabla^2 b - \left(b - e_y\right)\left(e_x^2 + e_y^2\right) = 0 \tag{4.54b}$$

where ∇^2 denotes the Laplacian operator (see [31] for details). The thus obtained solutions minimize ε (cf. (4.53)). Once $\mathbf{f}(x,y)$ is calculated, the snake can be optimized as described in the previous section.

Pseudocode

```
function optimizeCurveGVFSnake (in Image $I$, in segmentation threshold $t_I$, out boundary curve $\mathbf{v}(s_i)$)

// pre-processing
remove noise from $I$ if necessary, e.g. with anisotropic diffusion
```

```
init of edge map $e(x,y)$ with Gaussian blurred intensity gradient magnitude of $I$ (c.f. (4.45))
calculate GVF field $\mathbf{f}(x,y)$ by solving Equation 4.54

// init of snake: segment the object from the background and derive the initial curve from its outer boundary
for y = 1 to height (I)
  for x = 1 to width (I)
    if $I(x,y) \leq t_I$ then
        add pixel $[x,y]$ to object area $\mathbf{o}$
    end if
  next
next
get all boundary points $\mathbf{b}$ of $\mathbf{o}$
sample boundary points $\mathbf{b}$ in order to get a discrete representation of parametric curve $\mathbf{v}(s_i,0)$

// optimization (just outline, details see [10])
$t \leftarrow 0$
calculate matrix inverse $(\mathbf{A}+\gamma\cdot\mathbf{I})^{-1}$
calculate $\mathbf{g}_x$ and $\mathbf{g}_y$ according to positions defined by $\mathbf{v}(s_i,0)$
repeat
  $\mathbf{v}(s_i,t+1) \leftarrow$ result of update equation 4.51    // update curve
  update $\mathbf{g}_x$ and $\mathbf{g}_y$ according to the new positions defined by $\mathbf{v}(s_i,t+1)$
  $t \leftarrow t+1$
until convergence
```

4.5.2.2 Example: Lesion Detection

A medial image application of GVF snakes is presented by Tang [24], where the GVF snake is incorporated in a lesion detection scheme for skin cancer images. Starting from a color image showing one or more lesions of the skin, the exact boundary of the lesion(s) is extracted (cf. Fig. 4.14). As can be seen in Fig. 4.14, the images can contain more or less heavy clutter such as hairs or specular reflections in the lesion region.

The method consists of four major steps:

1. *Conversion* of the original color image to a gray value image.
2. *Noise removal* by applying a so-called anisotropic diffusion filter: The basic idea of anisotropic diffusion is to remove noise without blurring the gradients at true object borders at the same time. To this end, the image is iteratively smoothed by application of a diffusion process such that pixels with high intensity ("mountains") diffuse into neighboring pixels with lower intensity ("valleys").

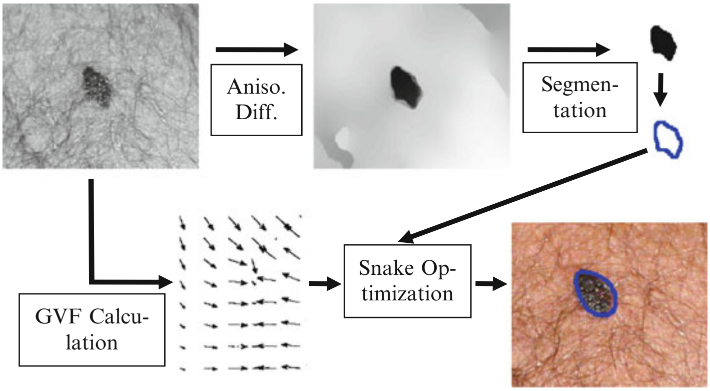

Fig. 4.14 Illustrating the boundary extraction of the lesions of skin cancer images (after the initial gray value conversion). The proceeding is explained in the text (From Treiber [27], with kind permission from Springer Science and Business Media, with images taken from Tang [24], with permission from Elsevier)

The main point is that this is done in an anisotropic way: diffusion should not take place in the direction of dominant gray value gradients (thereby gradient blurring is avoided!), but preferably perpendicular to it (where variations are attributed to noise). Details can be found in [24] and are beyond the scope of this book.

3. *Rough segmentation* by applying simple gray value thresholding: This step serves for the estimation of reasonable starting regions for the subsequent snake optimization.
4. *Fine segmentation* using a GVF snake. (To be correct, Tang [24] applied a modified version aiming at making the method suitable for multi-lesion images by modifying the force field, without giving any details here. In those cases the snake has to be prevented to partly converge to one lesion and party to another lesion in its vicinity.)

Especially to mention is that some restrictions of the standard snake scheme can be overcome or at least alleviated by the usage of GVF snakes. The additional degrees of freedom obtained by the introduction of more general force fields can be utilized to enlarge the convergence area or make the optimization more robust in situations where the scene image contains multiple objects. On the other hand, the calculation of the force field needs a second optimization procedure during recognition, which increases the computational complexity of the method.

References

1. Bakushinsky A, Goncharsky A (1994) Ill-posed problems: theory and applications. Kluwer Academic Publishers, Dordrecht. ISBN 978-0792330738
2. Briggs WL, Henson VE, McCormick SF (2000) A multigrid tutorial, 2nd edn. Society for Industrial and Applied Mathematics, Philadelphia

3. Chambolle A (2004) An algorithm for total variation minimization and applications. J Math Imaging Vis 20:89–97
4. Chambolle A (2005) Total variation minimization and a class of binary MRF models. Int Conf Energy Minimization Methods Comput Vision Pattern Recogn 5:136–152
5. Fergus R, Singh H, Hertzmann A, Rotweis S.T, Freeman W.T (2006) Removing camera shake from a single photograph. In: SIGGRAPH, Boston
6. Fischen, J (1999) Introduction to the calculus of variations. http://online.redwoods.cc.ca.us/instruct/darnold/staffdev/assignments/calcvarb.pdf. Published online
7. Golub GH, Van Loan CF (1996) Matrix computations, 3rd edn. Johns Hopkins University Press, Baltimore. ISBN 0-8018-5414-8
8. Horn K, Schunck B (1981) Determining optical flow. Artif Intell 17:185–203
9. Jordan M, Ghahramani Z, Jaakkola T, Saul L (1999) An introduction to variational methods for graphical models. Mach Learn 38:183–233
10. Kass M, Witkin A, Terzopoulos D (1988) Snakes: active contour models. Int J Comput Vis 1:321–331
11. Kirk D.B, Hwu W.W (2012) Programming massively parallel processors: a hands-on approach, 2nd edn. Morgan Kaufman, San Francisco. ISBN 978-0124159921
12. Kolev K, Klodt M, Brox T, Cremers D (2009) Continuous global optimization in multiview 3D reconstruction. Int J Comput Vis 84(1):80–96
13. Kundur D, Hatzinakos D (1996) Blind image deconvolution. IEEE Signal Proc Mag 13(3):43–64
14. Lellman J, Becker F, Schnörr C (2009) Convex optimization for multi-class image labeling with a novel family of total variation based regularizers. IEEE Int Conf Comput Vis 12:646–653
15. Levin A, Weiss Y, Durand F, Freeman WT (2009) Understanding blind deconvolution algorithms. Extended Technical Report
16. Levin A, Weiss Y, Durand F, Freeman WT (2011) Understanding blind deconvolution algorithms. IEEE Signal Proc Mag 33(12):2354–2367
17. Miskin J, MacKay DC (2000) Ensemble learning for blind image separation and deconvolution. In: Girolani M (ed) Advances in independent component analysis. Springer, London
18. Nixon M, Aguado A (2007) Feature extraction and image processing. Academic Press, New York. ISBN 978-0-12-372538-7
19. Oliveira JP, Bioucas-Dias JM, Figueiredo M (2009) Adaptive total variation image deblurring: a majorization-minimization approach. Signal Process 89(9):1683–1693
20. Pock T (2008) Fast total variation for computer vision. PhD thesis, TU, Graz
21. Richardson WH (1972) Bayesina-based iterative method of image restoration. J Opt Soc Am 62(1):55–59
22. Rudin LI, Osher S, Fatemi E (1992) Nonlinear total variation based noise removal algorithms. Physica D 60:259–268
23. Shan Q, Jia J, Agarwala A (2008) High-quality motion deblurring from a single image. ACM Trans Graphic 27(3)
24. Tang J (2009) A multi-direction GVF snake for the segmentation of skin cancer images. Pattern Recogn 42:1172–1179
25. Terzopoulos D (1983) Multilevel computational processes for visual surface reconstruction. Comput Vis Graph Image Process 24:52–96
26. Tikhonov AN, Arsenin VY (1997) Solutions of ill-posed problems. V.H. Winston, Washington, DC. ISBN 047-099-1240
27. Treiber M (2010) An introduction to object recognition – selected algorithms for a wide variety of applications. Springer, London. ISBN 978-1849962346
28. Wanner S, Goldluecke B (2012) Globally consistent depth labeling of 4D light fields. IEEE Conf Comput Vis Pattern Recogn 25:41–48

29. Wesselink JW (1996) Variational modeling of curves and surfaces. PhD thesis, Technische Universiteit Eindhoven
30. Whyte O, Sivic J, Zisserman A, Ponce J (2010) Non-uniform deblurring for shaken images. IEEE Conf Comput Vision Pattern Recogn 23:491–498
31. Xu C, Prince JL (1998) Snakes, shapes and gradient vector flow. IEEE Trans Image Process 7(3):359–369
32. Zach C, Pock T, Bischof H (2007) A duality based approach for realtime TV-L1 optical flow. In: Proceedings of the 29th DAGM conference on pattern recognition. Springer, Berlin, pp 214–223

Chapter 5
Correspondence Problems

Abstract Quite numerous computer vision applications require an assignment of the elements of a set of some extracted salient positions/descriptors to their corresponding counterpart in a model set, at some point of their proceeding. Examples are object recognition or image registration schemes. Because an exhaustive evaluation of all possible combinations of individual assignments is infeasible in terms of runtime, more sophisticated approaches are required, and some of them will be presented in this chapter. Possible ways of speeding up the search are applying heuristics, as done in the so-called search tree, or iterative approaches like the iterative closest point method. A typical challenge when trying to find the correct correspondences is the existence of a quite large number of outliers, e.g., positions being spoiled by gross errors. The straightforward approach of minimizing total deviations runs into difficulties in that cases, and consequently, methods being more robust to outliers are required. Examples of robust schemes are the random sample consensus (RANSAC) or methods transforming the problem into a graph representation, such as spectral graph matching or bipartite graph matching as done in the so-called Hungarian algorithm.

5.1 Applications

Various applications comprise a step where the elements $\mathbf{p}_{1,m}$ of one set of points $P_1 = \{\mathbf{p}_{1,m}; m \in [1, \ldots, M]\}; \mathbf{p}_{1,m} = [x_{1,m}, y_{1,m}]$ are to be matched to the elements $\mathbf{p}_{2,n}$ of a second point set $P_2 = \{\mathbf{p}_{2,n}; n \in [1, \ldots, N]\}; \mathbf{p}_{2,n} = [x_{2,n}, y_{2,n}]$, i.e., correspondences between the elements of P_1 and P_2 have to be established. This task is described as the *correspondence problem* in literature. A correspondence c_{mn} is found if a certain $\mathbf{p}_{1,m}$ matches “best” to $\mathbf{p}_{2,n}$. Some matching criteria will be described below. A typical scenario is the matching of a data point set to a set of model points.

These correspondences can be used, for example, in *image registration* tasks, where the content of different images is to be transformed into a single coordinate system. A classical approach to registration tasks is to find corresponding points in

M.A. Treiber, *Optimization for Computer Vision: An Introduction to Core Concepts and Methods*, Advances in Computer Vision and Pattern Recognition,
DOI 10.1007/978-1-4471-5283-5_5, © Springer-Verlag London 2013

different images and, subsequently, utilize the positions of corresponding points for an estimation of the parameters of an aligning transform, which maps the positions of the first image into the corresponding position of the second image. A special case of image registration is *image stitching*, where several images partly overlap. By finding corresponding points in the overlapping part of two images, the transformation between these two images can be estimated and the images can be combined into a single image frame. With this technique, it is possible to assemble a panorama image from multiple images. Correspondence problems can also arise in stereo vision, where the displacement between corresponding points in two images (which is called *disparity*) can be used to calculate the depth of the scene, i.e., the z-distance from the scene to the stereo camera system.

Establishing correspondences can also be very helpful in the context of object detection. Some object models consist of a spatial configuration of a set of points, e.g., each point specifies the center position of a salient part of the object to be found. By matching the set of characteristic points found in a query image to the model point set, the so-called object pose can be revealed. Here, the object pose denotes the set of parameters specifying the object location, e.g., x-/y-position, rotation, and scale.

Please note that in general the cardinality of the two point sets is different, i.e., $M \neq N$. In many applications, when correspondences between the points of two sets are to be found, it is not necessary to establish one-to-one mappings between all points in the two sets. There may be unmatched points in one of the sets, e.g., due to background clutter (which introduces some extra points in one of the sets) or occlusion (which makes some of the points invisible in one of the images). Some applications also allow a point to be matched to multiple points in the other set (so-called many-to-one mappings).

These examples illustrate the widespread appearance of correspondence problems in computer vision. Therefore, let's discuss how it can be solved in more detail in this chapter. Obviously, the brute force approach of evaluating all possible correspondences quickly becomes infeasible as the number of points increases, because the number of possible correspondences grows exponentially with the number of points. This exponential growth of possible assignments is sometimes called the combinatorial explosion. Consequently, something more elaborate has to be found in order to optimize the correspondences.

Before we take a closer look at the task of matching the points (i.e., finding the correspondences), let's first give a brief answer to the following two questions in order to get a better understanding of the applications.

1. How can we find the points?
2. What criteria can be defined for matching?

For the first question, two different strategies are to be mentioned:

- *Predefined filters*: If we know what we search for, e.g., the outer shape of the object parts, we can incorporate these shapes in the design of special filters, which are applied to the image and yield high responses at positions where the image content fits to the filter design. If a filter is shifted pixel-by-pixel over the search area and the filter response is calculated at each position, these responses can be accumulated in a two-dimensional matching function. The local maxima of the matching function being above a certain threshold indicate occurrences of the searched object part and can be used as points to be matched. This proceeding is well suited for industrial object detection (or inspection) applications, where the object to be searched is known in advance. Hence, the filter can, e.g., be derived from CAD data.

- *Interest point detection*: A more generic proceeding is to search for the so-called keypoints (also called *interest points*), which are to be located at highly informative positions. For example, the so-called Harris detector [8] aims at detecting positions where the image intensity changes in both directions (x and y), i.e., there is a significant intensity gradient in x- as well as in y-direction. This happens to be true at corners of objects, for example. In contrast to such points, positions of uniform or slowly varying intensity only contain little information, as they are very similar compared to their neighbors. Positions with significant gradient in just one direction, e.g., at lines or edges, allow for accurate localization in just one direction (at which the gradient points to), but not perpendicular to it. For a more detailed introduction, the interested reader is referred to, e.g., [23] or [17].

As far as the matching criteria are concerned, there are two main approaches:

- *Spatial configuration*: If just the position of the points is available, we can evaluate which elements $\mathbf{p}_{2,n}$ of P_2 are spatially consistent to which elements $\mathbf{p}_{1,m}$ of P_1, i.e., the spatial configuration defined by the matched points of P_2 has to be similar to the one defined by their corresponding elements of P_1. What is meant to be "similar" depends on the type of transformation a point set undergoes between the first and the second image. For pure translations and Euclidean transformations, for example, the distances between the points within a set have to be preserved. Similarity transforms maintain the ratio of distances and so on.
- *Descriptors*: Here, the spatial position of the points is not the only source of information which can be used for matching. In addition to the spatial positions, it can be assumed that the appearance of a local image patch around one element $\mathbf{p}_{2,n}$ of P_2 has to be similar to the appearance around its corresponding element $\mathbf{p}_{1,m}$ of P_1. Therefore, an additional matching criterion can be defined by comparing the image data of local patches around two matching candidates. Please note that in many situations, we have to deal with effects like varying illumination conditions, small deformations, or appearance change due to change of viewpoint. Therefore, a comparison of the raw image data would lead to a quick decline of similarity in the presence of those effects. A better approach is to derive a feature vector $\mathbf{d}$ (which is also called *descriptor*) from the image data, which on the one hand remains its discriminative power and on the other hand is invariant to the types of variations typically expected. A well-known and widely used example is the *SIFT descriptor* suggested by Lowe [14], which partitions the patch into a small number

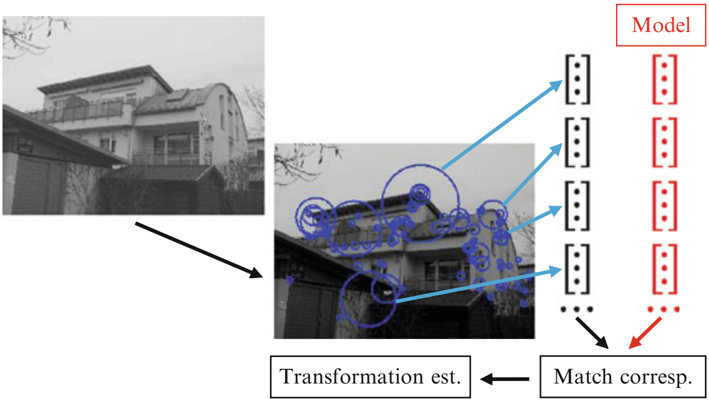

Fig. 5.1 Illustrating the proceeding suggested by Schmid and Mohr [21] in order to find correspondences: First, interest regions are detected (*middle part*, indicated by *blue circles*). Second, a descriptor is calculated for each interest region (*right part*), which can in turn be matched to some model or second data set (indicated by *red color*) (From Treiber [23], with kind permission from Springer Science and Business Media)

of cells and for each cell accumulates intensity gradient orientations into a 1D orientation histogram. The usage of intensity gradient orientations leads to a good invariance with respect to varying illumination, whereas the rather loose spatial binning into cells is quite robust to appearance changes due to change of perspective, e.g., viewpoint change (see e.g., [23] or [16] for a more detailed introduction).

In fact, the two-step paradigm of interest point detection (which concentrates on highly informative parts of the image), and subsequently using spatial configuration as well as descriptor information for finding the correct correspondences, has proven to be quite a powerful approach for generic object detection (see also Fig. 5.1). It was first introduced in [21], and in the meantime, many extensions/ variants have been reported in literature.

A rather simple and quite often used strategy for finding correspondences is to search for the nearest neighbor (NN) in descriptor space, i.e., for each $\mathbf{d}_{1,m}$ the descriptor $\mathbf{d}_{2,n}$ with highest similarity to $\mathbf{d}_{1,m}$ is selected. While being rather easy to implement, such a proceeding has two drawbacks: first, there might be a considerable number of outliers (i.e., incorrect correspondences) which introduce a gross error, because their spatial positions do not fit into the rest of the spatial distribution of point positions. Therefore, these outliers could seriously spoil a transformation estimation subsequent to matching (as done in image stitching applications, for example). Furthermore, the nearest neighbor search might not minimize the total error (especially if only one-to-one correspondences are allowed), because just the individual errors between descriptors of one correspondence are minimized. Instead, it could be better to match some point/descriptor to, e.g., its second closest NN, because the NN better matches to some other descriptor.

5.2 Heuristic: Search Tree

5.2.1 Main Idea

In the context of industrial object detection, the authors of [19] proposed a method which avoids the combinatorial explosion by accelerating the assignment of correspondences through the usage of a heuristic. To be more specific, the correspondences are assigned successively: just one correspondence is added at each step. In this context, a correspondence denotes a matching between a feature detected in a query image containing the object to be found and a feature being part of the object model.

In order to speed up the matching, knowledge about the matches already made is utilized for each new correspondence which is to be established. More specifically, it is possible to derive the parameters of an aligning transform between the two feature sets from the already matched features. Taking the estimated transform being based on the already matched features into account, a prediction about the position of a new matching candidate can be made. Please note that in general, industrial objects are very "rigid." This means that they show at most very little local deformations with respect to each other (at least if they are not defective). Due to the object rigidity, we can make a quite precise prediction of the expected position of the next feature to be matched. This leads to the selection of promising "candidates" at each matching step: we just have to consider the features which are located nearby the predicted position. As many possible correspondences can be sorted out this way, this proceeding usually results in a very fast matching.

This heuristic can be implemented by organizing the one-to-one correspondences already established between a model feature and a feature candidate of the scene image in a tree structure (c.f. the *search tree* approach proposed by Rummel and Beutel [19]). For a more detailed description, see also [23]. The rest of this section is a modified version of section 4.3.2 of [23].

Each node of this tree represents one correspondence. Two nodes are connected if they are spatially consistent. As already said, already established correspondences enable us to hypothesize an aligning transform for each node of the tree. Nodes (correspondences) are only connected to a specific node if their positions are consistent with this transform.

Starting from a root node, each level of the tree represents possible pairings for a single-specific model feature, i.e., the first level consists of the pairings containing model feature 1 (denoted as $f_{M,1}$, with position $\mathbf{p}_{M,1}$), the second level consists of the pairings containing model feature 2 (denoted as $f_{M,2}$, with position $\mathbf{p}_{M,2}$), and so on. This organization implies a ranking of the model features, which is defined prior to the recognition process. The ranking takes the ability of the features to reduce the uncertainty of the aligning transform estimation into account, e.g., features located far away from each other yield a more accurate rotation and scale estimate and therefore should get a high ranking. The search order is mainly geared to this ranking, as we will see shortly.

5.2.2 Recognition Phase

During recognition, this tree structure is built iteratively by expanding just one node (correspondence) at each iteration (see also Table 5.1 for an illustrative toy example). At start, the tree consists of a single root node. The root expanded by finding all possible correspondences for the first model feature$f_{M,1}$ ranked top in the search order. In some situations, we can restrict the position of matching candidates to some region; otherwise, we have to consider all features of the entire image plane. Each node $n_{k,1}$ of the first level of the tree represents one of these correspondences and can be seen as a hypothesis for the matching based on the correspondence between the model feature $f_{M,1}$ and some scene image feature $f_{S,k}$. Based on this matching hypothesis, information about the transformation parameters $\mathbf{t}$ can be derived.

Next, we try to expand the tree at one of the current leaf nodes by finding correspondences for the model feature $f_{M,2}$ ranked second. The position of the matching candidates can now be restricted based on the correspondence already established according to the node to be expanded as follows. Generally speaking, because of the model feature ranking, an edge between two nodes $n_{a,\mathrm{lv}}$ and $n_{b,\mathrm{lv}+1}$ can only be built between successive levels lv and $\mathrm{lv}+1$. Such an edge is established if the two correspondences are consistent. This is the case if the transformed position $T\left(\mathbf{t},\mathbf{p}_{M,\mathrm{lv}+1}\right)$ of the model feature being assigned to the "candidate node" (of level lv + 1) is located nearby the position $\mathbf{p}_{\mathrm{S},b}$ of the scene image feature of this candidate node. The transformation T used in this comparison is based on the current transform parameter estimates $\mathbf{t}$.

A bounded error model can be applied in the consistency check: for example, the deviation of the positions has to remain below a fixed threshold t_{d}:

$$\left\|\mathbf{p}_{\mathrm{S},b}-T\left(\mathbf{t},\mathbf{p}_{M,\mathrm{lv}+1}\right)\right\|\leq t_{\mathrm{d}} \tag{5.1}$$

Observe that it is possible that (5.1) holds for multiple features. Consequently, each node of level lv can be linked to multiple nodes of level lv + 1.

This process of expanding a single node by consistent correspondences can now be repeated iteratively. When expanding one node at a time, the topological structure resulting from this proceeding is a tree structure, where the number of levels equals the number of model features. From a node in the "bottom level" (which contains the "leafs" which define pairings for the lowest ranked model feature), the complete correspondence information for a consistent matching of all model features can be derived by tracking the tree back to the first level.

Up to now, an open question is how to choose the node to be expanded. A straightforward proceeding would be to choose one node by random, expand it, and repeat this proceeding until all leaf nodes are located in the bottom tree level relating to the model feature ranked lowest. However, please note that if we are interested in finding just one object instance, the tree doesn't have to be built completely. Instead, it suffices to proceed until one leaf node reaches the last level, because then one consistent set of correspondences for all model features is found. Therefore, it is most productive to select that node which is most likely to directly lead to a leaf node. This decision can be done with the help of a guide value g which is based on the quality value q of the node as well as the level number lv of the node:

$$g = w_q \cdot q + w_{\mathrm{lv}} \cdot \mathrm{lv} \tag{5.2}$$

The quality q should be a measure of consistency and can, e.g., be set to the inverse of the sum of the distances as defined in (5.1) over all correspondences encountered when tracing the current node under consideration back to the root node. Now we can select the node with the largest guide factor g.

With the help of the weighting factors w_q and w_{lv}, the search can be controlled: high w_q favors the selection of nodes at low lv (where q is usually higher because the deviations being accumulated when tracing back the path are usually smaller if just a few tree levels have to be considered). This leads to a mode complete construction of the tree, whereas high w_{lv} favors the selection of nodes at high lv and result in a rapid construction of "deep" branches.

The iteration proceeds until a leaf node with sufficient quality is found, e.g., $q \geq t_{\mathrm{r}}$, where t_{r} is the recognition quality threshold. As a result, only a part of the tree has to be built, and therefore the runtime is reduced considerably in most cases. In order to detect multiple instances of the object in a single image, a new tree can be reconstructed after all matched scene features are removed from the scene image feature set.

In the case of partial occlusion, no consistent pairings can be detected for the next level of some nodes. In order to compensate for this, a node $n_{e,\mathrm{lv}+1}$ containing the estimated position based on the current transformation can be added to the tree when no correspondence could be established. Its quality q is devalued by a predefined value (c.f. red node in the example of Table 5.1).

The overall recognition scheme in which the search tree is embedded can be characterized by four main steps (c.f. Fig. 5.2):

1. *Feature detection*: In the first step, all features $f_{\mathrm{S},k} = \left[\mathbf{p}_{\mathrm{S},k}, l_{\mathrm{S},k}\right]$ in a scene image are detected and summarized in the list $\mathbf{f}_{\mathrm{S}}$. Their data consists of the position $\mathbf{p}_{\mathrm{S},k}$ as well as a label $l_{\mathrm{S},k}$ indicating the feature type.
2. *Interpretation tree construction*: Based on the found feature candidates $\mathbf{f}_{\mathrm{S}}$ as well as the model features $\mathbf{f}_M$ the interpretation tree is built. As a result of the tree construction, correspondences for all model features have been established. This step is very robust in cases where additional feature candidates which cannot be matched to the model (e.g., originating from clutter) are detected. This robustness justifies the usage of a "simple" and fast method for feature detection, which possibly leads to a considerable number of false positives. Additionally, for many industrial applications the initial tolerances of rotation and scaling are rather small. A consideration of this fact often leads to a significant reduction of

Table 5.1 Tree search example showing the construction process of an interpretation tree consisting of five steps

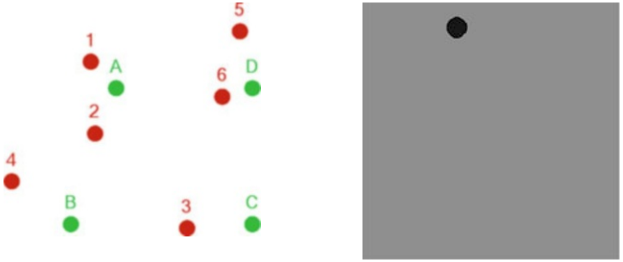 A scene image containing six features 1–6 (red) is to be matched to a model consisting of four features A–D (green). The search tree is initialized with an empty root node (black; right)	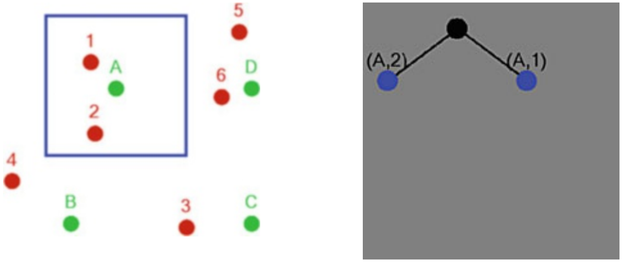 1 2 3 4 5 6 A B C D (A,2) (A,1) Based on a priori knowledge, the location of the first feature A can be limited to the blue region. As two image features are located within it, two correspondences are added to the tree
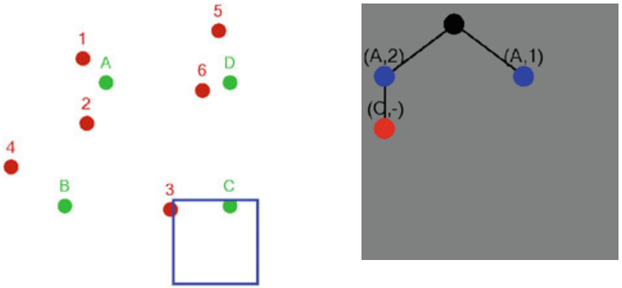 1 2 3 4 5 6 A B C D (A,2) (A,1) (C,-) Based on the guide factor, the (wrong) correspondence (A,2) is chosen to be further processed. A new ROI for searching correspondences to feature C can be derived (blue region). As no scene image feature is located within that ROI, the new node is only an "estimation node" (red)	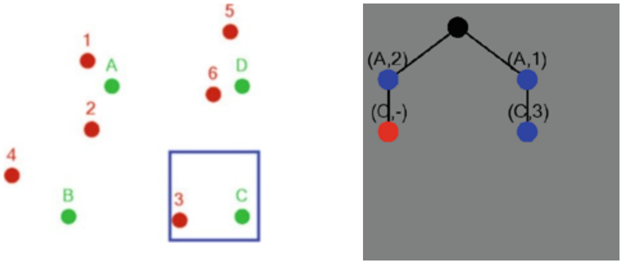 1 2 3 4 5 6 A B C D (A,2) (A,1) (C,-) (C,3) As the quality of the red node is devalued, the node (A,1) is processed next. A new correspondence (C,3) is found and inserted into the tree

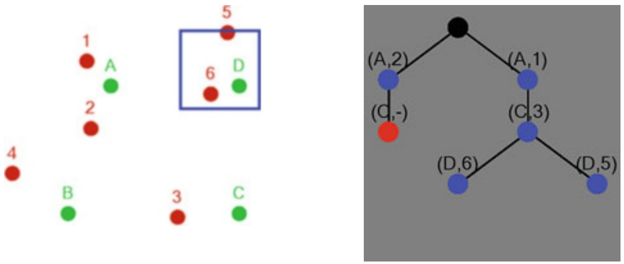 1 A 2 4 B 5 6 D 3 C (A,2) (A,1) (C,-) (C,3) (D,6) (D,5)	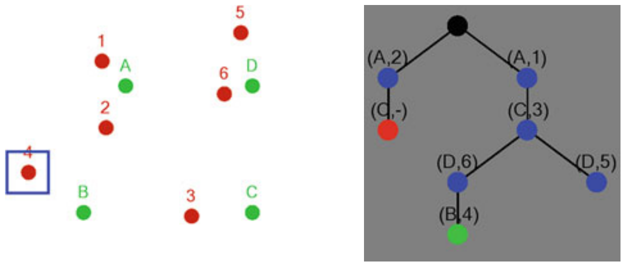 1 A 2 4 B 5 6 D 3 C (A,2) (A,1) (C,-) (C,3) (D,6) (D,5) (B,4)
In the next step, node (C,3) is expanded. The size of the search region (blue) can be reduced as the position estimate becomes more accurate. Two correspondences are found and added to the tree	In the next step, the ROI size can be reduced further, and a correspondence for last model feature of the search order (B) is found. Hence, a complete solution is available (green node). An accurate position estimation based on the found correspondences is also possible

From Treiber [23], with kind permission from Springer Science and Business Media

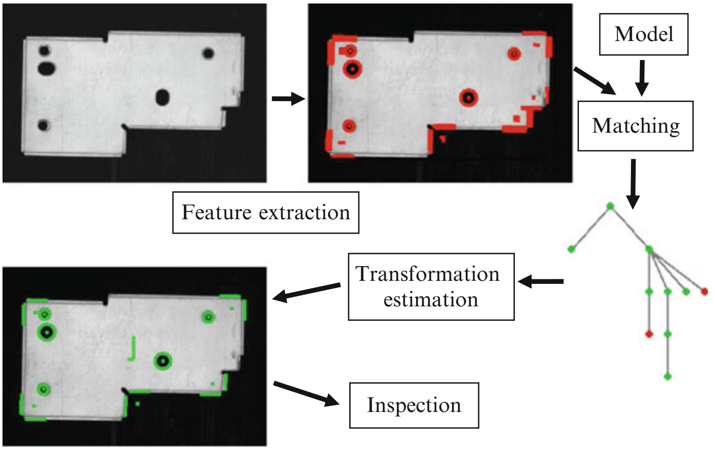

Fig. 5.2 Illustrating the proceeding of object detection with interpretation trees for a stamped sheet as a typical example for an industrial part (From Treiber [23], with kind permission from Springer Science and Business Media)

possible correspondences, too, because the search areas (blue regions in Table 5.1) can be kept rather small.

3. *Transformation estimation*: The parameters **t** of the transformation T (e.g., the four parameters translation $\left[t_x, t_y\right]$, rotation θ, and scale s of a similarity transform) are estimated with the help of the found correspondences.
4. *Inspection* (optional): Based on the detected features, it is often easy to decide whether the part has been manufactured with sufficient quality. For example, it could be checked whether the position of a drilling, which can easily be represented by a specific feature, is within its tolerances.

Pseudocode

```
function detectObjectPosInterpretationTree (in Image $I$, in ordered list $\mathbf{f}_M$ of model features $f_{M,i} = \left[\mathbf{p}_{M,i}, l_{M,i}\right]$, in distance threshold $t_d$, in recognition threshold $t_r$, out object position list $\mathbf{p}^*$)

// step 1: feature detection
detect all feature candidates $f_{S,k} = \left[\mathbf{p}_{S,k}, l_{S,k}\right]$ in scene image $I$ and arrange them in list $\mathbf{f}_S$
while $\mathbf{f}_S$ is not empty do // loop for multiple obj. detection
    init of tree $st$ with empty root node $n_{root}$; set its quality value $q_{root}$ to maximum quality
    bFound ← FALSE
    // step 2: search tree construction (loop for detection of a single object instance)
    $lv \leftarrow 0$
```

```
while unprocessed nodes exist in $st$ and bFound == FALSE do
  // expand interpretation tree at one candidate node
  choose the next unprocessed node $n_{i,lv}$ from $st$ with highest guide value $g$ (according to (5.2)) // this node becomes the candidate node of current iteration
  get next model feature $f_{M,lv+1}$ to be matched according to level $lv$ and model feature ranking
  update transformation parameters $\mathbf{t}$ according to all matched nodes of current path from root to $n_{i,lv}$
  calculate position estimate $T(\mathbf{t}, \mathbf{p}_{M,lv+1})$
  find all correspondences between elements of $\mathbf{f}_S$ and $f_{M,lv+1}$ ($f_{S,k}$ must be near $T(\mathbf{t}, \mathbf{p}_{M,lv+1})$, see (5.1), and features must be of the same type, i.e. $l_{S,k} = l_{M,lv+1}$) and arrange them in list $\mathbf{c}$
  if list $\mathbf{c}$ is not empty then
    for k = 1 to number of found new correspondences
      create new node $n_{k,lv+1}$ based on current $c_k$
      calculate quality value $q_k$ of $n_{k,lv+1}$
      if $q_k \geq t_r$ then
        mark $n_{k,lv+1}$ as unprocessed
      else
        mark $n_{k,lv+1}$ as processed  // expansion useless
      end if
      add $n_{k,lv+1}$to $st$ as child node of $n_{i,lv}$
    next
  else   // no match/correspondence could be found
    create new "estimation node" $n_{e,lv+1}$
    calculate quality value $q_e$ of $n_{e,lv+1}$
    if $q_e \geq t_r$ then
      mark $n_{e,lv+1}$ as unprocessed
    else
      mark $n_{e,lv+1}$ as processed   // expansion useless
    end if
    add $n_{e,lv+1}$ to $st$ as child node of $n_{i,lv}$
  end if
  mark node $n_{i,lv}$ as processed
  // are all model features matched?
  if $f_{M,lv+1}$ is last feature of search order then
    mark all "new nodes" $n_{k,lv+1}$ as processed
    find node $n_{goal}$ with highest qual. $q_{\max}$ among $n_{k,lv+1}$
    if $q_{\max} \geq t_r$ then
        bFound ← TRUE
    end if
  end if
```

```
        $lv \leftarrow lv + 1$
    end while
    if bFound = TRUE then
        // step 3: transformation estimation
        collect all correspondences by tracking the tree back
        from $n_{goal}$ to $n_{root}$
        estimate the parameters $\mathbf{t}^*$ of $T$ by performing minimiza-
        tion of position deviations for all correspondences
        add $\mathbf{t}^*$ to position list $\mathbf{p}^*$
        remove all matched features from list $\mathbf{f}_S$
    else
        return    // no more object instance could be found
    end if
end while
```

5.2.3 Example

An example of recognizing industrial parts like stamped sheets is presented in Table 5.2. The objects are recognized by utilizing different parts of their contour as features to be matched. Please observe that correct correspondences are found even in scenes with a significant amount of clutter.

Please note that the method is much more robust with respect to clutter (when trying to expand the tree at a node that is based on a correspondence originating from clutter, there is no consistent correspondence very quickly) compared to occlusion (disadvantageous trees are possible especially if the first correspondences to be evaluated don't exist because of occlusion).

To sum it up, interpretation trees are well suited for industrial applications, because the method is relatively fast, an additional inspection task fits well to the method, and we can concentrate on detecting characteristic details of the objects. On the other hand, the rigid object model is prohibitive for objects with considerable variations in shape.

5.3 Iterative Closest Point (ICP)

5.3.1 Standard Scheme

Another algorithmic concept which deals with the task of the registration of a data point set $P_D = \{\mathbf{p}_{D,i}\}; 1 \leq i \leq N_D$ to a set of model points $P_M = \left\{\mathbf{p}_{M,j}\right\}; 1 \leq j \leq N_M$ is the *Iterative Closest Point* algorithm (ICP). As the method provides a framework, it can be adapted to and used in various applications. Both the

Table 5.2 Giving more detailed information about the detection and position measurement of stamped sheets, which are a typical example of industrial parts

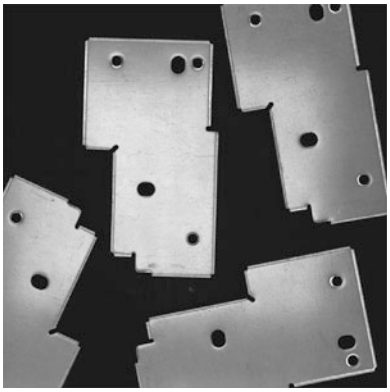 Scene image containing several stamped sheets. Due to specular reflections, the brightness of the planar surface is not uniform. One object is completely visible and shown in the upper-left area	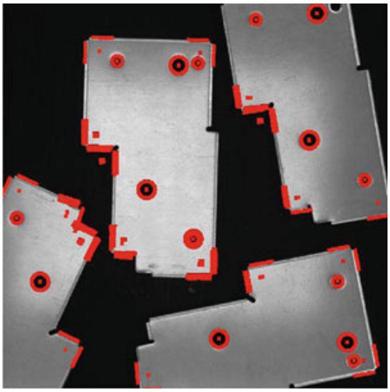 View of all detected features (marked red). The object model consists of the holes and some corners, which are detected independently. Several additional features are detected due to clutter
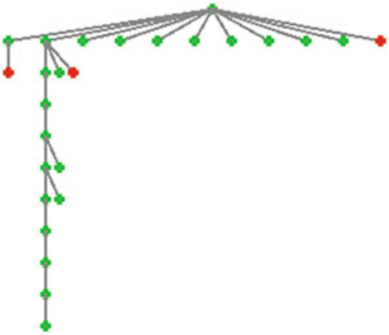 Interpretation tree: found correspondences are marked green; estimated correspondences are marked red. Due to clutter, many correspondences are found for the first feature of the search order. However, the search is very efficient, e.g., the solution is almost unique after the third level	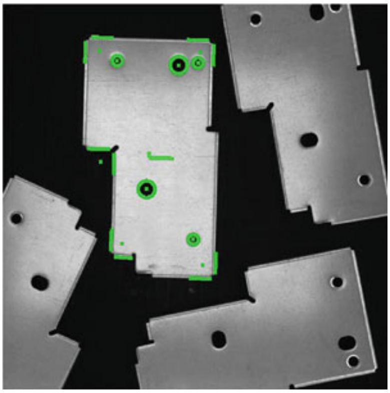 Matched features of the final solution of the tree (marked green). All correspondences are established correctly. An inspection step, e.g., for the holes, could follow

From Treiber [23], with kind permission from Springer Science and Business Media

registration of 2D and 3D point sets is possible with ICP. The basic form of the algorithm was initially proposed in [2].

The goal of registration is to find a common coordinate reference frame for both point sets and hence identify a transformation between the two sets. Consequently, the task is twofold:

- Establish the correct correspondences between the elements of P_D and P_M. In this context, this means that for each element i of the data point set, it should be matched to the "closest" model point j, where the function $j = \phi(i)$ describes the mapping.

- Estimate the parameters $\mathbf{t}$ of a transformation T, which describes the relationship between the two coordinate frames.

Now let's assume that some correspondences have been found already (i.e., a first estimate of ϕ is known). This is a reasonable assumption for some applications, e.g., initial correspondences could be estimated by matching descriptors. Then, a typical way to estimate the parameter vector $\mathbf{t}$ is to minimize an energy function $E(\mathbf{t}, \phi)$ being composed of the sum of squared distances between the positions of the transformed data points $\mathbf{p}_{D,i}$ and the positions of their corresponding model points $\mathbf{p}_{M,\phi(i)}$:

$$\mathbf{t}^* = \arg\min_{\mathbf{t}} [E(\mathbf{t}, \phi)] = \arg\min_{\mathbf{t}} \left[\sum_{i=1}^{N_D} \left\| \mathbf{p}_{M,\phi(i)} - T\left(\mathbf{t}, \mathbf{p}_{D,i}\right) \right\|^2 \right] \tag{5.3}$$

As ϕ has to be estimated in the optimization process, too, the energy $E(\mathbf{t}, \phi)$ can be reformulated as

$$E(\mathbf{t}) = \sum_{i=1}^{N_D} \min_j \left\| \mathbf{p}_{M,j} - T\left(\mathbf{t}, \mathbf{p}_{D,i}\right) \right\|^2 \tag{5.4}$$

where the min-operator selects that model point being located closest to a specific data point $\mathbf{p}_{D,i}$. Observe that the min-operator prohibits a straightforward closed form solution of (5.4). Therefore, the optimization of (5.4) is done iteratively, where two steps are performed in alternation. Starting at an initial transformation estimation $\mathbf{t}^0$, the following two steps are executed iteratively:

1. *Correspondence estimation*: While fixing the current transformation $\mathbf{t}^k$, for each data point, find the model point, which is located closest to the position of this data point after application of the current transformation estimation $\mathbf{t}^k$, i.e., for each data point $\mathbf{p}_{D,i}$ apply

$$\phi^k(i) = \arg\min_{j \in P_M} \left\| \mathbf{p}_{M,j} - T\left(\mathbf{t}^k, \mathbf{p}_{D,i}\right) \right\|^2 \tag{5.5}$$

2. *Transformation estimation*: Now, as ϕ^k is known, we can solve the following least mean squares problem in closed form, e.g., for linear transformations by applying linear regression:

$$\mathbf{t}^{k+1} = \arg\min_{\mathbf{t}} \sum_{i=1}^{N_D} \left\| \mathbf{p}_{M,\phi^k(i)} - T\left(\mathbf{t}^k, \mathbf{p}_{D,i}\right) \right\|^2 \tag{5.6}$$

The convergence criterion is quite obvious: if the correspondences ϕ^k don't change any more compared to the previous iteration, we will end up with an

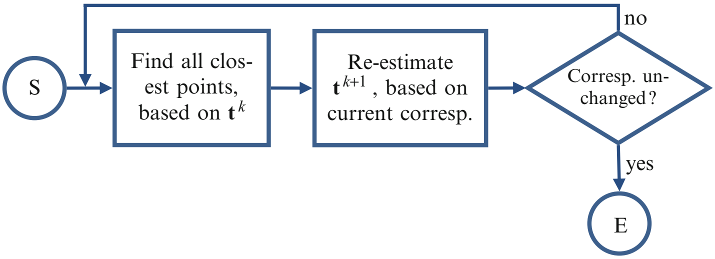
S
Find all closest points, based on $\mathbf{t}^k$
Re-estimate $\mathbf{t}^{k+1}$, based on current corresp.
Corresp. unchanged?
no
yes
E

Fig. 5.3 Flowchart of the ICP proceeding

unchanged transformation estimate, too. Consequently, the method has converged. An overview of the proceeding is given in the flowchart of Fig. 5.3.

The iterative nature implies that the ICP algorithm performs a local search around the current estimate. However, typically we cannot assume that $E(\mathbf{t})$ is convex. Therefore, we are in danger of being "trapped" in a local minimum if the initial estimate $\mathbf{t}^0$ is located too far from the global optimum. For that reason ICP is basically just a refinement scheme, i.e., it requires some reasonably good initial estimate, e.g., by evaluating descriptor information. In some cases, the method can start without any prior knowledge by taking the identity transform as starting point. However, this only works if the two point sets already are aligned sufficiently well at start.

A possible way out would be to perform the ICP algorithm multiple times with different initial transformations and select that solution yielding the lowest energy at convergence. However, this proceeding increases the runtime of the algorithm considerably and still we cannot be sure that one of the initial estimates is sufficiently close to the optimum.

5.3.2 Example: Robust Registration

In order to enlarge the limited convergence area of the standard ICP algorithm and thereby increase its robustness, many modifications have been proposed. Here we will present the work of Fitzgibbon (see [7]) in more detail. Fitzgibbon proposed to replace the Euclidean-based distance measure in (5.4) by a more robust estimate. However, the introduction of a robust distance measure involves difficulties when trying to estimate the transformation parameters in step 2 of ICP in closed form. Therefore, in [7] it is suggested to utilize a general purpose regression scheme like the Levenberg-Marquardt algorithm [15] instead. Consequently, we take a closer look how the Levenberg-Marquardt algorithm can be applied to this specific problem.

A first step to increase the robustness of ICP is to allow for unmatched points. Consider the situation where a point $\mathbf{p}_{D,i}$ in the data point set is present due to clutter and actually doesn't have a correspondence in the model point set. This situation occurs quite often in practice. However, standard ICP as presented above *always*

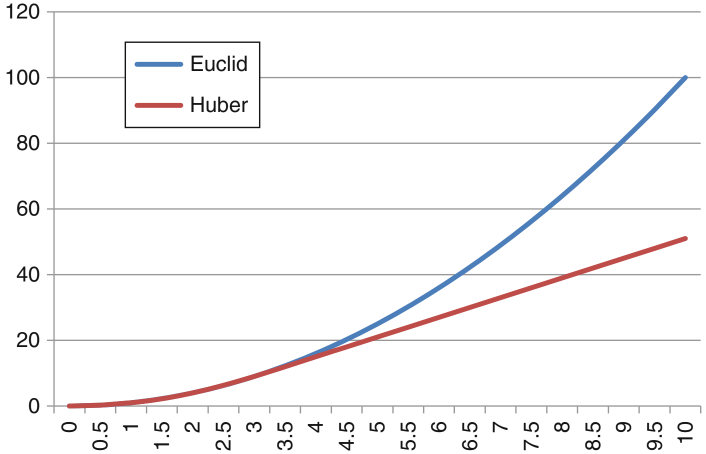

Fig. 5.4 Comparison of the Euclidean distance measure with the Huber kernel: the x-axis denotes the distance $\|\mathbf{x}\|$, and σ is set to 3

matches every data point to some model point. This could lead to a large distance for $\mathbf{p}_{D,i}$, and therefore, the (wrong) correspondence introduces a large error in (5.4).

This situation can be alleviated by introducing weights $w_i \in \{0; 1\}$ in step 2 of ICP. A weight w_i is set to zero if no correspondence could be found for $\mathbf{p}_{D,i}$, e.g., when its transformed position is too far away from any model point. If a correspondence was found, w_i is set to 1.

The main contribution Fitzgibbon [7] in order to increase robustness, however, is to replace the Euclidean-based distance $\left\|\mathbf{p}_{M,\phi(i)} - T\left(\mathbf{t}, \mathbf{p}_{D,i}\right)\right\|^2$ (abbreviated as $\|\mathbf{x}\|^2$ in the following) by a more robust measure $\varepsilon(\mathbf{x})^2$, such as the so-called Huber kernel:

$$\varepsilon(\mathbf{x})^2 = \begin{cases} \|\mathbf{x}\|^2 & \|\mathbf{x}\| < \sigma \\ 2\sigma\|\mathbf{x}\| - \sigma^2 & \text{otherwise} \end{cases} \tag{5.7}$$

Compared to the Euclidean distance measure, the Huber kernel takes smaller values for large distances, i.e., when $\|\mathbf{x}\| > \sigma$ (see Fig. 5.4, with $\sigma = 3$). As a consequence, the influence of large distances in (5.6) is reduced.

As can be seen in Fig. 5.5, the area of convergence can be increased considerably through the usage of the Huber kernel compared to standard ICP (compare the green to the light blue curve). The left part of the figure depicts an application where two 2D curves (black and blue dots) are to be aligned. For the tests, the lower right "C" has been rotated synthetically prior to matching it to the upper-left "C." In the diagram at the right, the x-axis denotes the rotation difference between the initial transformation estimation and the actual rotation between the two point sets in degrees, and the y-axis plots some error measure after the algorithm has converged. As clearly can be seen, the introduction of the Huber kernel allows for far larger errors in the initial

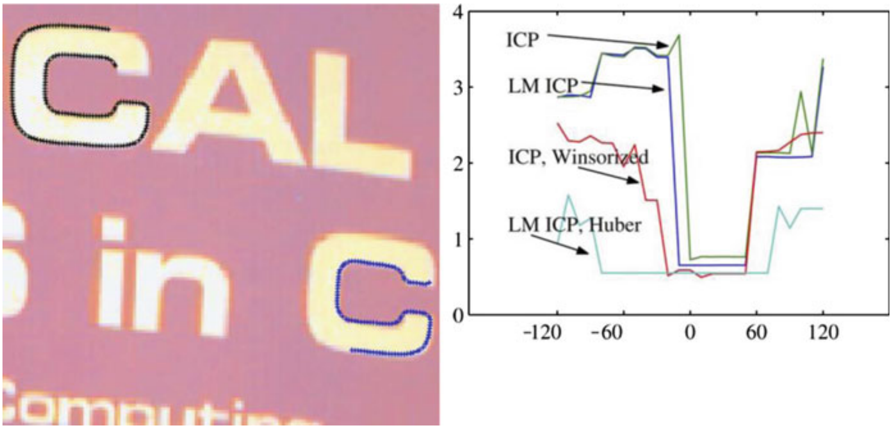

Fig. 5.5 Illustrating the improved area of convergence, when the robust Huber kernel is used (as far as rotation deviations are concerned) (Reprinted from Fitzgibbon [7], with permission from Elsevier)

rotation estimate as it leads to smaller total errors after convergence for a larger rotation deviation range.

The problem which is involved with the usage of the Huber kernel is that now the solution of the transformation estimation (step 2 of ICP) in closed form is complicated by the case-by-case analysis in (5.7). As a consequence, the minimization problem in the transformation step has to be solved numerically. Here we can make use of the fact that the total error measure is a sum of squared contributions $E_i(\mathbf{t})$ from the individual correspondences, which can be stacked into a vector $\mathbf{e}$:

$$\begin{aligned} E(\mathbf{t}) &= \sum_{i=1}^{N_D} E_i(\mathbf{t})^2 = \mathbf{e}^T \cdot \mathbf{e} \\ \text{with} \quad E_i(\mathbf{t}) &= \sqrt{w_i} \cdot \min_j \varepsilon\Big(\big|\mathbf{p}_{M,j} - T\big(\mathbf{t}, \mathbf{p}_{D,i}\big)\big|\Big) \end{aligned} \tag{5.8}$$

Through approximating (5.8) by a Taylor expansion around the current transformation estimate $\mathbf{t}^k$, applying a Gauss-Newton approximation (approximate the second order derivatives with the Jacobi matrix) and making use of the vector $\mathbf{e}$, we can write

$$E\big(\mathbf{t}^k + \Delta\big) \approx \mathbf{e}^T \cdot \mathbf{e} + 2 \cdot \Delta \cdot \mathbf{J}^T \cdot \mathbf{e} + \Delta^T \cdot \mathbf{J}^T \cdot \mathbf{J} \cdot \Delta \tag{5.9}$$

where the Δ vector denotes the transformation parameter differences with respect to $\mathbf{t}^k$ and Jacobi-Matrix $\mathbf{J}$ contains the partial first-order derivatives of the $E_i(\mathbf{t})$. It consists of $N_D \times L$ elements (L is the number of transformation parameters), which can be calculated via $J_{il} = \partial E_i\big(\mathbf{t}^k\big)/\partial t_l$.

An iterative optimization scheme can now estimate the Δ vector and then update the current transformation estimate accordingly: $\mathbf{t}^{k+1} = \mathbf{t}^{k} + \Delta$.

Fitzgibbon suggested to use the Levenberg-Marquardt optimization algorithm, which combines updates according to Gauss-Newton as well as gradient descent (see Chap. 2). With Gauss-Newton, Δ is set to $\Delta = -\left(\mathbf{J}^{T} \cdot \mathbf{J}\right)^{-1} \cdot \mathbf{J} \cdot \mathbf{e}$, whereas with gradient descent, we have $\Delta = -\lambda^{-1} \cdot \mathbf{J}^{T} \cdot \mathbf{e}$. Overall, the update of LM can be written as

$$\begin{aligned} \Delta &= -\left(\mathbf{J}^{T} \cdot \mathbf{J} + \lambda \cdot \mathbf{I}\right)^{-1} \cdot \mathbf{J} \cdot \mathbf{e} \\ \mathbf{t}^{k+1} &= \mathbf{t}^{k} + \Delta \end{aligned} \tag{5.10}$$

with $\mathbf{I}$ being the identity matrix. At each iteration of the second step of the modified ICP algorithm, one update step according to LM (see (5.10)) is performed. In order for LM algorithms to perform well, the parameter λ, which controls the relative weight of Gauss-Newton and gradient descent, has to be chosen sufficiently well. In early steps, λ is chosen large, such that the gradient descent dominates. Thereby, the method takes small steps, where we can be quite sure that the error function is actually reduced. As the iteration proceeds, λ is reduced successively, which gives more emphasis to Gauss-Newton, because it can be assumed that the Taylor approximation used in Gauss-Newton has little error near the optimum, and, therefore, we can make use of the fast convergence of Gauss-Newton.

One question still to be answered is how to calculate the elements J_{il} of the Jacobi matrix, which involve taking derivatives of $E_i(\mathbf{t})$. A numerical approach is to take finite differences, i.e., at the current transformation estimate $\mathbf{t}^{k}$, we calculate $E_i\left(\mathbf{t}^{k}\right)$, modify $\mathbf{t}^{k}$ by an arbitrarily chosen small amount $\delta\mathbf{t}^{k}$, calculate $E_i\left(\mathbf{t}^{k} + \delta\mathbf{t}^{k}\right)$, and take the difference to $E_i\left(\mathbf{t}^{k}\right)$. The author of [7] pointed out the importance of reestimating the correspondences when moving from $\mathbf{t}^{k}$ to $\mathbf{t}^{k} + \delta\mathbf{t}^{k}$. Hence, each $J_{il} = \partial E_i\left(\mathbf{t}^{k}\right)/\partial t_l$ can be calculated as follows:

1. calculate $E_i\left(\mathbf{t}^{k}\right)$, based on the current closest point of the model point set $\mathbf{p}_{M,\phi^{k}(i)}$, which was determined during step one of ICP.
2. Choose a small $\delta\mathbf{t}^{k}$ (where only the l-th component is different from zero) and reestimate the closest model point (yielding $\mathbf{p}'_{M,\phi^{k}(i)}$), based on the modified transformation $\mathbf{t}^{k} + \delta\mathbf{t}^{k}$. Please note that this correspondence could change as we move from $\mathbf{t}^{k}$ to $\mathbf{t}^{k} + \delta\mathbf{t}^{k}$.
3. calculate $E_i\left(\mathbf{t}^{k} + \delta\mathbf{t}^{k}\right)$, based on the (potentially) updated $\mathbf{p}'_{M,\phi^{k}(i)}$
4. set $J_{il} = \left(E_i\left(\mathbf{t}^{k}\right) - E_i\left(\mathbf{t}^{k} + \delta\mathbf{t}^{k}\right)\right)/\left\|\delta\mathbf{t}^{k}\right\|$

The usage of the robust measure $\varepsilon(\mathbf{x})$ in conjunction with the LM algorithm leads to better performance but at the same time to increased execution time, as the calculation of the derivatives needs extra time. Therefore, Fitzgibbon suggested a speedup of the algorithm through the usage of a so-called distance transform, which

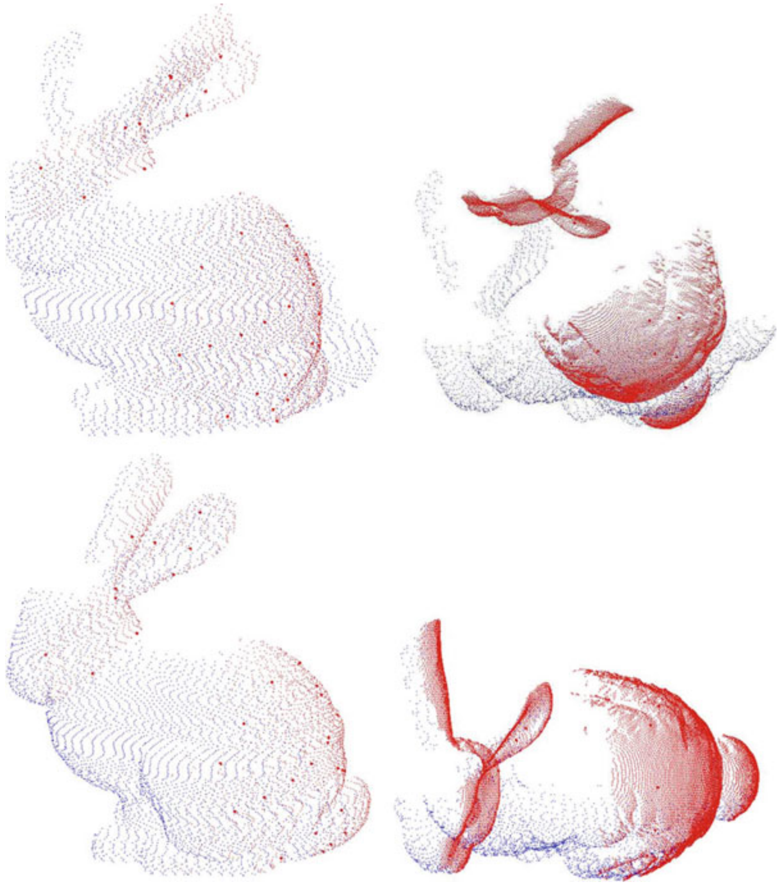

Fig. 5.6 Showing the performance gain of the algorithm of [7] (*bottom*), compared to standard ICP (*top*). In this application, two sets of 3D points located on the surface of a bunny (*blue* and *red points*) are to be aligned (Reprinted from Fitzgibbon [7], with permission from Elsevier)

exploits the fact that the penalties of transformed data points, compared to their closest model points depend only on the model point set for a given data point position. Consequently, they can be calculated prior to the ICP iterations and be reused for different data points $\mathbf{p}_{D,i}$ and transformations $\mathbf{t}$ (see [7] for details).

Figure 5.6 illustrates the superior performance of the modified algorithm as suggested in [7] compared to standard ICP for 3D point sets. The point sets which are to be aligned consist of points located on the surface of a bunny. The standard ICP method, whose result is displayed in the right part of the top row, clearly shows considerable deformations between model and transformed data point sets. Compared to this, the two sets are aligned much better when the algorithm of [7] is used.

Pseudocode

```
function robustICPRegistration (in data point set $P_D = \{\mathbf{p}_{D,i}\}$,
in model point set $P_M = \{\mathbf{p}_{M,j}\}$, in initial transformation
estimate $\mathbf{t}^0$, in maximum correspondence distance $d_{\max}$, out
correspondences $\phi^*$, out final transformation estimate $\mathbf{t}^*$

$k \leftarrow 0$
// main loop of ICP
repeat
   // step 1: find closest point for each data point
   for $i = 1$ to $N_D$
      $d_{i,\min} \leftarrow$ max_float
      for $j = 1$ to $N_M$
         $d_{ij} = \|\mathbf{p}_{M,j} - T(\mathbf{t}^k, \mathbf{p}_{D,i})\|$
         // do we have a new closest point candidate?
         if $d_{ij} < d_{i,\min}$ then
            $d_{i,\min} \leftarrow d_{ij}$
            $\phi^k(i) \leftarrow j$
         end if
         if $d_{ij} > d_{\max}$ then
            $w_i \leftarrow 0$  // max. distance exceeded -> no corresp.
         else
            $w_i \leftarrow 1$ // distance limit ok
         end if
      next
   next
   // step 2: update transformation parameters
   // calculate Jacobi matrix
   for $i = 1$ to $N_D$
      calculate $E_i(\mathbf{t}^k)$ according to (5.8)
      for $l = 1$ to $L$     // L: number of transformation params
         set $\delta\mathbf{t}^k = [0, 0, \ldots, \delta, 0, \ldots, 0]$ // only lth elem $\neq 0$
         re-estimate correspondence $\phi^k(i)'$
         calculate $E_i(\mathbf{t}^k + \delta\mathbf{t}^k)$ based on $\phi^k(i)'$ according to (5.8)
         set $J_{il} = (E_i(\mathbf{t}^k) - E_i(\mathbf{t}^k + \delta\mathbf{t}^k)) / \|\delta\mathbf{t}^k\|$
      next
   next
   update $\lambda$
   calculate $\Delta$ and update transformation estimate $\mathbf{t}^{k+1}$
   according to (5.10)
   $k \leftarrow k + 1$
until convergence, e.g. $\phi^{k+1} = \phi^k$ or $(E(\mathbf{t}^{k+1}) - E(\mathbf{t}^k)) / (E(\mathbf{t}^{k+1})$
$+E(\mathbf{t}^k)) \leq \delta$
$\mathbf{t}^* \leftarrow \mathbf{t}^k$
$\phi^* \leftarrow \phi^k$
```

5.4 Random Sample Consensus (RANSAC)

Considering the task of image registration, where we have to align two (or more) images which at least partly overlap, we can detect a set of interest points in both images ($P_1 = \left\{\mathbf{p}_{1,m}\,; m \in [1, \ldots, M]\right\}$ and $P_2 = \left\{\mathbf{p}_{2,n}\,; n \in [1, \ldots, N]\right\}$). We could then use the ICP algorithm which performs an iterative refinement of the correspondences as well as the transformation estimate between the two point sets. However, in order to work properly, the ICP algorithm needs a sufficiently well chosen initial estimate of the transformation, which allows the algorithm to converge to the desired optimum.

Additional information can be obtained if we derive descriptors from a local image patch around each interest point, e.g., by calculating SIFT descriptors [14]. This adds up to two sets of descriptors $D_1 = \left\{\mathbf{d}_{1,m}\right\}$ and $D_2 = \left\{\mathbf{d}_{2,n}\right\}$. As already mentioned, we can make use of this descriptor information in order to get a sufficiently "good" initial estimate of the aligning transform and then apply the ICP algorithm. A straightforward approach would be:

1. Detect the set of interest points P_1 and P_2 in both images, e.g., by detecting corner-like points with the Harris detector [8].
2. Derive a descriptor from the image patch around each interest point yielding the descriptor sets D_1 and D_2, e.g., SIFT [14].
3. Establish correspondences $n = \phi(m)$ between the elements of D_1 and the elements of D_2 yielding the correspondence set Φ. A correspondence is established if $f_{\text{sim}}\left(\mathbf{d}_{1,m}, \mathbf{d}_{2,n}\right) \geq t_{\text{sim}}$, where f_{sim} is some measure estimating the similarity between the two descriptors (e.g., the inverse of the Earth Mover's Distance or χ^2 distance; see e.g., [18]) and t_{sim} a similarity threshold.
4. Estimate the parameters $\mathbf{t}$ of the transformation T between the two images, e.g., by a least squares approach, which minimizes the sum of the distances between $\mathbf{p}_{1,m}$ and $T\left(\mathbf{t}, \mathbf{p}_{2,\phi(m)}\right)$.
5. Refine ϕ and $\mathbf{t}$ with the ICP algorithm.

The problem with this proceeding is that *all* correspondences are taken into account when estimating the transform parameters. Wrong correspondence estimates usually introduce gross errors and therefore can seriously spoil the transformation estimation. Averaging methods like least squares (which is optimal for Gaussian-distributed errors) assume that the maximum error between the "observation" (here: $\mathbf{p}_{1,m}$) and the "model" (here: $T\left(\mathbf{t}, \mathbf{p}_{2,\phi(m)}\right)$) is related to the size of the data set, and, therefore, averaging can successfully smooth large errors (this assumption is termed *smoothness assumption* in literature).

However, this doesn't have to be true here: a few wrongly estimated correspondences lead to some large error terms being far from the distribution of

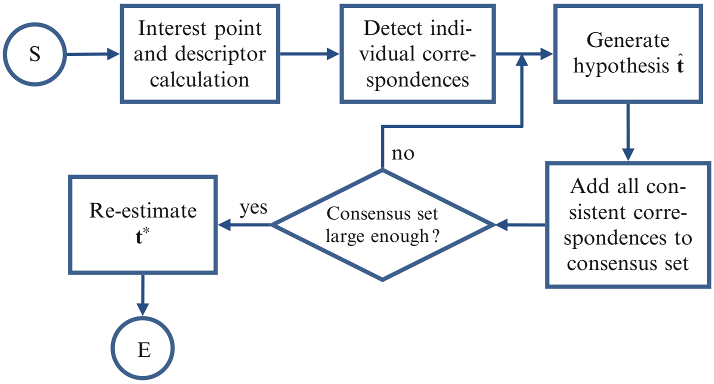
S
Interest point and descriptor calculation
Detect individual correspondences
Generate hypothesis $\hat{\mathbf{t}}$
Add all consistent correspondences to consensus set
Consensus set large enough?
no
yes
Re-estimate $\mathbf{t}^*$
E

Fig. 5.7 Flowchart of the RANSAC proceeding

the remaining errors. This is where RANSAC (*Ran*dom *Sa*mple *C*onsensus) [6] comes into play. The RANSAC proceeding is more a paradigm than a specific algorithm. It can also be used for the problem of image registration, and, therefore, we will present RANSAC in this context.

Fisher et al. [6] distinguish between two sources of error:

- *Measurement error*: This type of error is introduced when measuring the data, e.g., when the measured position of an interest point deviates a bit from its "true" position, e.g., due to sensor noise. Many sources of noise or other perturbations are normally distributed, and, therefore, usually the smoothness assumption holds for this type of errors.
- *Classification error*: Many algorithms feature a hard decision, which in our case is the assignment of correspondences. Errors like the estimation of a wrong correspondence (which can occur if many descriptors are very similar) can introduce large deviations and are in general not related to the data set size. Therefore, the smoothness assumption does *not* hold for this type of error.

As a consequence, we need a method which is robust in the sense that it features a mechanism which automatically *ignores* gross errors and not just tries to *average* them out. The RANSAC approach exactly aims at achieving this. It is designed such that it tolerates as many outliers as possible. The basic proceeding after estimating the correspondences (step 3 of the procedure outlined above) is as follows (see also the flowchart of Fig. 5.7):

4. *Random selection*: Randomly select a subset of the data (here: a subset Φ_R of all found correspondences). The size of this subset should be as small as possible. For example, for affine transformations in 2D, only three points are necessary in order to uniquely determine the six transformation parameters. Therefore, only three correspondences should be chosen at this step.

5. *Model instantiation*: Based on this subset, a first instance of the model should be derived. In our case, the transformation parameters $\hat{\mathbf{t}}$ can be calculated completely based on the selected correspondences.
6. *Consistency check*: Based on the initial model estimation (here: transformation estimation $\hat{\mathbf{t}}$), we can check all data (correspondences) whether they are consistent with this initial estimation. This mean here that the transformed position $T\left(\hat{\mathbf{t}}, \mathbf{p}_{2,\phi(m)}\right)$ has to be sufficiently close to $\mathbf{p}_{1,m}$: if $\left|T\left(\hat{\mathbf{t}}, \mathbf{p}_{2,\phi(m)}\right) - \mathbf{p}_{1,m}\right| \leq \varepsilon$, the correspondence $n = \phi(m)$ is added to the subset Φ_{R} (also called *consensus set*).
7. *Termination check*: If the size of the enlarged consensus set is above some threshold t_{size}, it can be assumed that only inliers were chosen as initial consensus set, and, therefore, the transformation estimate is broadly supported by the data. Therefore, the final transformation parameters $\mathbf{t}^*$ are reestimated based on the enlarged consensus set. If t_{size} is not reached, the process is restarted at step 4 until the maximum number of trials $N_{\max}$ is reached.

Observe that RANSAC fundamentally differs from the schemes up to now. Whereas methods like ICP, for example, try to *optimize* a current solution in some form, RANSAC is essentially a *hypothesis testing* scheme: basically, step 4 formulates a hypothesis about the solution, which is then tested for consistency with the rest of the data.

The RANSAC proceeding contains three parameters, (ε, t_{size} , and $N_{\max}$), whose values have to be chosen properly in advance. As far as ε is concerned, it is often determined empirically. To this end, a scenario with known correspondences can be created. Next, the data set is artificially corrupted by noise. Based on the errors which were introduced, the transformation estimation is affected more or less seriously. As we also know the "ground truth," it is possible to quantify the error introduced by the perturbation. Based on this quantification it should be possible to choose ε such that it separates correct from wrong correspondence estimates sufficiently well.

In contrast to that, the parameters t_{size} and $N_{\max}$ can be calculated in closed form. They are mainly influenced by the proportion of outliers as well as the desired probability that at least one random pick exclusively contains inliers. Details can be found in [6].

An illustration of the performance of a RANSAC-based correspondence/transformation estimation can be seen in Fig. 5.8. Here, two images of the same scene taken from different viewpoints can be seen in (a) and (b). The yellow points of (c) and (d) indicate the detected interest points. The initial estimation of correspondences is visualized by yellow lines in (e) and (f). Correspondences were estimated based on simple normalized cross correlations of the intensity values of a patch around each interest point. Clearly, these initial correspondences contain a significant proportion of outliers. The consensus set after applying the RANSAC procedure can be seen in (g) and (h). Their visual appearance indicates that all outliers were ignored by the procedure.

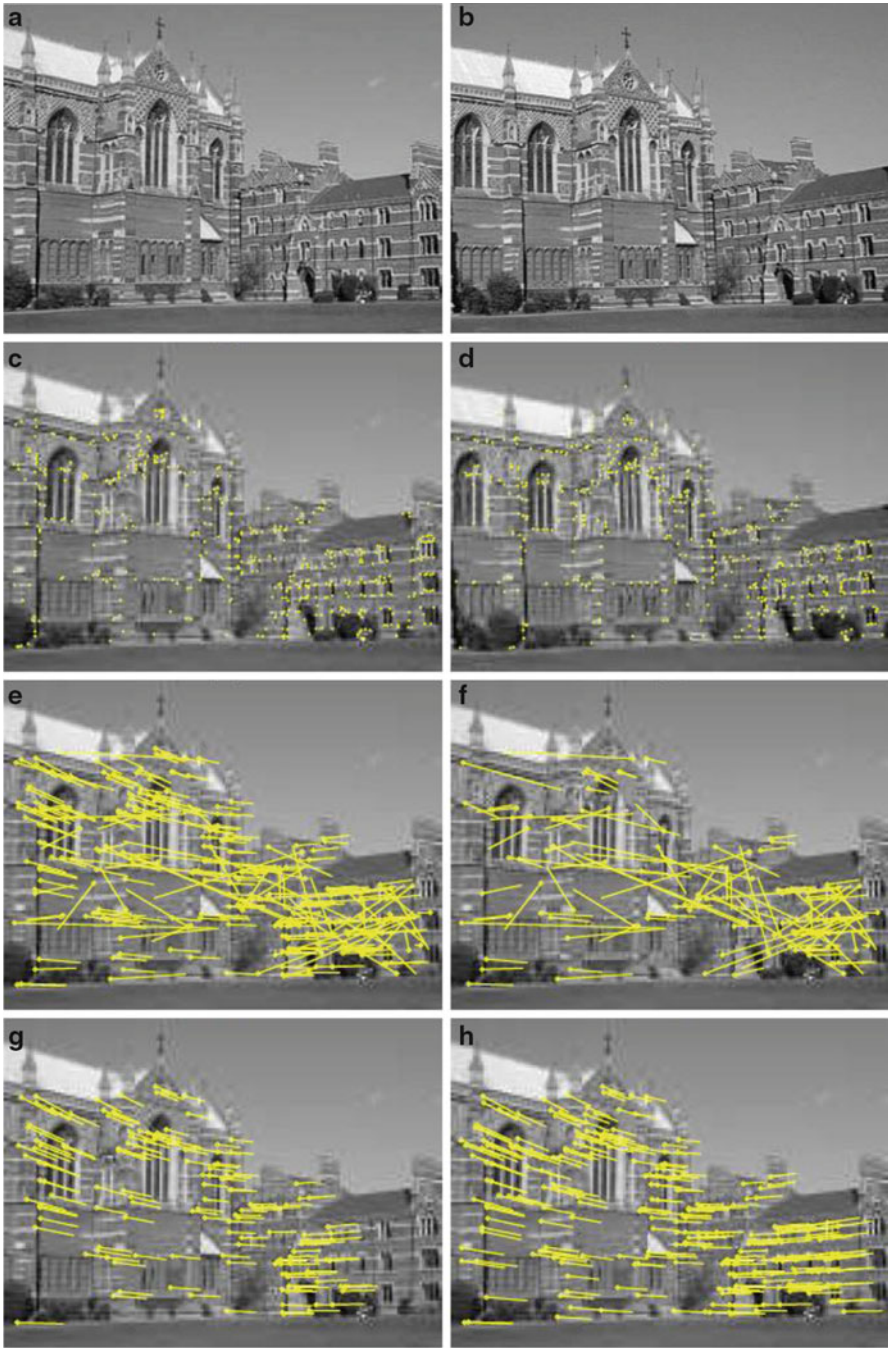

Fig. 5.8 Illustrating the performance of a RANSAC-based correspondence estimator. See text for details (From Hartley and Zisserman [9], with kind permission)

Pseudocode

```
function robustRANSACImageRegistration (in image $I_1$ , in image $I_2$ , in algorithm parameters $t_{sim}$ , $\varepsilon$ , $t_{size}$ , and $N_{\max}$ , out consensus set of consistent correspondences $\Phi_R$ , out final transformation estimate $\mathbf{t}^*$

// interest point and descriptor calculation
detect set of interest points $P_1 = \left\{ \mathbf{p}_{1,m}; m \in [1, \ldots, M] \right\}$ in image $I_1$ , e.g. with Harris detector
detect set of interest points $P_2 = \left\{ \mathbf{p}_{2,n}; n \in [1, \ldots, N] \right\}$ in image $I_2$, e.g. with Harris detector
derive a descriptor $\mathbf{d}_{1,m}$ for each interest point $\mathbf{p}_{1,m}$ from the patch of image $I_1$ around it, e.g. SIFT descriptor
derive a descriptor $\mathbf{d}_{2,n}$ for each interest point $\mathbf{p}_{2,n}$ from the patch of image $I_2$ around it, e.g. SIFT descriptor

// correspondence detection
$\Phi \leftarrow \{\}$
for $n = 1$ to $N$  // loops for every possible descr. combination
  for $m = 1$ to $M$
    if $f_{sim}\left(\mathbf{d}_{1,m}, \mathbf{d}_{2,n}\right) \geq t_{sim}$ then
      add $n = \phi(m)$ to the correspondence set: $\Phi \leftarrow \Phi \cup \{\phi\}$
    end if
  next
next

// robust RANSAC transformation estimation
$k \leftarrow 0$
repeat
  randomly select a subset $\Phi_R$ with minimum size out of $\Phi$ // step 1
  estimate $\hat{\mathbf{t}}$ based on $\Phi_R$ // step 2
  // enlarge $\Phi_R$ , if additional correspondences are consistent with $\hat{\mathbf{t}}$ (step 3)
  for $i = 1$ to $|\Phi|$ // loop for all "remaining" correspondences
    if $\phi_i \notin \Phi_R \wedge \left| T\left(\hat{\mathbf{t}}, \mathbf{p}_{2,\varphi_i(m)}\right) - \mathbf{p}_{1,m} \right| \leq \varepsilon$ then
      add $n = \phi(m)$ to the consensus set: $\Phi_R \leftarrow \Phi_R \cup \{\phi\}$
    end if
  next
  $k \leftarrow k + 1$
until $|\Phi_R| \geq t_{size}$ or $k = N_{\max}$ // step 4
re-estimate $\mathbf{t}^*$ based on the enlarged consensus set $\Phi_R$
```

In the meantime, quite numerous extensions/modifications in order to improve performance have been proposed (see e.g., [3] for a quick systematic overview). The authors of [3] classify the modifications according to the aspect of RANSAC they seek to improve:

- *Accuracy*: These modifications aim at optimizing the correctness of the estimated parameters $\mathbf{t}^*$ of the aligning transform. One possibility is to reestimate $\mathbf{t}^*$ by taking all consistent correspondences into account, as already mentioned. Apart from that, we can modify the way a hypothesis is evaluated. Standard RANSAC simply counts the number of inliers in step 7 of the proceeding outlined above. However, such a hard decision does not take the error distributions of inliers and outliers into account. A better way is to assign a cost to each tested datum which varies more smoothly with respect to the consistency with the hypothesis to be tested and then to sum up all these costs.
- *Speed*: Variations of this category intend to optimize the runtime of the algorithm. One way is to consider similarity scores of individual correspondences (e.g., descriptor similarity), if available. These similarity scores allow for a ranking of the correspondences. We can try to make use of this information by choosing top-ranked data with high probability during the random selection process of step 4. This accounts for the fact that correspondences being based on descriptors with high degree of similarity are more likely to be correct that those with low descriptor similarity. As a result, on average the method needs less iterations until convergence is achieved.
- *Robustness*: As the RANSAC method needs some parameters (ε, t_{size}, and $N_{\max}$), which affect its performance, care is required when choosing their values. To this end, there have been several suggestions to tune their parameters, either based on a priori considerations or depending on the nature of the data at hand (see [3] for details).

5.5 Spectral Methods

5.5.1 Spectral Graph Matching

The method proposed by Leordeanu and Herbert [13] takes an alternative approach in order to make the correspondence estimation more robust. Here, the problem is represented by a properly constructed graph, which is built in a first step. Next, the solution can be obtained by an adequate examination of the graph through utilizing its so-called spectral properties (see below). This method is also an example of the usage of relaxation methods for discrete optimization problems.

In [13] two issues are considered during correspondence estimation:

1. *Individual correspondence affinity*: This term measures the confidence that two points $\mathbf{p}_{1,m}$ and $\mathbf{p}_{2,n}$ (which are elements of two different point sets $P_1 = \left\{\mathbf{p}_{1,m}; m \in [1, \ldots, M]\right\}$ and $P_2 = \left\{\mathbf{p}_{2,n}; n \in [1, \ldots, N]\right\}$) form a correspondence if we just consider the properties of the points themselves, i.e., without

taking their relation to other points into account. This can be done by calculating a descriptor-like SIFT [14] for each point (yielding $\mathbf{d}_{1,m}$ and $\mathbf{d}_{2,n}$) and then measuring the individual affinity through the similarity between $\mathbf{d}_{1,m}$ and $\mathbf{d}_{2,n}$, for example. If a potential correspondence is very unlikely, e.g., because $\mathbf{d}_{1,m}$ differs much from $\mathbf{d}_{2,n}$, this correspondence is not accepted, i.e., no node is created in the graph.

2. *Pairwise affinity*: Here, a pair of possible correspondences is considered. Imagine that we want to evaluate how consistent it would be if we matched $\mathbf{p}_{1,m_1}$ to $\mathbf{p}_{2,n_1}$ (in the following denoted as possible correspondence a) and $\mathbf{p}_{1,m_2}$ to $\mathbf{p}_{2,n_2}$ (possible correspondence b). A measure of consistency between a and b could be based on the similarity of the distance between $\mathbf{p}_{1,m_1}$ and $\mathbf{p}_{1,m_2}$ to the distance between $\mathbf{p}_{2,n_1}$ and $\mathbf{p}_{2,n_2}$. If the distances are similar, it is likely that the relationship between the points of both correspondences can be expressed by the same transformation. Please note that this measure is only suitable for distance-preserving transformations like the Euclidean transformation considering translation and rotation. This metric doesn't work any longer when we also want to consider a significant amount of scaling, for example.

A measure $m(a,b)$ for the distance similarity used in [13] is given in the following, where $g(i,j)$ denotes some distance measure between i and j, whereas the parameter σ_d controls the sensitivity of the metric with respect to discrepancies in the distances. For small σ_d, $m(a,b)$ declines rapidly when the difference between the two distances increases.

$$m(a,b) = \begin{cases} 4.5 - \frac{[g(m_1,m_2)-g(n_1,n_2)]^2}{2\sigma_d{}^2} & \text{if } |g(m_1,m_2) - g(n_1,n_2)| < 3\sigma_d \\ 0 & \text{otherwise} \end{cases} \tag{5.11}$$

Based on these two types of affinity, the correspondence problem can be represented by an appropriately constructed graph. Each node n_a of the graph utilized in [13] correlates to a possible correspondence a between a point $\mathbf{p}_{1,m}$ of the first and a point $\mathbf{p}_{2,n}$ of the second point set. A weight depending on the individual correspondence affinity can be attributed to each node. For example, the degree of similarity between the two descriptors around the points represented by the potential correspondence can be taken as a weight, which can be set to some similarity measure $f_{\text{sim}}\left(\mathbf{d}_{1,m}, \mathbf{d}_{2,n}\right)$, e.g., the inverse of the Earth Mover's Distance or χ^2 distance (see e.g. [18]) being based on the descriptors derived for each point. Furthermore, two nodes n_a and n_b are linked by an edge e_{ab} if their pairwise affinity measure $m(a,b)$ is larger than zero. The weight associated with e_{ab} can be set equal to $m(a,b)$.

The key observation of Leordeanu et al. [13] is that potential correspondences, which are consistent to a common transformation, tend to form a large cluster in the graph, where the nodes are strongly connected to each other (connection strength is indicated by the pairwise affinities as defined above). Outliers, in turn, tend to form "isolated" connections. As a consequence, the task here is to find the largest strongly connected cluster of the graph.

This can be done by representing the graph through its so-called adjacency matrix $\mathbf{M}$, which incorporates the weights of the graph nodes and edges:

- The diagonal elements $m(a,a)$ represent the individual correspondence affinities, i.e., the weights associated to the nodes of the graph (e.g., the descriptor similarities). Observe that usually many possible correspondences can be excluded from the solution search, because their individual similarity is very low. In that case we can reduce the size of $\mathbf{M}$ by simply not considering those correspondences when $\mathbf{M}$ is constructed, i.e., by omitting row/column a. As a consequence, $\mathbf{M}$ stays rather small (of dimensionality $N_C \times N_C$, where N_C denotes the number of combinations between two descriptors of different sets with a similarity above some threshold t_{sim}). This accelerates the subsequent optimization considerably. If no individual correspondence affinity measure is available, the $m(a,a)$ can be set to zero. Of course, the size of $\mathbf{M}$ cannot be reduced in that case (which means that $\mathbf{M}$ is a $M \cdot N \times M \cdot N$–matrix in that case).
- The off-diagonal elements $m(a,b)$ represent the pairwise affinities, which can be calculated, e.g., via (5.11). Generally it can be assumed that $m(a,b) = m(b,a)$, and therefore, $\mathbf{M}$ is symmetric. Observe that $m(a,b)$ is zero if the distance difference between pairs of potential correspondences is large. This should be the case for many pairs, so in general $\mathbf{M}$ is a sparse matrix. As each weight $m(a,b)$ (and the $m(a,a)$, too) is nonnegative, $\mathbf{M}$ is a nonnegative matrix of dimensionality $N_C \times N_C$.

How can we utilize $\mathbf{M}$ in order to get a solution to our problem? The goal is to find the cluster in the graph with maximum cumulative weights. To this end, we can introduce an indicator vector $\mathbf{x}$ consisting of N_C elements, which indicates which of the possible correspondences are actually selected as (correct) correspondences. The element $\mathbf{x}(a)$ is equal to 1 if a represents a correct correspondence and zero otherwise. Then the sum S of those weights associated with the chosen correspondences can be calculated by $S = \mathbf{x}^T \cdot \mathbf{M} \cdot \mathbf{x}$. As we want to find the largest cluster in the graph where many correspondences are tightly connected, we seek for the indicator vector yielding the maximum value of S. Consequently, the correspondences to be found are specified by:

$$\mathbf{x}^* = \arg\max_{\mathbf{x}} \left(\mathbf{x}^T \cdot \mathbf{M} \cdot \mathbf{x} \right) \tag{5.12}$$

Please note that usually the value of one element of $\mathbf{x}$ influences some others, because the correspondences obey some constraints, depending on the application. A frequently used constraint is that a point in one set can be matched to at most one point of the other set. Consequently, if a represents the possible correspondence between $\mathbf{p}_{1,m_1}$ and $\mathbf{p}_{2,n_1}$ and $\mathbf{x}(a) = 1$, then all other elements of $\mathbf{x}$ related to $\mathbf{p}_{1,m_1}$ or $\mathbf{p}_{2,n_1}$ have to be equal to zero. Otherwise the solution of (5.12) would be trivial because of the nonnegativity of $\mathbf{M}$, the highest score would be achieved if we consider all possible correspondences, i.e., all entries of $\mathbf{x}$ are set to one. Hence, we have two constraints to be considered in (5.12):

- Matching constraints (as just described)
- The elements of $\mathbf{x}(a)$ can either be one or zero.

The authors of [13] now suggest a scheme which at first finds a solution by ignoring both of these constraints and then updates the solution by considering the constraints again. Ignoring the binary nature of the elements of the indicator vector (only two values are possible: one and zero) leads to relaxation, as now each element can take continuous values. In this case, we can set the L2-norm of $\mathbf{x}$ equal to one without influencing the solution, i.e., $\mathbf{x}^T \cdot \mathbf{x} = 1$.

Without constraints, (5.12) is a classical *Rayleigh quotient* problem (see e.g., [22]). This means that if $\mathbf{x}$ is set to some eigenvector $\mathbf{v}$ of $\mathbf{M}$, the Rayleigh quotient will yield the corresponding eigenvalue. As we seek indicator vectors which maximize (5.12), the solution of the relaxation of (5.12) is the eigenvector belonging to the largest eigenvalue of $\mathbf{M}$. The fact that the largest cluster of the graph is found with the help of some eigenvalue calculation explains why the method is termed “spectral.”

This principal eigenvector can be found efficiently with the so-called power iteration method (see e.g., [22]). Starting from some $\mathbf{v}^0$, the method performs the iterative update

$$\mathbf{v}^{k+1} = \frac{\mathbf{M} \cdot \mathbf{v}^k}{\|\mathbf{M} \cdot \mathbf{v}^k\|} \tag{5.13}$$

The iteration finally converges to the desired principal eigenvector $\mathbf{v}^*$. If all elements of $\mathbf{v}^0$ are set to nonnegative values, it is ensured that all elements of $\mathbf{v}^*$ will be within the interval $[0 \ldots 1]$. Remember that all elements of $\mathbf{M}$ are nonnegative, too, and therefore, multiplication with the nonnegative elements of $\mathbf{v}^k$ always yields nonnegative elements again. Moreover, the normalization step of the iteration ensures that the values are bounded by one. We can interpret a particular value $\mathbf{v}^*(a)$ as the confidence that the pairing of points expressed by a indeed is a valid correspondence, which belongs to the main cluster of the graph.

In order to obtain the final solution, we have to introduce the constraints again. To this end, in [13] the following iterative greedy proceeding is suggested (see also flowchart of Fig. 5.9):

1. *Acceptance*: Select the pairing $a_{\max} = \arg\max \mathbf{v}^*(a)$, i.e., choose that element of $\mathbf{v}^*$ which has the highest value and add it to the set of estimated correspondences Φ_{R}. For $a_{\max}$, we can have the highest confidence that it actually is a correct correspondence.
2. *Rejection*: Remove $a_{\max}$ as well as that elements from $\mathbf{v}^*$, where the underlying pairing is not consistent with $a_{\max}$. For example, if $a_{\max}$ contains a point $\mathbf{p}_{1,m}$ and we have to ensure that each point can be part of at most one correspondence, then we have to remove all elements from $\mathbf{v}^*$ which contain $\mathbf{p}_{1,m}$, too. After this, we

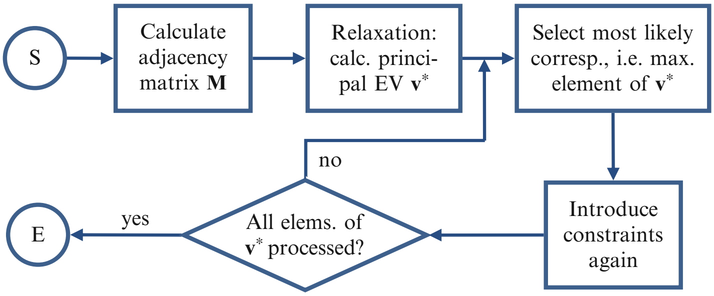
S
Calculate adjacency matrix **M**
Relaxation: calc. principal EV $\mathbf{v}^*$
Select most likely corresp., i.e. max. element of $\mathbf{v}^*$
Introduce constraints again
All elems. of $\mathbf{v}^*$ processed?
no
yes
E

Fig. 5.9 Flowchart of spectral graph matching as proposed in [13]

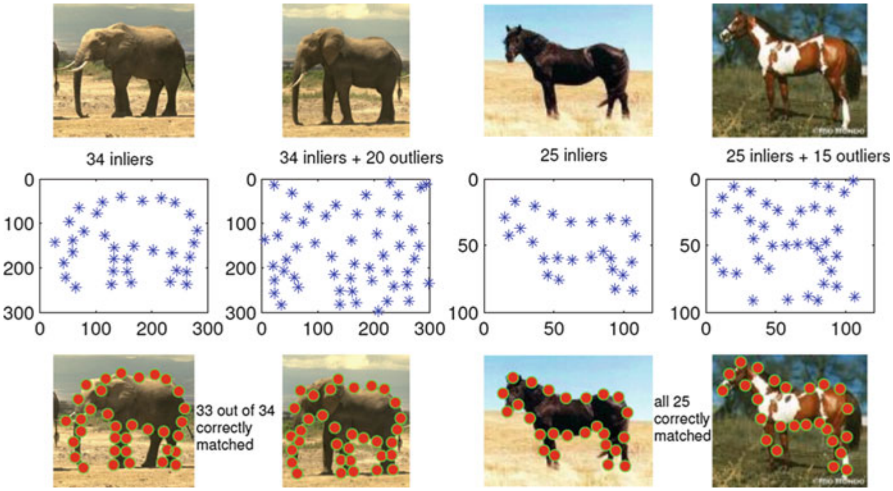

Fig. 5.10 Exemplifying the robustness of the method proposed in [13] to outliers. See text for details (© 2005 IEEE. Reprinted, with permission, from Leordeanu and Herbert [13])

can search the pairing which now has the highest confidence by going back to step 1 with truncated $\mathbf{v}^*$.

3. *Termination*: If all elements of the initial $\mathbf{v}^*$ are either accepted or rejected (i.e., $\mathbf{v}^*$ doesn't contain any elements any longer), we're finished.

Figure 5.10 illustrates the performance of the method, especially its robustness to outliers for two examples (elephant and horse). The images are shown in the top row, whereas the detected points are shown in the middle row. For each of the examples, a considerable amount of outliers is present. As can be seen in the bottom row, almost all outliers are rejected successfully.

Pseudocode

```
function spectralGraphMatching (in point set 1 $P_1 = \{\mathbf{p}_{1,m}; m \in [1,\ldots,M]\}$, in point set 2 $P_2 = \{\mathbf{p}_{2,n}; n \in [1,\ldots,N]\}$, in image $I_1$ , in image $I_2$ , in algorithm parameters $t_{sim}$ and bUseDescr, out set of consistent correspondences $\Phi_R$

// calculation of adjacency matrix $\mathbf{M}$
// 1st step: indiv. corresp. affinities (diag. elems of $\mathbf{M}$)
if bUseDescr == TRUE then
  // descriptor calculation
  derive a descr. $\mathbf{d}_{1,m}$ for each $\mathbf{p}_{1,m}$ from the patch of image $I_1$
  around it (e.g. SIFT) and $\mathbf{d}_{2,n}$ for all $\mathbf{p}_{2,n}$ accordingly
  // set individual correspondence affinities
  $N_C \leftarrow 0$
  for $n = 1$ to $N$
    for $m = 1$ to $M$
      if $f_{sim}(\mathbf{d}_{1,m}, \mathbf{d}_{2,n}) \geq t_{sim}$ then
        $m(N_C, N_C) = f_{sim}(\mathbf{d}_{1,m}, \mathbf{d}_{2,n})$
        $N_C \leftarrow N_C + 1$
      end if
    next
  next
else
  // don't use individual correspondences -> set diagonal
  elements of $\mathbf{M}$ to zero
  $N_C \leftarrow M \cdot N$ // exhaustive combination
  set all $m(a,a) = 0$
end if
// 2nd step: pairwise affinities (off-diagonal elems of $\mathbf{M}$)
for $a = 1$ to $N_C$
 for $b = 1$ to $a - 1$
    set $m(a,b) = m(b,a)$ according to (5.11)
 next
next

// calc. confidences in correspondence by relaxation: calculate principal eigenvector of $\mathbf{M}$ with power iteration method
$\mathbf{v}^0 = [1, 1, \ldots 1]$ // initialization of $\mathbf{v}$
$k \leftarrow 0$
repeat
  $\mathbf{v}^{k+1} = \mathbf{M} \cdot \mathbf{v}^k / \|\mathbf{M} \cdot \mathbf{v}^k\|$
  $k \leftarrow k + 1$
until convergence (yielding $\mathbf{v}^*$)
```

```
// introduce constraints again
$\Phi_R \leftarrow \{\}$
repeat
  select $a_{\max} = \arg\max \mathbf{v}^*(a)$
  add $a_{\max}$ to $\Phi_R$. // "correct" correspondence found
  $\mathbf{v}^*(a_{\max}) \leftarrow 0$
  for $a = 1$ to $N_C$
    if $a$ is not consistent with $a_{\max}$ then
      $\mathbf{v}^*(a) \leftarrow 0$
    end if
  next
until all $N_C$ elements of $\mathbf{v}^*$ are processed (are of value 0)
```

Observe that this proceeding can be extended to the so-called higher-order cliques, where affinities between more than two points can be considered. This is useful if the relation between the two point sets has to be characterized by more general transformations. For example, if we take triplets of points, the angles of the triangle spanned by such a triplet are invariant in case of the more general class of similarity transformations. The affinities can then be described by multidimensional tensors, whose principal eigenvector can be found by a generalization of the power iteration method (see [4] for a more detailed description).

Another very recent modification of the method is reported in [5], where a probabilistic interpretation of spectral graph matching is given. This leads to a modification of the power iteration method, which updates the adjacency matrix $\mathbf{M}$ at each iteration as well, such that high-probability correspondences are reinforced. The authors of [5] report performance superior to state-of-the-art methods in the presence of noise and outliers at the cost of increased runtime.

5.5.2 Spectral Embedding

Jain et al. [10] proposed to utilize the spectral domain in a different respect as follows. Imagine a situation where two 3D shapes are to be matched. It is assumed that the shapes are represented by a mesh of surface points. Instead of estimating the mutual consistence of two possible correspondences and cumulating them in a matrix as done in the previous section, the authors of [10] build a separate matrix for each shape.

Each of these two matrices $\mathbf{A}$ and $\mathbf{B}$ is composed of the distances between the vertices of the mesh representations. For example, the element a_{ij} represents the distance from the ith vertex of the first shape to the jth vertex of the same shape. The vertices should be sampled rather uniformly sampled for both shapes. Moreover, the vertex count should be similar for both shapes.

As far as the distances are concerned, Euclidean distances could be used. As we have a mesh representation, however, it is advisable to use the so-called geodesic distances, where the connection between two vertices (whose length defines the distance) is restricted to be located on the shape surface. Each row of such a so-called affinity matrix $\mathbf{A}$ or $\mathbf{B}$ characterizes the shape properties with respect to one vertex, as it accumulates distance information from that vertex to all other vertices of the mesh. Therefore, it could be used as a descriptor for estimating correspondences.

The correspondence search, however, is not done in the spatial domain. Instead, a transformation into the spectral domain is performed prior to the correspondence search. This means that an eigendecomposition of each of the matrices $\mathbf{A}$ and $\mathbf{B}$ takes place. When taking the top k eigenvectors of the $N \times N$ matrix $\mathbf{A}$ and concatenating them in the $N \times k$ matrix $\mathbf{E}_k$, we can project the affinity matrix $\mathbf{A}$ onto the spectral domain by calculating $\hat{\mathbf{A}}_k = \mathbf{E}_k^{\mathrm{T}} \cdot \mathbf{A}$. Now each column $\hat{\mathbf{a}}_i$ of $\hat{\mathbf{A}}_k$ represents a (k-dimensional) spectral embedding of a vertex descriptor. Correspondences can now be searched by comparing the analogously obtained $\hat{\mathbf{b}}_j$ with the $\hat{\mathbf{a}}_i$ in the spectral domain. Estimating the correspondence in the spectral domain has the following advantages:

- As usually $k << N$, potential correspondences can be evaluated much faster.
- Together with some suitable normalizations, the correspondence search becomes more robust compared to a search in the spatial domain, e.g., in the presence of scaling and moderate distortions.

The basic proceeding suggested in [10] can now be summarized as follows:

1. Calculation of the affinity matrices $\mathbf{A}$ and $\mathbf{B}$.
2. Spectral embedding with the help of an eigendecomposition of $\mathbf{A}$ and $\mathbf{B}$, yielding $\hat{\mathbf{A}}_k$ and $\hat{\mathbf{B}}_k$ if only the top k eigenvectors (i.e., the eigenvectors relating to the k largest eigenvalues) are chosen.
3. Iterative estimation of the correspondences by
   (a) comparing the columns $\hat{\mathbf{b}}_j$ with the $\hat{\mathbf{a}}_i$ and
   (b) updating the estimation of a transformation intending to align the two shapes in alternation in a modified ICP proceeding in the spectral domain.

Observe that this proceeding is just a rough outline of the method proposed in [10]. Details about normalization, re-sorting of the eigenvectors, modifications of the ICP algorithm employed in step 3 in order to increase robustness with respect to local distortions, etc., are omitted here for brevity. The interested reader is referred to [10]. As was shown there, the method outperforms many well-known registration schemes in the context of nonrigid 3D shape matching.

Essentially, this proceeding can be seen as an enhancement of the classical ICP approach. Apparently, the utilization of spectral embedding makes the method more robust with respect to quite common effects like scaling or surface bending.

5.6 Assignment Problem/Bipartite Graph Matching

A special case of the correspondence problem is the so-called assignment problem. Based on two sets P_1 and P_2 of same size, the task here is to assign exactly one element $\mathbf{p}_{2,n}$ of P_2 to each element $\mathbf{p}_{1,m}$ of P_1, i.e., to establish one-to-one correspondences between all elements of the two sets.

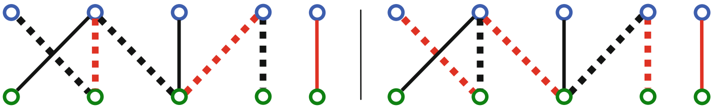

Fig. 5.11 Illustrating the principle of alternating paths

Additionally, a weight w_{mn} is associated to each possible assignment, which should reflect the plausibility of the assignment under consideration. The assignments have to be chosen such that the total weight of all assignments actually made is maximized. The weights w_{mn} can, e.g., be set to the similarity between $\mathbf{p}_{1,m}$ and $\mathbf{p}_{2,n}$. The similarity can, e.g., be calculated with the help of some similarity measure $f_{\text{sim}}\left(\mathbf{d}_{1,m}, \mathbf{d}_{2,n}\right)$ between some descriptors $\mathbf{d}_{1,m}$ and $\mathbf{d}_{2,n}$ derived from the image patches around $\mathbf{p}_{1,m}$ and $\mathbf{p}_{2,n}$, e.g., the inverse of the Earth Mover's Distance or χ^2 distance (see e.g., [18]),

The assignment problem can be reformulated as one of finding a *perfect matching* in a so-called bipartite graph, where the total similarity is maximized. In bipartite graphs, the node set N is separated into two disjoint sets A and B (see Chap. 1). If we take P_1 and P_2 as disjoint sets, the assignment problem can be represented by a bipartite graph $G = (N = A \cup B, E); A \cap B = \{\}$. Here, each node $n_{A,i}$ represents a point $\mathbf{p}_{1,m}$ of set P_1, whereas each node $n_{B,j}$ represents a point $\mathbf{p}_{2,n}$ of P_2.

The weight w_{ij} of edge $e_{ij} \in E$ represents the similarity $f_{\text{sim}}\left(\mathbf{d}_{1,m}, \mathbf{d}_{2,n}\right)$. All edges e_{ij} connect nodes of different sets. All correspondences being actually established can be summarized in the matching M, which a subset of the edges of the graph: $M \subseteq E$. It contains those edges which connect matched nodes. A matching is called perfect if it connects all nodes of the graph, i.e., it defines a correspondence for every node of G.

5.6.1 *The Hungarian Algorithm*

A method of finding a perfect matching with maximal similarity is the so-called Hungarian algorithm, which was developed by Kuhn [12] and later refined by Munkres [17]. It is largely based on earlier work of two Hungarian mathematicians, which explains its name.

Before we describe how the method works in detail, let's introduce some definitions in addition to the definitions already made in Chap. 1. Considering the bipartite graph shown in Fig. 5.11 on the left, the red edges form the matching M. The dashed edges form a so-called *alternating path*, because its edges alternate between being not part of M (black) and being part of M (red). Additionally, its two endpoints are *free*. A node is called free if it is not linked to an edge being part of M, i.e., it is not matched to a node of the other set. An alternating path with the additional property that both of its endpoints are free is called *augmenting*

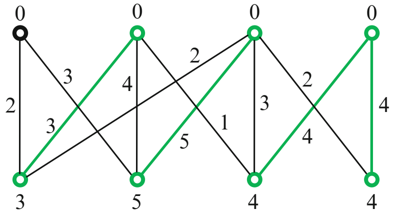

Fig. 5.12 Illustrating the definition of tight edges and equality graphs

path, because if we "toggle" the red and black edges (see Fig. 5.11, right part), we increase the size of the matching by one.

Moreover, we introduce the so-called labels in the graph. A real-valued label $l(n_k)$ is assigned to each node n_k of the graph. A labeling is called *feasible* if the following inequality holds for all edges:

$$l\left(n_{A,i}\right)+l\left(n_{B,j}\right)\geq w_{ij}\ \ \forall\ \ n_{A,i}\in A, n_{B,j}\in B \tag{5.14}$$

An edge e_{ij} for which (5.14) is an equality, i.e., $l\left(n_{A,i}\right)+l\left(n_{B,j}\right)=w_{ij}$ is called *tight*. The subgraph G_E of G which contains all tight edges as well as all nodes being connected to at least one tight edge is called *equality graph*. An example of a graph (with edge weights and labels) can be seen in Fig. 5.12, where all nodes and tight edges of the equality graph are shown in green.

A node $v\in N$ is called *neighbor* of a node $u\in N$, if u and v are connected by a tight edge (which is part of the equality graph G_{E}). All neighbors of u are summarized in the set $N_{\text{E}}(u)=\{v:e_{uv}\in G_{\text{E}}\}$. The set $N_{\text{E}}(S)=\cup_{u\in S}N_{\text{E}}(u)$ summarizes all neighbors of any of the nodes $u\in S$ being part of a set of nodes S.

With these definitions, we are in the position to introduce the Hungarian algorithm. Kuhn discovered that if a labeling of a bipartite graph is feasible (i.e., the inequality defined in (5.14) holds for all nodes of the graph) and, additionally, a perfect matching M is part of the equality subgraph G_{E} of G , i.e., $M\subset G_{\text{E}}$, then M is the desired solution, which maximizes the total weight of the edges of M. An important consequence of this finding is that the search of the solution can be confined to the set of tight edges.

The basic working principle of the Hungarian method is to iteratively either increase the size of the current matching estimate M (i.e., enlarge the set of estimated correspondences) or improve the labeling such that G_{E} is enlarged through the appearance of new tight edges (which can be used to enlarge M in later iterations). The method consists of the following steps (see also flowchart of Fig. 5.13):

1. *Graph initialization*: At the beginning, the bipartite graph which represents the assignment problem has to be constructed. To this end, we introduce nodes, which are partitioned into two disjoint sets A and B, where each node of A represents a point $\mathbf{p}_{1,m}$ and each node of B a point $\mathbf{p}_{2,n}$. Edges can be set between the nodes with weights w_{ij}, according to their similarity. During this step, a labeling which satisfies (5.14) for all labels has to be found, too. Without loss of

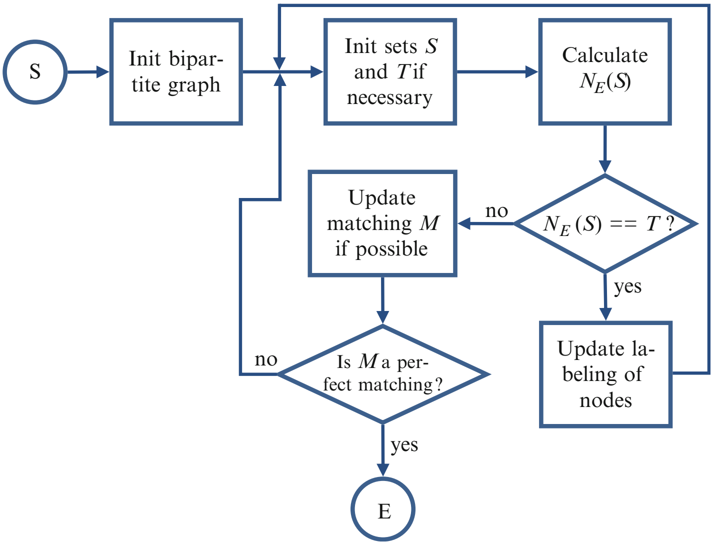
S
Init bipartite graph
Init sets S and T if necessary
Calculate $N_E(S)$
$N_E(S) == T$?
no
yes
Update matching M if possible
Is M a perfect matching?
no
yes
Update labeling of nodes
E

Fig. 5.13 Flowchart of the Hungarian algorithm

generality, we can set the label of all nodes of set B to zero (see also Fig. 5.12, where the nodes of set B are all placed in the top row of the graph). In order to satisfy (5.14), the label for each of the nodes of set A can be chosen such that it corresponds to the maximum weight of all edges which are connected to that node: $\forall n_{A,i} \in A : l\left(n_{A,i}\right) = \max\limits_{n_{B,j} \in B} w_{ij}$ (an example can be seen in Fig. 5.12). As a consequence, each node $n_{A,i}$ is connected to at least one tight edge. We can choose as subset of these tight edges as initial matching M.

2. *Iteration initialization*: The method works on two node sets S and T. At the beginning of each iteration, let be $T = \{\}$ (empty) and initialize S with one arbitrarily picked node u of set A: $S = \{u\}; u \in A$. Additionally, u has to meet the condition that it is free, i.e., that it is connected to at least one tight edge and that it is not part of the current matching M. Informally speaking, the set S contains points in A which are endpoints of potential matching extensions, whereas the set T contains points in B which are validated to be already part of the matching and therefore must not be used for new matching edges.
3. *Neighborhood definition*: In this step, we calculate $N_{\mathrm{E}}(S)$, which is the set of all nodes which are neighbors to a node of S. By comparing $N_{\mathrm{E}}(S)$ with T, we're in the position to determine whether the matching or the labeling has to be updated. Given that nodes of S serve as endpoints of potential matching extensions, $N_{\mathrm{E}}(S)$ contains the endpoints "on the other side" of potential new matching edges. In order to determine whether the labeling or the matching has to be updated, we compare $N_{\mathrm{E}}(S)$ with T (see step 4 and 5).
4. *Label update*: If $N_{\mathrm{E}}(S) = T$, all potential "counterparts" of new matching candidates of A already are part of the current matching. Therefore, we update

the labels with the goal to create new tight edges (in other words, we enforce $N_{\mathrm{E}}(S) \neq T$), which will be useful when extending the matching in later iterations. This is done with the following update rule, which is applied to all nodes n of the graph:

$$\Delta = \min_{x \in S, y \notin T} \left\{ l(x) + l(y) - w_{xy} \right\}$$

$$l_{\text{new}}(n) = \begin{cases} l(n) - \Delta & \text{if } n \in S \\ l(n) + \Delta & \text{if } n \in T \\ l(n) & \text{otherwise} \end{cases} \tag{5.15}$$

After this update, we go on with step 3 (Recalculation of $N_{\mathrm{E}}(S)$).

5. *Matching update*: If $N_{\mathrm{E}}(S) \neq T$, it could be possible to extend the matching. Therefore, we arbitrarily pick a node $y \in N_{\mathrm{E}}(S) - T$. If y is already matched to a node z, we must not take it as a new endpoint of an additional matching edge. Therefore, we extend the sets $S = S \cup \{z\}$ and $T = T \cup \{y\}$ (i.e., enlarge the set T containing all nodes validated to be already matched to some other node by y) and go on with the next iteration (step 3). If y is free, we're in the position to extend the matching. According to the above assumptions and definitions, the path from u to y has to be an augmenting path (alternation between tight edges which are part of M and not part of M with two free endpoints). Therefore, we can extend the matching by one edge if we alternate the affiliation of all edges of the path from u to y: if an edge $e_{ij} \in M$, we exclude it from M, if $e_{ij} \notin M$, we include it in M. Finally, the size of M is increased by one edge.
6. Convergence check: Stop if M is a perfect matching. Otherwise continue with step 2

A toy example which illustrates the mode of operation of the Hungarian method can be seen in Table 5.3. The bipartite graph shown there consists of two node sets $A = \{n_{A,i}\}; i = \{1, 2, 3, 4\}$ (bottom row of each graph) and $B = \{n_{B,j}\}; j = \{1, 2, 3, 4\}$ (top row of each graph), which are in some way connected by some edges with weights given next to each edge (see left graph of top row).

In the first step, an initial feasible labeling has to be found according to the proceeding explained above. According to the initial labeling, the graph contains four tight edges, from which two are selected more or less arbitrarily as being part of the initial matching This can be seen in the right graph of top row, where matching edges are in red; tight edges not being part of the matching are indicated by green color. Before we describe the proceeding of the method in detail, let's clarify the meaning of the different colors used in Table 5.3, which hopefully help to understand the method:

- Red edge: Part of the current matching (is therefore tight, too)
- Green edge: Tight edge but not part of the current matching
- Bold edge: Edge where an important change happens
- Dark yellow node: Node being part of set S
- Light blue node: Node being part of set $N_{\mathrm{E}}(S)$

Table 5.3 Illustrating the working principle of the Hungarian method

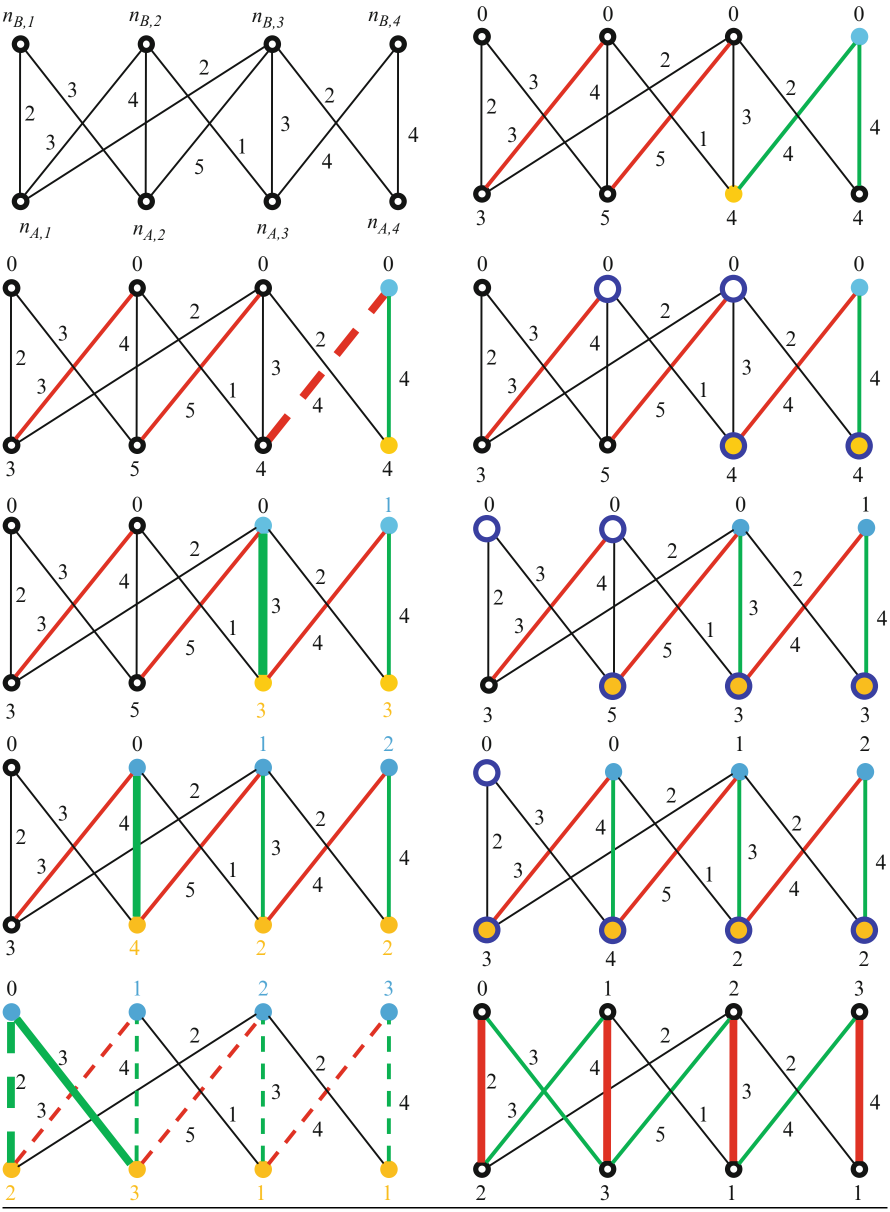

For details, see text

- Node framed blue: Node which is considered during the calculation of the label update Δ.
- Colored labels: Labels which have just been updated
- Dashed edges: Augmenting paths where the matching has been updated

The iteration is initialized with the sets $S = \{n_{A,3}\}$ (dark yellow node) and $T = \{\}$. Based on S, the neighborhood is defined by $N_{\mathrm{E}}(S) = \{n_{B,4}\}$ (Consequently, $n_{B,4}$ is marked light blue node, see right part of top row of Table 5.3). As $N_{\mathrm{E}}(S) \neq T$, we can try to extend the matching. Because $n_{B,4}$ is a free node, this is possible and the path between $n_{A,3}$ and $n_{B,4}$ is augmented. As this path contains only one edge, we just have to include the said edge into the matching in this simple case (see the bold edge in the left graph of the second row, which switches its color from green to red).

Now we can redefine the node sets according to $S = \{n_{A,4}\}$ and $T = \{\}$. Therefore, $N_{\mathrm{E}}(S) = \{n_{B,4}\}$ and again $N_{\mathrm{E}}(S) \neq T$ (see left graph in the second row). This time, however, $y = n_{B,4}$ is not free any longer. It is matched to $z = n_{A,3}$ instead. Therefore, we enlarge $S = \{n_{A,3}, n_{A,4}\}$ and $T = \{n_{B,4}\}$. This leads to N_{E} $(S) = \{n_{B,4}\}$ (c.f. right graph of second row). Now $N_{\mathrm{E}}(S) = T$, which means that we will update the labeling of all nodes of S and T. To this end, the update value Δ has to be determined according to (5.15). Δ is calculated under consideration of all nodes framed blue in the right graph of the second row and their connections and is therefore set to 1.

The new labeling can be seen in the left graph of the third row (all colored values have been updated). The label update has caused the emergence of an additional tight edge (bold green). As a result, the neighborhood is enlarged to $N_{\mathrm{E}}(S) = \{n_{B,3}, n_{B,4}\}$. This means that $N_{\mathrm{E}}(S) \neq T$ (indicating an update of the matching), but $n_{B,3} = N_{\mathrm{E}}(S)$ $-T$ is already part of the matching. Consequently, we enlarge $S = \{n_{A,2}, n_{A,3}, n_{A,4}\}$ and $T = \{n_{B,3}, n_{B,4}\}$ (right graph of the third row). Now $N_{\mathrm{E}}(S) = T$ and we perform another label update step based on all nodes framed blue (again, Δ is set to 1). This leads to a new labeling, another tight edge (bold green) and the updated $N_{\mathrm{E}}(S) = \{n_{B,2}, n_{B,3}, n_{B,4}\}$ (left graph of fourth row).

Thus, $N_{\mathrm{E}}(S) \neq T$, and as $n_{B,2} = N_{\mathrm{E}}(S) - T$ is already part of the matching, no matching update is to be performed (analogously to before). Instead, we enlarge $S = \{n_{A,1}, n_{A,2}, n_{A,3}, n_{A,4}\}$ and $T = \{n_{B,2}, n_{B,3}, n_{B,4}\}$ (right graph of the fourth row). As a consequence, $N_{\mathrm{E}}(S) = T$, which indicates one more label update step based on all nodes framed blue (Δ is set to 1). This leads to a new labeling, two new tight edges (bold green) and the updated $N_{\mathrm{E}}(S) = \{n_{B,1}, n_{B,2}, n_{B,3}, n_{B,4}\}$ (left graph of bottom row).

Accordingly, $N_{\mathrm{E}}(S) \neq T$, but in contrast to the previous steps, $n_{B,1} = N_{\mathrm{E}}(S) - T$ is free. Therefore, we have an augmenting path from $n_{B,1}$ to $n_{A,4}$, both of which are free endpoints (the path is indicated by dashed edges). Consequently, we can "toggle" each edge of the path, which leads to a new matching (see red edges in right graph of bottom row). Finally, this new matching is complete and we're finished. The total matching weight is 13.

The overall complexity is $O(n^3)$, with n being the cardinality of the two point sets.

Please note that the algorithm given above maximizes the sum of the weights w_{ij} of the matching. Many problems involve evaluating *costs* c_{ij} associated with each correspondence though, and thus the algorithm should *minimize* the sum of the weights of the matching. However, the minimization problem can easily be converted to a maximization problem by calculating the weights w_{ij} as differences $c_{\max} - c_{ij}$, where $c_{\max}$ is chosen sufficiently large in order to ensure that all w_{ij} are positive. Hence, small costs result in large weights.

In its initial form, the Hungarian algorithm can only match point sets of equal size, because it determines a matching for every node of the graph. However, the method can easily be extended to point sets of different size by the introduction of the so-called dummy nodes. For example, if the cardinality K of P_1 is larger than the cardinality L of P_2 (i.e., $K - L = D$), the introduction of D dummy nodes in node set B ensures that both node sets are of equal size. If a node of set A is matched to a dummy node, this means that it has no corresponding point in practice. Moreover, we can introduce some additional dummy nodes in both sets in order to allow unmatched points for both sets.

Each dummy node is connected to every node of the other set (such that every of those nodes could be connected to a dummy node). The weight of those edges can be set to t_{sim}, which defines the minimum similarity two nodes must have in order to be matched during recognition.

Pseudocode

```
function bipartiteGraphMatching (in point set 1 $P_1 = \{\mathbf{p}_{1,m}; m \in [1,\ldots,K]\}$, in point set 2 $P_2 = \{\mathbf{p}_{2,n}; n \in [1,\ldots,L]\}$, in number of dummy nodes $D$, in minimum similarity $t_{sim}$, out perfect matching $M$

// initialization of bipartite graph
$Num \leftarrow \max(K,L) + D$ // at least $D$ dummy nodes in each set
for $m = 1$ to $K$          // node set $A$
   for $n = 1$ to $L$          // node set $B$
      calculate similarity $f_{sim}$ between $\mathbf{p}_{1,m}$ and $\mathbf{p}_{2,n}$, e.g. $\chi^2$-distance between descriptors $\mathbf{d}_{1,m}$ and $\mathbf{d}_{2,n}$
      $w_{mn} \leftarrow f_{sim}$
   next
next
fill graph with dummy nodes and connect each dummy node to each node of the other set with edge weight $w_d = t_{sim}$.

// initial edge labeling
for $i = 1$ to $Num$
   $l(n_{A,i}) \leftarrow \max_{n_{B,j} \in B} w_{ij}$
   $l(n_{B,i}) \leftarrow 0$
next
choose initial matching $M$ as a subset of all tight edges
```

```
// main iteration loop
bInitSets ← true
repeat
   // initialization of $S$ and $T$, if necessary
   if bInitSets == true then
      for $i = 1$ to $Num$
         if $n_{A,i}$ is free then
            $S \leftarrow \{n_{A,i}\}$
            $i \leftarrow Num$ // a free node in $A$ is found → stop
         end if
   next
   $T \leftarrow \{\}$
   bInitSets ← false
end if
// calculation of $N_E(S)$
for all nodes of $S$ (index $r$)
   for all edges $e_{rt}$ connecting $n_{A,r}$
      if $e_{rt}$ is a tight edge and $n_{B,t} \notin N_E(S)$ then
         $N_E(S) \leftarrow N_E(S) \cup \{n_{B,t}\}$
      end if
   next
next
// check whether matching or labeling is to be updated
if $N_E(S) == T$ then
   // update labeling
   $\Delta \leftarrow \min_{x \in S, y \notin T} \{l(x) + l(y) - w_{xy}\}$
   for $i = 1$ to $Num$
      if $n_{A,i} \in S$ then
         $l(n_{A,i}) \leftarrow l(n_{A,i}) - \Delta$
      end if
      if $n_{B,i} \in T$ then
         $l(n_{B,i}) \leftarrow l(n_{B,i}) + \Delta$
      end if
   next
else           // update matching, if possible
   arbitrarily pick a node $y \in N_E(S) - T$
   if $y$ is free then
      for all edges $e_{ij}$ on path from $u$ to $y$
         if $e_{ij} \in M$ then
            $M \leftarrow M - \{e_{ij}\}$
         else
            $M \leftarrow M \cup \{e_{ij}\}$
         end if
```

```
        next
      bInitSets ← true    // restart iteration
      else   // $y$ is already matched to some node $z$
          $S \leftarrow S \cup \{z\}$
          $T \leftarrow T \cup \{y\}$
      end if
    end if
until $M$ is a perfect matching (all nodes belong to exactly
one element of $M$)
```

5.6.2 Example: Shape Contexts

One example of solving the correspondence problem with bipartite graph matching is a method for object recognition proposed by Belongie et al. [1]. The objects are recognized by utilizing an object model learned in a training phase. This object model is based on the so-called shape contexts, which are descriptors being built on the shapes of the object to be recognized. Briefly speaking, each shape context represents the spatial distribution of points being located on the object contour in a local neighborhood around one of those *contour points* (also called *landmark points*").

As we will see soon, bipartite graph matching is utilized in [1] in order to find correspondences between the shape contexts extracted from a scene image under investigation and shape contexts from the object model. Once the correspondences are estimated, the algorithm derives the parameters of a transformation between the two sets of shape contexts as well as a measure of similarity between the scene image shape context set and the model set. Based on this similarity measure, it is possible to distinguish between different kinds of objects: we simply can calculate the similarity measure for all models of a model database. The model with the highest score is considered as recognized if the score is above a certain threshold.

Bipartite graph matching should enable the algorithm to robustly find a consistent matching set which contains no or at least very few outliers, such that the subsequent transformation estimation ought to be successful. Before we take a closer look at how bipartite graph matching is employed in the method, let's first introduce the concept of shape context as well as the general algorithm flow of the method.

In order to understand the working principle of shape contexts, we assume that the object is represented by a set of so-called contour points, which are located at positions with rapid local changes of intensity. At each contour point, a shape context can be calculated. Each shape context defines a histogram of the spatial distribution of other landmark points relative to the current one. These histograms provide a distinctive characterization for each landmark point, which can be used as a descriptor.

A shape context example is depicted in Fig. 5.14: in the left part, sampled contour points of a handwritten character "A" are shown. At the location of each of them, the

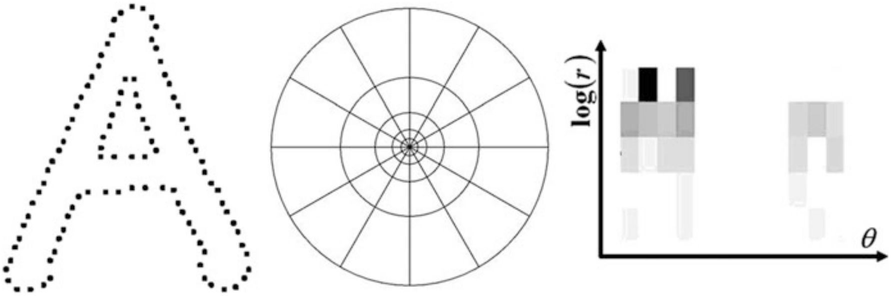

Fig. 5.14 With images taken from Belongie et al. [1] exemplifying shape context calculation (From Treiber [23], with kind permission from Springer Science and Business Media, using figures of [1], © 2002 IEEE. Reprinted with permission)

local neighborhood is partitioned into bins according to the log-polar grid shown in the middle. For each bin, the number of contour points located within that bin is calculated. The result is a 2D histogram of the spatial distribution of neighboring contour points: the shape context. One arbitrary example of these histograms is shown on the right, where dark regions indicate a high number of points.

Please observe that shape contexts are quite insensitive to local distortions of the objects, as each histogram bin covers a certain area of pixels. In case the exact location of the shape varies, a contour point still contributes to the same bin if its position deviation does not exceed a certain displacement. The maximum displacement "allowed" is related to the bin size. Thus, large bins allow for more deformation than small bins. For that reason a log-polar scale is chosen for bin partitioning: contour points located very close to the "center point" (for which the shape context shall be calculated) are expected to be less affected by deformations than points located rather far away. Accordingly, the bin size is small near the region center and large in the outer areas.

The recognition stage of the method consists of four steps (see also Fig. 5.15 for an overview):

1. *Sampling of the scene image*, such that it is represented by a set of contour points $P_S = \{\mathbf{p}_{S,n}\}; i \in [1, 2, \ldots, N]$. The method works best if these points are distributed quite uniformly across the contour of the object shown in the image.
2. *Calculation of shape context descriptors* $\mathbf{d}_{S,n}$: For each contour point $\mathbf{p}_{S,n}$ being located upon inner or outer contours of the object, one shape context $\mathbf{d}_{S,n}$ is calculated, where the log-polar grid is centered at $\mathbf{p}_{S,n}$.
3. *Establishment of correspondences* between the shape contexts $\mathbf{d}_{S,n}$ of the scene image and those of a stored model $\mathbf{d}_{M,k}$, i.e., find $k = \phi(n)$ for each shape context. This mapping is based on the individual similarities between the shape contexts. To this end, bipartite graph matching can be employed.
4. *Estimation of the parameters of an aligning transform* trying to match the location of each contour point $\mathbf{p}_{S,n}$ of the scene image to the location of the corresponding model point $\mathbf{p}_{M,\phi(n)}$ as exactly as possible. In order to allow for

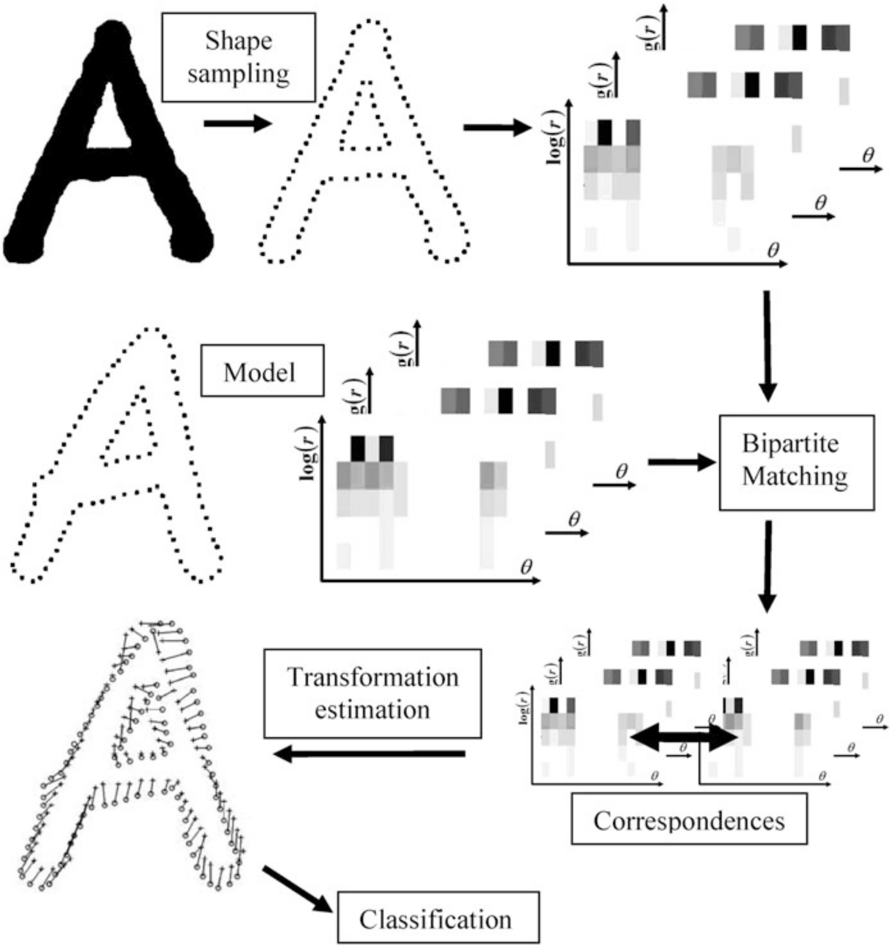

Fig. 5.15 Illustrating the algorithm flow of the shape context method (From Treiber [23], with kind permission from Springer Science and Business Media, using figures of [1], © 2002 IEEE. Reprinted with permission)

local deformations, the transformation is modeled by so-called thin plate splines (TPS). TPS are used when coordinate transforms performing nonlinear mappings and thus being able to model local deformations are needed.

5. *Computation of the distance between scene image shape and model shape:* One measure of this distance is the sum of matching errors between corresponding points. Based on this error sum, a classification of the scene image can be done by comparing the error sums for different models.

Bipartite graph matching comes into play in step 3 of this proceeding, where the correspondences $k = \phi(n)$ are to be established (the matching step in Fig. 5.15).

Therefore, we focus on this step and refer the interested reader to [1] for a detailed description of the other steps.

In order to find the correspondences, the problem has to be formulated as a bipartite graph. Accordingly, each landmark point is represented as a node in the graph, where all scene image landmark points $\mathbf{p}_{\mathrm{S},n}$ are collected in a node set A and all model landmark points $\mathbf{p}_{M,k}$ in a second set B. Edges are established only between nodes of different sets. Without the usage of any prior knowledge, each $\mathbf{p}_{\mathrm{S},n}$ is connected to all $\mathbf{p}_{M,k}$ by the edges e_{nk}.

Moreover, a cost c_{nk} can be calculated for each edge based on the dissimilarity between the shape contexts $\mathbf{d}_{\mathrm{S},n}$ and $\mathbf{d}_{M,k}$. To this end, the χ^2 test metric is suggested, which is given by

$$c_{nk} = \frac{1}{2} \sum_{r=1}^{\mathrm{R}} \frac{\left[d_{\mathrm{S},n}(r) - d_{M,k}(r)\right]^2}{d_{\mathrm{S},n}(r) + d_{M,k}(r)} \tag{5.16}$$

where $d(r)$ is the rth element of the descriptor vector $\mathbf{d}$. Possible modifications aim at considering further aspects in the costs c_{nk}, e.g., appearance similarities, which can be measured by normalized cross correlations of image patches around each landmark point. Observe that (5.16) is a measure of dissimilarity, i.e., in order to find the correct correspondence (5.16) has to be minimized. If we want to convert the problem into a maximization problem, a weight w_{nk} can be set such that $w_{nk} = c_{\max} - c_{nk}$.

The resulting bipartite graph matching problem can now be solved with the Hungarian method presented in the previous section. Belongie et al. [1], however, suggested to use the method of [11], which was considered to be more efficient in this case by the authors. Additionally, the total similarity value of the found matching can be utilized in a subsequent classification step (step 5 of the above proceeding).

Observe that with bipartite graph matching all correspondences are estimated through a joint optimization, whereas iterative methods like ICP search the best correspondence for each element individually. As a consequence, the estimated correspondences should contain less outliers, and, therefore, no iterative proceeding is needed; the aligning transform can (hopefully) be estimated reliably in a single step.

The authors of [1] tested object recognition with shape contexts in different applications, such as handwritten digit recognition and trademark retrieval. Figure 5.16 presents some of their results for trademark retrieval. The left icon of each group is the query trademark, whereas the three icons to the right of the query icon show the top three most similar icons of a model database as suggested by the algorithm. The numbers given below indicate the distance calculated by the system.

A very recent approach of estimating the correspondences between two 3D shapes uses bipartite graph matching as a building block (see [20]). There, the point set to be matched is sampled from a mesh representation of the shapes. The method does not make use of descriptors; the weights of the bipartite graph, which

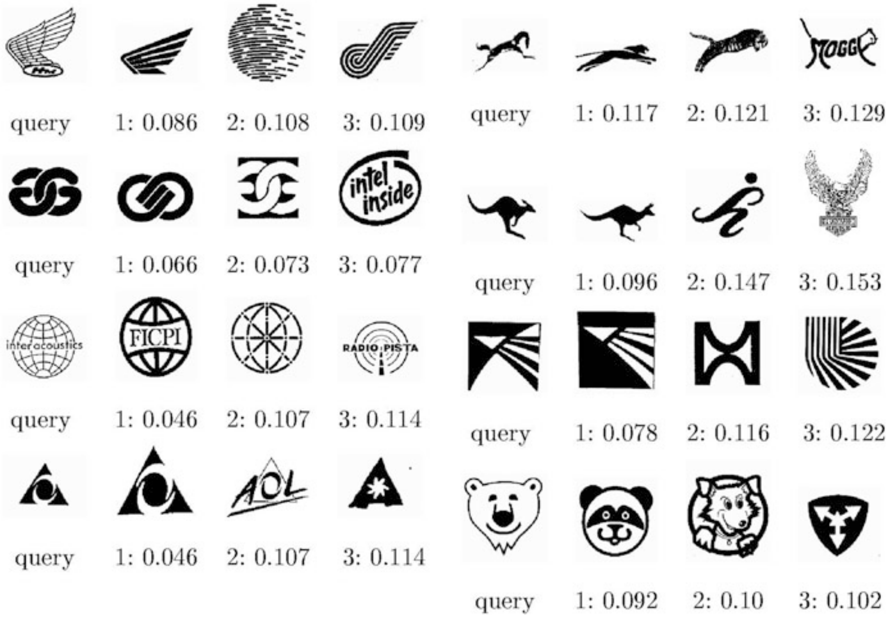

Fig. 5.16 Illustrating the performance of the algorithm in the context of trademark retrieval (© 2002 IEEE. Reprinted, with permission, from Belongie et al. [1])

indicate the probabilities that two points from different shapes correspond to each other, are derived from a spectral embedding of the sampled mesh points (as described earlier in this chapter, c.f. [10]) instead.

Subsequently, the correspondences are estimated in an iterative Expectation-Maximization (EM) algorithm. In the M-Step the correspondences are estimated via bipartite graph matching, followed by a refinement step which also allows for many-to-one mappings. The E-Step updates the weights of the bipartite graph, i.e., the probabilities that two points form a correspondence. M-Step and E-Step are performed in alternation until convergence.

The combination of various methods (spectral embedding, bipartite graph matching, iterative refinement) into one framework results in very accurate results, as was shown in [20]. In order to get an impression of the performance, the interested reader is referred to the figures presented in the original article [20].

References

1. Belongie S, Malik J, Puzicha J (2002) Shape matching and object recognition using shape contexts. IEEE Trans Pattern Anal Mach Intell 24(4):509–522
2. Besl PJ, McKay ND (1992) A method for registration of 3-D shapes. IEEE Trans Pattern Anal Mach Intell 14(2):239–256

3. Choi S, Kim T, Yu W (2009) Performance evaluation of RANSAC family. In: Proceedings of the British machine vision conference, London, pp 81.1–81.12
4. Duchenne O, Bach F, Kweon I-S, Ponce J (2011) A tensor-based algorithm for high-order graph matching. IEEE Trans Pattern Anal Mach Intell 33:2383–2395
5. Egozi A, Keller Y, Guterman H (2013) A probabilistic approach to spectral graph matching. IEEE Trans Pattern Anal Mach Intell 35(1):18–27
6. Fishler MA, Bolles RC (1981) Random sample consensus: a paradigm for model fitting with applications to image analysis and automated cartography. Mag Commun ACM 24 (6):381–395
7. Fitzgibbon AW (2003) Robust registration of 2D and 3D point sets. Image Vis Comput 21 (13–14):1145–1153
8. Harris C, Stephens M (1988) A combined corner and edge detector. In: Alvey vision conference, Manchester, pp 147–151
9. Hartley R, Zisserman A (2004) Multiple view geometry in computer vision, 2nd edn. Cambridge University Press, Cambridge. ISBN 978–0521540513
10. Jain V, Zhang H (2006) Robust 3D shape correspondence in the spectral domain. IEEE Int Conf Shape Model Appl 118–129
11. Jonker R, Volgenant A (1987) A shortest augmenting path algorithm for dense and sparse linear assignment problems. J Comput 38:325–340
12. Kuhn HW (1955) The Hungarian method for the assignment problem. Nav Res Logist Q 2:83–87
13. Leordeanu M, Herbert M (2005) A spectral technique for correspondence problems using pairwise constraints. In: Proceedings of the 10th IEEE international conference on computer vision, vol 2, Beijing, pp 1482–1489
14. Lowe DG (2004) Distinctive image features from scale-invariant viewpoints. Int J Comput Vis 60:91–111
15. Marquardt D (1963) An algorithm for least-squares estimation of nonlinear parameters. SIAM J Appl Math 11(2):431–441
16. Mikolajczyk K, Schmid C (2005) A performance evaluation of local descriptors. IEEE Trans Pattern Anal Mach Intell 27(10):1615–1630
17. Mikolajczyk K, Tuytelaars T, Schmid C, Zisserman A, Matas J, Schaffalitzky F, Kadir T, Van Gool L (2005) A comparison of affine region detectors. Int J Comput Vis 65:43–72
17. Munkres J (1957) Algorithms for assignment and transportation problems. J Soc Ind Appl Math 5(1):32–38
18. Rubner Y, Tomasi C, Leonidas JG (2000) The earth mover's distance as a metric for image retrieval. Int J Comput Vis 40(2):99–121
19. Rummel P, Beutel W (1984) Workpiece recognition and inspection by a model-based scene analysis system. Pattern Recognit 17(1):141–148
20. Sahilloglu Y, Yemez Y (2012) Minimum-distortion isometric shape correspondence using EM algorithm. IEEE Trans Pattern Anal Mach Intell 34(11):2203–2215
21. Schmid C, Mohr R (1997) Local grey value invariants for image retrieval. IEEE Trans Pattern Anal Mach Intell 19:530–535
22. Trefethen LN, Bau D (1997) Numerical linear algebra. Society for Industrial and Applied Mathematics, Philadelphia. ISBN 978-0898713619
23. Treiber M (2010) An introduction to object recognition – selected algorithms for a wide variety of applications. Springer, London. ISBN 978–1849962346

Chapter 6
Graph Cuts

Abstract Energy functions consisting of a pixel-wise sum of data-driven energies as well as a sum of terms affected by two adjacent pixels (aiming at ensuring consistency for neighboring pixels) are quite common in computer vision. This kind of energy can be represented well by Markov Random Fields (MRFs). If we have to take a binary decision, e.g., in binary segmentation, where each pixel has to be labeled as “object” or “background,” the MRF can be supplemented by two additional nodes, each representing one of the two labels. The globally optimal solution of the resulting graph can be found by finding its minimum cut (where the sum of the weights of all severed edges is minimized) in polynomial time by maximum flow algorithms. Graph cuts can be extended to the multi-label case, where it is either possible to find the exact solution when the labels are linearly ordered or the solution is approximated by iteratively solving binary decisions. An instance of the max-flow algorithm, binary segmentation, as well as stereo matching and optical flow calculation, which can both be interpreted as multi-labeling tasks, is presented in this chapter. Normalized cuts seeking a spectral, i.e., eigenvalue solution, complete the chapter.

6.1 Binary Optimization with Graph Cuts

6.1.1 Problem Formulation

Many computer vision problems can be modeled by a *Markov Random Field* (MRF), because MRFs are well suited for representing a class of energy functions which are of widespread use in computer vision. These energy functions mainly consist of two terms (cf. (6.1)):

- A *data-driven* term E_{d}, where we can evaluate for each pixel p (represented by a node in the MRF) how well our estimations correspond to the observed data.

M.A. Treiber, *Optimization for Computer Vision: An Introduction to Core Concepts and Methods*, Advances in Computer Vision and Pattern Recognition,
DOI 10.1007/978-1-4471-5283-5_6, © Springer-Verlag London 2013

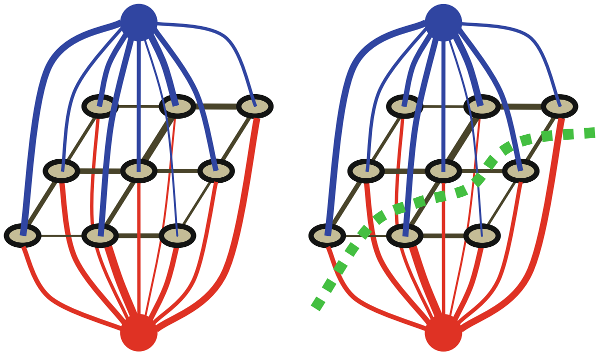

Fig. 6.1 Illustrating the topology of a two-terminal graph (*left*), for which a minimum cut is to be calculated (*right*, *cut in green*)

- *Interaction potentials* E_{int} between adjacent pixels (nodes of the MRF), which measure the "consistency" between estimations of adjacent pixels p and q, e.g., all pixels within a 4-neighborhood $\mathcal{N}$.

$$E_{MRF} = \sum_{p} E_{\text{d}}(p) + \sum_{p,q \in \mathcal{N}} E_{\text{int}}(p,q) \tag{6.1}$$

Consider a binary segmentation task, for example, where we want to partition an image into object and background, i.e., we have to decide for each pixel p whether it can be classified as "object" or "background." Informally speaking, a "good" segmentation is obtained when all pixels of the same class have similar intensities (or colors) and if the boundaries between pixels labeled as "object" and "background" are located such that adjacent pixels of different labels have dissimilar intensities/colors. The mapping of these criteria to the two terms of the energy of (6.1) is straightforward as follows:

- E_{d} measuring data fidelity can be derived from an evaluation how well the observed data at pixel p fits into intensity/color statistics obtained from pixels with known labeling, which could, e.g., be brightness histograms or Gaussian mixture models of color distributions.
- The interaction potentials E_{int}, which measure the cost of assigning different labels to adjacent pixels, can be based on the intensity or color difference between adjacent pixels p and q (e.g., where q is located within a 4-neighborhood around p). High differences are mapped to low costs and vice versa.

This kind of energy function can be modeled by an MRF, where each pixel p is represented by a node (see Fig. 6.1 for a small example covering just 3 × 3 pixels). In accordance to the pixel grid, these nodes are arranged in a rectangular two-dimensional grid. Adjacent nodes p and q are connected by an edge e_{pq} (black lines in Fig. 6.1). For example, a node p can be connected to all nodes within its 4-neighborhood. Another common choice is connecting all nodes within an 8-neighborhood. The weight w_{pq} of each edge e_{pq} represents the interaction potentials $E_{\text{int}}(p,q)$ between adjacent pixels. w_{pq} should be high when the intensities/colors of

p and q are similar. The numerical value of the weights is indicated by the thickness of the connections in Fig. 6.1.

In order to incorporate the data-driven terms E_{d}, two additional so-called terminal nodes (one "*source*" node s and one "*sink*" t) are introduced. Every nonterminal node can be connected to s as well as t by additional edges e_{ps} and e_{pt}. These edges are also called *t-links* (terminal links), whereas edges between two nonterminal nodes are called *n-links* (neighborhood links). Each terminal node represents a label, e.g., for binary segmentation s can be chosen as "object terminal" and t as "background terminal."

The weights w_{ps} reflect the fidelity of the intensity/color at pixel p to the object pixel statistics (and w_{pt} the fidelity to the statistics of the background pixels). Hence, w_{ps} should be high (and w_{pt} low) if the data observed at p fits well into the statistics of all known object pixels. Respectively, w_{ps} should be low (and w_{pt} high) when the appearance at p is in accordance with background appearance.

As a summary, the whole setting is described by a graph $G = (N, E)$ consisting of nonterminal nodes representing the pixels of the image, two terminal nodes representing the two labels "object" and "background," as well as edges connecting the nodes, whose weights represent the energies as defined in (6.1).

A binary segmentation of the image can now be represented by a so-called graph cut. A cut C of a graph is a subset of edges ($C \subset E$), which separate the node set N of the graph into two disjoint subsets A and B, i.e., $N = A \cup B$ and $A \cap B = \{\}$. C defines a valid binary segmentation if the two terminals are contained in different subsets. This implies that each nonterminal node remains either connected to s or t, which can be interpreted as follows: if the node of a pixel still is connected to s, it is classified as "object"; if it remains connected to t, it is assigned to the "background" label.

For each cut C, we can define a so-called cut function E_C, which can be set to the sum of the weights of the edges it severs:

$$E_C = \sum_{e \in C} w_e \tag{6.2}$$

Consequently, the optimal segmentation can be found if we find the minimum cut, e.g., the subset of edges which minimizes (6.2):

$$C^* = \arg\min \sum_{e \in C} w_e \tag{6.3}$$

In the general case, the problem of finding the minimum cut is NP-hard, but for the special case of two terminals, it has been proven that the minimum cut can be found in polynomial time. Efficient algorithms are presented in the next section.

The main advantage of graph cuts is that in contrast to many other methods, it is possible to find a *global* optimum of the energy function defined in (6.1) if appropriate algorithms are employed to find the minimum cut. Moreover, the computational complexity of the worst case is quadratic with the number of pixels and in practice allows a rather fast optimization for typical image sizes. However, up to now, as we just have two terminals, only binary decisions can be modeled by graph cuts.

In fact, Grieg et al. [13] were the first to introduce graph cuts in computer vision applications by proposing to solve the problem of restoring binary images with graph cuts. Probably mainly due to this restriction, their work remained unnoticed for a long time. However, in the meantime it was discovered that a fairly large amount of vision problems can be tackled by binary decisions, and, furthermore, graph cuts can be extended to a multi-label case efficiently. As a consequence, this field became a quite active area of research over the last decade.

6.1.2 The Maximum Flow Algorithm

Now that we know how to build a graph representing energy functions for binary labeling problems in the form of (6.1), let's turn to the question how to find the minimum cut of the graph. Please note that most algorithms do not try to solve the optimization problem of (6.3) directly. Instead, they seek for the so-called maximum flow through the graph, which was shown by Ford and Fulkerson [9] to yield the same solution as finding the minimum cut.

Here, the edges of the graph are interpreted as "pipes," which can be used to pump water through them. The maximum total amount of water which can be pumped from the source to the sink is called the maximum flow. The weight of each edge can be interpreted as the "capacity" defining the maximum amount of water which can run through the corresponding pipe segment. An edge is called "saturated" if it contains as much water as possible and, consequently, there is no spare capacity left. We can increase the total flow through the graph until the maximum flow is found. At that point, every possible path from s to t contains at least one saturated edge, because if there would exist a path where every segment has spare capacity left, we could further increase the flow.

According to Ford and Fulkerson, the maximum flow solution, which yields a set of saturated edges, is equivalent to the minimum cut solution. After calculating the maximum flow, the set of saturated edges directly leads to the minimum cut solution (if a unique solution exists) as follows: If we exclude all saturated edges from the graph, every nonterminal node remains connected either to the source or the sink. Consequently, the set of saturated edges partitions the graph into two disjoint node subsets. Consequently, all former edges between nodes belonging to different subsets must be part of the minimum cut.

Informally speaking, evidence for equivalence of the maximum flow and minimum cut solution is given because of two reasons:

- Every path from s to t has to contain at least one saturated edge. Otherwise, there would be some capacity left at each pipe segment of the path and we could increase the flow. The fact that there is at least one saturated edge in every path

from s to t ensures the fact that s and t are contained in different subsets of the partitioned graph.
- Pipes with small capacity are expected to saturate soon as the flow through the graph increases. This corresponds to the fact that the minimum cut should contain many edges with small weight.

Basically, there are two main classes of algorithms intending to find the maximum flow:

- *Augmenting path* algorithms: This type dates back to the article of Dinic [8] and is an iterative procedure, which maintains a "valid" flow at each iteration. In order to be a valid solution, the incoming flow has to be equal to the outgoing flow at every node of the graph. Starting from zero flow, these methods try to iteratively increase ("augment") the total flow by first identifying a path with spare capacity left and then increasing the flow through this path as much as possible in each iteration step. The iteration terminates when no more increase is possible.
- *Push/relabel* algorithms introduced by Goldberg [11] allow the nodes to have a flow "excess," when the incoming flow is larger than the outgoing flow. As the occurrence of an excess represents an invalid total flow, the excess has to be eliminated again at some point of the proceeding. To this end, the algorithm seeks to distribute the excess occurring at a node among its neighbors. Without going into details here, we refer the interested reader to [7], which gives a good explanation of this class of algorithms.

In the following, we want to present the algorithm of Boykov and Kolmogorov [3], which falls into the class of augmenting path algorithms and tries to reuse information gathered at previous iterations during the search for paths with spare capacity. While it is commonly accepted that push/relabel algorithms perform best for general graph cut applications, the authors of [3] experimentally showed that their algorithm outperformed other max-flow methods in the special context of typical vision applications.

As already mentioned, augmenting path algorithms fall into the class of iterative procedures, where in each iteration a path from s to t with spare capacity is identified first. Next, we can try to increase the flow along this path as much as possible. The iteration stops when no more growth of the flow is possible. Because the total flow is augmented at each step (and never reduced), the algorithm is guaranteed to converge.

In order to identify paths with spare capacity in an efficient manner, the algorithm maintains two data structures, a so-called residual graph and a search tree:

- The *residual graph* has the same topology as the graph to be optimized, but in contrast to the "main" graph, the weights of its edges are set to the spare capacity which can be used to augment the flow along these edges. At start (where the total flow is zero), the residual graph is identical to the main graph. As iteration proceeds, the weights of its edges will successively be reduced. As a consequence, saturated edges will disappear, because their spare capacity (and consequently their weight in the residual graph) will be zero. With the help of the

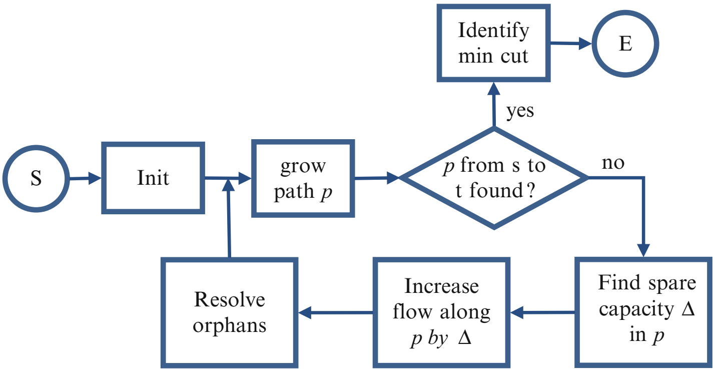

Fig. 6.2 Flowchart of the max-flow algorithm

residual graph, the algorithm is able to identify the amount of "delta flow" we can add to the total flow, once an augmenting path is identified. Additionally, it helps when building the second data structure (the so-called search tree).

- The *search tree* enables the scheme to identify the path to be augmented at each iteration in an efficient manner. It consists of "active" as well as "passive" nodes. Nodes are called active if the tree can grow at these nodes, i.e., new children can be connected to these nodes (all active nodes are summarized in the set A). Potential children of a node n are the set of neighbors of n in the residual graph. Passive nodes cannot grow any longer. At start, the set S, which summarizes all nodes the tree contains, consists of just the source node s: $S = \{s\}$. At each iteration, the algorithm intends to grow the tree until it contains the sink t. To this end, it selects a node from the set T, which is composed of all "free" nodes not being part of the search tree yet. Once t is added to the tree, a path from s to t which can be augmented is found. As the augmentation involves the appearance of saturated edges, the tree has to be pruned accordingly at the end of each iteration. The modified tree can be reused in the next iteration. Because the search tree is maintained and modified throughout the whole procedure, it gathers knowledge of previous iterations, which helps to accelerate the search for new paths.

Overall, each iteration comprises the following three steps (see also flowchart of Fig. 6.2):

- *Growth stage*: This stage expands the search tree until the sink is added to the tree. After that, a path with spare capacity, which can be used to augment the total flow, can be identified in the next stage. During expansion, the algorithm iteratively picks a node a of the active node set A and adds free nodes which are picked from set T to the tree. The condition for this purpose is that a free node b is linked to a in the residual graph, i.e., that it is a neighbor of the pixel which is represented by a and the edge e_{ab} linking both nodes has spare capacity left. The iteration stops either if T becomes empty (then the scheme has terminated as no more augmentation is possible) or if the sink t is added to the tree.

- *Augmentation stage*: Starting from t, the tree can be traced back to the source s, which allows us to identify the path p to be augmented: p consists of all nodes we passed when tracing back the tree. The next task is to identify the smallest spare capacity Δ along p. This can be done by evaluating the edge strengths of the residual graph. Now we can augment the flow by adding Δ. Consequently, the strength of all edges along p has to be reduced by Δ in the residual graph. Please note that now at least one edge becomes saturated. Accordingly, all newly saturated edges are removed from the residual graph and from the tree as well. As a result, some nodes of the search tree become "orphans," i.e., they don't have a parent any longer. These nodes are collected in the set O. In other words, the tree splits into a "forest," where the newly emerged trees have some node of O as root.
- *Adaption stage*: In this stage, the aim is to recover a single tree from the forest. To this end, either a new parent has to be found for each orphan or, if this is not possible, the orphan has to be removed from the tree and added to the set of free nodes T. In that case, all of the children of that orphan have to be added to O (and subsequently processed in the adaption stage) as well. This stage terminates when O becomes empty. In order to find a parent for an orphan $o \in O$, all nodes q, which are linked to o via a non-saturated edge, are checked. If $q \in S$, and if the tree to which q belongs to has the source s as root, then q can be accepted as a new parent of o. If these conditions are met by none of the members, o is removed from the tree and all children of o are added to O. These nodes are also added to the active node set A (if they are not active already), because those nodes are neighbors of o, which has just been added to the free node set. This means that there exists a free neighbor for all those nodes, i.e., a possibility to expand the tree, and consequently their status has to be set to "active."

Pseudocode

```
function augmentingPathMinGraphCut (in graph $G = (N, E)$, out
minimum cut $C^*$)

// initialization
$S \leftarrow \{s\}$          // the only node of search tree is source node
$A \leftarrow \{s\}$          // the only active node is the source node
$T \leftarrow N - \{s\}$      // all other nodes are "free" nodes
$O \leftarrow \{\}$           // no "orphans"
$G_R = G$                     // residual graph $G_R$ is equal to "main" graph

// main iteration loop
repeat
  // growth stage
  $p = \{\}$                  // no augmenting path is known at this point
  if $t \in S$ then           // tree contains sink from previous step
    trace back tree from $t$ to $s \rightarrow$ identify and set path $p$
  end if
  while $p == \{\} \wedge A \neq \{\}$   // active nodes for expansion exist
     randomly pick an active node $a \in A$
```

```
   for all non-saturated edges $e_{aq}$ linking $a$ to some neighbor $q$
     if $q \in T$ then    // $q$ is a free node
       $S \leftarrow S \cup \{q\}$      // add $q$ to search tree
       $A \leftarrow A \cup \{q\}$      // $q$ is an active node
       $T \leftarrow T - \{q\}$      // remove $q$ form free node set
       Remember $a$ as parent of $q$ (for backtracking)
       if $q == t$ then // path to sink found
         trace back tree from $t$ to $s$ → identify $p$
         break  // path found → terminate while-loop of growth stage
       end if
     end if
  next
  $A \leftarrow A - \{a\}$     // all neighbors of $a$ are processed
end while

// augmentation stage
if $p \neq \{\}$ then   // augmenting path is found: $p$ not empty)
  find smallest free capacity $\Delta$ along $p$
  update $G_R$ by decreasing all data weights along $p$ by $\Delta$
  for each edge $e_{qr}$ becoming saturated
     $O \leftarrow O \cup \{r\}$          // $r$ becomes an "orphan"
  next

  // adaption stage
  while  $O \neq \{\}$      // orphans still exist and must be eliminated
     randomly pick an orphan $o \in O$
     bParentFound ← false
     for all non-saturated edges $e_{qo}$ linking a potential new parent $q$ of $o$ to $o$
       if $q \in S$ and $q$ is linked to source $s$ then
         // parent found
         connect $o$ to $q$ in search tree
         bParentFound ← true
         break  // abort for-loop as new parent is found
       end if
     next
     if bParentFound == false then // no parent found
       $S \leftarrow S - \{o\}$         // remove $o$ from tree
       $A \leftarrow A - \{o\}$ if $o \in A$      // free node can't be active
       $T \leftarrow T \cup \{o\}$         // add $o$ to free node set
       add all children of $o$ to the set of orphans $O$
       add all children of $o$ to active node set $A$, if they currently are $\notin A$
     end if
```

```
            $O \leftarrow O - \{o\}$            // o is processed now
        end while
    end if
until $p == \{\}$        // terminate when no augmentation path is
found

// find minimum cut
$C^* \leftarrow \{\}$
for all edges $e \in E$
    if $e \notin G_R$ then    // e is saturated (not part of $G_R$)
        $C^* \leftarrow C^* \cup \{e\}$    // add e to minimum cut
    end if
next
```

6.1.3 Example: Interactive Object Segmentation/GrabCut

As already mentioned, graph cuts can be used for binary segmentation (see, e.g., [1, 2]), where the task is to partition every pixel of an image into one of two sets ("object" and "background").

This task can be accomplished by finding the minimum cut of a graph G as presented above, where the nodes are arranged in a rectangular grid. Each pixel is represented by one node p, which is linked to its neighbors. In [2] an 8-neighborhood is used, but other topologies are possible. Additionally, G contains two terminal nodes, where the source s is called "object terminal" and the sink t represents the "background terminal."

A cut of G, which partitions the node set into two disjoint subsets A and B, where s and t are forced to belong to different subsets, defines a segmentation such that all pixels remaining connected to s are considered to be classified as "object" pixels. Accordingly, all pixels remaining connected to t are considered to be classified as "background" pixels. The segmentation boundary is defined by all n-links between two nonterminal nodes being severed by the cut. Observe that such a cut imposes no topology constraints, i.e., the "object area" can be split into multiple regions, which can also have holes, and so on.

A segmentation can be specified by a binary vector $\mathbf{l}$, whose number of elements is equal to the number of pixels. The entry $l_p \in \{0, 1\}$ relating to pixel/node p is set to 1 if p belongs to the object region and set to 0 if p belongs to the background region, respectively.

The "quality" of a segmentation can be measured by a cost function $E(\mathbf{l})$ consisting of two terms:

$$\begin{aligned} E(\mathbf{l}) &= \quad = \lambda \cdot R(\mathbf{l}) + B(\mathbf{l}) \\ &= \sum_p R_p(l_p) + \sum_{\{p,q\} \in \mathcal{N}} B_{pq} \cdot \delta_{l_p \neq l_q} \end{aligned} \tag{6.4}$$

where λ is a weighting factor balancing the two terms. The two contributions of the cost can be explained as follows:

- The *regional term* $R(\mathbf{l})$ evaluates how well the pixels fit into the region they are assigned to (which is defined by $\mathbf{l}$). To this end, it sums up the contributions $R_p(l_p)$ of each pixel p (the $R_p(l_p)$ sometimes are also called unary term, as they are affected by only one pixel). A simple measure is how well the intensity (or color) of p fits into an intensity (or color) distribution, which for now is assumed to be known for both regions. The R_p's should act as a cost: if the intensity I_p of p correlates well with the intensity distribution of the "object class," $R_p(1)$ should be low (conversely, $R_p(0)$ should be low if I_p fits well into the background statistic). The R_p's can be represented by the edge weights of the t-links in the graph. For example, if I_p is in accordance with the "object distribution," there should be a strong link to the source (object) terminal s and a weak link to the sink (background) terminal t. Therefore, the edge weight w_{pt} of the edge connecting p with the terminal is set to $R_p(1)$ (which is low in case I_p fits well into the object intensity distribution and can therefore be severed at low cost). The edge weight w_{ps} to the source is set to $R_p(0)$, respectively.
- The *boundary term* $B(\mathbf{l})$ defines the cost of assigning adjacent pixels to different regions. It therefore consists of the sum of the contributions B_{pq} of all combinations of pixels p and q located in a neighborhood $\mathcal{N}$, e.g., 8-neighborhood. The δ-function ensures that we only count costs when p and q are assigned to different regions, i.e., $l_p \neq l_q$. A simple measure for B_{pq} is based on the intensity difference between p and q: if I_p is similar to I_q, B_{pq} should be high, because it is unlikely that adjacent pixels with similar appearance belong to different regions. The B_{pq} can be represented by the edge weights w_{pq} of the n-links in the graph.

The aim of the segmentation algorithm is to find a segmentation $\mathbf{l}^*$ such that $E(\mathbf{l})$ is minimized: $\mathbf{l}^* = \arg\min_{\mathbf{l}} E(\mathbf{l})$. In order to find $\mathbf{l}^*$, we can apply a minimum graph cut algorithm, because – if we set the edge weights as just explained – $E(\mathbf{l})$ is defined by the sum of the weights of all edges of G being severed by a particular cut. Hence, finding the minimum cut also reveals an optimal segmentation in the sense that $E(\mathbf{l})$ is minimized.

Up to now, an open question is how to calculate the individual costs R_p and B_{pq}. Considering the boundary costs B_{pq}, it can be assumed that the cost of a cut is high, if the intensities of p and q are similar. This can be expressed by

$$B_{pq} = \exp\left(-\frac{(I_p - I_q)^2}{2\sigma^2}\right) \cdot \frac{1}{d(p,q)} \tag{6.5}$$

where $d(p,q)$ denotes the spatial distance between p and q. In a 4-neighborhood this term can be neglected, but in a 8-neighborhood it can be used to devalue the diagonal relationships.

As desired, B_{pq} takes low values when I_p and I_q are quite different. However, please note that intensity differences between single pixels are sensitive to camera noise. Generally, it is not indented to obtain low values of B_{pq} because of noise. Therefore, the factor σ is introduced. σ determines how much I_p and I_q have to differ for a low cost. Roughly speaking, the cost is small if $\left| I_p - I_q \right| < \sigma$. Hence, a proper value of σ can be derived from camera noise estimation.

As far as the regional terms R_p are concerned, we need to define a quantity measuring how well the intensity I_p fits into intensity statistics of the object or background pixels. For the moment, let's assume that we know the intensity histograms H_{O} of the "object" class and H_{B} of the "background class," respectively. After appropriate smoothing, H_{O} and H_{B} can directly be interpreted as a probability that a pixel with intensity I belongs to the corresponding class: $P\left(l_p = 1\right) \propto H_{\mathrm{O}}\left(I_p\right)$ and $P\left(l_p = 0\right) \propto H_{\mathrm{B}}\left(I_p\right)$, respectively. However, we need costs instead of probabilities. Observe that probabilities can easily be converted into costs if we take the negative logarithm of the probability distribution. Consequently, the R_p can be expressed as

$$R_p\left(l_p\right) = \begin{cases} -\ln\left[\tilde{H}_{\mathrm{O}}\left(I_p\right)\right] & \text{if } l_p = 1 \\ -\ln\left[\tilde{H}_{\mathrm{B}}\left(I_p\right)\right] & \text{if } l_p = 0 \end{cases} \tag{6.6}$$

where the $\tilde{H}_{\mathrm{O}}$ and $\tilde{H}_{\mathrm{B}}$ are smoothed and scaled versions (such that the sum of all entries equals 1) of the intensity histograms. With (6.5) and (6.6) the graph is completely defined. Its minimum cut can, e.g., be found by applying the method described in the previous section.

But there still is the open question how to get knowledge about the distributions $\tilde{H}_{\mathrm{O}}$ and $\tilde{H}_{\mathrm{B}}$. In some applications, $\tilde{H}_{\mathrm{O}}$ and $\tilde{H}_{\mathrm{B}}$ can be derived from a priori knowledge. However, this might not be possible in every case. Therefore, [2] suggest an interactive procedure: At start, the user marks some pixels as "object" and some as "background" by drawing brushes upon the image. Now the system can derive the histograms from the regions covered by the brushes.

Because the marked pixels just have to be located somewhere within the object and background regions, the exact position of the brush is not crucial. This fact makes this type of user input rather convenient (compared, e.g., to a definition of boundary pixels as necessary in the "intelligent scissors" method presented in the next chapter, where the positions should be as accurate as possible).

Please note that there is a second way of making use of the brushes: In fact, the pixels of the brushed regions have already been classified by the user. This classification acts as "hard constraints" for the subsequent automatic segmentation, as it must not be changed by the system. Consequently, we can set the R_p's of those pixels such that it is ensured that the label of those pixels remains unchanged. Observe that these hard constraints simplify the problem, because the number of unknowns is reduced.

An example of the performance of graph cut segmentation can be seen in Fig. 6.3, where the segmentation result is indicated by the coloring. While the original images are grayscale, the segmented background is colored blue, whereas the object area is indicated by red color. The solid red and blue brushes indicate the user input serving as hard constraints. As clearly can be seen, the method is capable

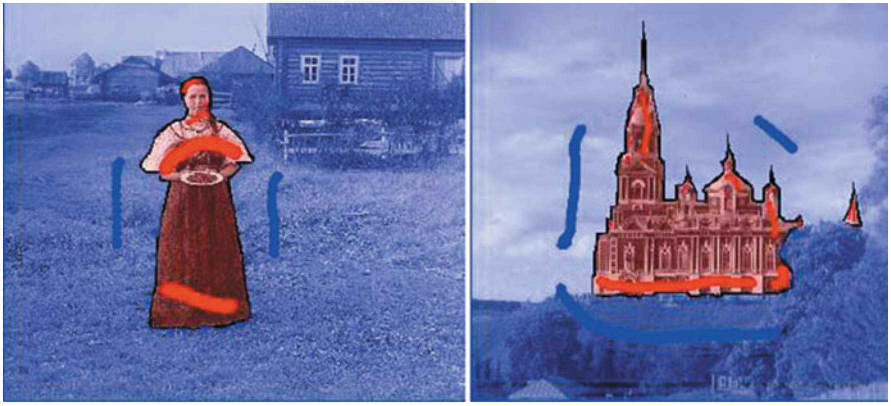

Fig. 6.3 Exemplifying the performance of graph cut segmentation for two grayscale photographs (From Boykov and Funka-Lea [1], with kind permission from Springer Science and Business Media)

of accurately separating the object of interest from the background, even in the presence of considerable texture in both regions.

Observe that the segmentation process can also be implemented as an interactive update procedure: after a first "round" of user input, the system calculates the minimum cut according to this input and presents the segmentation result to the user. Now, the user can add additional brushes in order to refine the result. The newly added brushes lead to new hard constraints and the graph is adjusted accordingly by changing the weights of the affected *t*-links. Based on the former solution, the system can now calculate a refined segmentation very quickly. Of course, additional update steps are possible.

However, new user input leads to an altered segmentation result only if the user-specified label differs from the automatic labeling. Moreover, the change of the *t*-link weights might involve a reduction of weights such that the constraint that all paths from the source terminal to the sink contain a valid flow gets violated. This would mean that the new solution would have to be calculated from scratch again.

Such a situation can be avoided, though, if the weight is increased for both *t*-links of a node being affected by the new hard constraints appropriately (see [1] for details)

One advantage of graph cuts is that an extension to higher dimensional data is straightforward. For example, the two-dimensional graph grid can be extended to a 3D volume of nodes, which are connected by 6- or 26-neighborhoods. Then, the minimum cut defines a 2D surface, which optimally separates object volumes from the background.

A typical application is the segmentation of volumetric data in medical imaging. Figure 6.4 shows an example of this, where the task is to separate bone tissue in a 3D volume acquired by a CT scanner. The user can specify the hard constraints in one (or more) 2D slice(s) of the data (left image, red: bone tissue, blue: background). After that, the system is able to generate a 3D segmentation based on this input (right image, showing the extracted bone tissue volume).

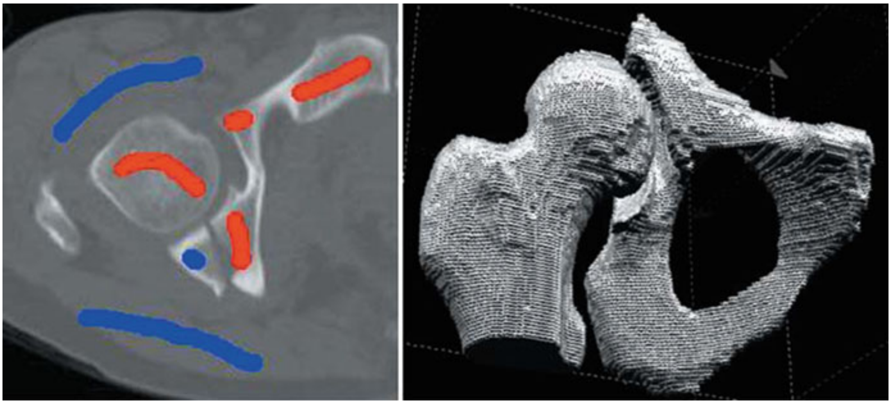

Fig. 6.4 Showing an example of the usage of graph cuts in 3D segmentation for a medical imaging application (From Boykov and Funka-Lea [1], with kind permission)

A further modification is to introduce *directed* edges in the graph. In doing so, neighboring nonterminal nodes are connected via a *pair* of directed n-links of opposite direction (see the graph example in left of Fig. 6.5). If a cut separates two neighboring nodes, exactly one of the edge weights is contained in the total cut cost, whereas the other is ignored. For example, if p remains connected to the source (object) terminal and q to the sink (background), we can specify that the weight w_{pq} contributes to the cut cost and w_{qp} is ignored. Respectively, if p remains connected to the sink and q to the source, w_{qp} is considered in the cut cost calculation and w_{pq} is ignored.

Such a modeling helps to incorporate contrast direction information, for example. Suppose we know in advance that the object we want to segment should be brighter than the background. Then, we can set w_{pq} to a high constant value in the case of $I_p < I_q$, because if the cut separates p and q such that p remains connected to the source/"object" terminal, by definition we have to include w_{pq} into the cost. Taking a priori knowledge into account, this should not occur and therefore has to be punished. As far as the w_{qp} are concerned, they can be set according to (6.5), because the higher the difference $I_p - I_q$, the lower the cut cost should be.

Such a refined modeling can help to considerably improve segmentation result, as Fig. 6.5 shows. Here, we want to segment the liver tissue from the background. The liver tissue is known to appear brighter than the muscle tissue, which surrounds it. However, very bright bone tissue can be located very close to the liver. Without this knowledge, the system calculates a segmentation boundary along the bone, because there the local contrast is very high (second image from the right in Fig. 6.5). Considering contrast direction information leads to the result shown in the right image of Fig. 6.5, which is more accurate (especially near the bone tissue).

The *GrabCut* system proposed by Rother et al. [16] enhances the binary segmentation scheme of [2] in three respects:

- As the method is designed for color images, the region costs R_p are derived from the similarity of the color at pixel p to a mixture of Gaussian distributions

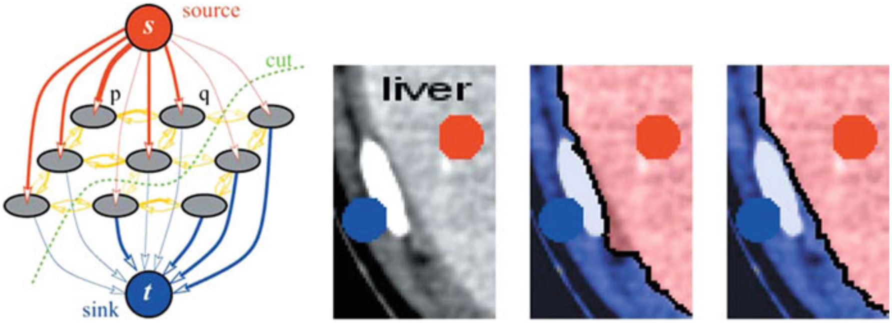

Fig. 6.5 Illustrating the improvement when using directed graphs (*left*). The *right part* exemplifies this enhancement for an example of a medical image segmentation (see text for details) (From Boykov and Funka-Lea [1], with kind permission from Springer Science and Business Media)

(Gaussian mixture model/GMM) instead of simple intensity histograms. This allows for a more precise modeling of the object and background statistics and hence improves the segmentation quality.

- The segmentation is calculated in an iterative manner without additional user input between the iterations. Starting with an initial GMM, the algorithm calculates an initial segmentation and then iteratively alternates between an update of the GMM based on the segmentation result and an update of the segmentation based on the improved GMM, until convergence is achieved. This simplifies the user input in two respects: First, the algorithm can start with a single rectangular bounding box containing the object specified by the user instead of multiple brushed regions. Second, less "correction steps" with additional hard constraints specified by the user are needed.
- A border matting process is performed after "hard" segmentation, which calculates alpha values in a small strip around the segmentation boundary which was found by the minimum cut. This allows for soft transitions between object and background and thereby reduces artifacts caused by pixels showing a mixture of foreground and background (e.g., due to blur) in the original image.

An example of the good performance of the algorithm can be seen in Fig. 6.6, where, despite the challenging situation, the scheme is able to produce a good segmentation result.

6.1.3.1 Rating

Let's give some notes about what distinguishes graph cuts from other optimization methods. At first, there is to mention that graph cuts are able to find the *global* optimum, whereas, e.g., variational methods conceptually just search just a local optimum (if the energy functional is not convex) by solving the Euler-Lagrange equation. In that case we have no guarantee how close the local solution gets to the

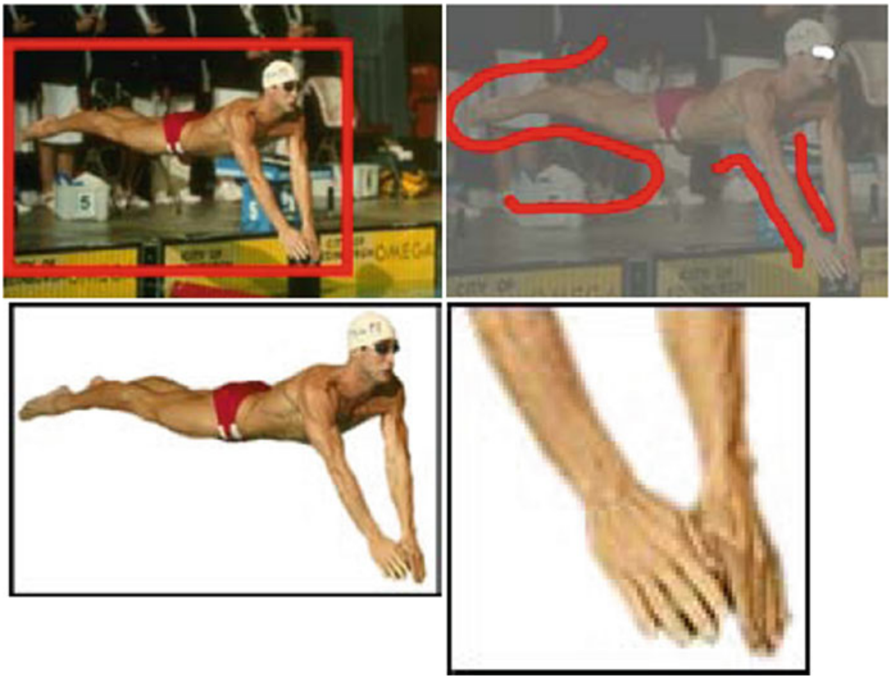

Fig. 6.6 Exemplifying the performance of the iterative GrabCut segmentation. The original image (*red rectangle*: initial user-specified region) is shown *upper left*. The *lower left image* shows the segmentation result after additionally adding some hard constraints (shown in the *upper right image*; background: *red brushes*, foreground: *white brush*). A close-up of the region around the hands, which is particularly difficult to segment is shown *lower right* ([16] © 2004 Association for Computing Machinery, Inc. Reprinted by permission)

global optimum. Compared to other segmentation methods using shortest path algorithms (like intelligent scissors; see next chapter), it can be seen that those methods only use boundary terms during optimization, whereas with graph cuts it is possible to include regional terms as well and, additionally, to perform a relative weighting of these two parts. Moreover, graph cuts offer the possibility of a straightforward extension to higher dimensions.

On the other hand, graph cuts are said to have a so-called shrinking bias, because there is a trend that the total cost sinks if only a few n-links are severed, especially in setups where the regional terms get high weighting.

6.1.4 Example: Automatic Segmentation for Object Recognition

Very recent applications of graph cuts and max-flow algorithms can be found in [5, 6] as well as [15], for example. We don't want to present these two algorithms in full detail here. Instead, they are included in order to stress that graph cuts and their

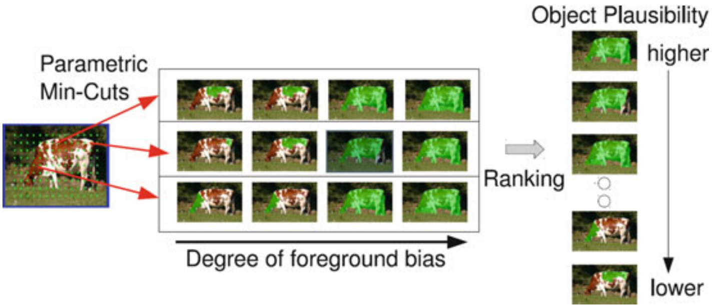

Fig. 6.7 Illustrating the algorithm flow of the parametric min-cut algorithm proposed by [5]: for each of the multiple foreground seeds, which are arranged on a rectangular grid structure (*green dots* in *leftmost image*), multiple minimum graph cut-based segmentations are calculated. The weights used in the according graphs differ in the bias for each pixel to belong to the foreground, and consequently, foreground regions of different size are found for each foreground seed (*middle part*, each row depicts the segmentation results of different graph cuts obtained from one seed). Each segmentation is ranked, where the top-ranked segmentations should represent valid segmentation results (*right part*) (© 2012 IEEE. Reprinted, with permission, from Carreira and Sminchisescu [6])

application still are an active area of research as well as to show that quite impressive results can be achieved, even in extremely challenging situations.

Now let's turn to the method proposed by Carreira and Sminchisescu [5, 6]. In contrast to the segmentation methods presented up to now, they suggest to perform *multiple* binary segmentations of the same image into foreground (object) and background regions in a first step. This is followed by a ranking and suppressing step, where redundant and obviously meaningless segmentations are suppressed. The remaining segmentations are ranked according to some criteria based on mid-level features like object area and compactness. The top-ranked segmentations could serve as input to a subsequent object recognition scheme. Figure 6.7 exemplifies the algorithm flow.

The currently prevailing proceeding for object recognition tasks is to avoid segmentation, mainly because of the ambiguity of low-level vision cues typically used for segmentation. Carreira and Sminchisescu argue that instead of a single segmentation, the proceeding of first computing *several* segmentations and subsequently ranking them could alleviate these problems. Besides, some applications like gripping, for example, require a precise separation of the object from the background, which requires a segmentation step at some point anyway. Imagine a gripping task, where a vision robot has to grasp the handle of a cup. In order to do this, it has to know the precise location of the handle, and therefore a pure detection of the object class "cup" in some rectangular window is not sufficient.

Carreira and Sminchisescu employ graph cuts for segmentation, too, but here no user interaction is required. Instead, they run multiple min-cut algorithms, each starting with an automatic assignment of some pixels to the two terminal nodes. To this end, the inner part of the image is sampled by a rectangular grid, and for each run of the graph cut algorithm, some pixels located near one particular grid position (the foreground seed) are linked to the foreground terminal. As far as the background terminal is concerned, some pixels of the image border are treated as background seeds at each run.

Additionally, the cost function employed for the regional term features a parameter λ, whose value can be chosen arbitrarily. Different values of λ result in a different bias of the cost function for assigning the pixels to the foreground. Consequently, multiple segmentations can be produced with the same seed pixels, as different values of λ are used. Please note that it is not necessary to run a separate max-flow algorithm for each value of λ. Instead, a variant of the max-flow algorithm, called *parametric max flow*, is able to calculate the minimum cuts for all values of λ in a single run.

In a last step, the segmentations are ranked based on a vector of different region properties like area, perimeter, and value of the cut (see [6] for details). As was shown by the authors, the top-ranked segmentations allow for a plausible interpretation of the scene, even in challenging situations. Their scheme performed best in the VOC 2009 and VOC 2010 image segmentation and labeling challenges, which supply a tough test bed and compare state-of-the-art algorithms. However, due to the multiple runs of the min-cut algorithm, their method is rather slow.

Another recent approach using graph cuts in order to obtain a binary segmentation is presented by [15]. Within their method, the segmentation task is formulated as the problem of finding the optimal boundary surrounding the region around a so-called fixation point, which roughly speaking defines a point of special interest which could be fixated by the eyes of a human observer. The fixation point can be estimated automatically by evaluating the saliency of all pixels of the interest region and taking the most salient one. This proceeding tries to imitate the human visual system, where there is evidence that humans first fixate a characteristic point and subsequently recognize the object around it.

Furthermore, the algorithm calculates a probability map being composed of the probabilities of each pixel for being part of the region border. Various cues are combined in order to estimate these probabilities. Obviously, intensity or color discontinuities or changes in the texture around a pixel indicate a high probability of being a border pixel. However, this can also occur inside an object.

In order to resolve this ambiguity, other cues like depth discontinuities (if a stereo camera system is used) or motion (if a video sequence is available) can be used (see [15] for details about how to combine the cues as well as the probability map calculation). These so-called dynamic cues are much more unlikely to appear in the interior of objects. For example, a sharp change of scene depth strongly indicates that there is a transition form background to a foreground object being located much closer to the camera at this position.

These probabilities are used for the boundary term B_{pq} of (6.4) and the according graph to be cut. This means that the weights of the n-links of pixels with high border probability should be low. The R_p's of (6.4) are chosen such that they represent all knowledge about the segmentation before calculating the minimum graph cut. More specifically, it can be assumed that the fixation point is part of the foreground,

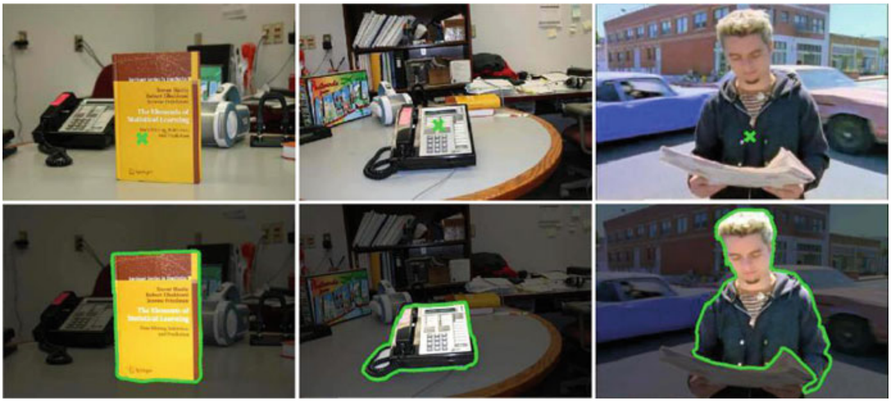

Fig. 6.8 Demonstrating the performance of the algorithm proposed in [15]. See text for details (© 2012 IEEE. Reprinted, with permission, from Mishra et al. [15])

whereas the image border pixels are part of the background. The R_p's of those pixels are set accordingly, whereas the R_p's of all other pixels are set to zero, as no information about their bias is available. Now the graph is completely defined and can be cut, e.g., via a max-flow algorithm.

As far as the shrinking bias is concerned, the authors of [15] try to avoid this drawback by transforming the image into the polar space with equal spacing in the annular as well as radial direction, where the fixation point coincides with the center of the polar transform. Observe that circular contours of different diameter have equal length in polar space. Therefore, it can be argued that the problem of graph cuts tending to favor a segmentation of small regions with rather short boundaries can effectively be suppressed by applying a polar transform and then building the graph based on the polar space representation of the image, because then the number of nodes to be severed is relatively independent of the region size.

The performance of the method is illustrated in Fig. 6.8. In the top row, three challenging situations can be seen. The fixation point is marked by a green cross. The images of the bottom row show the segmentation result (the segmented foreground is highlighted and enclosed by a green contour). Despite significant interior gradients, heavy background clutter, as well as objects featuring colors similar to the background in some cases, the algorithm segments the object of interest (almost) perfectly from the background.

6.1.5 Restriction of Energy Functions

This section deals with the following question: Which properties of a function are necessary such that it can be minimized via graph cuts? This question is important, because its answer can be used to guide the design of suitable energy functions as well as to decide whether graph cuts can be employed for a given problem or not. The paper of [14] investigates this issue and we will briefly mention the main points here.

The energy function defined in (6.4) being used for segmentation is one example of modeling a binary problem by a function which can be minimized by a graph cut algorithm. A generalization of (6.4) can be written as

$$E(l) = \sum_{p \in P} D_p\left(l_p\right) + \sum_{\{p,q\} \in \mathcal{N}} V_{pq}\left(l_p, l_q\right) \tag{6.7}$$

where P denotes the image domain, l_p defines some kind of binary assignment to each pixel p (i.e., $l_p \in [0, 1]$), D_p models the penalty of assigning label l_p to p, and V_{pq} models the cost of assigning l_p to p and l_q to q, with p and q being adjacent pixels. Despite their compact and simple formulation, energy functions in the form of (6.7) are hard to optimize, mainly because the dimensionality of the space of unknowns is extremely large, as every pixel is treated as a separate unknown. Hence, such problems often contain millions of unknowns. Consequently, fast and efficient optimization algorithms are required (related to the number of unknowns), and that's where graph cuts come into play.

According to [14], energy functions of the type of (6.7) can be minimized via graph cuts if the following condition holds:

$$V_{pq}(0,0) + V_{pq}(1,1) \leq V_{pq}(0,1) + V_{pq}(1,0) \tag{6.8}$$

In other words, the sum of costs of assigning the same labels to p and q has to be at most equal to the sum of costs when p and q are assigned to opposite labels. Such functions are said to be *submodular*. In the energy definition of (6.4), the δ-function ensures that the cost of assigning the same label to neighboring pixels is always zero. Consequently, (6.8) holds if we assume nonnegative costs V_{pq}.

Informally speaking, the D_p 's are data-driven cost terms and ensure that the solution, i.e., the assigned labels, "fit well" to the observed data. The V_{pq} 's represent some prior information about the optimal solution. Because only neighboring pixels are considered, the V_{pq} 's essentially enforce spatial smoothness by penalizing adjacent pixels with different labels.

This interpretation of (6.7) fits well into the demands of quite a variety of vision applications including segmentation, object extraction, video texture synthesis, and stereo reconstruction. Fortunately, the restrictions imposed by (6.8) are rather loose and can be fulfilled in many cases as well. Together with the fact that graph cuts can be extended to the multi-label case (which will be shown in the next sections), this explains to a large extent why graph cuts have become increasingly popular among the vision community over the last decade.

6.2 Extension to the Multi-label Case

With the graph cut methods presented up to now, only binary optimization problems, which assign one out of two possible states to each pixel in an image (or, more generally, voxel in a N-D data volume), can be solved. Because graph cut optimization methods have the nice property of finding a global optimum, it is desirable to extend the proceeding from the two-label case to the more general multi-labeling problems, if possible.

In the multi-labeling problem, the task is to assign a label l_p to each pixel p with $l_p \in [1, 2, \ldots, L]$, i.e., each label can take one value out of a finite set of values with cardinality L. If we want to find an optimal labeling, the same kind of energy function as in (6.7) can be applied, but now the l_p's (and l_q's) can take more than two values.

As we will see below, there exist two ways in order to achieve this:

- *Adaption of the topology of the graph*: Essentially, each pixel is represented by multiple nodes here. The number of nodes being necessary to represent one pixel is in accord with the number of labels L: each pixel is represented by as many nodes as are necessary such that one edge exists for each label. This means that in order to get L edges, each pixel has to be represented by $L - 1$ nonterminal nodes. This results in an extension of the graph to higher dimensions. When calculating the minimum cut, it has to be ensured that exactly one of the edges connecting the nodes belonging to the same pixel is severed by the minimum cut. Now the severed edge uniquely identifies the value of the label of that pixel. Observe that this proceeding is only applicable if the labels satisfy the so-called linear ordering constraint (see below).
- *Conversion into an iterative approximation scheme*: Here, the multi-label problem is converted into a series of binary labeling problems, which are iteratively solved and finally give an approximation of the multi-label solution. While an exact calculation of the global solution typically is not possible, it can be shown that the approximate solution lies within some constant factor of the "true" global optimum. In other words, the approximate solution is sufficiently "good" in many practical applications.

6.2.1 Exact Solution: Linearly Ordered Labeling Problems

A special case of multi-label problems is problems where the labels can be *linearly ordered*. Informally speaking, this means that considering any two labels a and b, there exists a measure which allows us to decide which of the two labels is smaller. Moreover, we can assume that if $a < b$ and $b < c$, a has to be smaller than c ($a < c$). Now we're in the position to order all labels of the finite set in a linear ascending order, i.e., $a < b < c < \ldots$.

For example, consider the task of estimating disparities d in the two-camera stereo matching problem, where we have to find a disparity d for each pixel. The disparity d defines the position shift between a pixel in the left camera image and the corresponding pixel in the image of the right camera, which depicts the same point of the 3D scene being covered by the cameras. After a proper quantization of d, the problem of identifying the (quantized) disparities for each pixel is a multi-labeling problem where the labels (i.e., the quantized disparities) are linearly ordered. For example, it is obvious that a disparity value of one pixel is smaller than a disparity value of two pixels.

In contrast to that, consider a multi-label segmentation, where the image is partitioned into multiple regions and each region is described by a unique label. These labels cannot be linearly ordered, because it doesn't make sense to define one label as "smaller" than another.

6.2.1.1 Graph Construction

If a linear ordering of the labels is possible, we can give a natural definition of the pairwise costs V_{pq}, which depends on the difference between their labels l_p and l_q. In the simplest case, V_{pq} can be set to the absolute differences $\left|l_p - l_q\right|$. Then, the energy function can be written as

$$E(l) = \sum_{p \in P} D_p\left(l_p\right) + \sum_{\{p,q\} \in \mathcal{N}} \lambda_{pq} \left|l_p - l_q\right| \tag{6.9}$$

where λ_{pq} is a weighting factor for setting the relative importance of the smoothness term, which can be chosen differently for each pair of pixels, but is often set to a constant: $\lambda_{pq} \equiv \lambda \;\forall\; p, q$.

Without loss of generality, let's further assume that the labels are integer values in the range $[1, 2, \ldots, L]$. Then, the graph can be constructed as follows (see also Fig. 6.9 for the simple illustrative case of only two pixels p and q). As usual, the graph contains the two terminal vertices s and t. Additionally, $L - 1$ nodes $p_1, p_2, \ldots, p_{L-1}$ are introduced for each pixel p.

These nodes are connected with the edges $e_{sp_1}, e_{p_1p_2}, \ldots, e_{p_{L-1}t}$ (black lines in Fig. 6.9). Hence, there exist L such edges in the graph for each p and consequently, each edge defines a (possible) labeling with one specific value. Therefore, let's call these edges "label edges." The weights of those edges directly depend on the data-driven costs D_p, which specify the cost of applying a specific label to a node. We can set $w_{p_{l-1}p_l} = D_p(l) + K_p$, where K_p is a constant (i.e., K_p takes identical values for all edges relating to node p). The meaning of K_p will become clear later on.

Additionally, the graph also contains edges $e_{p_lq_l}$ connecting neighboring nodes (cf. gray edges in Fig. 6.9. As we have only two pixels p and q, each node contains only one of those edges for this example). Usually a 4-neighborhood is assumed. The weight $w_{p_lq_l}$ of these edges should reflect the penalty when assigning different labels to neighboring nodes. Therefore, these edges are also called "penalty edges."

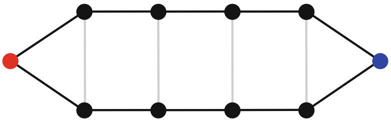

Fig. 6.9 Exemplifying the graph construction for multi-label problems with just two pixels p and q, where each pixel is related to the black nodes of one row of the graph. The terminal nodes are indicated by *red* and *blue color*

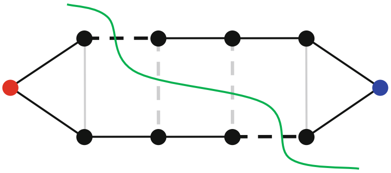

Fig. 6.10 Illustrating how a cut (*green*) helps identifying the label assignment

The weight of those edges is set equal to the smoothness weighting factor: $w_{p_l q_l} = \lambda_{pq} \ \forall \ l \in [1, 2, \ldots, L]$. The reason for this will be clear soon.

A cut separating s from t (green line in Fig. 6.10) severs label edges as well as penalty edges (dashed lines in Fig. 6.10). The severed label edges directly define the labels assigned to each node. If, for example, the cut severs the edge $e_{p_1 p_2}$, the label $l_p = 2$ is assigned to pixel p. In the example of Fig. 6.10, based on the cut, we can make the assignments $l_p = 2$ and $l_q = 4$.

Observe that the number of penalty edges of adjacent nodes p and q being severed by the cut is equal to the absolute difference of the labels assigned to these nodes, i.e., $\left| l_p - l_q \right|$. The sum of the weights of the severed edges should be equal to V_{pq}. Considering the definition of V_{pq} in (6.9) (which is $V_{pq} = \lambda_{pq} \cdot \left| l_p - l_q \right|$), this can be achieved by setting the weight of each penalty edge $w_{p_l q_l}$ to λ_{pq}.

If the cut shall uniquely define the labeling of each node (which is what we aim for), it has to be ensured that it severs exactly one of the label edges belonging to one node, i.e., the graph must not contain "folds." This can be enforced by an appropriate choice of K_p: if the K_p's are sufficiently large, a cut severing multiple label ledges belonging to the same pixel will become too costly. Therefore, the K_p is set slightly larger than the sum of the weights of all penalty edges belonging to pixel $p : K_p = 1 + (L - 1) \cdot \sum_{q \in \mathcal{N}_p} \lambda_{pq}$ where $\mathcal{N}_p$ defines the neighborhood of p. As the same K_p is added to all label edges relating to node p, the relative influence of the $D_p(l_p)$ is not affected by the introduction of the K_p.

Please note that the property of finding the global optimum can only be assured through the special design of the V_{pq} term of the energy function, which takes the L1 norm.

On the other hand, however, the L1 norm might tend to produce oversmoothing in the vicinity of sharp boundaries in the data (e.g., large jumps of disparity in stereo matching), because large jumps between adjacent pixels lead to a costly cut severing many penalty edges. Consequently, the optimization intends to minimize the number of pixels where such a large jump occurs and therefore irregularly shaped object boundaries tend to be smoothed. This behavior could be improved by truncating the L1 norm, but truncated L1 norms cannot be represented by the graph topology introduced in this section. Truncated, discontinuity-preserving energy functions can be treated by the approximation methods presented in Sect. 6.2.2.

6.2.1.2 Example: Stereo Matching

Graphs with a topology just described are suitable for usage in stereo matching (see [17, 18]). Consider the standard two-camera stereo setup, where the same scene is captured by two spatially separated cameras, whose optical axes are parallel, i.e., they have the same viewing direction. Due to the displacement between the two cameras, the same scene position is depicted with a slight shift when we compare the images acquired by the two cameras. This shift is called *disparity d*.

The disparity d directly relates to the geometry of the setup of the two cameras. In the standard setup, the cameras are shifted only horizontally, i.e., the line connecting the two camera centers (also called *baseline*) is parallel to the x-axis. As a result, the positions in the two camera images depicting the same scene point also feature a horizontal shift, i.e., $I_1(x,y) = I_2(x-d,y)$.

If we know the disparity d as well as some camera calibration parameters, we can infer the depth of the scene position from the tuple $[x,y,d]$. Therefore, the task of stereo matching results in identifying the disparity d for each $[x,y]$-position of one of the two camera images. Without loss of generality we further assume that I_1 is acquired by the left of the two cameras. As a consequence, d is always nonnegative.

As we know that pixels depicting the same scene point must be located upon straight lines (which are called *epipolar lines*), it is sufficient to perform independent searches along these epipolar lines (which are horizontal lines in our case), i.e., jointly estimate the disparity for one row of the image in a separate step and then move on to the next row. The optimization of each row can be solved efficiently with a dynamic programming approach, for example.

However, the independent optimization leads to artifacts, because the disparity usually tends to be smooth in both directions in the image plane. This effect can be tackled by a post-processing of the calculated disparities after estimating them for each row independently. It would be more convenient though to perform a global optimization of the entire image plane, which could incorporate smoothness constraints in *both* directions (x and y) in a natural way.

This can be achieved by the usage of graph cuts adapted for multi-labeling problems as presented in the previous section. In order to apply graph cuts, we have to quantize and constrain the search space such that the searched disparities can be expressed by a finite set of integer values: $d \in [0,1,\ldots,d_{\max}]$. In [17], it is suggested to construct the graph as follows (see also Fig. 6.11):

Each pixel p is represented by $d_{\max}+2$ nodes in the d-direction, which are connected by label edges as described in the previous section. Consequently, there

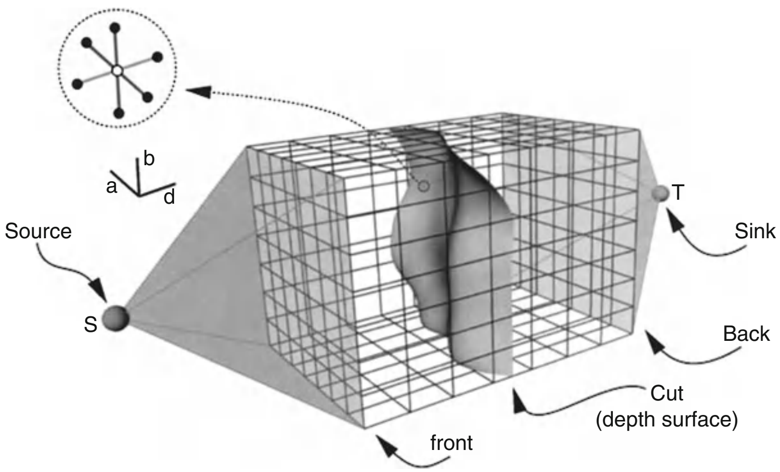

Fig. 6.11 Depicting the graph topology utilized in [17] for stereo matching. Please note that the axes denoted as a and b correspond to x and y, which is the notation used in the text (From Roy [17], with kind permission from Springer Science and Business Media)

exist $d_{\max} + 1$ label edges for each pixel p, and each label edge represents one disparity of the set $[0, 1, \ldots, d_{\max}]$. In order to catch the whole image, there exist $W \times H$ nodes at each disparity level (where W and H denote the image dimensions). All "front" nodes p_0 are connected to the source s of the graph, whereas all "back" nodes $p_{d_{\max}+1}$ are connected to the sink t. Adjacent nodes of the same disparity level (which are of equal d value) are connected by penalty edges. As can be seen in Fig. 6.11, a 4-neighborhood is assumed (cf. the encircled close-up).

A cut through this graph separating s from t can be interpreted as a hyperplane separating the matching volume. The label edges severed by the cut define the disparities as follows: if edge $e_{p_d p_{d+1}}$ is severed by the cut, then the disparity d is assigned to pixel p.

Concerning the edge weights, the weights of all t-links connecting s or t to some other node are set to infinity. This ensures that these edges are never severed by the minimum cut. The weight of all penalty edges is set to a constant K, which is a smoothness factor. If $K = 0$, there is no penalty even for large disparity jumps between adjacent pixels. On the other hand, a value of $K = \infty$ would enforce that no penalty edge is severed at all by the minimum cut, and consequently all pixels would be assigned to the same disparity. Reasonable values of K are in between these two extremes and should lead to a well-balanced trade-off between data fidelity and smoothness.

The weight of the label edges should reflect the suitability of a given disparity to explain the data. If the assumption that we have a certain disparity d at pixel $p = [x, y]$ is correct, the intensity $I_1(x, y)$ observed in the first camera image at position $[x, y]$ should be very similar to the intensity $I_2(x - d, y)$ of the second camera image observed at position $[x - d, y]$, because both pixels depict the same scene object.

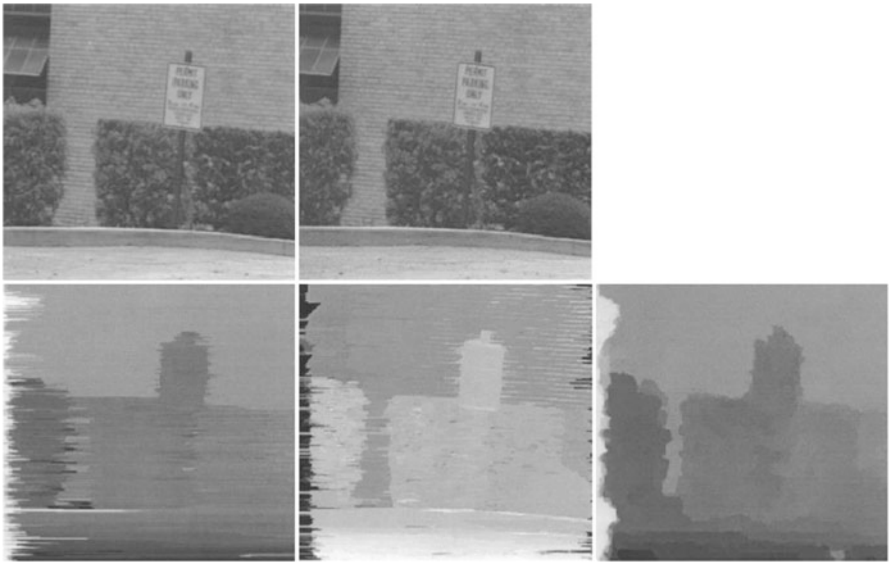

Fig. 6.12 Illustrating the performance of graph cuts used in stereo matching. The *top row* shows a pair of stereo images, whereas the *bottom row* shows the solutions obtained with the standard DP approach of stereo matching (*left*), DP with post-processing (*middle*), and graph cuts (*right*) (From Roy [17], with kind permission from Springer Science and Business Media)

Consequently, the weight $w_{p_d p_{d+1}}$ can be set to the L2 norm of the intensity difference between corresponding pixels in both camera images:

$$w_{p_d p_{d+1}} = [I_1(x,y) - I_2(x-d,y)]^2 + C \tag{6.10}$$

where C is a constant which is chosen sufficiently large enough in order to ensure that exactly one label edge is cut for each pixel (and thus prohibits folds of the cut). If the intensity difference between $I_1(x,y)$ and $I_2(x+d,y)$ is low, this indicates that the corresponding disparity is a good solution and consequently $w_{p_d p_{d+1}}$ is low.

Now the graph is completely defined. As it is a two-terminal graph, the minimum cut can be calculated with any max-flow method, such as the augmenting path algorithm presented in Sect. 6.1.2.

An example of the performance of the method can be seen in Fig. 6.12, which shows a pair of stereo images depicting a house wall with some shrubs and a sign placed in front of it (first row). The second row shows disparity maps calculated by various methods. The left map is calculated by a standard dynamic programming approach, which performs separate optimizations for each row. The artifacts in the vertical direction introduced by separately optimizing disparities for each row are clearly visible. Post-processing (middle map, histogram equalized) improves the situation but cannot eliminate the artifacts completely. The usage of the max-flow graph cut method presented in this chapter (right map), however, clearly gives the best

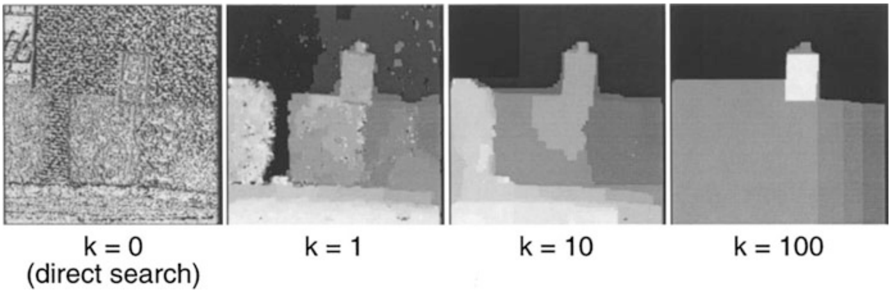

Fig. 6.13 Depicting the role of the smoothing parameter K of the min-cut method for the stereo image pair presented in Fig. 6.12 (From Roy [17], with kind permission from Springer Science and Business Media)

results, as disparities are smoothed in both directions such that a global optimum of the underlying energy function is found. Please note, however, that dynamic programming approaches typically are significantly faster than the max-flow method used here.

This indicates that the quality of the solution can significantly be improved by the spatial smoothing introduced with the weights of the penalty edges, which is set to K. The influence of different choices of K is visualized in Fig. 6.13 (also for the shrub example depicted in the top row of Fig. 6.12). Whereas not considering any smoothing at all ($K = 0$) produces very noisy results of poor quality, it can be seen that a fairly wide range of smoothing parameters lead to good results (middle images). Of course, very high smoothing parameters lead to oversmoothed results (right image).

6.2.2 Iterative Approximation Solutions

One drawback of the exact solution of the multi-labeling problem presented in the previous section is that it requires non-discontinuity-preserving interaction potentials such as $V_{pq} \propto |l_p - l_q|$. However, such functions tend to oversmoothing, because V_{pq} is not bounded and can get very large at discontinuities where the labels l_p and l_q differ significantly between adjacent pixels p and q (which will occur at some position in most images). Consequently, the algorithm tends to avoid large discontinuities by reducing the number of pixels they occur at as much as possible.

A possible solution is to bound the cost of assigning different labels, such as $V_{pq} = \lambda_{pq} \cdot \min(|l_p - l_q|, K)$, where $\lambda_{pq} \cdot K$ is the upper bound. Now, large discontinuities don’t lead to increased costs any longer and therefore are chosen with higher probability by the optimization algorithm. A special case is the simplest of such bounded functions, the so-called Potts model, where all different labelings between adjacent pixels are punished by the same cost:

$$V_{pq} = \lambda_{pq} \cdot T(l_p \neq l_q) \quad \text{with} \quad T = \begin{cases} 0 & \text{if} \quad l_p = l_q \\ 1 & \text{if} \quad l_p \neq l_q \end{cases} \tag{6.11}$$

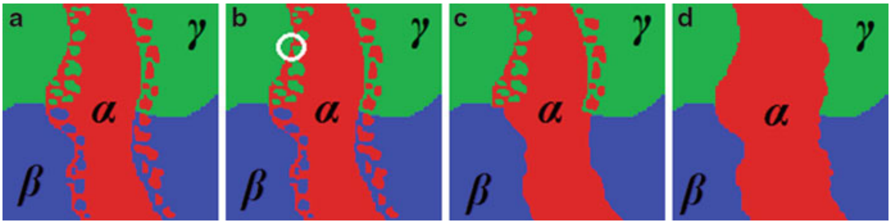

Fig. 6.14 Illustrating different single moves of an iterative approximation. Suppose an initial labeling consisting of three labels α, β, and γ (**a**). In a standard move, which is used by many iterative optimization schemes, the label of only one pixel is allowed to change during a single iteration (highlighted by a *white circle* in (**b**)). An $\alpha - \beta -$ swap move (**c**) allows all pixels with current label α or β to swap their label. An expansion move (**d**) allows the expansion of the label α to many pixels with a previous labeling different from α at once. As clearly can be seen, both move types allow for significant changes in a single step

Observe that the Potts model can also be used for problems where the values of the unknowns cannot be linearly ordered. Imagine a segmentation problem where the task is to partition the image into multiple regions. Setting the interaction potentials according to (6.11) allows to equally punish all positions where the labels of adjacent pixels are different, regardless of the actual values.

Such bounded functions, however, don't allow for a global minimum cut solution, even for the simplest case of the Potts model. Therefore, Boykov et al. [4] suggested an iterative scheme, which approximates the solution. They also showed that the approximate solution lies within a small multiplicative constant of the global optimum, which makes the method interesting for practical use.

At each iteration, the authors of [4] propose to solve a binary decision problem, which can be modeled by a two-terminal graph we are already familiarized with. Hence, each of those binary problems can be solved by the min-cut/max-flow algorithm already presented.

Iterative algorithms for that type of energy minimization problems were already used before graph cuts emerged. A formerly quite commonly used algorithm is the so-called simulated annealing method (see, e.g., Chap. 2 or [10]). However, many of those algorithms performed what the authors of [4] call a "standard move" at each iteration. Within a standard move, the labeling of just *one single pixel* is allowed to change. As a consequence, a very large number of iterations have to be performed until the solution is finally found.

In order to overcome this drawback, Boykov et al. proposed to perform the so-called large moves. During execution of each large move, the labeling of *many* pixels is allowed to change in a single iteration. They suggested two types of such moves, namely, *expansion moves* and *swap moves* (see also Fig. 6.14).

During one swap move, all pixels with current label α are allowed to change their label to β, and, respectively, all pixels with current label β are allowed to change their label to α, if this reduces the total cost. All pixels labeled different from α or β have to keep their label (see (c) in Fig. 6.14, where the transition between the red and blue areas in the lower part of the image is rectified).

In one $\alpha -$ expansion move, the label α is allowed to "expand," i.e., the label of all pixels with current labeling different from α is allowed to be changed to α if this improves the situation. Moreover, all pixels with current label α maintain their label (see (d) in Fig. 6.14, where the red area of all pixels labeled α is expanded).

The possibility to change the labels of many pixels simultaneously in one iteration step significantly accelerates the optimization, which is quite obvious if we compare the labeling changes of (c) or (d) with (b) in Fig. 6.14.

An important observation is that the decision which label has to be assigned to each pixel during one expansion move or swap move essentially is a binary decision. Due to the nature of the large moves, the pixels either keep their labels or change it, but there is only one value to which the labels can switch. In $\alpha -$ expansion moves, for example, all pixels labeled different from α can either keep their current label or change it to α. Similarly, all pixels labeled α (or β) can either keep their label or change it to β (or α, respectively) in one swap move.

These binary decisions are well suited for being represented by a two-terminal graph, which reveals the optimal decision through the calculation of its minimum cut. Observe that in contrast to the examples of Sect. 6.1, the topology of the graphs involved here depends on the current labeling, and, consequently, a different graph has to be built at each iteration.

As far as the overall proceeding when expansion moves are employed is concerned, we can iterate through the set of all possible labels $[1, 2, \ldots, L]$, by beginning with an $\alpha -$ expansion move with $\alpha = 1$ (i.e., solve this binary decision problem by calculating the min-cut/max-flow of the according graph), then continue to do the same with $\alpha = 2$, and so on, until $\alpha = L$ is reached. This is what is called a "cycle" in [4]. Consequently, a cycle consists of $O(L)$ single moves. If any of these L expansion moves was able to make any progress, i.e., could achieve a reduction of the overall cost, the system performs another cycle, and so on, until none of the expansion moves of the cycle was able to reduce the total cost (see also the flowchart of Fig. 6.15). Similarly, one cycle of $\alpha - \beta -$ swap moves consists of finding a minimum graph cut for every combination of α and β labels.

6.2.2.1 Graph Cut Optimization with Swap Moves

If swap moves are to be utilized, we have to perform an $\alpha - \beta -$ swap move for all possible combinations of α and β in each cycle with the only restriction that it suffices to consider only combinations where $\alpha < \beta$. This is because V_{pq} has to be symmetric, as we will see later. Therefore, combinations with $\alpha > \beta$ can be omitted. Furthermore, swapping doesn't make sense if $\alpha = \beta$. Hence, each cycle contains $O(L^2)$ single moves when $\alpha - \beta -$ swap moves are carried out.

Now let's turn to the question how to build the graph for solving the binary decision problem of each single move. For swap moves, we just have to include all pixels into the graph whose current label is α or β, because the label of all other nodes/pixels must not change and therefore these pixels don't need to be

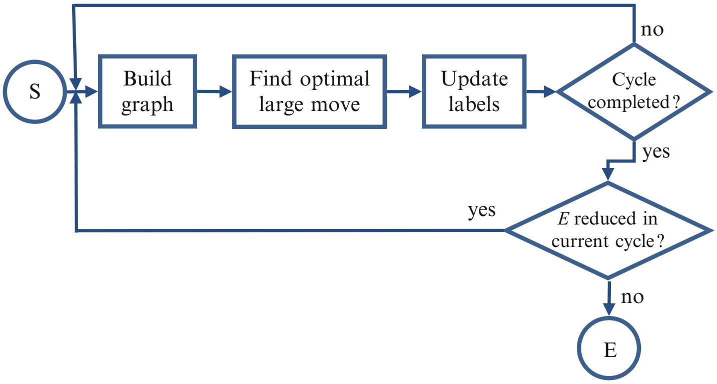

Fig. 6.15 Flowchart of the optimization of multi-labeling problems with iteratively performed binary graph cuts

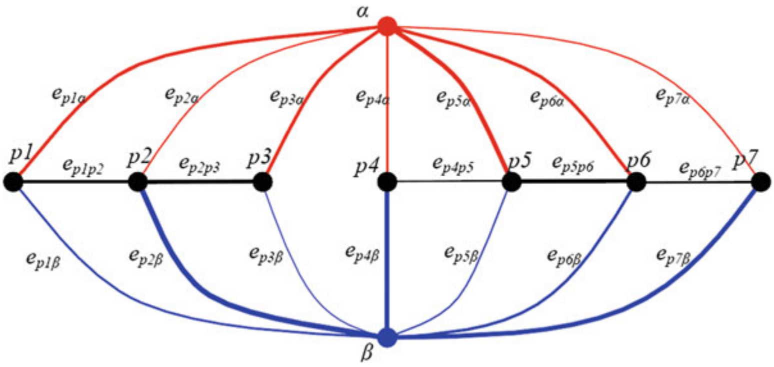

Fig. 6.16 Illustrating the graph utilized when calculating the optimal $\alpha - \beta -$ swap move

considered. For clarity, let's denote the set of all pixels with label α or β by $P_{\alpha\beta}$ (where P denotes the set of all pixels).

An illustrative 1D example of such a graph with just seven pixels $p1$ to $p7$ can be seen in Fig. 6.16. Neighboring pixels are connected by the n-link edges e_{p1p2}, e_{p2p3}, etc. Observe that some neighboring nodes in the graph may not be connected by an edge, because they don't correspond to adjacent pixels in the image. Pixels/nodes $p3$ and $p4$ in Fig. 6.16 are an example of this. The reason is that all neighboring pixels of $p3$ as well as $p4$ may have a labeling different from α or β (i.e., are all $\notin P_{\alpha\beta}$) and therefore are not included in the graph. Additionally, the two terminal nodes of the graph represent the labels α and β. Each nonterminal node is connected to both terminals by the edges $e_{p3\alpha}$ and $e_{p3\beta}$ (t-links). The thickness of the connections of the nodes in Fig. 6.16 indicates the edge weights.

As in Sect. 6.1, a graph cut separates the nodes into two disjoint subsets such that each of the two terminals is contained in a different subset. This fact ensures that a specific labeling is uniquely defined, because then it can be assumed that the cut severs exactly one t-link of each nonterminal node. In contrast to the examples of Sect. 6.1, however, here a node is assigned to the label whose corresponding edge is actually severed. For example, if the cut severs $e_{p1\beta}$, the pixel $p1$ is assigned to label β. This can be ensured by a proper choice of the edge weights.

Moreover, the weights have to be chosen such that the minimum cut defines a labeling of all pixels $p \in P_{\alpha\beta}$ which reduces the cost function as much as possible. This is in fact just a local minimum of the total cost, because the labeling of all other pixels is enforced to remain constant during one $\alpha - \beta -$ swap move and therefore the global optimum is not reached. We can set the weights w_{pq} of the n-links to V_{pq}, because if a cut severs neighboring nodes, this means that one pixel is assigned to label α and the other to β and, according to the definition of the cost function (6.7), this assignment should be punished by the quantity $V_{pq}(\alpha, \beta)$.

As far as the weights of the t-links are concerned, they are set according to

$$w_{p\alpha} = D_p(\alpha) + \sum_{q \in \mathcal{N}_p, q \notin P_{\alpha\beta}} V_{pq}(\alpha, l_q)\ ;\ w_{p\beta} = D_p(\beta) + \sum_{q \in \mathcal{N}_p, q \notin P_{\alpha\beta}} V_{pq}(\beta, l_q) \tag{6.12}$$

Clearly, these weights should contain the data term D_p. Additionally, some costs for all pixels adjacent to p with a labeling different from α or β (i.e., $q \in \mathcal{N}_p, q \notin P_{\alpha\beta}$) have to be included. The reason for this is that the interaction costs of the pixel pairs consisting of p and one of those pixels are not considered in the current graph so far, simply because those pixels are not included in the current graph. Therefore, these costs should be added to the according t-link cost.

If we assign the label α to p, for example, this induces pairwise costs for all pixels q adjacent to p with a labeling different from α (i.e., $l_q \neq \alpha$). Some of those pixels already are included in the current graph (namely, the ones with label β), and, consequently, their pairwise cost is considered by the weight of the n-link linking both nodes. However, all neighbors of p which are not contained in $P_{\alpha\beta}$ are missing in the current graph and therefore these pairwise costs are added to $w_{p\alpha}$. Similar considerations can be made for the $w_{p\beta}$.

Now the graph is completely defined, the minimum cut can be efficiently obtained by a max-flow algorithm, such as the one presented in Sect. 6.1.

As $\alpha - \beta -$ swap moves work with undirected graphs with positive edge weights, we have to constrain the pairwise costs such that they are symmetric and nonnegative, i.e., $V_{pq}(\alpha, \beta) = V_{pq}(\beta, \alpha) \geq 0$. Furthermore, the V_{pq} is set to zero where the neighbors p and q are assigned the same value: $V_{pq}(\alpha, \alpha) = 0$. Any function V_{pq} satisfying these two conditions is said to be a *semi-metric*. Hence, $\alpha - \beta -$ swap moves are applicable if V_{pq} is a semi-metric.

Pseudocode

```
function multiLabelOptSwap (in image $I$, in data-driven cost function $D_p$, in pairwise cost function $V_{pq}$, in initial labeling $\mathbf{l}^0$ (arbitrary), out optimized labeling $\mathbf{l}^*$)

$k \leftarrow 0$
// main iteration loop (one pass is one cycle)
```

```
repeat
  // loop for all swap moves within one cycle (all
  combinations of $\alpha$ and $\beta$)
  bSuccess $\leftarrow$ false // flag indicating whether reduction of
                            total cost was possible in current cycle
  for $\alpha = 1$ to $L$
    for $\beta = \alpha + 1$ to $L$
      // construction of graph $G = (N, E)$
      $N \leftarrow \{s_\alpha, t_\beta\}$          // add the two terminals
      for all pixels $p \in P$
        if $p \in P_{\alpha\beta}$ then  // label of p is either $\alpha$ or $\beta$
          $N \leftarrow N \cup \{p\}$  // add p to node set
          $E \leftarrow E \cup \{e_{p\alpha}, e_{p\beta}\}$ // connect p to src and sink
          set $w_{p\alpha}$ and $w_{p\beta}$ according to (6.12)
        end if
      next
      for all neighboring pixels $p \in P_{\alpha\beta}$ and $q \in P_{\alpha\beta}$
        $E \leftarrow E \cup \{e_{pq}\}$, $w_{pq} \leftarrow V_{pq}(\alpha, \beta)$
      next
      // find optimal $\alpha - \beta -$ swap move
       calculate minimum cut $C^*$ of $G$
       for all pixels $p \in P_{\alpha\beta}$
          if $e_{p\alpha} \in C^*$ then
            $l_p^{k+1} \leftarrow \alpha$        // assign label $\alpha$ to pixel p
          else
            $l_p^{k+1} \leftarrow \beta$        // assign label $\beta$ to pixel p
          end if
       next
       // check convergence
       if $E(\mathbf{l}^{k+1}) < E(\mathbf{l}^k)$ then
          bSuccess $\leftarrow$ true // total energy could be reduced
       end if
     next
   next
   $k \leftarrow k + 1$
until bSuccess == false

// set solution to current labeling
$\mathbf{l}^* \leftarrow \mathbf{l}^k$
```

6.2.2.2 Graph Cut Optimization with Expansion Moves

The other possibility of approximating multi-label optimization by iteratively solving binary problems suggested in [4] is to perform $\alpha-$ expansion moves,

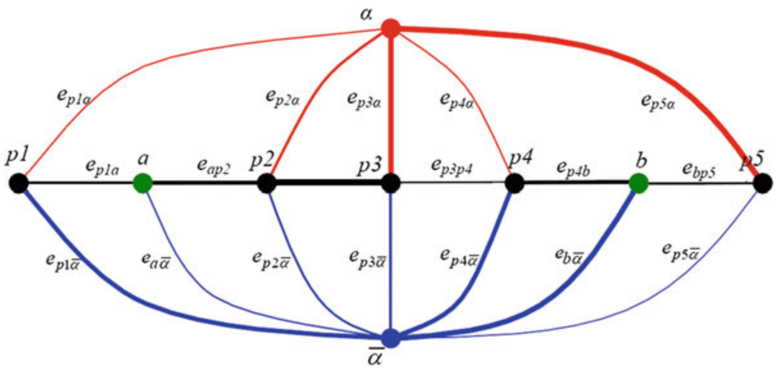

Fig. 6.17 Illustrating the graph utilized when calculating the optimal $\alpha -$ expansion move, where $p1$ is currently assigned to α, $p2$, $p3$, and $p4$ are all assigned to some other label β, whereas $p5$ is assigned to label γ

where the label α is allowed to "expand," i.e., any pixel currently labeled different from α is allowed to change its label to α at each iteration, whereas all pixels already labeled α keep their label. As with swap moves, the optimal $\alpha -$ expansion move can also be found by the construction of an appropriate two-terminal graph, followed by the calculation of the minimum cut of this graph as follows.

The two terminals of this graph represent the labels α and $\bar{\alpha}$ (see Fig. 6.17). Pixels associated to the $\bar{\alpha}$-terminal keep their current labels, which are different from α. Like with expansion moves, all edges severed by a cut indicate to which terminal a particular node/pixel p belongs: If edge $e_{p\alpha}$ is severed by the cut, the label of p is α; if $e_{p\bar{\alpha}}$ is severed, p keeps its current label l_p, which is different from α.

Because every pixel of an image is labeled either to α or to $\bar{\alpha}$, all pixels are included in the graph here. Every node is connected to both terminals by the edges $e_{p\alpha}$ and $e_{p\bar{\alpha}}$, where the weight $w_{p\alpha}$ is set to the data-driven cost of assigning α to p: $w_{p\alpha} = D_p(\alpha)$. As far as the weights $w_{p\bar{\alpha}}$ are concerned, we have to distinguish whether the current label of p is α or not. Because the region of pixels labeled α can be expanded only, we have to ensure that no node with current label α is assigned to the $\bar{\alpha}$-terminal by the cut. This can be done by setting $w_{p\bar{\alpha}} = \infty$ for all pixels $p \in P_\alpha$ ($p1$ in Fig. 6.17). For all other nodes $p \notin P_\alpha,$ we can set $w_{p\bar{\alpha}} = D_p\left(l_p\right)$, where l_p denotes the current label of p.

As far as the n-links are concerned, there is a fundamental difference between neighbors p and q which are assigned to the same label and neighbors with different labeling.

If p and q share the same label l_p, an assignment of one of them to α and the other to $\bar{\alpha}$ means that the cut must sever the n-link e_{pq} between them. Because both nodes previously had the same label, the cost w_{pq} for this assignment can be set to $V_{pq}\left(l_p, \alpha\right)$, regardless of whether p or q is now assigned to α.

Obviously, for pairs p and q with different labels ($l_p \neq l_q$), this does not work any longer. Here, the costs are different depending on whether p or q is assigned to α

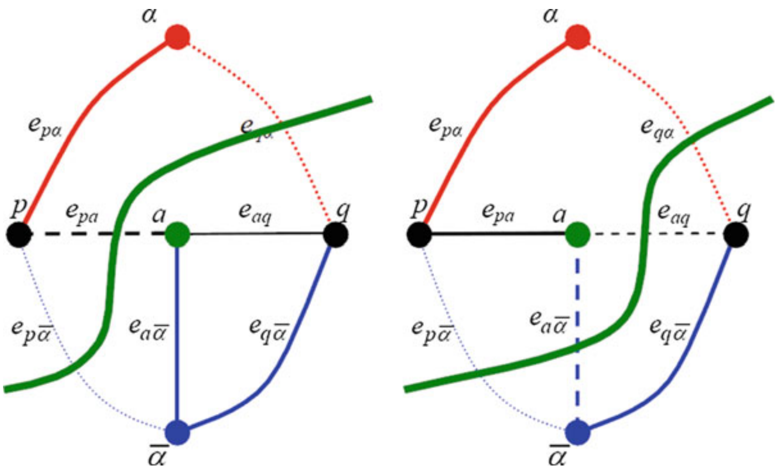

Fig. 6.18 Exemplifying the two possibilities of a cut when p and q are assigned to different labels (cut in *bold green*)

after the current move (i.e., $V_{pq}(l_p, \alpha)$ or $V_{pq}(l_q, \alpha)$). This can be resolved by the introduction of an auxiliary node a, which is placed in between p and q (there are two examples of such auxiliary nodes in Fig. 6.17, which are shown in green, as $l_{p1} \neq l_{p2}$ and $l_{p4} \neq l_{p5}$). Now we have two n-links e_{pa} and e_{aq}, where we can define the weights $w_{pa} = V_{pq}(l_p, \alpha)$ and $w_{aq} = V_{pq}(\alpha, l_q)$. Now the costs of both possibilities are modeled in the graph.

But how to connect the auxiliary node to the terminals and how to choose the weights for those links? Figure 6.18, where a part of the graph containing an auxiliary node a is shown, helps to explain the choice. First, we note that a is only connected to the $\bar{\alpha}$-terminal. Then, there exist two possible ways of a cut which assigns p to $\bar{\alpha}$ and q to α (left and right part of Fig. 6.18, cut in green). Both possible cuts sever edges $e_{p\bar{\alpha}}$ and $e_{\alpha q}$ (indicated by dotted edges), but the cut on the left additionally severs e_{pa}, whereas the cut on the right severs $e_{a\alpha}$ and e_{aq}.

Obviously, the left cut is "correct," because it correctly accounts for the pairwise cost $V_{pq}(l_p, \alpha)$ to be considered as p is assigned to $\bar{\alpha}$ (i.e., keeps its current label l_p) and q is labeled with α. An appropriate choice $w_{a\bar{\alpha}}$ should make sure that the graph is always cut in this way. When we set $w_{a\bar{\alpha}} = V_{pq}(l_p, l_q)$, it can be enforced that the cut severs e_{pa} if we impose additional constraints on the pairwise cost function. More specifically, the so-called triangle inequality has to hold:

$$V_{pq}(l_p, \alpha) \leq V_{pq}(l_p, l_q) + V_{pq}(l_q, \alpha) \tag{6.13}$$

Additionally, V_{pq} has to be nonnegative and symmetric as well, because it has to be ensured that $V_{pq}(l_p, l_p) = 0$, which are the same constraints as with swap moves. All conditions are fulfilled if V_{pq} is a (true) *metric*. For example, the Potts model (6.11) meets all of these conditions.

Observe that the constraints for swap moves are not as restrictive as for expansion moves (no triangle inequality required), which makes swap moves applicable to a broader range of applications. In terms of runtime, however, expansion moves typically converge faster, mainly because each cycle contains less single moves. This overcompensates the effect that each single move has a higher complexity compared to swap moves.

Pseudocode

function **multiLabelOptExpansion** (in image I, in data-driven cost function D_p, in pairwise cost function V_{pq}, in initial labeling $\mathbf{l}^0$ (arbitrary), out optimized labeling $\mathbf{l}^*$)

```
$k \leftarrow 0$
// main iteration loop (one pass is one cycle)
repeat
  bSuccess ← false // flag indicating whether reduction of
                      total cost was possible in current cycle
  // loop for all expansion moves within one cycle
  for $\alpha = 1$ to $L$
     // construction of graph $G = (N, E)$
     create one node for each pixel
     $N \leftarrow N \cup \{s_\alpha, t_{\bar{\alpha}}\}$        // add the two terminals
     // add t-links to both terminals for each node/pixel
     for all pixels $p \in P$
        $E \leftarrow E \cup \{e_{p\alpha}, e_{p\bar{\alpha}}\}$
        set t-link weights appropriately
     next
     for all neighboring pixels $p$ and $q$
        if $l_p^k \neq l_q^k$ then    // p and q have different labels
           $N \leftarrow N \cup \{a\}$       // add an auxiliary node a
           $E \leftarrow E \cup \{e_{pa}, e_{aq}, e_{a\bar{\alpha}}\}$   // connect a to p, q and sink
           $w_{a\bar{\alpha}} \leftarrow V_{pq}\left(l_p^k, l_q^k\right), w_{pa} \leftarrow V_{pq}\left(l_p^k, \alpha\right), w_{aq} \leftarrow V_{pq}\left(\alpha, l_q^k\right)$
        else      // p and q have the same label
           $E \leftarrow E \cup \{e_{pq}\}$, $w_{pq} \leftarrow V_{pq}\left(l_p^k, \alpha\right)$
        end if
     next
     // find optimal $\alpha -$ expansion move
     calculate minimum cut $C^*$ of $G$
     for all pixels $p \in P$
        if $e_{p\alpha} \in C^*$ then
           $l_p^{k+1} \leftarrow \alpha$           // assign label α to pixel p
        else
           $l_p^{k+1} \leftarrow l_p^k$           // keep current labeling for p
```

```
            end if
        next
        // check convergence
        if $E(\mathbf{l}^{k+1}) < E(\mathbf{l}^{k})$ then
            bSuccess ← true  // total energy could be reduced
        end if
    next
    $k \leftarrow k + 1$
until bSuccess == false

// set solution to current labeling
$\mathbf{l}^{*} \leftarrow \mathbf{l}^{k}$
```

6.2.2.3 Example: Nonrigid Cat Motion

Boykov et al. tested the performance of their algorithm in various applications. One of them, namely, a motion prediction (aka optical flow), is presented here. Taking a pair of images depicting the same scene at different times, the task is to predict for each scene element how much it has moved within the period of time between both image acquisitions, i.e., to calculate the disparity between a pixel showing the same scene element.

Because motion is two-dimensional, we have a vertical as well as a horizontal displacement. Two-dimensional disparity can be modeled by a labeling such that the label of a pixel p consists of two components: l_p^h indicating horizontal motion and l_p^v indicating vertical motion, respectively. As graph cuts only work with scalars, every combination of l_p^h and l_p^v can be represented by a scalar number l_p. In [4], eight horizontal and five vertical displacements are used; hence, this amounts to 40 labels altogether.

As with stereo, the displacements attributed to adjacent pixels should be similar for most positions. However, usually discontinuities occur at the borders of moving objects. Therefore, the pairwise cost $V_{pq}(l_p, l_q)$ is set to the truncated measure $V_{pq}(l_p, l_q) = K \cdot \min\left[8, \left(l_p^h - l_q^h\right)^2 + \left(l_p^v - l_q^v\right)^2\right]$. Because this measure doesn't fulfill the triangle inequality, the swap algorithm is used for optimization.

Figure 6.19 shows an example of a cat moving in front of a highly textured background (a). Despite texture helps to calculate a dense motion field, its calculation still is a difficult task as the cat's motion is nonrigid. The horizontal movement result is shown in (b) and vertical movement in (c) (gray coded). As can be seen, the cat is clearly separated from the background and was accurately detected by the algorithm. The running time reported in [4] has to be seen in the context of the hardware available at reporting date and should be in the order of seconds for images of several 100,000 s of pixels with up-to-date hardware.

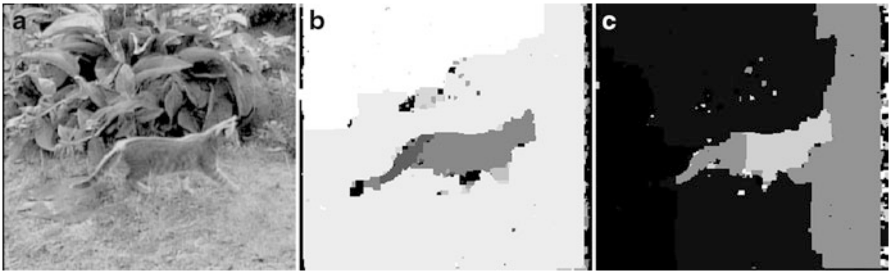

Fig. 6.19 Illustrating the horizontal (**b**) and vertical (**c**) motion of a cat moving before a highly structured background (**a**) as calculated by the swap move graph cut approximation (© 2001 IEEE. Reprinted, with permission, from Boykov et al. [4])

6.3 Normalized Cuts

Shi and Malik [19] proposed a segmentation method which is based on graph cuts, too, but compared to the algorithms presented up to now, their scheme mainly differs in two respects:

- *Graph construction*: The graph $G = (N, E)$ suggested in [19] doesn't contain terminals. Furthermore, the connections between the nodes are not restricted to adjacent pixels. This makes it possible to model the influence of more pixels on the state of a certain pixel. At the same time, though, the considerable increase in the number of edges implies higher computational efforts.
- *Solution calculation*: Because finding the exact solution is computationally too complex for the graph topology suggested in [19], they apply an approximation method in order to save runtime. Namely, they suggest to embed the problem into a continuous space. Now the (relaxed) continuous solution can be computed by solving a generalized eigenvalue problem. The final solution is then found in a subsequent discretization step.

In the following, the method is presented in more detail. First, let's have a closer look at the graph topology. As already mentioned, the graph does not contain terminals. Each pixel p of the image to segment is represented by one node in the graph.

Additionally, the nodes are connected by edges e_{pq}, but in contrast to most graph cut methods, these n-links are not restricted to adjacent pixels. In fact, every node can be connected to all other nodes of the graph. However, in practice links are usually limited to nearby nodes which have a distance below some upper bound in order to keep the running time feasible. The weights w_{pq} of the edges should reflect the "similarity" of pixels p and q, and consequently the weight is high if both nodes are likely to be in the same region. Some examples of definitions of w_{pq} will be given below.

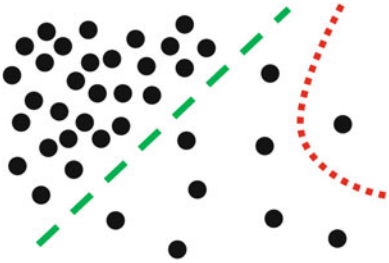

Fig. 6.20 Illustrating the strong bias of non-normalized graph cuts in the absence of terminal nodes. The *green dashed line* indicates a suitable cut of the point set, whereas non-normalized cuts rather produce cuts indicated by the *dotted red curve*

A cut of the graph partitions the node set N into two disjoint subsets A and B and therefore defines a binary segmentation. The cost of the graph cut amounts to the sum of the weights of all edges it severs:

$$C(A,B) = \sum_{p \in A, q \in B} w_{pq} \tag{6.14}$$

Optimal segmentations could be found by minimizing (6.14). However, please note that in the absence of terminals and t-links, a direct minimization of (6.14) has a strong shrinking bias, i.e., tends to produce solutions where either A or B contains very few nodes, because then only a few edges have to be severed. An example of this is illustrated in Fig. 6.20. The points show there can clearly be separated in two groups: the densely populated region on the upper left and the “sparse” region in the lower right part. If we set the edge weights inversely proportional to the distance between two points, we suppose the algorithm to sever the set according to the green dashed line. However, a direct minimization of (6.14) would rather lead to a cut as shown by the red-colored dotted curve, because then very few edges would have to be severed.

Therefore, Shi et al. suggested performing a normalization step such that the normalized cost reflects the ratio of the weight sum of all severed edges as defined in (6.14) to the total sum of edge weights from the nodes of each set to all nodes in the graph:

$$C_N(A,B) = \frac{C(A,B)}{\sum_{p \in A, q \in N} w_{pq}} + \frac{C(A,B)}{\sum_{p \in B, q \in N} w_{pq}} \tag{6.15}$$

As can be seen, the normalization factor contains the sum of all edge weights from every node of set A (or B respectively) to *all* other nodes in the graph, whereas the enumerators just sum up all edge weights connecting nodes of *different sets*. Suppose we want to evaluate the cost of a cut which severs G such that A contains just very few nodes. Then there should exist only a few edges connecting two nodes which are both elements of A. Consequently, a large fraction of all edges connecting a node of A to some other node is severed by the cut (as there should be more edges e_{pq} connecting $p \in A$ to some node $q \in B$ than edges connecting $p \in A$ to $q \in A$). As a result, the first summand of (6.15) should be near 1 and therefore the relative cost of such a cut should be high compared to other cuts.

Now, we are interested how to find a cut which minimizes (6.15). Assume that the binary segmentation is indicated by a vector $\mathbf{x}$ of dimensionality n (where n denotes the number of pixels), whose elements can take two values. If $x_p = 1$, then p is assigned to A, whereas a value of $x_p = -1$ indicates that $p \in B$. Moreover, the total sum of the weights of all edges containing p is denoted by $d_p = \sum_q w_{pq}$. Now we can rewrite the cut cost in terms of $\mathbf{x}$ and the d_p's. In order to find a proper segmentation, we have to minimize the following expression:

$$\mathbf{x}^* = \arg\min_{\mathbf{x}} C_N(\mathbf{x}) = \arg\min_{\mathbf{x}} \frac{\sum\limits_{x_p>0,\,x_q<0} -w_{pq}x_px_q}{\sum_{x_p>0} d_p} + \frac{\sum\limits_{x_p<0,\,x_q>0} -w_{pq}x_px_q}{\sum_{x_p<0} d_p} \tag{6.16}$$

However, it turns out that finding the exact solution $\mathbf{x}^*$ is NP-complete and therefore infeasible, because typically n can amount up to hundreds of thousands or even millions. Therefore, Shi et al. suggest calculating an approximate solution. Let $\mathbf{D}$ be a diagonal matrix of dimensionality $n \times n$, whose diagonal elements are set to the d_p's and $\mathbf{W}$ denote the $n \times n$ matrix with its elements equal to the edge weights, i.e., $W(p,q) = w_{pq}$. Together with the introduction of $k = \sum_{x_p>0} d_p \Big/ \sum_p d_p$, $b = \frac{k}{1-k}$, and $\mathbf{y} = (\mathbf{1} + \mathbf{x}) - b(\mathbf{1} - \mathbf{x})$, the authors of [19] showed that a minimization of (6.16) is equal to the following relation:

$$\mathbf{y}^* = \arg\min_{\mathbf{x}} C_N(\mathbf{x}) = \arg\min_{\mathbf{y}} \frac{\mathbf{y}^T(\mathbf{D} - \mathbf{W})\mathbf{y}}{\mathbf{y}^T\mathbf{D}\mathbf{y}} \tag{6.17}$$

where the elements of $\mathbf{y}$ can take the binary values $\{-b, 1\}$, i.e., $y_p \in \{-b, 1\}$. Please observe that the right part of (6.17) is the well-known *Rayleigh quotient*. If we relax the binary constraint and allow the y_p to take real values (i.e., embed the problem in a continuous space), then we can make use of the fact that the Rayleigh quotient can be minimized by calculating the eigenvectors of the generalized eigensystem $(\mathbf{D} - \mathbf{W})\mathbf{y} = \lambda\mathbf{D}\mathbf{y}$ (see, e.g., [12]). In other words, Shi et al. transform the original problem to a more convenient representation (we now seek an indicator vector $\mathbf{y}$ instead of $\mathbf{x}$) and then employ a continuous spectral (i.e., eigenvalue) method to obtain the graph cut (which is discrete by nature). Of course, this is totally different to the discrete methods described up to now in this chapter.

For the relaxed continuous problem, there exist n generalized eigenvectors $\mathbf{v}_i$, which can be sorted according to their eigenvalues λ_i. Please note that there always exists the trivial solution $\lambda_1 = 0$, $\mathbf{v}_1 = \mathbf{1}$, because by definition d_p is the sum of all edge weights associated with node p, which are exactly the elements of the pth row

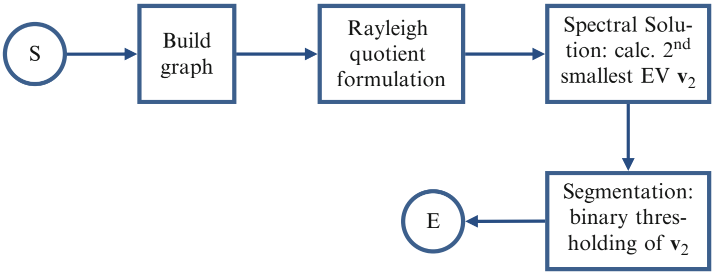
S
Build graph
Rayleigh quotient formulation
Spectral Solution: calc. 2nd smallest EV $\mathbf{v}_2$
Segmentation: binary thresholding of $\mathbf{v}_2$
E

Fig. 6.21 Flowchart of the normalized cut algorithm

of **W**. Without going into details, a property of the Rayleigh quotient is that we can obtain our solution by taking the eigenvector $\mathbf{v}_2$ associated to the second smallest eigenvalue (see [12]): $\mathbf{y}^* = \mathbf{v}_2$.

Because $\mathbf{v}_2$ is real-valued, we have to threshold its elements in order to determine the segmentation, i.e., transform the solution back to the discrete domain. To this end, various simple methods exist, e.g., a simple thresholding operation, where the pixels corresponding to all elements above the threshold t are assigned to one node set and the pixels corresponding to all elements below t are assigned to the other node set, respectively. As far as the choice of t is concerned, it can, e.g., be set to the median of the elements of $\mathbf{v}_2$.

Overall, the algorithm comprises the following steps (see also flowchart of Fig. 6.21):

1. *Graph construction*: Given an image I, build the graph $G = (N, E)$ such that any pixel p is represented by one node and is connected to the other nodes according to the weights w_{pq} (examples of a proper choice of the weighs will follow below).
2. *Rayleigh quotient formulation*: Derive **D** and **W** from the edge weights.
3. *Spectral solution*: Calculate the eigenvalues of the generalized eigenvalue system $(\mathbf{D} - \mathbf{W})\mathbf{y} = \lambda\mathbf{D}\mathbf{y}$.
4. *Binary decision*: Take the second smallest eigenvector $\mathbf{v}_2$ and perform a binary partitioning of the image according to the values of the elements of $\mathbf{v}_2$ (above or below threshold t).

The suitability of the spectral solution of the normalized cut is illustrated in Fig. 6.22, which shows a baseball sports scene (a) for which some generalized eigenvectors are calculated as described above ((b)–(i)). The eigenvector corresponding to the second smallest eigenvalue is depicted in (b). It clearly structures the scene such that a separation of the dominant object (the player in the lower left area of the image) is possible by a simple thresholding of the pixel values.

In their contribution, Shi et al. pointed out that for most scenes, there doesn't exist a single best solution of the segmentation problem. If a human person is asked to segment a scene manually, he/she generally produces different segmentations depending on the level of detail. At a "coarse" level, it suffices to perform a binary segmentation which separates a dominant object from the rest of the scene. If details are to be taken into account, it is usually necessary to do a multi-label

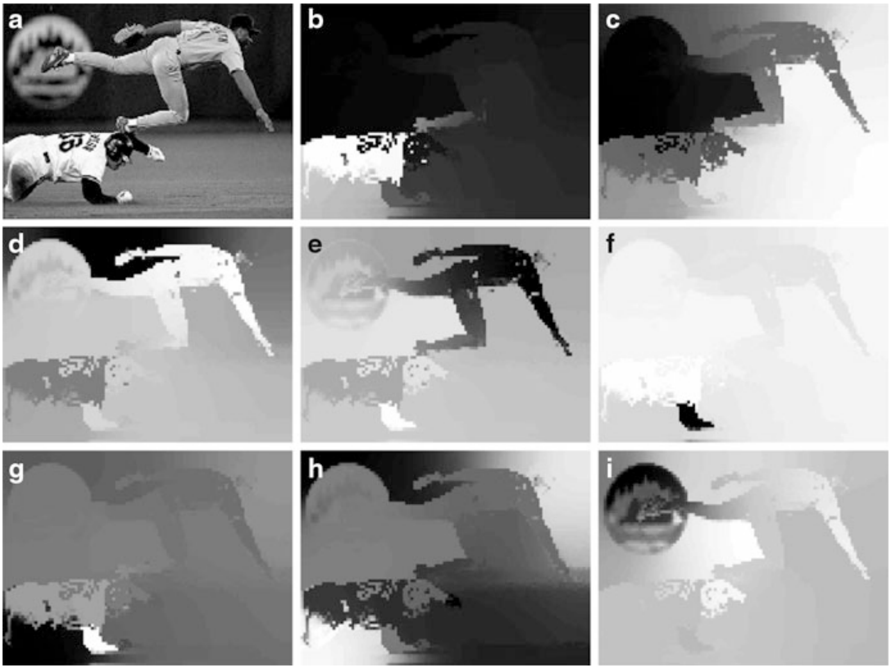

Fig. 6.22 Depicting a baseball sports scene (**a**) as well as some generalized eigenvectors associated with the smallest eigenvalues of the relaxed Rayleigh quotient solution of the graph cut problem ((**b**)–(**i**)). A binary segmentation can be performed based on the eigenvector belonging to the second smallest eigenvalue (**b**), whereas eigenvectors of higher eigenvalues (**c**)–(**i**) can be used for a multi-label segmentation (© 2000 IEEE. Reprinted, with permission, from Shi and Malik [19])

segmentation resulting in multiple regions, where each region shows a particular detail/object. The number of regions depends on the level of detail requested. Consider a scene depicting a house in front of a garden as background. At a coarse level, there are two dominant regions: house and garden. However, a more detailed segmentation further partitioning both regions (door, windows, roof, etc. for the house and trees, bushes, etc. for the garden) is also "valid".

The normalized cut method can easily be extended to produce more detailed segmentations, because this information is contained in the eigenvectors related to the higher eigenvalues. This is illustrated if we take a look at these eigenvectors of the baseball example ((c)–(i) in Fig. 6.22). As clearly can be seen, these eigenvectors can be utilized to generate finer segmentations. For example, the second player could easily be extracted using the eigenvector shown in (e), whereas the vector of (i) indicates the logo visible in the background. In fact, several ways to perform a multi-label segmentation are proposed in [19]:

- *Recursive iteration*: In a first step, a binary segmentation is derived from the eigenvector belonging to the second smallest eigenvalue as described above.

Next, for each of the both regions, the whole method is applied again, i.e., a new subgraph for all pixels of one region is built, spectrally solved, and so on. This leads to a further binary partition of both regions. The recursion stops when the normalized cut cost exceeds a certain threshold. In that case a region is not split any further. This proceeding produces stable results but is computationally wasteful, because only the second smallest eigenvector is used at each iteration. The information contained in the other eigenvectors is ignored.

- *Recursive splitting*: Here, the generalized eigensystem is calculated only once. After performing a binary segmentation with the second smallest eigenvector, we can use the eigenvector of the third smallest eigenvalue to recursively subdivide the regions by thresholding this eigenvector (e.g., by calculating a separate threshold for each region, where the threshold is based on a subset of the eigenvector values belonging to this region). Next, we move on to the vector of the fourth smallest eigenvalue, which further sub-partitions the subregions, and so on, until the normalized cut costs exceed a certain threshold (see [19] for details). While this is computationally more efficient, some care is required here:
  - There may exist eigenvectors which are not suited for partitioning, because their values vary smoothly. A simple way of dealing with this problem is to skip these eigenvectors, e.g., by checking the distribution of the values of the eigenvector elements, i.e., the histogram of the element values (see [19] for details).
  - Because the segmentation is derived from a real-valued approximation, the approximation error accumulates at each step and eventually makes the segmentation unreliable.
- *Simultaneous splitting*: Here, for each pixel a vector $\mathbf{z}_p$ is built, which accumulates all "its" values of the eigenvectors of the M smallest eigenvalues (i.e., for pixel p this vector contains all $v_{m,p}$, where $2 \leq m \leq M$). These vectors are clustered, e.g., by a k-means algorithm into k clusters, yielding a segmentation into k regions. Practically, k is chosen such that an over-segmentation is produced. In a subsequent cleanup step, regions are combined again, if necessary.

Let's now turn to some implementation issues. The first is how we should choose the edge weights w_{pq}. Shi and Malik proposed a weight which considers both similarity of the appearance of pixels p and q as well as their spatial distance. As the weights should reflect the likelihood that p and q belong to the same object, w_{pq} should be large in case of similar appearance as well as spatial proximity. Both terms can be combined as follows:

$$w_{pq} = \exp\left(\frac{-\|F(p) - F(q)\|^2}{\sigma_F^2}\right) \cdot \left\{ \begin{matrix} \exp\left(\frac{-\|X(p)-X(q)\|^2}{\sigma_X^2}\right) & \text{if } \|X(p) - X(q)\| < r \\ 0 & \text{otherwise} \end{matrix} \right\} \tag{6.18}$$

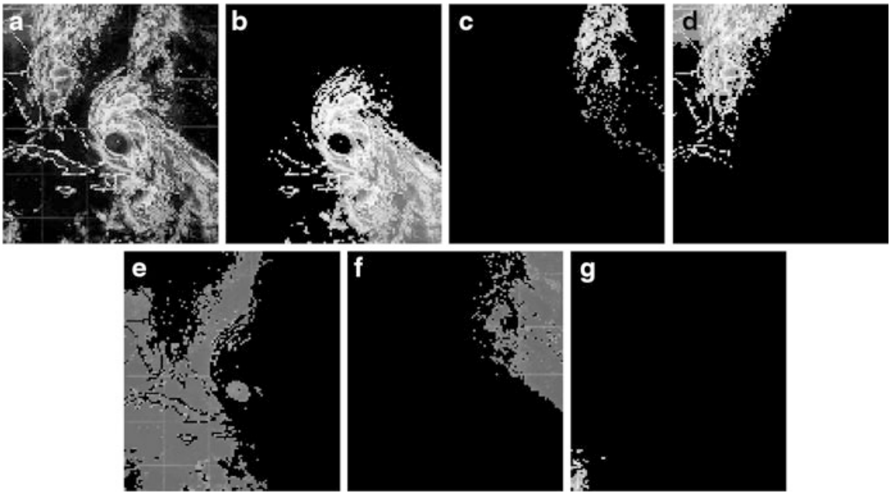

Fig. 6.23 Depicting a weather radar image (**a**) along with the multi-label segmentation (**b**)–(**g**) calculated by the normalized cut method (© 2000 IEEE. Reprinted, with permission, from Shi and Malik [19])

where $F(p)$ denotes an appearance parameter, which could, e.g., be chosen to the brightness of p, its RGB values for color images, or some more elaborate function like a descriptor. $X(p)$ denotes the position of p such that $\|X(p) - X(q)\|$ is the Euclidean distance between p and q. σ_F^2 are parameters controlling the falloff rate of the exponential terms. If the distance between p and q exceeds a certain maximum distance r, the w_{pq} will become zero and therefore the threshold r effectively leads to graphs which are connected only locally.

Another point is that computing the complete generalized eigensystem would be computationally too expensive, as $\mathbf{D}$ and $\mathbf{W}$ are matrices of size $n \times n$, with n denoting the number of pixels. However, please note that due to local connectivity $\mathbf{W}$ is usually sparse and, additionally, we're only interested in just a few eigenvectors. An efficient solver taking these two circumstances into account is the so-called Lanczos method (see, e.g., [12]), which makes the running times feasible. A usage of the Lanczos method is possible, because we can transform the generalized eigensystem into an "ordinary" eigensystem, which is denoted by $\mathbf{D}^{-1/2}(\mathbf{D} - \mathbf{W})\mathbf{D}^{-1/2}\mathbf{y} = \lambda\mathbf{y}$.

The performance of the method is illustrated in Fig. 6.23, where a weather image is separated into multiple segments (multi-labeling is performed with the "recursive splitting" method). Observe that the objects here have rather ill-defined boundaries but could be segmented quite accurately by the system.

Pseudocode

```
function normalizedCutSegmentation (in image $I$, in pairwise cost function $w$, out segmentation labeling $\mathbf{l}^*$)

// set-up of graph (i.e. calculation of the weights $w_{pq}$)
for all pixels $p \in P$ // $P$ denotes set of all pixels in $I$
  for all pixels $q \in P$
    if $\|X(p) - X(q)\| < r$ && $p \neq q$ then  // distance between $p$ and $q$ below threshold $\rightarrow$ $p$ and $q$ are "connected"
      derive $F(p)$ and $F(p)$ from $I$ and set $w_{pq}$ according to (6.18)
    else      // no connection between $p$ and $q$
      $w_{pq} \leftarrow 0$
    end if
  next
next

// spectral (eigenvalue) solution (in continuous domain)
set-up of $\mathbf{W}$ $(n \times n)$: arrange all $w_{pq}$ into matrix form
set-up of $\mathbf{D}$ $(n \times n)$: diagonal matrix with $D_{pp} = \sum_q w_{pq}$
solve real-valued eigensystem $\mathbf{D}^{-\frac{1}{2}}(\mathbf{D} - \mathbf{W})\mathbf{D}^{-\frac{1}{2}}\mathbf{y} = \lambda\mathbf{y}$ with a fast solver, e.g. Lanczos-method yielding the "top" $M$ eigenvectors $\mathbf{y}_m; m \in [1, 2, \ldots, M]$ related to the $M$ smallest eigenvalues

// derive discrete solution (simultaneous splitting)
// for each pixel, stack all of its $M$ eigenvector elements in a vector $\mathbf{z}_p$
$Z \leftarrow \{\}$
for $p = 1$ to $n$
  for $m = 2$ to $M$ // consider $M$ top eigenvectors
    $z_{p,m-1} \leftarrow v_{m,p}$ // stack all values related to $p$ in $\mathbf{z}_p$
  next
  $Z \leftarrow Z \cup \{\mathbf{z}_p\}$
next
// over-segmentation
cluster set $Z$ into $k' > k$ clusters, e.g. with k-means algorithm, yielding a labeling $l_p = CL(\mathbf{z}_p)$ for each pixel $p$, where $CL(\mathbf{z}_p)$ denotes the cluster to which $\mathbf{z}_p$ belongs to.
// clean-up until desired number $k$ of segments is reached
while $k' > k$
```

```
    merge two segments into one, e.g. according to k-way minimum cut criterion (see [19] for details) (i.e. adjust labeling $\mathbf{l}$)
    $k' \leftarrow k' - 1$
end while
// set solution to current labeling
$\mathbf{l}^* \leftarrow \mathbf{l}$
```

References

1. Boykov J, Funka-Lea G (2006) Graph cuts and efficient N-D image segmentation. Int J Comput Vis 70(2):109–131
2. Boykov J, Jolly MP (2001) Interactive graph cuts for optimal boundary and region segmentation of objects in N-D images. Int Conf Comput Vis 1:105–112
3. Boykov J, Kolmogorov V (2004) An experimental comparison of min-cut/max-flow algorithms for energy minimization in vision. IEEE Trans Pattern Anal Mach Intell 26 (9):1124–1137
4. Boykov J, Veksler O, Zabih R (2001) Fast approximate energy minimization via graph cuts. IEEE Trans Pattern Anal Mach Intell 23(11):1222–1239
5. Carreira J, Sminchisescu C (2010) Constrained parametric min-cuts for automatic object segmentation. Proc IEEE Int Conf Comput Vis Pattern Recognit 23:3241–3248
6. Carreira J, Sminchisescu C (2012) CPMC: automatic object segmentation using constrained parametric min-cuts. IEEE Trans Pattern Anal Mach Intell 34(7):1312–1328
7. Cook WJ, Cunningham WH, Pulleyblank WR, Schrijver A (1998) Combinatorial optimization. Wiley, New York. ISBN 978–0471558941
8. Dinic EA (1970) Algorithm for solution of a problem of maximum flow in networks with power estimation. Soviet Math Doklad 11:1277–1280
9. Ford L, Fulkerson D (1962) Flows in networks. Princeton University Press, Princeton. ISBN 978–0691146676
10. Geman S, Geman D (1984) Stochastic relaxation, Gibbs distributions, and the Bayesian restoration if images. IEEE Trans Pattern Anal Mach Intell 6(6):721–741
11. Goldberg A, Tarjan R (1988) A new approach to the maximum flow problem. J Assoc Comput Mach 35(4):921–940
12. Golub GH, Van Loan CF (1996) Matrix computations, 3rd edn. Johns Hopkins University Press, Baltimore. ISBN 0-8018-5414-8
13. Grieg B, Porteous B, Scheult A (1989) Exact maximum a posteriori estimation for binary images. J R Stat Soc B 51(2):271–279
14. Kolmogorov V, Zabih R (2004) What energy functions can be minimized via graph cuts? IEEE Trans Pattern Anal Mach Intell 26(2):147–159
15. Mishra AK, Aloimonos Y, Cheong L-F, Kassim AA (2012) Active visual segmentation. IEEE Trans Pattern Anal Mach Intell 34(4):639–653
16. Rother C, Kolmogorov V, Blake A (2004) GrabCut – interactive foreground extraction using iterated graph cuts. ACM Trans Graphic 23(3):309–314
17. Roy S (1999) Stereo without epipolar lines: a maximum-flow formulation. Int J Comput Vis 34 (2/3):147–161
18. Roy S, Cox IJ (1998) A maximum-flow formulation of the n-camera stereo correspondence problem. Int Conf Comput Vis 6:492–499
19. Shi J, Malik J (2000) Normalized cuts and image segmentation. IEEE Trans Pattern Anal Mach Intell 22(8):888–905

Chapter 7
Dynamic Programming (DP)

Abstract Some problems of computer vision can be formulated in a recursive manner. For this class of problems, the paradigm of dynamic programming (DP) represents an interesting tool in order to obtain a fast discrete solution. Here, the overall problem is broken down into a series of sub-problems, which are built upon each other and can therefore be solved iteratively. This way computation can be sped up considerably through the reusage of information gathered in already solved sub-problems. This chapter starts with presenting the well-known method of Dijkstra as an example of shortest path algorithms, which are closely related to DP. "Intelligent scissors" interactively segmenting an image are one example application. Furthermore, this chapter deals with two ways of applying the dynamic programming paradigm. First, dynamic programming is applicable if optimal positions or labels are to be found for a sequence of points, where the optimality criterion for each point depends on its predecessor(s). The task of calculating active contours can be reformulated in this manner. Second, some problems show a treelike structure, which makes a recursive formulation possible, too. The recognition of objects which are modeled as a configuration of parts is one example of this.

Dynamic programming (often abbreviated by DP) is based on the work of Bellman and is more a paradigm than a specific algorithm. It can accelerate discrete optimization considerably if the problem at hand has a special structure. Dynamic programming algorithms try to split the overall problem into a series of smaller sub-problems, which are easier to solve. Typically, the solution of the first sub-problem is more or less obvious or at least very simple. The other sub-problems get increasingly complex but can be solved quite fast as well in a recursive manner, because their solution is based on the solutions of the sub-problems they depend on.

In other words, we start by solving the smallest sub-problem and then iteratively go on with solving increasingly larger sub-problems, where we can make use of the solutions already obtained. This is a typical bottom-up approach, where information about the solutions of the sub-problems is stored and can then be reused when calculating the solutions of the larger problems.

M.A. Treiber, *Optimization for Computer Vision: An Introduction to Core Concepts and Methods*, Advances in Computer Vision and Pattern Recognition,
DOI 10.1007/978-1-4471-5283-5_7, © Springer-Verlag London 2013

However, such a proceeding requires that there exists a direct relation between the larger sub-problems and the sub-problems they depend on. This relation is termed the *Bellman equation* in literature.

In order to decide whether the dynamic programming paradigm is applicable for a given problem, we can check whether the problem features the following two key characteristics:

- *Optimal substructure*: This means that the solution of the problem can be derived from a combination of the solutions of some sub-problems. Usually, this is the case if a recursive problem formulation is possible.
- *Overlapping sub-problems*: Ideally, the solution of all sub-problems can be calculated by the same proceeding, e.g., by applying the same recursive formula. This is desirable because it allows for a straightforward implementation. Hence, this property states that there are at most just a few calculation rules for the solution of the sub-problems. If every sub-problem had its own rules, an efficient implementation in a computer program would not be possible.

After this short rather general introduction, we directly go on to some application fields of dynamic programming, because a deeper understanding of the working principle behind dynamic programming is probably best obtained by examining the applications. We start with shortest path algorithms and subsequently present dynamic programming along a sequence and in a tree.

7.1 Shortest Paths

7.1.1 Dijkstra's Algorithm

Consider a graph $G = (N, E)$ consisting of nodes of the set N, which are linked by edges of the set E, where each edge e_{ij} has a nonnegative weight w_{ij}. A quite common question is to find a shortest path between two nodes u and v, i.e., the path from u to v which has the smallest sum of edge weights. One well-known application of this shortest path algorithm is the problem to find the shortest route in a satnav system. Here, the e_{ij} corresponds to roads and the w_{ij} to their lengths.

Such problems can be solved with *Dijkstra's algorithm* (see [3]). Dijkstra makes use of the fact that if a specific path between u and v actually is the shortest path between these two nodes, the sub-path between u and any "intermediate" node r along the path as well as the sub-path between r and v are shortest paths, too.

This observation directly leads to a recursive formulation of the problem, where the total length of the shortest path between u and v can be calculated based on the lengths of the shortest paths between u and all neighbors of v. Let l_{uv} be the length of the shortest path between u and v. Furthermore, $R(v)$ shall denote the set of all neighbors of v, where each $r_i \in R(v)$ is connected to v by just one edge with weight

$w_{r_i v}$. We can then calculate l_{uv} by examining the l_{ur_i} as well as the $w_{r_i v}$. The relation between l_{uv} and the l_{ur_i} is given by

$$l_{uv} = \min_{r_i \in R(v)} \left(l_{ur_i} + w_{r_i v} \right) \tag{7.1}$$

The relation of (7.1) helps to identify the shortest path as follows. Suppose we pick one node x where the shortest path length l_{ux} between u and x is already known. This information can now be utilized for an update of the of the shortest path length estimates between u and all neighbors of x: suppose that for a neighbor r_i of x, there already exists an estimate $l^k_{ur_i}$ of the length of the shortest path form u to r_i. From (7.1) we now know that the new estimate under consideration of x can be set to $l^{k+1}_{ur_i} = \min\left(l^k_{ur_i}, l_{ux} + w_{xr_i} \right)$.

We can start at u and then iteratively expand the knowledge of the shortest paths across the graph by applying the same update formula at each iteration. This clearly shows that the problem has optimal substructure, which relates Dijkstra's method closely to dynamic programming.

Please observe that such a proceeding does not try to go straight to the destination node. Instead, the algorithm assumes that the destination will be reached anyway sooner or later and just goes on until exactly this happens. In other words, because the scheme performs an iterative update of the path lengths of *all* neighbors, it has no bias that the nodes under consideration gravitate quickly toward the destination node.

Before we describe how algorithm works in detail, let's first state that the node set N can be split into three disjoint subsets in the following way:

- ***Analyzed nodes***: This set A contains all nodes where the calculation is "finished", i.e., the lengths of the shortest path from u to $r; r \in A$ are already known.
- ***Candidate nodes***: Nodes of this set B already have been considered at least once. When we use the algorithm presented below, this means that there is at least one estimate for the length of the shortest path between u and $x_k; x_k \in B$. In contrast to the nodes of set A, however, not all edges which connect x_k to some other node have been examined yet. Therefore, it might still be possible to reduce the shortest path length estimate. At each iteration, Dijkstra's algorithm picks one node out of set B.
- ***Unvisited nodes***: This set C consists of nodes which have not been considered at all, i.e., have never been visited so far. Therefore, currently there is no estimate for the length of the shortest path from u to any node of this set available yet.

Utilizing this node classification, we can assign a cost l_{ur} between the starting node u and more and more nodes r and try to expand the set of known shortest paths to the neighbors of r as the iteration proceeds. Because usually we don't want to just calculate the lowest cost but also the route of the shortest path, the algorithm additionally remembers the incoming edge which belongs to the shortest path

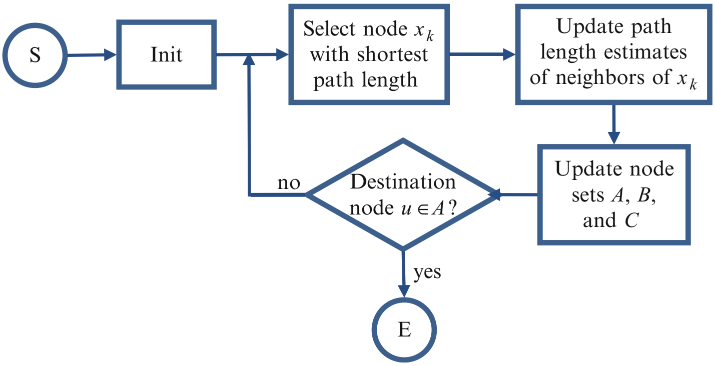
S
Init
Select node x_k with shortest path length
Update path length estimates of neighbors of x_k
Update node sets A, B, and C
Destination node $u \in A$?
no
yes
E

Fig. 7.1 Flowchart of the Dijkstra algorithm

from u to r for each node of set A. With the help of this information, the shortest path can be traced back from any node of set A to the starting node u.

The proceeding of the scheme first initializes the node sets with $A = \{\}$ (empty), $B = \{u\}$ (contains just the starting node u), and $C = N - \{u\}$. The length of the start node u to itself is equal to zero: $l_{uu} = 0$. All other lengths are set to infinity as we don't know anything about these values yet. The iteration which reveals the shortest paths comprises the following steps, which are performed repeatedly (see also flowchart in Fig. 7.1):

1. Take the node x_k from B, which has the lowest current shortest path estimate: $x_k = \arg\min(l_{ux_k})$. This node is considered most promising when trying to enlarge the set A.
2. Examine all neighbors r_i of x_k which are not part of A already ($r_i \notin A$). If $l_{ux_k} + w_{x_k r_i} < l_{ur_i}$, then we have found a shorter path from u to r_i. This new estimate of the shortest path from u to r_i passes through x_k. We can update the shortest path length estimate according to $l_{ur_i} = l_{ux_k} + w_{x_k r_i}$. In order to be able to restore the route of the shortest path, we additionally remember a pointer to x_k for each updated r_i, i.e., the edge $s(r_i)$ between r_i and x_k. We also transfer r_i to B, if it still is part of C (i.e., visited for the first time).
3. Transfer x_k from B to A, because now all edges connecting x_k are already examined and consequently l_{ux_k} will not change any longer.

This iteration terminates if either the destination node v is added to A (and hence the desired solution is found, so we can stop the iteration) or the set B gets empty. If B gets empty before v is reached, this means that v is unreachable from u. If v is reached, we know the total sum of edge weights along the shortest path. In order to recover the course of the shortest path, we trace back the stored edges, starting with $s(v)$, and collect them in the set S, until we reach the start node u.

Efficient implementations of the method have a complexity in the order of $O(E \cdot \log(N))$.

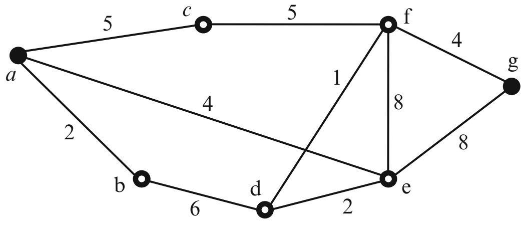

Fig. 7.2 Exemplifying a graph, where the shortest path from node *a* to node *g* has to be found. The edge weights are given next to each edge

Example

The working principle of the method is best shown with a small toy example. Consider the graph shown in Fig. 7.2, where the shortest path from node *a* to node *g* has to be found. The weights of the edges along the path are given next to each edge.

In the initialization stage of Dijkstra's algorithm, the node sets are initialized as follows: $A = \{\}, B = \{a\}$, and $C = \{b, c, d, e, f, g\}$. The distance estimate to *a* is set to zero ($l_{aa} = 0$), whereas all other distance estimates are set to infinity ($l_{ab} = l_{ac} = \ldots = l_{ag} = \infty$). A complete overview of the proceeding of the method for this example can be seen in Table 7.1.

In the first iteration, we pick node *a* from *B* (as it is the only node of this set) and update the distance estimates of the neighbors *b*, *c*, and *e* according to the weights of the edges between these nodes and node *a*. Moreover, these nodes are transferred from set *C* to *B*. Because all of its edges are now examined, *a* is transferred from *B* to *A* (for a summary, see column "Iter. 1" of Table 7.1). In order to be able to trace back the shortest path, set $s(b) = s(c) = s(e) = a$.

Iteration 2 starts with picking the node of set *B* with the smallest distance estimate, which is node *b*. The only neighbor of *b* which is not examined completely yet is node *d*, which is transferred to *B*. The distance estimate is set to $l_{ad} = l_{ab} + w_{bd} = 2 + 6 = 8$, $s(d) = b$. All other updates can be seen in column "Iter. 2" of Table 7.1.

The third iteration (see "Iter. 3") begins with the selection of node *e*, which can be used for a first estimate of l_{af} and l_{ag}. Moreover, we can see that the route to *d* via *e* is shorter than the previous estimate, as $l_{ae} + w_{ed} = 4 + 2 = 6 < 8$. Consequently, we reduce l_{ad} to six and change $s(d)$ to *e*. From now on, each node is visited at least once, and accordingly set *C* gets empty.

The main impact of iterations 4 and 5 is the reduction of l_{af} from 12 to 10 and 7, respectively, because we find a shorter path for *f* in each step. Additionally, $s(f)$ is finally changed to *d*.

In the last iteration, we find a better route to the destination node *g*. Tracing back the predecessors, the path $g \rightarrow f \rightarrow d \rightarrow e \rightarrow a$ is revealed (see Fig. 7.3).

Table. 7.1 Summarizing the proceeding of Dijkstra's algorithm for the example shown in Fig. 7.2.

	Init	Iter. 1	Iter. 2	Iter. 3	Iter. 4	Iter. 5	Iter. 6
A	$\{\}$	$\{a\}$	$\{a,b\}$	$\{a,b,e\}$	$\{a,b,c,e\}$	$\{a,b,c,d,e\}$	$\{a,b,c,d,e,f\}$
B	$\{a\}$	$\{b,c,e\}$	$\{c,e,d\}$	$\{c,d,f,g\}$	$\{d,f,g\}$	$\{f,g\}$	$\{g\}$
C	$\{b,c,d,e,f,g\}$	$\{d,f,g\}$	$\{f,g\}$	$\{\}$	$\{\}$	$\{\}$	$\{\}$
$\min(B)$		a	b	e	c	d	f
l_{aa}	0	0	0	0	0	0	0
l_{ab}	∞	**2**	2	2	2	2	2
l_{ac}	∞	**5**	5	5	5	5	5
l_{ad}	∞	∞	**8**	**6**	6	6	6
l_{ae}	∞	**4**	4	4	4	4	4
l_{af}	∞	∞	∞	**12**	**10**	**7**	7
l_{ag}	∞	∞	∞	**12**	12	12	**11**
$s(b)$	–	$\boldsymbol{a}$	a	a	a	a	a
$s(c)$	–	$\boldsymbol{a}$	a	a	a	a	a
$s(d)$	–	–	$\boldsymbol{b}$	$\boldsymbol{e}$	e	e	e
$s(e)$	–	$\boldsymbol{a}$	a	a	a	a	a
$s(f)$	–	–	–	$\boldsymbol{e}$	$\boldsymbol{c}$	$\boldsymbol{d}$	d
$s(g)$	–	–	–	$\boldsymbol{e}$	e	e	$\boldsymbol{f}$

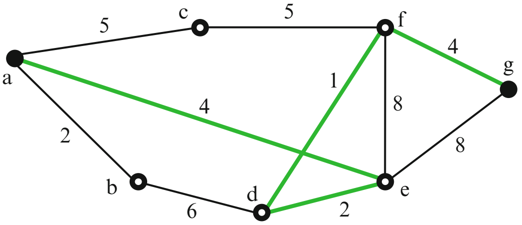

Fig. 7.3 Same path as in Fig. 7.2, where the shortest path from node *a* to node *g* is shown in bold *green*

Pseudocode

```
function shortestPathDijkstra (in graph $G = (N,E)$, in start node $u$, in destination node $v$, in edge weighs $W = \{w_{ij}\}$, out edges of shortest path $S = \{s(x)\}$

// initialization
$A \leftarrow \{\}$
$B \leftarrow \{u\}$; $l_{uu} \leftarrow 0$
$C \leftarrow N - \{u\}$

// main loop
repeat
    // step 1: select the most "promising" node $x_k$ of $B$
    $l_{ux_k} \leftarrow$ FLOAT_MAX
    for all nodes $b$ of $B$
        if $l_{ub} < l_{ux_k}$ then
            $l_{ux_k} \leftarrow l_{ub}$
            $x_k \leftarrow b$
        end if
    next
    // step 2: examine all neighbors $r_i$ of $x_k$ which are $\notin A$
    for all nodes $r_i$ linked to $x_k$ by an edge $e_{x_k r_i}$ && $r_i \notin A$
        if $l_{ux_k} + w_{x_k r_i} < l_{ur_i}$ then
            // shorter path between $u$ and $r_i$ found
            $l_{ur_i} \leftarrow l_{ux_k} + w_{x_k r_i}$ // update shortest path estimate
            $s(r_i) \leftarrow e_{x_k r_i}$     // remember edge for path tracing
            if $r_i \in C$ then
                $B \leftarrow B \cup \{r_i\}$
                $C \leftarrow C - \{r_i\}$
            end if
        end if
    next
    // step 3: update node sets
    $A \leftarrow A \cup \{x_k\}$
    $B \leftarrow B - \{x_k\}$
until $x_k == v$ (convergence) || $B == \{\}$ (abort)
// trace back shortest path
```

```
$x_k \leftarrow v$
repeat
    $S \leftarrow S \cup \{s(x_k)\}$
    set $x_k$ to the "other" node of $s(x_k)$
until $x_k == u$ (start node reached)
```

A disadvantage of Dijkstra's algorithm is that it does not make any effort to directly search the shortest path from u to the destination node v. This just happens "accidentally" sooner or later. As a consequence, the scheme does a lot of unnecessary work in unfavorable situations.

In order to overcome this weakness, some variants have been proposed over the years. Especially to mention is the A* method [10], which is a variant of Dijkstra's algorithm, which tries to select a "better" node x_k at each iteration than the original algorithm does. In this context, "better" means that the node choice is steered toward the destination node.

To this end, the node selection in step 1 is modified such that the decision value not only reflects the cost of the path traveled so far but also includes a term $d_{x_k v}$, which estimates the distance to the destination node. We can now define the modified decision value ld_{ux_k} by $ld_{ux_k} = l_{ux_k} + d_{x_k v}$. Consequently, the A* algorithm selects the node x_k of B with the lowest ld_{ux_k}.

However, some care is required, because the $d_{x_k v}$ must not overemphasize the distance to the destination node. Otherwise we might choose nodes with a current shortest path estimate which could be reduced if we had considered all of its neighbors. This situation can be avoided if the following relation holds: $\left| d_{xv} - d_{yv} \right| \leq w_{xy}$, i.e., the absolute difference of the $d_{\cdot v}$'s between adjacent nodes x and y is at most the weight w_{xy} of the edge connecting these two nodes.

7.1.2 *Example: Intelligent Scissors*

Shortest path algorithms can also be used for vision applications. One method utilizing shortest paths is termed "*intelligent scissors*" [11], which is a scheme for an interactive segmentation of images.

The segmentation of images, i.e., the separation of one or more objects shown in an image from the background, is a difficult task, among other reasons because both objects as well as the background can be highly structured, which makes it difficult to recognize them as connected regions. As a consequence, a fully automatic segmentation is often error-prone. Therefore, an interactive scheme for segmentation, which is guided by user input, is suggested in [11].

The general proceeding of the method is an interactive derivation of a curve, which separates an object from its surrounding background. To this end the user first selects a "seed point" where the curve should start. This point is placed at the boundary of the object to be segmented. Subsequently, the system automatically calculates "optimal" segmentation curves from the seed point to *every* other pixel of the image. These curves should follow the object boundary as much as possible. As

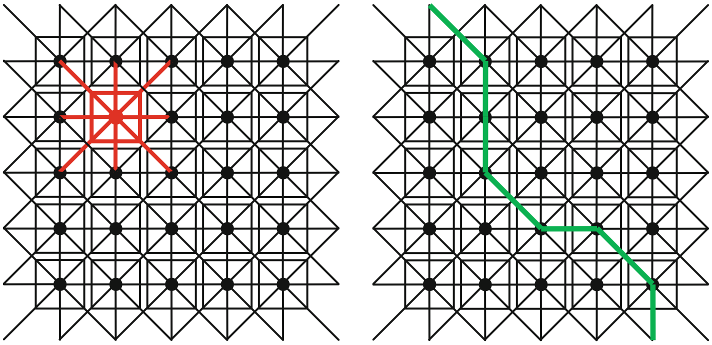

Fig. 7.4 Exemplifying the representation of a pixel grid as a graph. Each pixel (*square*) is represented by a node (*circle*), which is connected to its eight neighbors (*left grid*: one pixel is highlighted *red* as an example). *Right grid*: a segmentation is represented by contiguous edges in *bold green*

the user moves a mouse pointer within the image, the system displays the "optimal" curve from the seed point to the pixel currently covered by the mouse pointer. If the user wants to accept the curve as part of the object boundary, she/he can select it via mouse click.

In the next step, the user can select another starting point in order to define the next segment, probably near the end of the just determined curve segment. Again, the system calculates optimal curves to all other points, and one of them is selected by the user. This process is repeated until the segmentation is fully defined.

Now let's turn to the question how to calculate "optimal" curves from a seed point to all other pixels. To this end, the image is represented by a graph, where each pixel is represented by a node. Neighboring pixels p and q are connected by edges e_{pq} such that each pixel is connected to all pixels in its 8-neighborhood (see Fig. 7.4). Consequently, a segmentation can be represented by a set of contiguous edges (see edges *marked green* in the *right part* of Fig. 7.4). In order to select the edges which represent a segmentation, a weight $w(p,q)$ is attributed to each edge e_{pq}. The weight should reflect the suitability of an edge of being part of the segmentation. High probabilities of being part of an object boundary should lead to low edge weights.

Within this setup, we can determine the "optimal" segmentation curve from start pixel s to a termination pixel t with a shortest path algorithm. In order to calculate the shortest paths between s and all other pixels of the image, Mortensen et al. [11] utilize a variant of Dijkstra's algorithm, which proceeds until all pixels of the image are contained in set A.

The edge weights $w(p,q)$ between the pixels p and q are composed of three terms:

- ***Laplacian***: Second-order derivative information can be useful in order to judge whether a pixel p is likely to be located on the boundary of an object. Usually, the object intensity or color is different from the background. Positions where the second derivative of image intensity changes its sign (zero-crossing) indicate object boundaries, because zero-crossings in the second derivative correspond to local maxima (or minima) of the gradient. In order to approximate the second derivative of the image intensities, the image I can be convolved with a Laplacian kernel K_L, i.e., $L(x) = I(x) * K_L$, where * denotes the convolution operator. The Laplacian-based edge weight $w_L(q)$ can be calculated as follows:

$$w_L(q) = \begin{cases} 0 & \text{if } \operatorname{sign}(L(q)) \neq \operatorname{sign}(L(r));\ r \in \mathcal{N}_8(q) \\ 1 & \text{otherwise} \end{cases} \tag{7.2}$$

where $\mathcal{N}_8(q)$ denotes the 8-neighborhood of pixel q. In other words, $w_L(q)$, which has the meaning of a cost, is set to zero if a zero-crossing of L occurs between pixel q and any of its 8 neighbors; otherwise it is set to one.

- ***Gradient Magnitude***: It is well known that gradient strength is a good indicator for object boundaries, too. Usually, the larger the gradient magnitude $G(q) = \sqrt{(\partial I(q)/\partial x)^2 + (\partial I(q)/\partial y)^2}$ of a pixel q gets, the higher is the probability of q being part of an object boundary. Consequently, we can use $G(q)$ as another contribution $w_G(q)$ to $w(p,q)$:

$$w_G(q) = 1 - \frac{G(q)}{G_{\max}} \tag{7.3}$$

where $G_{\max}$ is the maximum gradient of the entire image, which ensures that $w_G(q)$ is between 0 and 1. Please note that $w_G(q)$ is small if $G(q)$ is near the maximum gradient and large otherwise.

- ***Gradient direction***: Object boundaries typically don't have many sharp changes of direction when we move from one boundary pixel to a second one being adjacent to it. Therefore, the third term $w_D(p,q)$ should reflect this bias to smooth edges by penalizing sharp changes in boundary direction. To this end, gradient directions can be used as follows. Consider the direction $\mathbf{d}(p) = [\partial I(p)/\partial y, -\partial I(p)/\partial x]^{\mathrm{T}}$, which is perpendicular to the direction of the intensity gradient of p and usually reflects the direction of the object boundary if the boundary is straight. We can therefore compare $\mathbf{d}(p)$ as well as $\mathbf{d}(q)$ with the direction $\mathbf{l}(p,q)$ of the link between p and q. If $\mathbf{l}(p,q)$ deviates much from $\mathbf{d}(p)$ or $\mathbf{d}(q)$, this indicates that we have a sharp change of boundary direction. "Smooth" boundaries in turn have only small deviations between $\mathbf{l}(p,q)$ and $\mathbf{d}(p)$ or $\mathbf{d}(q)$. Consequently, $w_D(p,q)$ should be small for smooth boundaries. The dot product $\langle \cdot \rangle$ is a good measure for direction differences, and the authors of [11] suggest to calculate $w_D(p,q)$ by

$$\begin{aligned} w_D(p,q) &= \frac{1}{\pi}\left[\frac{1}{\cos(\langle \mathbf{d}(p), \mathbf{l}(p,q)\rangle)} + \frac{1}{\cos(\langle \mathbf{l}(p,q), \mathbf{d}(q)\rangle)}\right] \\ \text{with } \mathbf{l}(p,q) &= \begin{cases} q-p & \text{if } \langle \mathbf{d}(p), q-p\rangle \geq 0 \\ p-q & \text{if } \langle \mathbf{d}(p), q-p\rangle < 0 \end{cases} \end{aligned} \tag{7.4}$$

Overall, $w(p,q)$ is calculated by

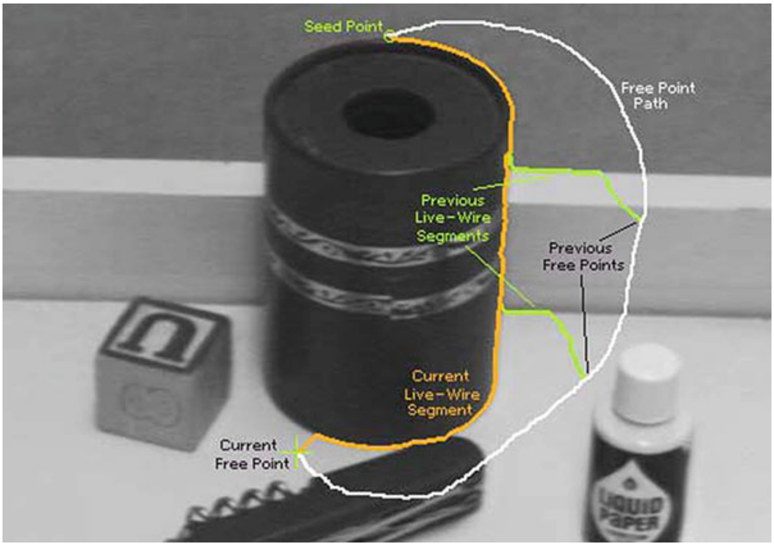

Fig. 7.5 Exemplifying the proceeding of the intelligence scissors method (Mortensen and Barett [11] © 1995 Association for Computing Machinery, Inc. Reprinted by permission)

$$w(p,q) = \alpha \cdot w_L(q) + \beta \cdot w_G(q) + \gamma \cdot w_D(p,q) \tag{7.5}$$

where α, β, and γ are weighting terms reflecting the relative influence of the corresponding term and are chosen empirically.

The application of (7.5) in a shortest path algorithm together with interactive user assistance yields a quite powerful and easy to handle method. Figure 7.5 illustrates the proceeding as well as the result. There you can see how the user moves the mouse pointer after selecting a seed point (white curve). Different positions on the white curve involve different shortest paths, which follow the true object contour as much as possible, and the branch to the current mouse pointer position (orange – true boundary, green paths: "branches" through the background to some selected mouse pointer positions). The orange path is the shortest path to the last known mouse pointer position as calculated by the system. As can easily be seen, this path is a very good approximation of the true object contour.

The image in Fig. 7.6 illustrates that the method works well even in challenging situations. This exemplifies the performance of the method, which is achieved with very little user input.

Usually, the user-selected endpoint does not lie exactly on the object boundary. A convenient possibility to "correct" this is to select the next starting point some pixels away from the current endpoint such that it coincides with the object boundary. Another possibility is to use the snap-in functionality of the algorithm, which forces the mouse pointer to positions of maximum gradient magnitude within a small neighborhood, e.g., 11×11 pixel.

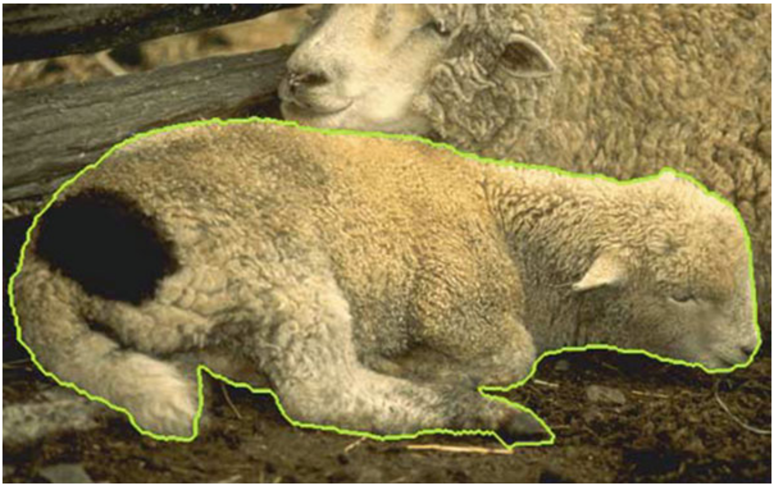

Fig. 7.6 Illustrating the performance of the shortest path-based scheme, even in challenging situations (Mortensen and Barett [11] © 1995 Association for Computing Machinery, Inc. Reprinted by permission)

A modification of the method is to modify (7.3) such that $w_G(q)$ reflects the *expected* properties of the gradient. This can be achieved by utilizing the last part of the already calculated object boundary in order to train the expected gradient properties (e.g., a gradient histogram). The calculation of $w_G(q)$ can then be modified such that $w_G(q)$ takes low values if the gradient strength is within the expected range of the gradient magnitudes observed in the training segment, e.g., if the trained histogram shows a high frequency for this gradient magnitude. This modification allows the system to select paths along object boundaries with rather low brightness changes to the background, even if very strong gradients are present in its vicinity.

7.2 Dynamic Programming Along a Sequence

7.2.1 General Proceeding

Consider the following situation: suppose we have a sequential arrangement of N elements p_n and we want to assign a label $x_n; n \in [1, 2, \ldots N]$ to each of those elements. Each x_n can take a specific value from a discrete label set $L = \{l_k\}; k \in [1, 2, \ldots, K]$ consisting of K elements. The assigned labels can be summarized in a vector $\mathbf{x} = (x_1, x_2, \ldots, x_N)$. Moreover, we can define a cost (which we can also term energy, as in the previous chapters) $E(\mathbf{x})$ for each labeling. The task then is to find the solution $\mathbf{x}^* = \left(x_1^*, x_2^*, \ldots, x_N^*\right)$, which minimizes the total cost: $\mathbf{x}^* = \arg\min[E(\mathbf{x})]$. As both the set of elements p_n as well as the label set are finite, we talk about a discrete optimization technique here.

In many applications, $E(\mathbf{x})$ can be defined to have the following structure (see also [6]; examples will follow later on):

$$E(\mathbf{x}) = \sum_{n=1}^{N} D_n(x_n) + \sum_{n=1}^{N-1} V(x_n, x_{n+1}) \tag{7.6}$$

Usually, the $D_n(x_n)$ are data-dependent terms, which describe the cost of assigning the label x_n to the nth element of the sequence, based on some observed data. The $V(x_n, x_{n+1})$ represent priors, which should reflect the probabilities of a joint labeling of two successive elements of the sequence. They are independent of the data and can therefore be calculated in advance for any possible combination of labels.

A closer look at (7.6) reveals that the energy defined here has the same structure as many energies utilized in the previous chapters: it is also composed of two terms, where one reflects the fidelity to some observed data, whereas the other incorporates some kind of prior knowledge, e.g., smoothness constraints. However, observe that the sums are taken along a (one-dimensional) sequence of elements, which is opposed to the two-dimensional sums along a pixel grid we already encountered.

In order to find the solution $\mathbf{x}^*$, dynamic programming can be used. The special case that the elements p_n are arranged along a one-dimensional sequence enables us to formulate the calculation of the energy in a recursive manner. Consider a labeling of a part of the sequence $(x_1, x_2, \ldots, x_n); n \leq N$. The cost for this labeling depends on the cost of the labeling of the subsequence $(x_1, x_2, \ldots, x_{n-1})$ where the last element p_n is excluded as follows:

$$E(x_1, x_2, \ldots, x_n) = E(x_1, x_2, \ldots, x_{n-1}) + D_n(x_n) + V(x_{n-1}, x_n) \tag{7.7}$$

Clearly, this is a recursive formulation. This fact can be exploited in dynamic programming by first calculating the minimum energy for a part of the sequence (i.e., solving a smaller sub-problem) and then reusing this information when extending the sequence by one additional element (i.e., extending the solution to a larger problem), until the minimum cost for the entire sequence is found.

In practice, for each element p_n of the sequence, a table B_n can be calculated, where each entry of $B_n(x_n)$ denotes the minimum cost of the subsequence from the first to the nth element p_n, under the assumption that the label x_n takes a specific value l_k. Therefore, each B_n is composed of K elements. The initialization for the first element of the sequence is trivial, because we can simply set $B_1(x_1) = D_1(x_1)$. The entries of all other tables can be calculated via the recursive formulation:

$$B_n(x_n) = D_n(x_n) + \min_{x_{n-1}} \left(B_{n-1}(x_{n-1}) + V(x_{n-1}, x_n)\right) \tag{7.8}$$

In other words, after starting with the trivial calculation of the minimum costs for the first table B_1, we can recursively extend the solution by one element in each step according to (7.8). Observe that previously computed tables B_{n-1} are reused in a later iteration, which is a typical characteristic of the dynamic programming paradigm.

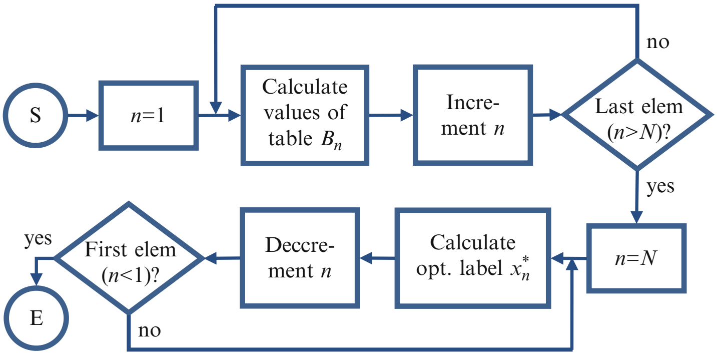

Fig. 7.7 Flowchart of the general dynamic programming algorithm flow. The forward step can be seen in the *top row*, the backward step in the *bottom row*

This speeds up calculations, because the reusage of previous computations accelerates the solution of each sub-problem significantly.

Up to now, we just calculate minimum costs, but we haven't determined the optimal labeling yet. However, as soon as the last element is reached, we can determine the labeling of the last element by examining the values of $B_N(x_N)$: The solution x_N^* can be identified such that the energy associated to x_N^* becomes minimal: $x_N^* = \arg\min_{x_N}(B_N(x_N))$. Once x_N^* is determined, we can trace back the solution according to

$$x_n^* = \arg\min_{x_n}\left(B_n(x_n) + V\left(x_n, x_{n+1}^*\right)\right) \tag{7.9}$$

until the first element of the sequence is reached. Again, we can see that previously computed $B_n(x_n)$ are reused to find the solution.

To sum it up, the general proceeding consists of two steps (Fig. 7.7):

1. *Forward step*: First, the optimal costs $B_n(x_n)$ under the assumption that the last element of the sequence is labeled with the specific value are calculated recursively using (7.8) and stored in the tables B_n while moving "forward" from the first element to the last.
2. *Backward step*: Once the optimal costs are known, we can trace back the solution according to (7.9) while moving "backward" from the end of the sequence to the beginning.

The complexity of the algorithm is given by $O(NK^2)$, because we have N tables to be filled, where each of them consists of K entries. The time necessary for calculating each table entry is of $O(K)$. Without giving any details here, let's note that this complexity can be reduced in many cases through the usage of so-called distance transforms (e.g., the interested reader is referred to [4]).

Observe that the problem given here can also be represented by a graph (see Fig. 7.8). Each element of the (horizontally arranged) sequence is represented

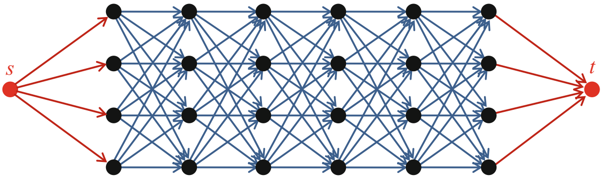

Fig. 7.8 Illustrating how the problem of finding a sequence of minimum cost can be represented by a graph (see text for details)

by K nodes (one vertical column in Fig. 7.8), which amounts to NK nodes for the whole sequence. Each node is connected to all K nodes of the subsequent element, which results in $NK(K-1)$ edges in total. Moreover, a weight $D_{n+1}(x_{n+1} = l_{k2}) + V(x_n = l_{k1}, x_{n+1} = l_{k2})$ can be attributed to the edge from node $(n, k1)$ to node $(n+1, k2)$. Additionally, two "special" nodes s and t are introduced (red nodes), where the edges from s to $(1, k)$ are weighted by $D_1(x_1 = l_k)$, whereas all edges to node t have weight zero. Figure 7.8 shows such a situation with $N = 6$ and $K = 4$.

With this setup, it is possible to obtain the solution by an algorithm, which finds the shortest path from s to t. If we apply Dijkstra's algorithm, for example, the overall complexity is of $O(NK^2 \cdot \log(NK))$ (because there are approximately NK^2 edges and NK nodes). Compared to the recursive dynamic programming approach, the higher complexity of Dijkstra's algorithm can be explained by the fact that those algorithms can handle more general situations, i.e., graphs with cycles. The DP method presented here is faster, because it exploits the special structure of the problem. This is another piece of evidence that, in general, optimization methods specializing in the problem at hand also are very fast.

7.2.2 Application: Active Contour Models

Now that the theory is clear, let's turn to the question which problems can be formulated such that their solution can be obtained by finding the optimal path through a sequence of points. Interestingly, it turns out that the method outlined above can be applied to the problem of finding a suitable deformable curve, which we encountered when dealing with active contours (see also Chap. 4).

Briefly summarized, active contours try to find a curve which fits best to the observed data, i.e., is located upon locations of high intensity gradient, but also satisfies some smoothness constraints, i.e., its first- and second-order derivatives should be rather low. The "classical" approach to find a solution is to set up an energy functional, which is based on data fidelity ("external energy") as well as smoothness constraints ("internal energy"), and obtain a solution by a variational approach, which seeks a solution of the Euler-Lagrange equation derived from the functional.

However, a problem with this proceeding is that a solution satisfying the Euler-Lagrange equation only provides a necessary condition for optimality. Consequently, there is no guarantee that the result is a global or even at least a local minimum in fact. Moreover, the calculations involve the estimation of higher-order derivatives, which are typically numerically derived from discrete data and therefore prone to sensor noise. In contrast to that, the DP approach guarantees to find the global optimum within the specified search space. However, it is a discrete optimization technique, so if we want to apply it to find a continuous contour, we must find a way to reformulate it as a discrete optimization problem (see, e.g., [1]).

Discretization can be done if we approximate the contour to be estimated by a finite set of N control points $p_n; 1 \leq n \leq N$. Furthermore, the location x_n of each control point can be approximated by a finite set of K discrete positions (see [6]). This approximation allows us to use the model described in the previous section as follows:

- Each control point can be interpreted as a specific element of a sequence of points.
- Each of the K possible positions of a specific control point can be interpreted as a state (or a label) of an element of the sequence just defined.

The data-dependent term $D_n(x_n)$ can be derived from the intensity gradient at position x_n. Hence, the $D_n(x_n)$ can be seen as a representation of the external energy used in variational optimization. $D_n(x_n)$ should be low at positions where the gradient is high, as these positions are likely to be part of an object border. For example, a linear dependence on the intensity gradient $G(x_n)$ can be used:

$$\begin{aligned} &D_n(x_n) = 1 - G(x_n)/G_{\max} \text{ with} \\ &G(x_n) = \sqrt{(\partial I(x_n)/\partial x)^2 + (\partial I(x_n)/\partial y)^2}; \quad G_{\max} = \max_{(x,y)\in I} G(x,y) \end{aligned} \tag{7.10}$$

The pairwise cost $V(x_n, x_{n+1})$ can be set proportional to the distance between successive control points, which steers the solution toward short curves. For example, we can take

$$V(x_n, x_{n+1}) = \alpha \cdot \|x_n - x_{n+1}\|^2 \tag{7.11}$$

where $\|\cdot\|$ denotes the L2 norm and α serves as a weighting factor controlling the relative influence of the different terms during optimization.

However, an important part of the internal energy in variational optimization is the bending energy, which is high if the second derivative of the curve is high. Therefore, considering the bending energy in the energy functional devalues parts of high curvature and encourages the solution to be smooth. Second-order derivative information can be approximated by considering three successive control points, e.g., by

$$H(x_n, x_{n+1}, x_{n+2}) = \beta \cdot \|x_n - 2 \cdot x_{n+1} + x_{n+2}\|^2 \tag{7.12}$$

Again, β is a weighting factor. H is high at positions of high curvature and therefore penalizes such control point position combinations.

Fortunately, there is a way of incorporating H into the dynamic programming approach. To this end, $E(\mathbf{x})$ is extended to

$$E(\mathbf{x}) = \sum_{n=1}^{N} D_n(x_n) + \sum_{n=1}^{N-1} V(x_n, x_{n+1}) + \sum_{n=1}^{N-2} H(x_n, x_{n+1}, x_{n+2}) \tag{7.13}$$

If we want to perform a recursive update of the solution, the introduction of H leads to the following modifications. Now each B_n depends on two variables, i.e., the position x_n of the current control point p_n as well as the position x_{n-1} of the preceding control point p_{n-1}. That is, the table $B_n(x_{n-1}, x_n)$ now depends on the position of two control points and represents the minimum cost from the start of the curve to p_n under the assumption that the position of p_n is fixed to x_n and the position of p_{n-1} is fixed to x_{n-1}. Consequently, each table B_n is a two-dimensional array consisting of K^2 entries.

An exception is the table of the first control point p_1, whose elements can simply be set to $B_1(x_1) = D_1(x_1)$. The table entries of the second control point are given by $B_2(x_1, x_2) = D_1(x_1) + D_2(x_2) + V(x_1, x_2)$. All following tables are calculated recursively by

$$\begin{aligned} B_n(x_{n-1}, x_n) =& D_n(x_n) + V(x_{n-1}, x_n) + \\ & + \min_{x_{n-2}} \left[B_{n-1}(x_{n-2}, x_{n-1}) + H(x_{n-2}, x_{n-1}, x_n) \right] \end{aligned} \tag{7.14}$$

The forward step can be performed through the usage of (7.14). In the backward step, we can set the solution of the last two points according to $\left(x_{N-1}^*, x_N^*\right) = \arg \min_{x_{N-1}, x_N} \left(B_N(x_{N-1}, x_N)\right)$ and then trace the solution back with

$$x_n^* = \arg \min_{x_n} \left(B_{n+1}\left(x_n, x_{n+1}^*\right) + H\left(x_n, x_{n+1}^*, x_{n+2}^*\right) \right) \tag{7.15}$$

Observe that until now, this proceeding only works for open curves. However, many applications require determining a closed contour, which leads to terms like $H(x_{N-1}, x_N, x_1)$ in the energy function, for example. These cyclic relationships are prohibitive for dynamic programming, because this means that the table entries of the "start" depend on values of the "end" of the sequence. Fortunately, there is a way out of this dilemma if we specify the position of two successive control points prior to optimization, leave these positions unchanged during optimization, and optimize just the remaining control point positions as just described.

In contrast to variational optimization, the discrete DP approach guarantees to find the global optimum if the set of values for each x_n ranges over the entire image, i.e., each p_n is allowed to take the position of any pixel. However, such a proceeding usually is infeasible in terms of runtime, as there are $(W \cdot H)^N$ possible combinations to examine (W: image width; H: image height). In order to alleviate this problem, we limit the set of positions each x_n can take to a neighborhood around an initial estimate.

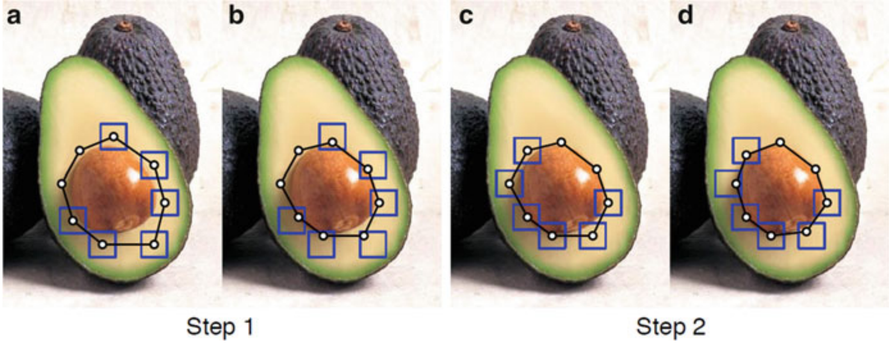

Fig. 7.9 Illustrating the proceeding of finding the optimal contour of avocado pits (see text for details) (© 2011 IEEE. Reprinted, with permission, from Felzenszwalb and Zabih [6])

Consequently, each solution calculated by (7.15) is only a local minimum. The convergence area can be enlarged by an iterative application of the same proceeding at the just found solution. This is in line with the need to fix two of the control points of a closed contour, because now we can fix two different points at each iteration step such that eventually all control points are optimized.

An example can be seen in Fig. 7.9. The initial estimation can be seen in the image on the left (step 1 (a) where the position of each control point is indicated by a black circle). The neighborhood around each control point being considered during optimization is indicated by a blue square. The two control points without square are fixed in the first iteration. The solution can be seen in step1 (b): Most of the optimized positions are located upon the true object contour, but some points in the lower right part are not optimal yet, simply because the correct solution was located outside the control point neighborhoods. However, principally due to the internal constraints, their position has moved considerably toward the correct solution.

The repeated calculations (Step 2) are done with modified neighborhoods. The control points being fixed in the current iteration have moved, too. The result of this second iteration already is the desired optimum (d).

Pseudocode

```
function **optimizeActiveContourWithDP** (in image $I$, in start positions of control points $\mathbf{x}^0 = \left(x_1^0, x_2^0, \ldots, x_N^0\right)$ (closed curve), in convergence criterion $\varepsilon$, out optimized control point positions $\mathbf{x}^* = \left(x_1^*, x_2^*, \ldots, x_N^*\right)$

// initialization
calculate intensity gradient magnitudes $G(x,y)$ and set $G_{\max} = \max_{(x,y)\in I} G(x,y)$.

// main loop: repeated optimization until convergence is achieved
$k \leftarrow 0$
```

```
repeat
    // forward step: calculate minimum costs
    randomly choose two successive points $x_{s-1}$ and $x_s$ as "fixed
    points" (where the position doesn't change in current
    iteration); $1 \leq s \leq N$
    init of recursion: $B_{s-1}\left(x_{s-1}^k\right) = D_{s-1}\left(x_{s-1}^k\right)$ and $B_s\left(x_{s-1}^k, x_s^k\right) =$
    $D_{s-1}\left(x_{s-1}^k\right) + D_s\left(x_s^k\right) + V\left(x_{s-1}^k, x_s^k\right)$.
    $n \leftarrow s+1$
    if $n > N$ then
      $n \leftarrow n-N$          // "cyclic" permutation
    end if
    while $n \neq s$
      for all positions of the neighborhood around current
      estimate $x_n^k$
        for all positions of the neighborhood around current
        position estimate $x_{n-1}^k$
          calculate $B_n(x_{n-1}, x_n)$ according to (7.14)
        next
      next
      $n \leftarrow (n \mod N) + 1$          // "cyclic" increment
    end while
    re-calculation of total cost for the two fixed points by
    usage of $B_s^*\left(x_{s-1}^k, x_s^k\right) = \min\limits_{x_{s-2}} \left[B_{s-1}\left(x_{s-2}, x_{s-1}^k\right) + H\left(x_{s-2}, x_{s-1}^k, x_s^k\right)\right]$
    // backward step: trace back and update solution
    $x_s^* \leftarrow x_s^k$          // position is fixed
    $x_{s-1}^* \leftarrow x_{s-1}^k$          // position is fixed
    $n \leftarrow s-2$
    if $n < 1$ then
      $n \leftarrow n+N$     // "cyclic" permutation
    end if
    repeat
      calculate $x_n^*$ according to (7.15)
      $n \leftarrow n-1$
      if $n < 1$ then
        $n \leftarrow n+N$          // "cyclic" permutation
      end if
    until $n == s$
    // prepare next iteration
    $\Delta \leftarrow \sum_{n=1}^{N} \left\|x_n^* - x_n^k\right\|$
    $k \leftarrow k+1$
    $\mathbf{x}^k \leftarrow \mathbf{x}^*$
until $\Delta < \varepsilon$ // $\Delta < \varepsilon$ indicates convergence ($\Delta$ is cumulative
displacement between solutions of two successive
iterations)
```

Please note that the pseudocode given above works for closed curves, as this is more common than open curves. However, for closed curves we have to take care that all indices $s - 1$, $n - 1$, etc. have to be within the bounds given by $[1, \ldots, N]$. This can be ensured by a cyclic permutation, i.e., by setting $N + 1$ to $1, N$ to 0, and so on. For reasons of clarity this cyclic permutation is not explicitly performed for all indices used in the pseudocode above, but of course has to be done in a real implementation.

7.3 Dynamic Programming Along a Tree

As we will see in this section, some applications make use of a tree-shaped model, e.g., object recognition tasks, where the object model can be split into several parts which are allowed to move with respect to each other. Consider so-called articulated shapes, for example. This object model dates back to [9] and consists of several parts, where some of them have a special relationship between each other. A model of the human body, for example, could be split into different parts, such as head, torso, legs, and arms. Some of the parts are "connected" to each other in a hierarchical manner, e.g., arms to head and hand to arm. Articulation here means that the parts are allowed to move with respect to each other, at least up to a certain extent.

If we want to detect objects of varying appearance due to articulation, the modeling by a tree is an elegant way of incorporating these intra-class variations. It makes the object detection method more invariant to those variations, because despite the overall appearance of the object can vary considerably, the appearance of each part remains rather static and can therefore be detected more reliably. Through usage of the articulation model, we can bring together the individual detections of the object parts.

It turns out that dynamic programming is applicable to tree-based models as well. The next section describes what has to be done in general such that DP can be applied to the optimization of tree-shaped models. After that, the example of utilizing such tree-shaped models for object recognition is presented in more detail.

7.3.1 General Proceeding

Consider a tree consisting of a set of nodes $N = \{n_i\}; 1 \leq i \leq \|N\|$, where $\|\cdot\|$ denotes the cardinality of a set (i.e., the number of its elements). Furthermore, we can assign a label x_i to each node n_i with $x_i \in L; \|L\| = K$, where $L = \{l_k\}$; $k \in [1, 2, \ldots, K]$ represents the set of labels which can be applied to each node with a cardinality of K.

Moreover, two nodes n_i and n_j are connected by an edge e_{ij} if they have a special relationship. We can assign a cost $V_{ij}\left(x_i, x_j\right)$ to each e_{ij}, depending on the labeling of n_i and n_j.

Similar to the sequence case, we can define an energy measure which considers the labeling of the whole tree and is defined by

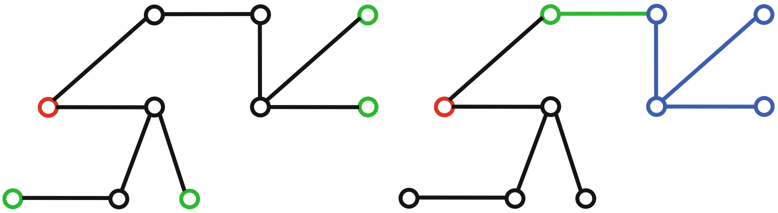

Fig. 7.10 Exemplifying a tree structure (*left*) and illustrating the suitability of trees for dynamic programming (*right*)

$$E(x_1, x_2, \ldots, x_N) = E(\mathbf{x}) = \sum_{i=1}^{N} D_i(x_i) + \sum_{e_{ij}} V_{ij}\left(x_i, x_j\right) \tag{7.16}$$

Now the task is to find a labeling $\mathbf{x}^* = \left(x_1^*, x_2^*, \ldots, x_N^*\right)$ of the whole tree which globally minimizes (7.16).

The nature of trees prohibits the existence of cycles in the graph. This is essential for the applicability of a DP approach, because only then it is possible to formulate the minimization problem in a recursive manner. If the graph contains no cycles, we can arbitrarily pick one node as the root node n_r. The nodes connected to n_r are called *children* of n_r, and n_r is called their *parent node*. A node can have one or more children, but all nodes (except the root) have exactly one parent. Nodes without children are called *leaf nodes*. As a tree doesn't contain cycles, each node n_i has a certain *depth* d_i, which amounts to the number of edges between n_i and the root n_r. The depth of n_i and its parent n_p differ exactly by one: $d_i = d_p + 1$. An example of a tree can be seen in Fig. 7.10 (left), where the root node is marked red and all leaf nodes are marked green.

This special structure of a tree can be exploited for a recursive formulation of the proceeding of finding the global minimum $\mathbf{x}^*$. The main observation here is that the solution of a subtree, i.e., the optimal labeling if we consider only a part of the tree, doesn't change if we enlarge the subtree and recalculate the solution. This is illustrated in the right part of Fig. 7.10: suppose we already have found an optimal labeling for the subtree marked blue. If we expand the tree by the unique parent (marked green) and recalculate the solution of the expanded subtree, the optimal labeling of the blue part remains unchanged.

Consequently, we can start at the leaf nodes, where the minimum cost can be found very quickly, and then enlarge the solution by expanding the subtrees by including parent nodes. Based on this, we can calculate the solution of the whole tree in two steps (just as in the sequence case) as follows:

1. ***Forward step***: In this step, we want to find the minimum costs of the subtrees starting at the leaf nodes up to a certain node n_i under the assumption that the last element of the subtree is labeled with the specific value x_i. That is, our aim is to calculate the optimal costs $B_i(x_i)$ for all nodes, where each $B_i(x_i)$ is a table consisting of K elements. One element contains the minimal subtree cost under

the assumption that $x_i = l_k$, as in the sequence case. We start at the leaf nodes, where we can simply set $B_l(x_l) = D_l(x_l)$. After this, all subtrees (which after the first step consist of only one leaf node) are expanded iteratively by inclusion of the unique parent of the "newest" node (i.e., the node which was included most recently in the subtree currently under consideration) until the root is reached. If we include a node n_i in the subtree, we set the $B_i(x_i)$ according to

$$B_i(x_i) = D_i(x_i) + \sum_{n_j \in C_i} \min\left(B_j\left(x_j\right) + V_{ij}\left(x_i, x_j\right)\right) \tag{7.17}$$

where C_i denotes the set of all children of n_i. Just a quick look at (7.17) reveals that the table entries can be calculated once and be reused in later iterations when examining the parent nodes.

Please note that in order to calculate the $B_i(x_i)$ as defined in (7.17), the $B_j\left(x_j\right)$ of *all* child nodes have to be known already. This implies certain constraints, which have to be fulfilled when we choose the subtree which is to be expanded next. One idea is to take only nodes where the cumulated costs of all children are known already. An example of the proceeding is given in Fig. 7.11, where the nodes already processed are marked blue and all possible expansions are marked green. Observe that not all parent nodes are marked green, because the minimum costs of the subtrees of those potential parents are not known for all subtrees. An alternative approach is to expand the subtrees according to the depth of the nodes. Starting with all nodes having maximum depth of the tree (which by definition must all be leaf nodes), we can expand all nodes of the same depth at each step. In each iteration, the depth is decreased by one until the root is reached: decreasing by one ensures that all child nodes of the "new" nodes have been processed already.

2. ***Backward step***: Once the optimal costs are known, we can trace back the solution starting at the root node and moving "backward" to the child nodes until a leaf node is reached. At the root, we can pick the label x_r^* according to $x_r^* = \arg\min_{x_r} \left(B_r(x_r)\right)$. If we move backward to some child n_i, its label x_i^* is given by

$$x_i^* = \arg\min_{x_i} \left(B_i(x_i) + V_{ij}\left(x_i, x_j^*\right)\right) \tag{7.18}$$

where x_j^* denotes the solution of the (unique) parent node n_j of n_i. This proceeding stops if the optimal labeling of *all* nodes is determined.

The computational complexity of this proceeding is given by $O(\|N\| \cdot K^2)$, because the runtime is largely determined by the forward step where we have to calculate a table of optimal values for each of the nodes of the tree, each table consists of K entries, and for each entry, $O(K)$ operations are necessary for finding the minimum according to (7.17). This can be further reduced through the usage of distance transforms.

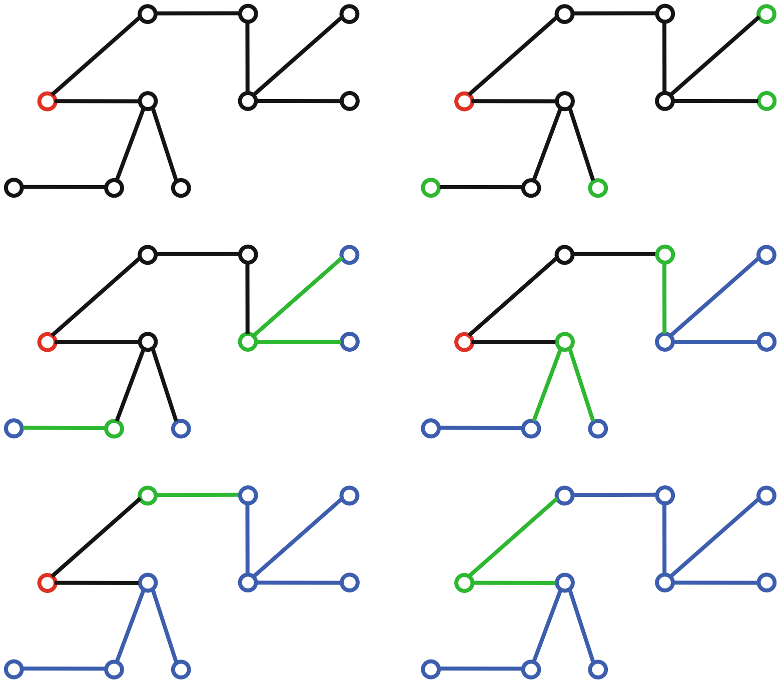

Fig. 7.11 Illustrating the proceeding of the forward step of the dynamic programming approach considering a tree. At start, the costs of the leafs can be calculated (*marked green* in the graph on the right side of the first row). All possible expansions are shown in the *left graph* of the second row. Right to this, we can see the expansions of the next iteration. This proceeding is repeated until the costs of the root node can be calculated (*right graph* of the bottom row)

7.3.2 Example: Pictorial Structures for Object Recognition

7.3.2.1 Framework

A major challenge in object recognition is to handle the large intra-class variations of some object classes. Consider the task of detecting human persons, for example. Their appearance can vary considerably, because particularly the limbs can take quite different positions compared to the rest of the body. Consequently, a detector relying on a rather rigid object model will run into difficulties.

One way of tackling this problem is to split up the model into multiple parts: Here, the model consists of a separate modeling of each part (e.g., head, torso) as well as their spatial relationships with respect to each other. By splitting the model into parts and allowing to move each part around its expected position (relative to the object center), we get extra degrees of freedom allowing to handle local deformations of the object, which could be articulation in our case. This paradigm was first introduced in [9]. A further example is a scheme proposed by Felzenszwalb and Huttenlocher, which is called “Pictorial Structures for Object

Recognition" [5]. In the meantime, this quite powerful method has been refined by the same research group (cf. [7], [8]) and shall be presented in more detail in the following.

As already mentioned, Felzenszwalb and Huttenlocher adopt the approach of splitting the object into different parts, too. Each part n_i is described by some appearance parameters $\mathbf{u}_i$ and its position $\mathbf{l}_i$. The relationship between the parts is modeled by a graph $G = (N, E)$, where the nodes $N = \{n_1, \ldots, n_M\}$ correspond to the M parts. A pair of nodes n_i and n_j is linked by an edge $\left(n_i, n_j\right) \in E$ if n_i and n_j feature a characteristic relationship. The properties of this relationship, in turn, is modeled by some connection parameters $\mathbf{c}_{ij}$.

Now let's assume that G has the form of a tree, i.e., does not contain any cycles. For most object classes, this assumption not really constitutes a noteworthy restriction. If we prohibit cycles in G, however, we are able to apply dynamic programming in the object recognition process. A part-based modeling in a tree is quite natural for many object classes. For example, in [5] it is suggested to model the human body by a tree of ten parts, consisting of head, torso, and the four limbs, which are split into two parts each (cf. *left image* of Fig. 7.12). This configuration is flexible enough for modeling considerable articulation, as the right image of Fig. 7.12 shows.

Star-based models have also been suggested. They are composed of a root node which covers the whole object at coarse resolution and leaf nodes where each node covers one part of the object at a finer resolution. Hence, a star-based model is a simple form of a tree, which consists of the root and leaf nodes only. This simple model is suitable for modeling a large variety of object classes (like cars, different kind of animals), where the relative position of the parts is subject to variations, e.g., due to viewpoint change, local deformations, and so on.

During recognition, the aim of the method is to find the positions of all parts of the searched model in a query image. This can be summarized in a vector $L = (\mathbf{l}_1, \ldots, \mathbf{l}_M)$ called *configuration* by the authors of [5], where each $\mathbf{l}_i$ denotes the (center) position of a part. To this end, we can define an energy function F, which is composed of two terms:

1. *Appearance-based term* $m_i(\mathbf{l}_i, \mathbf{u}_i)$ measuring the degree of mismatch between model and query image if part i is placed at location $\mathbf{l}_i$ in the query image. Usually, $m_i(\mathbf{l}_i, \mathbf{u}_i)$ is calculated by comparing the image content in a neighborhood around $\mathbf{l}_i$ (appearance) with the part model (represented by the appearance parameters $\mathbf{u}_i$). These appearance parameters $\mathbf{u}_i$ have to be learned in a training stage.
2. *Deformation-based term* $d_{ij}\left(\mathbf{l}_i, \mathbf{l}_j, \mathbf{c}_{ij}\right)$ reflecting the degree of deformation if we place part i at location $\mathbf{l}_i$ and part j at location $\mathbf{l}_j$. Observe that $d_{ij}\left(\mathbf{l}_i, \mathbf{l}_j, \mathbf{c}_{ij}\right)$ is only calculated if n_i and n_j are connected by an edge e_{ij}. During training, we can learn the likelihood of particular location combinations. This distribution is represented by the connection parameters $\mathbf{c}_{ij}$.

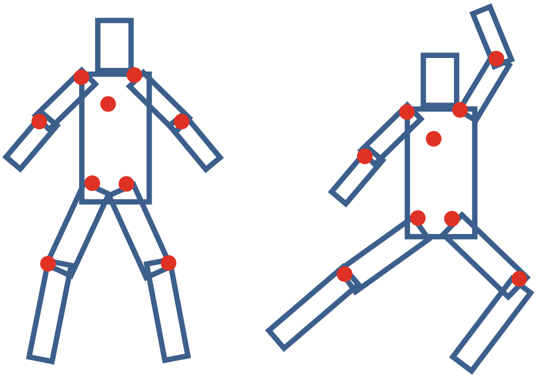

Fig. 7.12 Illustrating the human body model of [5], where each part is represented by a rectangle. Connections between parts are indicated by *red circles* at the joints between the parts. The basic configuration can be seen in the *left part*, whereas an example of an articulated model is depicted in the *right part*

In total, we have

$$F(L) = \sum_{i=1}^{M} m_i(\mathbf{l}_i, \mathbf{u}_i) + \sum_{(n_i,n_j)\in E} d_{ij}\left(\mathbf{l}_i, \mathbf{l}_j, \mathbf{c}_{ij}\right) \tag{7.19}$$

Now the goal is to find the configuration $L^* = \arg\min_L F(L)$ which minimizes (7.19). Observe that L^* is a global minimum of L, which jointly considers the appearance of each part as well as their relative positions. This is in contrast to (and superior to) many other part-based methods, which first make some hard decisions about the location of the parts and then evaluate the geometric configuration. The problem with the joint consideration of appearance and geometry is the computational complexity, because the search space of each $\mathbf{l}_i$ is in the order of the image size, which can amount up to millions of pixels. However, due to the structure of (7.19) and the tree model, we can apply dynamic programming, which, together with further speedups through distance transforms, makes a joint processing feasible.

Another advantage of this approach is that the modeling of the appearance of each part as well as their positional arrangement takes place separately. Hence, the object model allows for variations in the appearance of each part and deformations of the relative positions of the parts at the same time. This kind of object representation is very generic and can be applied to a large number of object classes. Please note that (7.19) only provides a framework, and we are free to model the parameters m_i, $\mathbf{u}_i$, d_{ij}, and $\mathbf{c}_{ij}$ such that they best fit to a particular problem at hand.

7.3.2.2 Example: Star Model with HOG Appearance

It was shown in [7] and [8] that a tree-based object model is flexible enough for a detection of a wide variety of object classes. Felzenszwalb et al. reported similar or leading recognition performance compared to state-of-the-art algorithms on diverse VOC (Visual Object Classes Challenge) data sets ([12], [13]), which are acknowledged to be very challenging. The research group suggested several ways of modeling the objects for different applications. In the following, one example of applying this framework utilizing a so-called star model (consisting of a root node, which is connected to multiple leaf nodes) together with appearance modeling with the help of HOG descriptors is presented.

Modeling of Geometry

As far as the geometric modeling of the parts is concerned, the authors of [7], [8] utilize a star model (as just mentioned), where the entire object at a coarse resolution is used as a root. The root is connected to all parts, which are evaluated at twice resolution compared to the root. Because of the reduction of resolution, it is possible to model the entire object in a single more or less rigid manner, as variations due to deformation / articulation are reduced during downsampling, too.

The deformation between the parts and the root (second term of (7.19)) can be measured by comparing the relative distance of part i to the position of the root (which shall from now on be denoted by subscript one). If we take $\mathbf{l}_i = [x_i, y_i]$ as part position currently under consideration, $\mathbf{l}_1 = [x_1, y_1]$ as supposed root position, and $\mathbf{v}_i$ as nominal value of the relative displacement between part i and the root, we can calculate the deformation $[\mathrm{d}x_i, \mathrm{d}y_i]$ by $[\mathrm{d}x_i, \mathrm{d}y_i] = (\mathbf{l}_i - \mathbf{l}_1) - \mathbf{v}_i$, i.e., the difference between actual and expected displacement between the ith part and the root. The deformation cost can then be set to the sum of the deformations and their squares, weighted by factors $\mathbf{w}_i$ ($\langle\cdot\rangle$ denotes the dot product):

$$d_{i1}(\mathbf{l}_i, \mathbf{l}_1, \mathbf{v}_i, \mathbf{w}_i) = \langle \mathbf{w}_i, \mathbf{d}_i \rangle \tag{7.20}$$

where the vector $\mathbf{d}_i = [\mathrm{d}x_i, \mathrm{d}y_i, \mathrm{d}x_i{}^2, \mathrm{d}y_i{}^2]$ summarizes the displacement information. Hence, the connection parameters $\mathbf{c}_{i1}$ comprise the expected displacement $\mathbf{v}_i$ between the part and root as well as the weighting factors $\mathbf{w}_i$. The optimal splitting of the object into parts, the relative position $\mathbf{v}_i$ of the parts compared to the root, and the parameters $\mathbf{w}_i$ of the deformation cost are all learned in a training stage in an automatic manner (see below).

Modeling of Appearance

As far as the appearance is concerned, a descriptor-based modeling is suggested in [7], [8].[1] To this end, the HOG descriptor (Histogram of Oriented Gradients) [2] is chosen, which already has been presented in more detail in Chap. 2.

[1] Please note that in [7] and especially [8] several modifications for performance-tuning are proposed, which have been omitted here for clarity reasons. In this section, we just describe the outline of the method. The interested reader is referred to the references for details.

Briefly summarized, we can represent the appearance by first calculating the intensity gradient magnitude and orientation at each pixel and quantizing the orientation into a moderate number of discrete orientations (a typical number of orientation bins is 9, ranging from 0 to just 180° in order to be contrast-insensitive). Furthermore, the image is divided into nonoverlapping cells of, e.g., 8×8 pixels size, and the discretized orientations of all pixels within one cell are accumulated into a 9-bin histogram. The contribution of each pixel is weighted by its gradient magnitude. Finally, the orientation histogram of a cell is normalized with respect to multiple neighborhoods. Specifically, four separate normalizations are performed, which eventually leads to a descriptor consisting of $4 \times 9 = 36$ elements for each cell.

Up to now, an open question is how to evaluate the appearance costs $m_i(\mathbf{l}_i, \mathbf{u}_i)$ during recognition. In the method presented here, we are only interested in finding translated and scaled versions of the object model, but don't consider rotation.[2] Therefore, the HOG descriptor is calculated "densely" (i.e., at every possible x/y location). The concatenation of all descriptors which are supposed to cover part i (under the assumption that it is located at position $\mathbf{l}_i$) can then be compared to the model (represented by the appearance parameters $\mathbf{u}_i$).

Actually, instead of calculating costs, a similarity measure is calculated, which takes high values when the HOG descriptors are similar to the model. Consequently, during recognition we have to perform a maximization instead of a minimization. However, this can be done by the same dynamic programming proceeding; we just have to replace the min-operators by max-operators.

Because we want to consider scale, too, the descriptors are also calculated and compared at different resolutions, which are obtained by a repeated downsampling of the original image. This proceeding is illustrated in Fig. 7.13: At first, the image is downsampled repeatedly by a predefined factor λ (e.g., $\lambda = 1.15$, which leads to five images for each "octave." Within each octave, the resolution is decreased by a factor of 2). Stacking all images on top of each other in the order of decreasing resolution leads to a so-called image pyramid (*left part* of Fig. 7.13).

For each image of the pyramid, the HOG descriptors are calculated separately and accumulated in a so-called feature pyramid. This is symbolized in the right part of Fig. 7.13, where each gray square represents one descriptor. At each location $\mathbf{l} = [x, y, s]$ (s denotes the scale index, i.e., the pyramid index of the image), we can calculate a descriptor $H(x, y, s)$ containing the 9-bin histogram of oriented gradients of a cell whose upper left pixel is located at position $[x, y]$. Each $H(x, y, s)$ is normalized with respect to four different neighborhoods, leading to a 36-element descriptor at each location and scale.

The appearance similarity $m_i(\mathbf{l}_i, \mathbf{u}_i)$ is then calculated by at first concatenating the descriptors of all pixels, which are supposed to be covered by part i (termed

[2] However, the method can be extended to account for rotated versions of the object as well by introducing a rotation parameter in the $\mathbf{l}_i$.

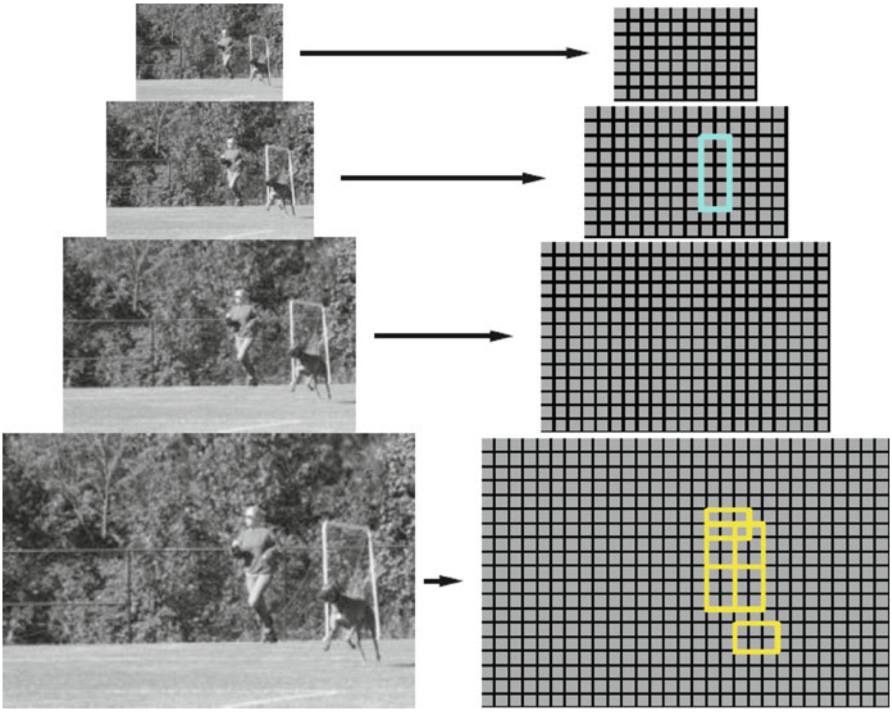

Fig. 7.13 Illustrating the hierarchical search of the root filter (*cyan*) and the parts (*yellow*) (© 2008 IEEE. Reprinted, with permission, from Felzenszwalb et al. [7])

$\phi(H, x, y, s)$, illustrated by colored rectangles in Fig. 7.13), and then calculating the dot product between ϕ and the appearance parameters $\mathbf{u}_i$ of part i:

$$m_i(\mathbf{l}_i, \mathbf{u}_i) = \langle \mathbf{u}_i, \phi(H, \mathbf{l}_i) \rangle \tag{7.21}$$

Because the root position has to be calculated at a coarser resolution compared to the parts, it has to be located at higher levels of the pyramid (cyan rectangle), compared to the parts (yellow rectangles).

Training Phase

The model parameters are summarized in θ, which consists of the appearance parameters, the graph structure, and the connection parameters: $\theta = (\mathbf{u}, E, \mathbf{c})$. All parameters of θ have to be determined in a training stage. With the VOC data set, this can be done in a weakly supervised manner. The data set contains training images, where the objects are user labeled by a rectangular bounding box. However, no partitioning into parts is given. Therefore, Felzenszwalb et al. use a latent

Support Vector Machine (SVM) approach in order to learn the model parameters, where the (unknown) positions of the parts are treated as latent variables. Furthermore, the configuration of the parts is automatically determined by the system, too.

As we concentrate on dynamic programming, we do not give any details about training here and assume that θ is known for all object classes to be detected. However, please note that the training stage is critical for good detection performance, because the number of model parameters utilized by the system is quite high. Therefore, we need an effective training procedure as well as rich training data in order to obtain a correct modeling. If too few training images are used, we are in danger of running into difficulties called "overfitting," where the model is not capable to represent unseen instances of the object sufficiently well. Probably, this is the reason why simpler methods, which contain much less parameters and therefore are much easier to train, often achieve quite competitive performance in practice despite of their limitations.

Recognition Phase

Coming back to the recognition phase, instances of objects are detected by maximizing the score function

$$\begin{aligned} S(\mathbf{l}_1,\ldots,\mathbf{l}_M) &= \sum_{i=1}^{M} m_i(\mathbf{l}_i,\mathbf{u}_i) - \sum_{i=2}^{M} d_{i1}(\mathbf{l}_i,\mathbf{l}_1,\mathbf{v}_i,\mathbf{w}_i) \\ &= \sum_{i=1}^{M} \langle \mathbf{u}_i, \phi(H,\mathbf{l}_i)\rangle - \sum_{i=2}^{M} \langle \mathbf{w}_i, \mathbf{d}_i\rangle \end{aligned} \tag{7.22}$$

where the solution is given by $\left(\mathbf{l}_1^*,\ldots,\mathbf{l}_M^*\right) = \arg\max S(\mathbf{l}_1,\ldots,\mathbf{l}_M)$. As a star-shaped model is used, the forward step of a dynamic programming optimization of (7.22) consists of just two iterations. A direct application of the DP approach in the forward step would involve calculating $S(\mathbf{l}_i) = m_i(\mathbf{l}_i,\mathbf{u}_i)$ for each part separately (for every possible location $[x,y,s]$ in the image pyramid) in the first iteration. In the second iteration, we could then calculate the overall score function S for each possible location of the root part by fixing $\mathbf{l}_1$, calculate the maximum score for that particular fixed $\mathbf{l}_1$ on the basis of (7.17), and repeat this proceeding for all possible $\mathbf{l}_1$. Compared exhaustive combination, the DP approach significantly reduces computational complexity, because according to (7.17) each non-root part can be treated *separately* during maximization. This eventually leads to a computational complexity which is quadratic in the pyramid size.

However, this complexity still is infeasible for typical image sizes. Therefore, Felzenszwalb et al. make use of a generalized distance transform, which makes it possible to reduce the complexity to be linear in the image size. The proceeding is described in more detail in [4], [5], and we give only a short summary here.

Briefly summarized, the modified proceeding rearranges (7.22) by calculating the quantities

$$D_{i,s}(x,y) = \max_{\mathrm{d}x,\mathrm{d}y} \left[\langle \mathbf{u}_i, \phi(H, x+\mathrm{d}x, y+\mathrm{d}y, s) \rangle - \langle \mathbf{w}_i, \mathbf{d}_i(\mathrm{d}x, \mathrm{d}y) \rangle \right] \tag{7.23}$$

which can be interpreted as the maximum possible contribution of part i to the overall score S, under the assumption that the root is located at position $\mathbf{l}_1$. Fixing $\mathbf{l}_1$ involves an expected location of part i at pixel $[x, y]$ (according to the offsets $\mathbf{v}_i$ learned during training) and pyramid level s (under consideration of the nominal offset vector $\mathbf{v}_i$ only, i.e., in absence of any deformation). The $D_{i,s}(x,y)$ are calculated by taking the dot product of the appearance model vector $\mathbf{u}_i$ with the concatenated HOG descriptors at position $[x+\mathrm{d}x, y+\mathrm{d}y]$ (first term in the argument of the max-operator), considering the deformation cost based on $[\mathrm{d}x, \mathrm{d}y]$ (second term in the argument of the max-operator), and maximizing this difference in a neighborhood around $[x, y]$. Hence, this operation propagates high appearance similarities to nearby locations under consideration of the deformation involved if we move away from the expected part location. By usage of the generalized distance transform, the $D_{i,s}(x,y)$ can be calculated in a time linear in the number of pixels. Now, the overall score can be calculated by summing the appearance similarity of the root part and the $D_{i,s}(x,y)$:

$$S(x_1, y_1, s_1) = \langle \mathbf{u}_1, \phi(H, x_1, y_1, s_1) \rangle + \sum_{i=2}^{M} D_{i,s_1-k}((x_1, y_1) - \mathbf{v}_i) \tag{7.24}$$

where k denotes the change of scale between the root and the object parts. Through rearranging (7.22) by the introduction of the $D_{i,s}(x,y)$, (7.24) can be maximized with a complexity being linear in the pyramid size.

In addition to that, generalized distance transforms can also be used for the calculation of optimal displacements $P_i = \left[\mathrm{d}x_i^*, \mathrm{d}y_i^*\right]$, which specify the optimal position of a part, if we already know the position $\left[x_1^*, y_1^*\right]$ of the root. This is needed in the backward step of DP optimization, when the optimal root position is known already and where we have to derive the optimal position for each part, given $\left[x_1^*, y_1^*\right]$. The optimal displacements are given by

$$P_i(x,y,s) = \operatorname*{arg\,max}_{\mathrm{d}x,\mathrm{d}y} \left[\langle \mathbf{u}_i, \phi(H, x+\mathrm{d}x, y+\mathrm{d}y, s) \rangle - \langle \mathbf{w}_i, \mathbf{d}_i(\mathrm{d}x, \mathrm{d}y) \rangle \right] \tag{7.25}$$

Hence, it is possible to store the $[\mathrm{d}x, \mathrm{d}y]$ which maximize (7.23) for every $D_{i,s}(x,y)$ and reuse this data in the DP backward step.

The whole recognition process is visualized in Fig. 7.14. Here, we want to localize humans in upright position. The model is depicted in the upper right, where we can see the HOG model of the root in its left picture (dominant gradient

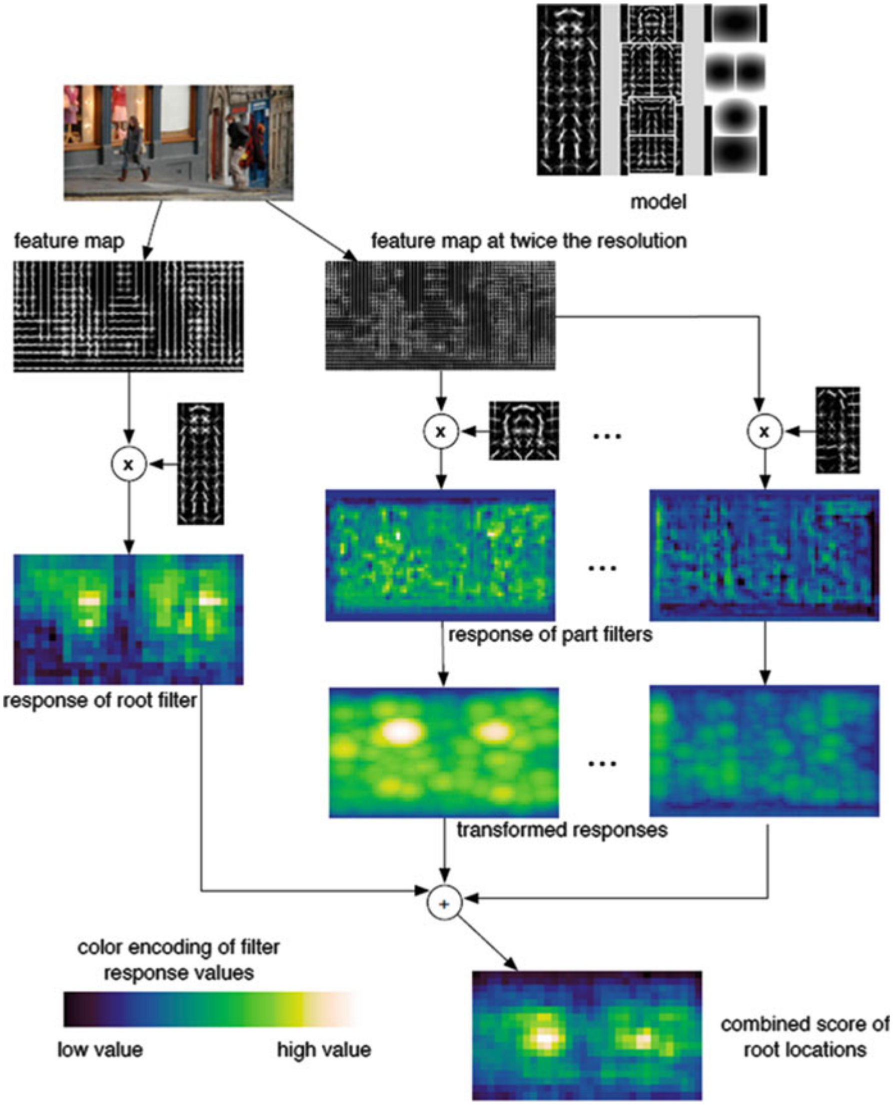

Fig. 7.14 Exemplifying the overall measurement flow in the recognition process of part-based pedestrian detection (© 2010 IEEE. Reprinted, with permission, from Felzenszwalb et al. [8])

orientations are marked as bold white line segments), the part models at finer resolution in the middle picture (five parts: head, right shoulder, left shoulder, thighs, and lower legs), and the deformation model in the right picture, where for each part a rectangle of "allowed" positions exists (bright positions indicate high, dark positions low deformation costs).

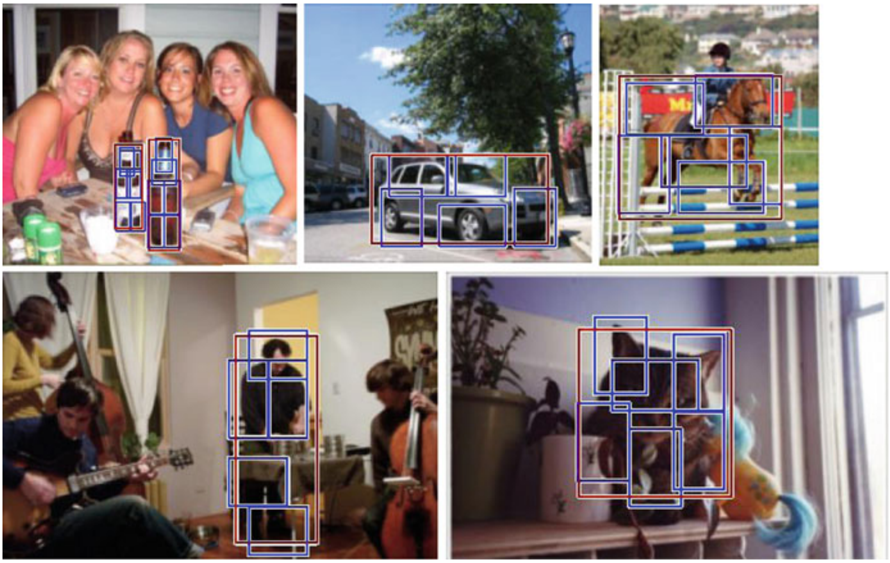

Fig. 7.15 Exemplifying the recognition performance for challenging images of various object classes: bottle, car, horse (*top row*), and person, cat (*bottom row*) (© 2010 IEEE. Reprinted, with permission, from Felzenszwalb et al. [8])

In a first step of the recognition phase, the feature maps at all levels of the image pyramid are calculated. Subsequently, these feature maps are used during the evaluation of the appearance similarity to the model by calculating the dot product according to (7.21) (exemplified here for the root, the head part and the right shoulder part). Observe that the resolution for the parts equals twice the resolution for the root. Bright location in the similarity filter responses indicate high similarity values (see color scale at the bottom left corner). Concerning the part similarities, they are transformed according to (7.23) before finally all similarity values are summed when calculating the overall score.

For this example we can see that there are two distinct maxima in the score function, which correctly correspond to locations of the searched human objects. Hence, we can easily detect multiple instances of the searched object class in one image. The only thing which has to be done is accepting all local maxima above a certain threshold instead of just searching the global maximum of the score function. Observe also that the head part is more discriminative than the right shoulder part.

In order to illustrate the recognition performance, some correctly detected objects are visualized as overlays in Fig. 7.15. The test images are taken from the Pascal VOC Challenge 2007 [12], which is acknowledged to be a challenging data set. In each image, the object position is indicated by a red rectangle, whereas the detected part positions are notified by a blue rectangle.

Pseudocode

```
function partbasedObjectRecgonition (in image $I$, in object model $\theta = (\mathbf{u}, E, \mathbf{v}, \mathbf{w})$, in threshold $t_{score}$, out object location list $\mathbf{L}^* = \left(L_1^*, L_2^*, \ldots, L_Z^*\right)$)

// build image pyramid
$I_1 \leftarrow I$            // set lowest level of pyramid to input image
for $s = 1$ to $K$            // $K$ : number of pyramid levels
   $I_G \leftarrow I_s * G$            // convolve $I_s$ with Gaussian kernel $G$
   calculate $I_{s+1}$ by subsampling of $I_s$ with factor $\lambda$
next

// build HOG feature pyramid
for $s = 1$ to $K$
   calculate gradient orientation image $I_{\varphi,s}$ and gradient magnitude image $I_{Mag,s}$
   for $y = 1$ to $H$ step 8 (cell size 8; $H$: image height)
      for $x = 1$ to $W$ step 8 (cell size 8; $W$: image width)
         set $H'(x,y,s)$ as gradient orientation histogram, based
         on $I_{\varphi,s}$ and weighted by $I_{Mag,s}$
      next
   next
   calculate $H(x,y,s)$ through normalization of $H'(x,y,s)$ with
   respect to 4 different blocks (of size 2x2 cells each)
   containing current cell
next

// forward DP step: calculate matching score function $S$
for $s = 1$ to $K$
   for $y = 1$ to $H$ step 8 (cell size 8; $H$: image height)
      for $x = 1$ to $W$ step 8 (cell size 8; $W$: image width)
         for $i = 1$ to $M$   // for each part (including root)
            calculate appearance similarity $m_i(x,y,s,\mathbf{u}_i)$ (7.21)
            if $i \neq 1$ then        // for every non-root part
               "spread" similarity to nearby locations,
               i.e. calculate $D_{i,s}(x,y)$ according to (7.23) with
               generalized distance transform
               calculate $P_i(x,y,s)$ (7.25) for subsequent backward
               DP step
            end if
         next
      next
   next
next
for $s = 1$ to $K$        // calculate optimal matching score contribution for each part i.
```

```
    for $y = 1$ to $H$ step 8 (cell size 8; $H$: image height)
        for $x = 1$ to $W$ step 8 (cell size 8; $W$: image width)
            calculate $S(x_1, y_1, s_1)$ acc. to (7.24)
        next
    next
next

// backward DP step: find all local max. $(L_1^*, L_2^*, \ldots, L_Z^*)$
find all local maxima $\mathbf{l}_{1,z}^*$ ( $z \in [1, 2, \ldots, Z]$ ) of root part above
similarity threshold $t_{score}$
for $z = 1$ to $Z$     // loop for all found position candidates
    for $i = 2$ to $M$    // for each part
        $\mathbf{l}_{i,z}^* \leftarrow P_i\left(\mathbf{l}_{1,z}^* + \mathbf{v}_{i,}, s_{1,z}^* - k\right)$
    next
next
```

References

1. Amini A, Weymouth T, Jain R (1990) Using dynamic programming for solving variational problems in vision. IEEE Trans Pattern Anal Mach Intell 12(9):855–867
2. Dalal N, Triggs B (2005) Histograms of oriented gradients for human detection. Comput Vis Pattern Recogn 1:886–893
3. Dijkstra EW (1959) A note on two problems in connection with graphs. Numer Math 1:269–271
4. Felzenszwalb P, Huttenlocher D (2004) Distance transform of sampled functions. Technical Report 2004-1963, Cornell University CIS
5. Felzenszwalb P, Huttenlocher D (2005) Pictorial structures for object recognition. Int J Comput Vis 61(1):55–79
6. Felzenszwalb P, Zabih R (2011) Dynamic programming and graph algorithms in computer vision. IEEE Trans Pattern Anal Mach Intell 33(4):721–740
7. Felzenszwalb P, McAllester D, Ramanan, D (2008) A discriminatively trained, multiscale, deformable part model. IEEE Conf Comput Vision Pattern Recogn 1:1–8
8. Felzenszwalb P, Girshick R, McAllester D, Ramanan D (2010) Object detection with discriminatively trained part-based models. IEEE Trans Pattern Anal Mach Intell 32(9):1627–1645
9. Fischler MA, Elschlager RA (1973) The representation and matching of pictorial structures. IEEE Trans Comput 22(1):67–92
10. Hart PE, Nilsson NJ, Raphael B (1968) A formal basis for the heuristic determination of minimum cost paths. IEEE Trans Syst Sci Cyb 4(2):100–107
11. Mortensen EN, Barett WA (1995) Intelligent scissors for image composition. In: Proceedings of the 22nd annual conference on computer graphics and interactive techniques. ACM Press, New York, pp 191–198
12. Everingham M, Van Gool L, Williams CKI, Winn J, Zisserman A (2007) The PASCAL Visual Object Classes Challenge 2007 (VOC 2007) results. [Online] http://www.pascal-network.org/challenges/VOC/voc2007/
13. Everingham M, Van Gool L, Williams C.K.I, Winn J, Zisserman A (2008) The PASCAL Visual Object Classes Challenge 2008 (VOC 2008) results. [Online] http://www.pascal-network.org/challenges/VOC/voc2008/

Index

M.A. Treiber, *Optimization for Computer Vision: An Introduction to Core Concepts and Methods*, Advances in Computer Vision and Pattern Recognition,
DOI 10.1007/978-1-4471-5283-5, © Springer-Verlag London 2013